TECHNISCHE
UNIVERSITÄT
WIEN
Vienna | Austria

Dissertation

Structure, Dynamics, and Electrochemistry of Covalently Modified Gold Surfaces

Ausgeführt zum Zwecke der Erlangung des akademischen Grades eines Doktors der
technischen Wissenschaften unter der Leitung von
Univ. Prof. Dr. Stijn F.L. Mertens
und Co-Leitung von
Univ. Prof. Dipl.-Ing. Dr.techn. Markus Valtiner
Institut für Angewandte Physik, E134

eingereicht an der Technischen Universität Wien
Fakultät für Physik

von

Mandana Azmi

Matrikelnummer: 01636715

July 2025

Abstract

The electrochemical properties of an electrode can be modified by the chemical adsorption of species onto its surface. Future molecular and hybrid electronics, therefore, depend on the mastery of chemical binding between dissimilar materials down to the individual bond. Only with a clear understanding of the adsorption and bonding of both inorganic and carbonaceous materials can new materials and devices be developed, with wide-reaching applications such as electrocatalysis, energy storage, sensors, and corrosion protection.

Although covalent grafting using diazonium chemistry on mostly carbonaceous surfaces is widely reported in the literature, direct covalent carbon-metal bonds have been relatively less studied. In this dissertation, we present a detailed study of the covalent grafting of aryl radicals on single- and polycrystalline gold surfaces and investigate their electrochemical stability and oxidative desorption. Voltammetry in a redox electrolyte is used to explore the barrier properties of the resulting layers and to inquire under which conditions ultramicroelectrode array behavior can be observed. Copper underpotential deposition and Gaussian deconvolution of its current-potential trace were used to map the thermodynamic and kinetic landscape of the modified Au surface and to check for signs of metal intercalation and other nanoscale effects. Electrochemical impedance measurements, principally requiring a time-invariant system, are integrated with an intermittent grafting/open circuit potential protocol to allow *operando* monitoring of the grafting process. Scanning tunneling microscopy in a high-boiling point organic solvent suggests that grafting is accompanied by the formation of vacancy islands on the Au surface, while iodide adsorption heals these vacancies, enabling high-contrast imaging of individual covalent grafts.

Here, we investigate the structure and dynamics of structural changes in the iodine adlayer adsorbed on Au(111) at varying potentials over time using electrochemical scanning tunneling microscopy (EC-STM). While the structure of iodine on the Au(111) surface has been extensively studied, we focus our EC-STM study on the bright chains on the surface previously identified as polyiodide. In this study, the chains' identity is revisited, and the dynamic changes of these polymers at the surface are explored.

Zusammenfassung

Die elektrochemischen Eigenschaften einer Elektrode können durch die chemische Adsorption von Spezies auf ihrer Oberfläche verändert werden. Zukünftige molekulare und hybride Elektronik hängt daher von der Beherrschung der chemischen Bindung zwischen ungleichen Materialien bis hin zur einzelnen Bindung ab. Nur mit einem klaren Verständnis der Adsorption und Bindung sowohl anorganischer als auch kohlenstoffhaltiger Materialien können neue Materialien und Geräte mit weitreichenden Anwendungen wie Elektrokatalyse, Energiespeicherung, Sensoren und Korrosionsschutz entwickelt werden.

Obwohl kovalente Pfropfung mittels Diazoniumchemie auf meist kohlenstoffhaltigen Oberflächen in der Literatur ausführlich beschrieben wird, wurden direkte kovalente Kohlenstoff-Metall-Bindungen relativ wenig untersucht. In dieser Dissertation präsentieren wir eine detaillierte Studie der kovalenten Pfropfung von Arylradikalen auf ein- und polykristallinen Goldoberflächen und untersuchen ihre elektrochemische Stabilität und oxidative Desorption. Die Voltammetrie in einem Redoxelektrolyten wird verwendet, um die Barriereeigenschaften der resultierenden Schichten zu untersuchen und um herauszufinden, unter welchen Bedingungen das Verhalten von Ultramikroelektrodenarrays beobachtet werden kann. Die Unterspannungsabscheidung von Kupfer und die Gaußsche Dekonvolution seiner Strom-Spannungs-Kurve wurden verwendet, um die thermodynamische und kinetische Landschaft der modifizierten Au-Oberfläche abzubilden und nach Anzeichen von Metallinterkalation und anderen Nanoeffekten zu suchen. Elektrochemische Impedanzmessungen, die grundsätzlich ein zeitinvariantes System erfordern, werden in ein Protokoll für intermittierendes Pfropfen/offenes Stromkreispotential integriert, um eine operando-Überwachung des Pfropfprozesses zu ermöglichen. Rastertunnelmikroskopie in einem hochsiedenden organischen Lösungsmittel lässt darauf schließen, dass das Pfropfen mit der Bildung von Leerstelleninseln auf der Au-Oberfläche einhergeht, während die Iodid-Adsorption diese Leerstellen heilt und so eine kontrastreiche Abbildung einzelner kovalenter Pfropfungen ermöglicht.

Hier untersuchen wir die Struktur und Dynamik struktureller Veränderungen in der Iod-Adsorptionsschicht, die auf Au(111) bei unterschiedlichen Potentialen über die Zeit adsorbiert wird, mithilfe elektrochemischer Rastertunnelmikroskopie (EC-STM).

Während die Struktur von Iod auf der Au(111)-Oberfläche bereits umfassend untersucht wurde, konzentrieren wir uns bei unserer EC-STM-Studie auf die hellen Ketten auf der Oberfläche, die zuvor als Polyiod identifiziert wurden. In dieser Studie wird die Identität der Ketten erneut untersucht und die dynamischen Veränderungen dieser Polymere an der Oberfläche erforscht.

Acknowledgements

The journey towards this PhD presented numerous challenges, including relocating from Austria to the UK, establishing a new lab, adapting to a project change, navigating the significant experimental limitations imposed by the Corona lockdown, and ultimately returning to Austria without a research group. Completing this journey would not have been possible without the support of several key individuals, whom I wish to acknowledge.

I am grateful to my primary supervisor, Stijn Mertens, currently at Lancaster University. His guidance, along with the practical insights from colleagues Matthias Müllner and Iris Dorner during my time within his group, which was then part of the Surface Physics group, were invaluable during my initial years. I am thankful to Ulrike Diebold, who not only welcomed me into her group but also provided insightful advice and support during a challenging time. I also appreciate the opportunity to observe and learn from her successful research group specializing in UHV systems. My sincere thanks also go to Michael Schmid, whose expertise and patience were instrumental in resolving technical issues and for his dedication to teaching scientific concepts. I am also grateful to Shahin Nikman, who was essential in setting up the lab at Lancaster University.

I would like to express my gratitude to Markus Valtiner and Laura Mears, whose involvement in the later stages of my PhD provided significant support and encouragement.

My heartfelt thanks extend to my family and friends, whose unwavering support was crucial throughout this process.

Finally, I gratefully acknowledge the Austrian Science Fund (FWF) for partially funding this research.

Contents

Abbreviations

AFM	**a**tomic **f**orce **m**icroscopy
STM	**s**canning **t**unneling **m**icroscopy
EC-STM	**e**lectrochemical **s**canning **t**unneling **m**icroscopy
SHE	**s**tandard **h**ydrogen **e**lectrode
RHE	**r**eversible **h**ydrogen **e**lectrode
SCE	**s**aturated **c**alomel **e**lectrode
EIS	**e**lectrochemical **i**mpedance **s**pectroscopy
CV	**c**yclic **v**oltammetry
CA	**c**hrono**a**mperometry
OCP	**o**pen **c**ircuit **p**otential
UPD	**u**nder**p**otential **d**eposition
OPD	**o**ver**p**otential **d**eposition
CPE	**c**onstant **p**hase **e**lement
DOS	**d**ensity **o**f **s**tates
XPS	**X**-ray **p**hotoelectron **s**pectroscopy
FFT	**f**ast **F**ourier **t**ransform
EQCM	**e**lectrochemical **q**uartz **c**rystal **m**icrobalance
SAM	**s**elf-**a**ssembled **m**onolayer
ML	**m**ono**l**ayer
SERS	**s**urface-**e**nhanced **R**aman **s**pectroscopy
UHV	**u**ltra-**h**igh **v**acuum
HOPG	**h**ighly **o**riented **p**yrolytic **g**raphite

Chapter 1

Introduction and Motivation

The strong adsorption and covalent attachment of molecules or films to the surface offer technologically exploitable surface modifications. The control over modifying the surfaces has enabled scientists to find new properties that are different from those of unmodified (electrode) surfaces. These new properties can build a base for new applications and improve (electrochemical) devices [1]. The adsorption of species to modify the electrode is strong and sometimes irreversible. These modified electrodes are frequently called chemically modified electrodes, which can often change the electrochemical properties of the electrode. Different methods exist for chemically modifying the electrode, including modifications via reduction of diazonium salt and self-assembled monolayer (SAM) formation [2]. Another example of chemisorption is the adsorption of halides such as Cl^-, Br^-, and I^- at the metal-electrolyte interface. Although SAMs, especially thiols on noble metals, were one of the most extensively studied systems in the 1980s and 1990s [3–6], and also covalent grafting using diazonium chemistry on mostly carbonaceous surfaces is characterized by a vast literature [7–13], direct covalent carbon-metal bonds have been relatively less studied.

1.1 Covalent modification of electrode by reduction of diazonium salt

The modified surfaces with reduction of diazonium salt have applications in sensing and biosensing [14, 15] formation of composites [7, 16], modification of nanomaterials [17, 18], electronics and molecular electronics [19, 20], energy storage [21], electrocatalysis [22, 23], and corrosion resistance [24, 25].

The covalent modification by reduction of diazonium salt was developed by the pioneering work of Saveant and Pinson [26]. In such a process the reduction of diazonium cations leads to the elimination of N_2 molecules and the formation of free radicals in the vicinity of the surface where they can make covalent bonds to the surfaces or so-called graft onto the surface [27]. This procedure can lead to the formation of either a monolayer or a multilayer. The Schematic of surface modification via diazonium salt reduction is illustrated in Figure 1.1.

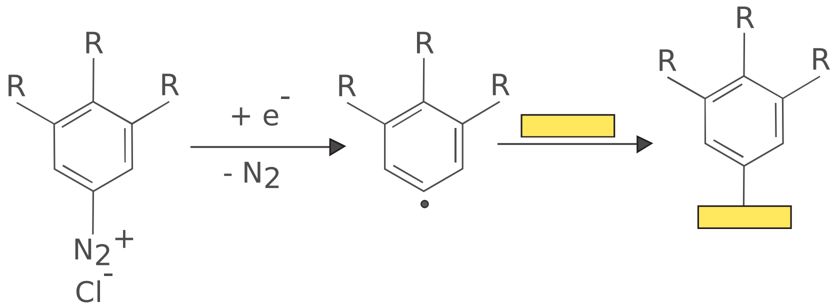

FIGURE 1.1: Schematic illustration of the one-electron reduction process of diazonium salts for the generation of free aryl radicals to attack the surface and make a covalent bond to it.

Covalent modification by reduction of diazonium salt is one of the most attractive methods for surface modification because it is a fast and easy method that can be used for a wide range of surfaces including metals, oxides, carbon, and semiconductors [7, 11, 28–35]. Moreover, it does not involve oxidative conditions that can lead to damaging oxidation of substrates, specifically carbon, which produces larger background currents in electrochemical measurements [7, 26, 36]. The possibility of grafting the surface with a wide variety of functional aryl groups is another useful property of the method. Today, many diazonium salts are commercially available or can be easily synthesized from aromatic amines. The covalently bound organic film shows good thermal and mechanical stability. For instance, the thermal stability of 4-nitrophenyl modified carbon black by *in situ* generated diazonium salt was studied and thermogravimetric analysis (TGA) showed that a temperature above 200 °C is needed to break most of these bonds [37]. Another study on the covalently aryl group bonded to HOPG reveals that bond cleavage starts at temperatures below 200 °C, and at 200 °C almost all the bonds are broken, and breakdown products remain physisorbed on the surface[38].

The covalent bond formed on carbon electrodes via the reduction of diazonium salt shows high stability to ultrasonication in various solvents, including ethanol, benzene, benzonitrile, dimethylformamide, and trichloroethane. The covalent bond formed on the carbon is strong enough that leaving the electrode on the laboratory bench for several months will not affect it [26]. The grafted carbon surface is electrochemically stable in the potential range between -2 and 1.8 V vs Ag/AgCl (saturated KCl) 0.1 M KCl at pH 7 [8] and the covalently bonded molecules would not leave the surface by evolution of gases (such as H_2, O_2 and/or Cl_2) at extremely negative and positive potentials [8].

Although grafting the surface with diazonium salt reduction has many advantages such as high thermal, mechanical, and electrochemical stability [8, 26, 37, 38], it suffers from a big drawback which is the formation of disordered multilayers up to several micrometer thicknesses. The free radicals produced from the diazonium salt reduction not only make a covalent bond to the surface but can also attach themselves to the already attached graft molecules and form a multilayer. The multilayer is intertwined, disordered, and has an ill-defined structure (Fig. 1.2).

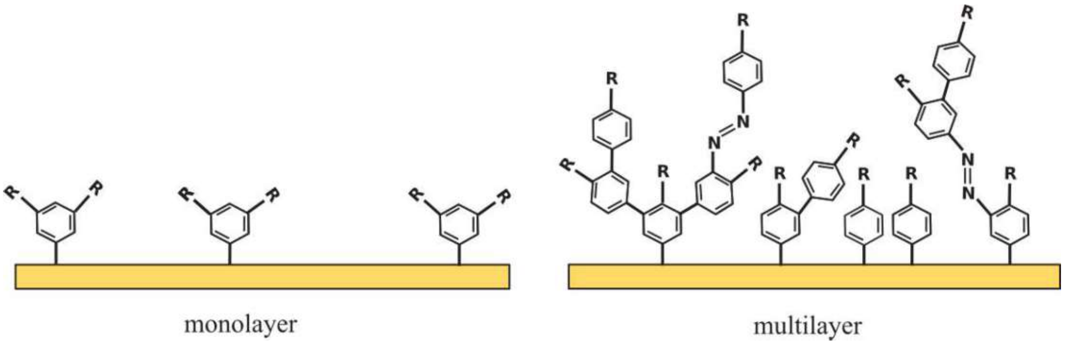

FIGURE 1.2: Monolayer and multilayer formed via reduction of the diazonium salt on a generic substrate.

The studies showed that using certain aryldiazoniums with sterically encumbered substituents on the aryl ring can lead to monolayer formation [39, 40]. The diazonium molecules with bulky substituents at 3- and 5- positions on the aryl ring can prevent multilayer formation. The free aryl radicals cannot attack the 2- and 6- positions of the aryl ring already bonded to the surface, as they are sterically protected via the surface material. Moreover, the two bulky substituents at 3- and 5- positions make attachment of free radicals to the 4-position (or para position) disfavored (Fig. 1.3). Therefore, only a monolayer can form on the surface. For example, 3,5-bis-*tert*-butylbenzenediazonium (3,5-TBD) ions form a monolayer, while

4-nitrobenzenediazonium (4-NBD) ions form a multilayer [39, 40]. The substituents at positions 3 and 5 must be sufficiently bulky to inhibit multilayer formation. For example, the reduction of 3,5-trifluoromethylbenzenediazonium and pentafluorobenzenediazonium salts leads to the formation of multilayers rather than a monolayer [39].

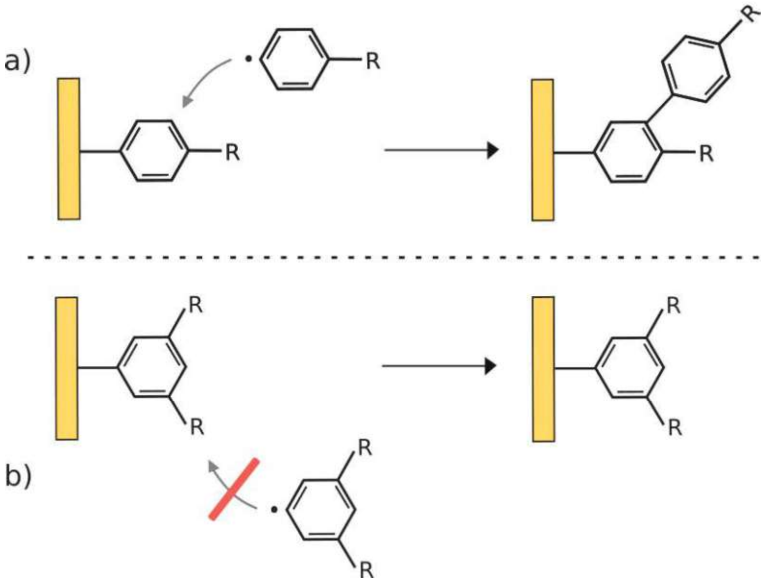

FIGURE 1.3: Attack of an aryl radical on an attached aryl. While the attack of the free radicals to the 3- and 5- positions on the 4- substituted aromatic ring attached to the surface is favored (a), the attack to the 4- position on the 3- and 5- substituted aromatic ring attached to the surface is disfavored (b).

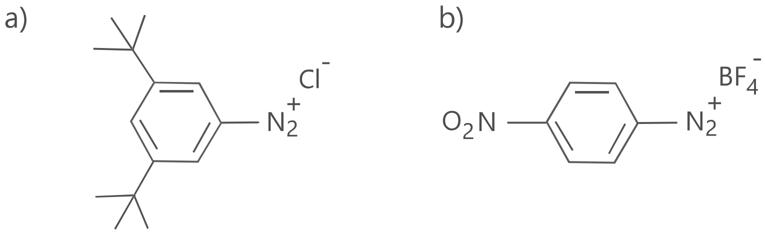

FIGURE 1.4: Chemical structures of: a) 3,5-bis-*tert*-butylbenzenediazonium (3,5-TBD) chloride, b) 4-nitrobenzenediazonium (4-NBD) tetrafluoroborate.

The fact that the sterically hindered 3,5-TBD leads to strict (sub)monolayer formation is important, as we learn more about true interfacial aspects of the grafting and the resulting modified surface. Early work almost without exception dealt with 4-substituted diazonium precursors (e.g., nitrobenzene) that unavoidably yielded a difficult-to-control level of multilayer formation, resulting in highly convoluted behavior that is hard to quantify [7]. The structures of the 3,5-TBD and 4-NBD are shown in Figure 1.4.

There are several methods for reducing diazonium cations, and the most efficient technique is electrochemical reduction or electrografting. The electrochemical reduction can be performed by either cyclic voltammetry or holding the potential at a constant value for a certain period (i.e., chronoamperometry). Several parameters control the thickness of the grafted layer, including the concentration of the diazonium salt, grafting time, potential, type of diazonium, and substrate [40].

Another grafting technique is spontaneous grafting or covalent grafting at open circuit potential (OCP) that can be achieved by simple immersion of substrates in the diazonium salt solution for a relatively long time (for at least 1 hour) [41–43]. The grafted film made by spontaneous grafting is generally thinner and consequently has lower blocking properties [41]. This method is useful, especially for modification of the powders such as carbon black [44] and gold nanoparticles [45] or nanotubes like single-walled carbon nanotubes [46] because the immobilization on the electrode can be eliminated. Furthermore, it can be simply done in any lab, without a potentiostat. The grafting at OCP has been reported for a limited number of surfaces [47]. Besides the redox properties of the substrate, the redox properties of the diazonium have an impact on the grafting process [41]. Studies showed that along with the substrate and the diazonium electronic properties of para-substitutes (with electron-donor or withdrawing), solvent (acid or ACN) [48, 49], temperature, time of immersion and the concentration of diazonium can control the thickness of the final film [41]. Moreover, adding reducing agents can reduce diazonium and graft the surface without applying any potential [35, 50, 51].

In addition to electrochemical, spontaneous, and chemical methods for diazonium reduction, photochemical approaches [52–54] and less common techniques, such as ultrasonication, heating, microwave treatment, and ball milling, have been reported for surface grafting [55].

1.2 Chemisorption of halides at the metal-electrolyte interface

The adsorption of halides can considerably alter the electrochemical reactivity of the metal substrate, for instance, in the deposition and dissolution of metals [56]. Studies have shown that the addition of Cl^-, Br^- can significantly modify the growth mode of bulk deposition of Pb on polycrystalline Au and Cu by blocking Pb nucleation sites [57, 58]. The presence of specifically adsorbed halides can also improve CO_2 electroreduction on Cu [59, 60] and, inhibit oxygen reduction and hydrogen oxidation reaction on Pt and Au single crystals [61–63]. Besides that, the pre-adsorbed halide adlayer on the surface of single crystal electrodes can be used as a platform for formation of highly ordered arrays of organic molecules which can be visualized by *in situ* STM [64–72]. A recent study showed that the electrocatalytic activity of iron(II) phthalocyanine for the oxygen reduction reaction can improve on an I-modified Au(111) surface [73]. Therefore, detailed information on the structure of the halide adlayer and its impact on electrochemical reactivity is crucial for understanding the fundamental microscopic mechanisms driving these reactions.

The adsorption of weakly solvated halide ions at the metal-electrolyte, Cl^-, Br^-, and I^-, is considered chemisorption. Because these ions can shed part of their solvation layer closest to the surface and form a chemical bond with it. The adsorption of these ions onto the surface is known as specific adsorption [74]. Among the three halides, the adsorption of iodide on the Au(111) electrode surface is the strongest, and the chemical bond exhibits the highest degree of covalent character [75].

The oxidative chemisorption of iodides on Au(111) surface results in the formation of essentially uncharged iodine adatoms [76]. Iodine adsorption on Au(111) has been studied extensively using various surface techniques, particularly scanning tunneling microscopy (STM) [77–82] and low-energy electron diffraction (LEED) [80, 83–85]. The structures of iodine on the gold surface at different potentials in electrolytes have been analyzed with electrochemical scanning tunneling microscopy (EC-STM) [72, 78, 79, 84, 86]. Surface-enhanced Raman spectroscopy (SERS) studies have shown that during the electrooxidation of iodide solution, both triiodide ($I_3{}^-$) and molecular iodine (I_2) are formed, serving as building blocks for polyiodides [87, 87, 88]. An EC-STM study demonstrated that these polyiodides form chain-like structures on the Au(111) surface [78]. The formation of chains on the surface has received little attention [89–91], despite the extensive reports on the structure of iodine adlayers at different potentials.

1.3 Goals and questions

Given the state of the research as described above, my thesis is based on the following scientific questions regarding the adsorption of grafted molecules and polyiodide on the Au surface:

- How are the electrochemical stability and blocking properties of the film modified by reductive electrografting of diazonium salt 3,5-TBD on polycrystalline Au? Under what conditions does the grafted surface with local defects behave as an ultramicroelectrode array?
- What information can be obtained from underpotential deposition (upd) of copper on the grafted Au(111)? What is the possible configuration of the overpotentially deposited copper on grafted Au(111)?
- Can we achieve a molecular resolution of the grafts on the Au(111) surface?
- Can electrochemical impedance spectroscopy (EIS) be used as an *operando* technique to reveal what happens on the surface of the polycrystalline Au during the grafting procedure?
- What are the chains seen in the EC-STM images recorded in the presence of iodide solution on Au(111) at different potentials? Are these adsorbed polyiodides?

This thesis is organized into chapters dedicated to exploring the scientific questions. The following paragraphs provide an overview of the focus and contributions of each chapter.

In Chapter 2, the experimental methods and in Chapter 3 the experimental setups and procedures used to prepare and characterize the samples are explained.

In Chapter 4, the fundamental aspect of grafted surfaces is studied by investigating Au surfaces grafted via the reduction of 3,5-TBD. The electrochemical stability of the grafts and oxidative desorption are analyzed by measuring cyclic voltammetry. The effect of the grafts on the voltammetric response in a supporting electrolyte and in the presence of redox species is investigated.

In Chapter 5, we combine single-crystal voltammetry of grafted Au (111) with Cu upd to pursue a molecular-scale understanding of grafting. While an ensemble-averaging technique, upd shows exceptional sensitivity for surface crystallography and other features, and has the advantage of scalability over scanning probe techniques of investigation, allowing for integration over macroscopic areas and curved structures that elude microscopies [92].

In Chapter 6, we image the grafted Au(111) surface with STM, under ambient conditions in different liquids, aiming to achieve molecular resolution of the grafts. Moreover, we also perform EC-STM on the grafted Au(111) in an iodide electrolyte at different potentials.

In Chapter 7, EIS is used to compare the electrode surface before and after surface modification. However, in this work, we use electrochemical impedance spectroscopy as an *operando* technique to study the grafting procedure in real time.

In Chapter 8, we investigate the structure and the dynamics of structural changes in the iodine adlayer on Au(111) at varying potentials over time using EC-STM. In this chapter, we explore the origin of these chains and discuss the possibility that they may consist of polyiodide species.

In Chapter 9, the main results are summarized and an outlook for further work is provided.

Chapter 2

Experimental Methods

This chapter introduces some fundamental concepts of electrochemistry, following the notation by Girault [93]. It also explains the electrochemical methods used in this thesis. Moreover, the basics of scanning tunneling microscopy and electrochemical scanning tunneling microscopy are discussed. The final section provides a brief introduction to Raman spectroscopy.

2.1 Electrochemical potentials

In thermodynamics, for a chemical system, the change in the Gibbs energy ΔG determines the direction of the chemical reaction. If $\Delta G \leq 0$, the reaction is spontaneous, and if $\Delta G > 0$, the reaction is non-spontaneous; therefore, external energy is needed for the reaction to occur. At chemical equilibrium at constant pressure and temperature, $\Delta G = 0$. The partial derivative of the Gibbs energy with respect to species j at constant pressure and temperature is the chemical potential potential μ of a species j is μ_j. In other words, μ_j is the Gibbs energy per mole of species j.

$$\mu_j = \left(\frac{\partial G}{\partial n_j}\right)_{T,p,n_i \neq n_j} \tag{2.1}$$

The change of Gibbs energy associated with the conversion of ν_j moles of reactants to products is written as

$$\Delta G = \Sigma_{prod}\nu_j\mu_j - \Sigma_{react}\nu_j\mu_j \tag{2.2}$$

In chemical thermodynamics, there is an equation that relates the chemical potential of a system in a standard state, to a real by employing a parameter called activity a

$$\mu_j = \mu_j^0 + RT\ln a_j \tag{2.3}$$

μ_j^0 is the standard chemical potential and a_j is the activity of the species j. Thus, the activity of the species j can determine the chemical potential of j. The value of the activity is related to concentration, c, following Equation 2.4. In this thesis, the concentration is represented by a lowercase c to distinguish it from capacitance, which is denoted by an uppercase C.

$$a_j = \gamma_j\, c_j \tag{2.4}$$

Where γ_j is a dimensionless activity coefficient. For an electrochemical system, the presence of the charged ions and electrostatic field must be considered. Therefore, for an electrochemical system, the electrochemical potential $\tilde{\mu_j}$ of ion j, consists of two terms. First term is chemical potential of j and the second term, $z_jF\phi$, is the electrical energy of the species j

$$\tilde{\mu_j} = \mu_j + z_jF\phi \tag{2.5}$$

Where z_j is the charge, F is Faraday constant ($96\,485\ \mathrm{C\,mol^{-1}}$) and ϕ is the potential of a certain phase in which j is found. The ϕ is defined as the inner potential of a phase or Galvani potential which is equal to the sum of surface and outer potential ($\phi = \chi + \psi$). Therefore, based on Equation 2.3 and Equation 2.5 the electrochemical potential is

$$\tilde{\mu_j} = {\mu_j}^0 + RT\ln a_j + z_jF\phi \tag{2.6}$$

The electrochemical potential can also be defined as the partial molar Gibbs energy of species j at the specified electric potential.

$$\tilde{\mu_j} = \left(\frac{\partial G}{\partial n_j}\right)_{T,p,n_i \neq n_j} \tag{2.7}$$

The electrochemical potential of a charged species in a standard state is standard electrochemical potential defined as

$$\tilde{\mu_j}^0 = \mu_j{}^0 + z_j F \phi \tag{2.8}$$

The redox reaction at a metal electrode M in solution S containing the redox couple is shown by

$$\mathrm{OX^S + ne^{-M} \rightleftharpoons Red^S} \tag{2.9}$$

Ox^S and Red^S are referred to as oxidized and reduced species in solution, respectively. The n is the number of electrons transferred between metal M and species. In electrochemical equilibrium $\tilde{\Delta G} = 0$ and like equation 2.2 for chemical reaction, we have

$$\tilde{\Delta G} = \tilde{\mu}^S_{Red} - (n\tilde{\mu}^M_e + \tilde{\mu}^S_{Ox}) = 0 \tag{2.10}$$

By combining Equation 2.10 and Equation 2.6 we have

$$[\mu^{0,S}_{Red} + RT \ln a_{Red}{}^S + z_{Red} F \phi^S] - n[\mu^M_e - F\phi^M] - [\mu^{0,S}_{Ox} + RT \ln a_{Ox}{}^S + z_{Ox} F \phi^S] = 0 \tag{2.11}$$

$\mu^{0,S}_j$ is the standard chemical potential and a^S_j is the activity of the species j in the molarity scale. The number of exchanged electrons is $n = z_{Ox} - z_{Red}$, hence it can be written as

$$nF(\phi^M - \phi^S) = (\mu^{0,S}_{Ox} - \mu^{0,S}_{Red} + n\mu^{0,M}_e) + RT \ln \frac{a^S_{Ox}}{a^S_{Red}} \tag{2.12}$$

Where $(\phi^M - \phi^S)$ is the Galvani potential difference between the metal and the solution. $F(\phi^M - \phi^S)$ is defined as electrical work required for transferring one mole of elementary charge from the inside of the metal to the bulk solution. The Equation 2.12 can be simplified into

$$nF(\phi^M - \phi^S) = -\Delta G^0 + RT \ln \frac{a^S_{Ox}}{a^S_{Red}} = -\Delta G \tag{2.13}$$

Where ΔG^0 is the standard Gibbs energy and ΔG is the chemical contribution of the Gibbs energy in redox reaction at electrodes. Therefore, based on Equation 2.13, the Galvani potential difference and the activity (ca. concentration) of the species in the solution are major characteristics of the redox reaction. The equilibrium constant K_e for a redox equilibrium is defined as

$$K_e = \frac{a^S_{Red}}{a^S_{Ox}} = \exp\left(\frac{-\Delta G^0}{RT}\right) \exp\left(\frac{-nF(\phi^M - \phi^S)}{RT}\right) \tag{2.14}$$

Which K_e is changed by the difference in inner potential between the electrode and the solution [93].

2.2 Nernst equation for redox electrodes

When a metal M is placed in the solution containing ions of that metal, eventually an equilibrium is established. For example, for a copper wire placed in the aqueous copper sulfate

$$\mathrm{Cu^{2}\,(aq) + 2\,e^{-}\,(M)} \rightleftharpoons \mathrm{Cu^{0}} \tag{2.15}$$

At the equilibrium condition, following 2.16

$$\tilde{\mu}_{Cu}(M) = \tilde{\mu}_{Cu^{+2}}(aq) + 2\ \tilde{\mu}_{e^-} \tag{2.16}$$

By assuming that for the copper atoms in the metal to be neutral $\tilde{\mu}_{Cu} = \mu_{Cu}$, then Equation 2.16 is written as

$$\mu^0_{Cu}(M)+RT\ln a_{Cu}(M) = {\mu^0}_{Cu^{2+}}+RT\ln a_{Cu^{2+}}+2F\phi^S+2{\mu^0}_{e^-}(M)+2RT\ln a_{e^-}-2F\phi^M \tag{2.17}$$

Since $\ln a_{Cu}$ and $\ln a_{e^-}$ are zero, it can be rearranged into

$$\Delta\phi \equiv \phi^M - \phi^S = \frac{{\mu^0}_{Cu^{2+}} + 2{\mu^0}_{e^-} - \mu^0_{Cu}}{2F} + \frac{RT}{2F}\ln a_{Cu^{2+}} \equiv \Delta\phi^0 + \frac{RT}{2F}\ln a_{Cu^{2+}} \tag{2.18}$$

Where $\Delta\phi^0$ is the standard Galvani potential difference in case $a_{Cu^{2+}} = 1$. $\Delta\phi^0$ and $\Delta\phi$ are not experimentally measurable, another electrode with a constant Galvani potential difference, $\Delta\phi'$, is needed. In this case, the potential at the main electrode (working electrode) to the second electrode (reference electrode) can be measured ($E = \Delta\phi - \Delta\phi'$). The standard electrode potential at a unit activity is E^0 that $E^0 = \Delta\phi^0 - \Delta\phi'$, thus

$$E - E^0 = \Delta\phi - \Delta\phi^0 \tag{2.19}$$

By combining Equation 2.18 and Equation 2.19 we can write that

$$E = E^0 + \frac{RT}{2F}\ln a_{Cu^{2+}} \tag{2.20}$$

Equation 2.20, in general form, is used for calculating the potential of a metal electrode in a solution containing its ions M^{n+}

$$E = E^0 + \frac{RT}{nF}\ln a_{M^{n+}} \tag{2.21}$$

Besides the metal-ion electrode mentioned above, the electrode potential for a system consisting of an inert electrode immersed in a solution containing oxidized and reduced forms of species can also be predicted. For the general case of redox reaction at equilibrium condition, we have

$$\nu_{\mathrm{Ox}}\,\mathrm{Ox} + \mathrm{ne}^- \rightleftharpoons \nu_{\mathrm{Red}}\,\mathrm{Red} \tag{2.22}$$

As for the case of the metal-ion electrode, it is only possible to measure the Galvani potential difference to a reference electrode. Therefore

$$E = E^0 + \frac{RT}{nF} \ln \frac{a_{Ox}^{\nu_{Ox}}}{a_{Red}^{\nu_{Red}}} \tag{2.23}$$

This is known as the Nernst equation, where E^0 is the standard electrode potential of the Ox/Red couple and a is the activity of oxidized and reduced forms. R is the gas constant (R= 8.3144 $\mathrm{JK^{-1}mol^{-1}}$), T the temperature in Kelvin, and n the number of electrons transferred, and F is the Faraday constant (F=96 485 $\mathrm{C\,mol^{-1}}$). At equilibrium conditions, at which no current flows through the cell, E is measured at a working electrode versus a reference electrode and is called open circuit potential (OCP). Since there is no knowledge about the relevant activity coefficients and their concentration dependence, the formal potential, E_f^0, is introduced, where

$$E_f^0 = E^0 + \frac{RT}{nF} \ln \frac{\gamma_{Ox}}{\gamma_{Red}} \tag{2.24}$$

Thus, the Nernst equation and its dependence on the concentration of reactants and products is written as

$$E = E_f^0 + \frac{RT}{nF} \ln \frac{c_{Ox}}{c_{Red}} \tag{2.25}$$

2.3 Electrochemical kinetics

The current or electrode reaction rate is governed by the rate of two major processes of mass transport and the electron transfer at the electrode surface (electrode kinetics). The two processes are illustrated in Figure 2.1. The rate of these two processes determines the overall rate of an electrochemical process. When the mass transfer(rate) is faster than the electron transfer reaction, the reaction is said to be irreversible, and when the electron transfer is faster than the electron transfer is said to be reversible. In the latter case, the Ox/Red activity ratio at the electrode-electrolyte interface is always adequately described by the (equilibrium) Nernst equation, hence the term 'reversible'. If the mass transfer and the electron transfer occur in comparable time scales, the reaction is known as quasi-reversible [93].

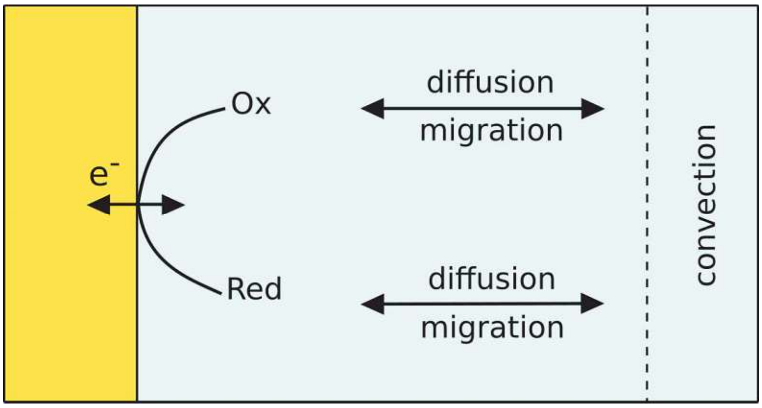

FIGURE 2.1: Electron transfer and mass transport. Adapted from [93] with permission from EPFL Press.

The mass transfer of reactants to the electrode and products away from the electrode occurs through three mechanisms: diffusion, migration, and convection. The diffusion is considered as the major mechanism of mass transport in many electrolysis reactions. Based on Fick's first law (Eq. 2.26), diffusion occurs because of a concentration gradient.

$$j = -D\frac{\partial c}{\partial x} \tag{2.26}$$

Where j is the flux (mol cm^{-2} s^{-1}), D the diffusion coefficient (cm^2 s^{-1}) and $\frac{\partial c}{\partial x}$ is the local concentration gradient at point x. The change of the concentration with time is explained by Fick's second law (Eq. 2.27).

$$\frac{\partial c}{\partial t} = D\frac{\partial^2 c}{\partial x^2} \tag{2.27}$$

The redox reaction and consequently transfer of electrons at the electrode surface leads to the passage of an electric current. The corresponding anodic current I_a and cathodic current I_c follow

$$I_a = nFAk_a c_R(0) \tag{2.28}$$

$$I_c = -nFAk_c c_O(0) \tag{2.29}$$

Where A is the electrode area. In the equations above the current I with unit of amp can change into current density j ($j = \frac{I}{A}$) with a unit of $\mathrm{A\,cm^{-2}}$. The $c_O(0)$ and $c_R(0)$ are reactant concentrations at the surface. The concentration of reactants at the electrode surface is generally different from that in the bulk solution. The electrochemical rate constants for oxidation (k_a) and reduction (k_c), both potential-dependent, have units of $\mathrm{cms^{-1}}$. For an ideal solution in the standard case, the bulk concentrations of the reduced and oxidized forms are equal $c_O(\infty) = c_R(\infty)$ and because the activity coefficients are equal to unity, therefore the equilibrium potential is equal to E^0. At equilibrium, if we assume the mass transport is infinitely rapid, the rate of oxidation and reduction rates can be assumed equal $k_a c_R(0) = k_c c_O(0)$ and it can also be assumed that the concentration of the reactants at the surface and in the bulk is the same. In such a case $k_a = k_c = k^0$ which k^0 is the standard rate constant. Based on the transition state theory

$$k^0 = \delta\Big(\frac{KT}{h}\Big)\exp\Big(\frac{-\Delta G^0_{act}}{RT}\Big) \tag{2.30}$$

Where δ is a minimum distance between reactants and electrode, h the Planck constant and ΔG^0_{act} is the standard Gibbs activation energy of electron transfer. However, in the general case, the concentration of the oxidized and reduced species is not equal. At equilibrium, we still have $k_a c_R(0) = k_c c_O(0)$ although $k_a \neq k_c$. In a non-equilibrium condition where an electrode potential increase of $E - E_{eq}$ is imposed on the electrode, the anodic and cathodic activation energy are

$$\Delta G_a = \Delta G_a^{eq} - \alpha n F(E - E_{eq}) \tag{2.31}$$

$$\Delta G_c = \Delta G_c^{eq} + (1-\alpha) n F(E - E_{eq}) \tag{2.32}$$

Where α is the charge transfer coefficient (Fig. 2.2).

By combining Equations 2.30, 2.31, and 2.32, the anodic and cathodic rate constants as a function of electrode potential are

$$k_a = k_a^0 \exp\big(\frac{\alpha n F E}{RT}\big) \tag{2.33}$$

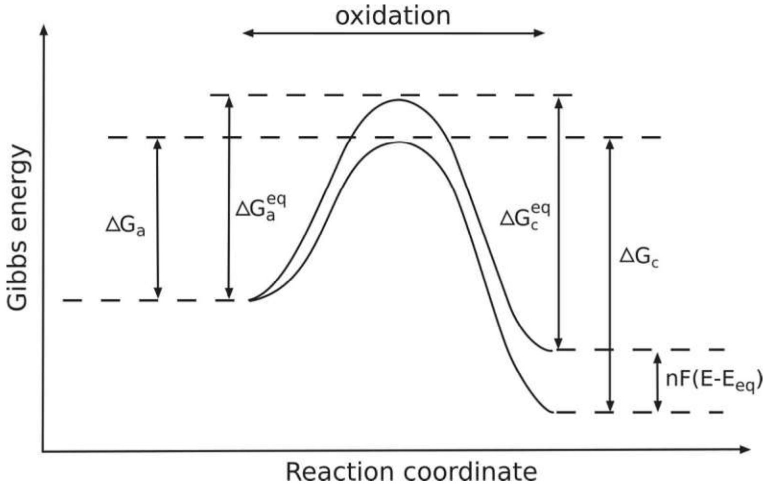

FIGURE 2.2: The activation barrier for an oxidation reaction and effect of electrode polarization. Reproduced from [93] with permission from EPFL Press.

$$k_c = k_c^0 \exp\left(\frac{-(1-\alpha)nFE}{RT}\right) \tag{2.34}$$

At formal redox potential E_f^0, the activation barrier is symmetrical.

$$k^{\ominus} = k_a^0 \exp\left(\frac{\alpha nFE_f^0}{RT}\right) = k_c^0 \exp\left(\frac{-(1-\alpha)nFE_f^0}{RT}\right) \tag{2.35}$$

$k^{\ominus}$ is the standard rate constant. According to the Nernst equation (Eq. 2.36) the equilibrium potential (the net current is zero) is

$$E_{eq} = E_f^0 + \frac{RT}{nF}\ln\left(\frac{c_O(\infty)}{c_R(\infty)}\right) \tag{2.36}$$

And since $\eta = E - E_{eq}$ is the overpotential we have

$$E - E_f^0 = \eta + \frac{RT}{nF}\ln\left(\frac{c_O(\infty)}{c_R(\infty)}\right) \tag{2.37}$$

Therefore, the total current as a function of overpotential is written as

$$I = I_0\left[\left(\frac{c_R(0)}{c_R(\infty)}\right)\exp\left(\frac{\alpha nF\eta}{RT}\right) - \left(\frac{c_O(0)}{c_O(\infty)}\right)\exp\left(\frac{-(1-\alpha)nF\eta}{RT}\right)\right] \tag{2.38}$$

I_0 is the exchange current density given by

$$I_0 = nFAK^{\ominus}[c_R(\infty)]^{1-\alpha}[c_O(\infty)]^{\alpha} \tag{2.39}$$

Equation 2.38 is the general form of the Butler-Volmer equation. If the mass transfer is considered as infinitely fast, the concentration of the reactants at the surface and in the bulk are equal. Therefore, it can be simplified into more common form of the Butler-Volmer equation.

$$I = I_0\left[\exp\left(\frac{\alpha nF\eta}{RT}\right) - \exp\left(\frac{-(1-\alpha)nF\eta}{RT}\right)\right] \tag{2.40}$$

This Equation (Eq. 2.40) is a fundamental equation in electrochemical kinetics which shows the relation between current (or current density) and overpotential (Fig. 2.3-a). The graph of $\log|I|$ or $\log|j|$ as a function of η is called Tafel plot (Fig. 2.3-b). The plot can be used to extract the exchange current density and calculate the charge transfer coefficient from the slope [93].

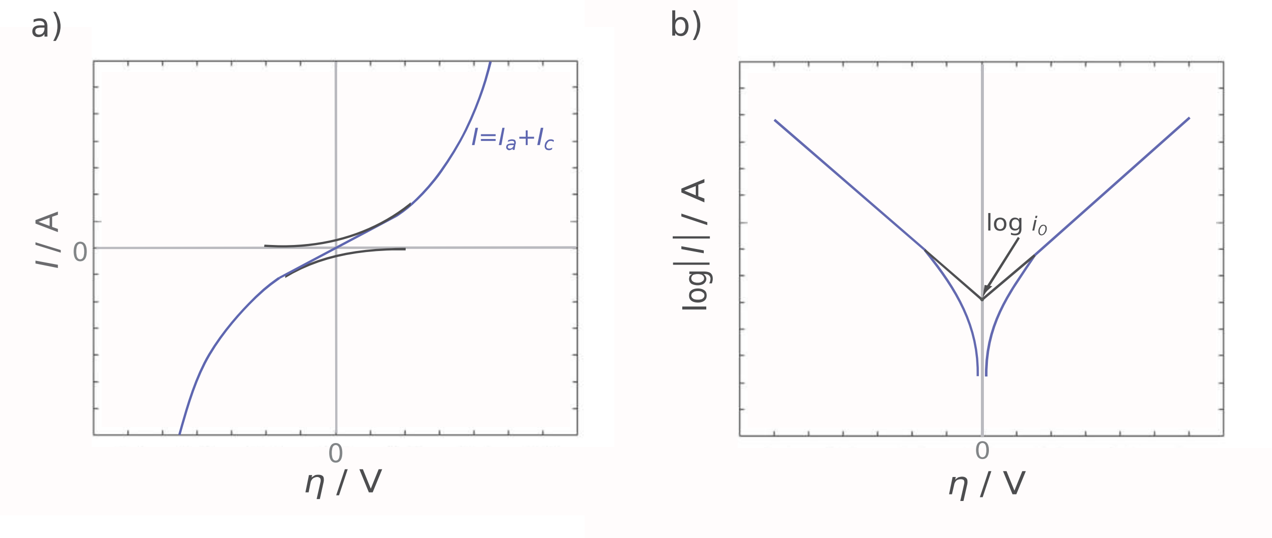

FIGURE 2.3: a) Current as a function of overpotential, based on the Butler-Volmer equation, and b) Tafel plot.

2.4 Electrochemical techniques

Electrochemical cell: Electrochemical phenomena are studied in an electrochemical cell consisting of at least two electrodes and an electrolyte. If the current is flowing (so not for equilibrium potential measurements), a three-electrode setup is typically used. The three-electrode cell consists of a working electrode (WE), a reference electrode (RE), and a counter electrode (CE) immersed in an electrolyte (Fig. 2.4). WE is an electrode where the reaction of interest happens at it. RE is an electrode of known potential used as a reference for monitoring the potential of WE. The CE (or auxiliary) electrode is used for completing the electric circuit. All these electrodes are controlled by an electric device called a potentiostat. While the potentiostat controls the voltage across the WE and CE electrodes, it keeps the potential difference between WE and RE constant via a high-impedance feedback loop.

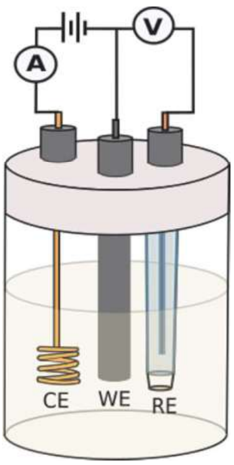

FIGURE 2.4: A three-electrode cell consists of a working electrode (WE), a reference electrode (RE), and a counter electrode (CE)

Reference electrode: By convention, the potential of the standard hydrogen electrode (SHE) is defined as 0 V and is used as a primary reference for all standard redox reactions. The SHE consists of a platinized platinum electrode immersed in a 1 M H^+(aq) in contact with hydrogen gas at a pressure of one atmosphere and temperature of 298.15 K, where the reaction below occurs.

$$H^+ + e^- \rightleftharpoons \frac{1}{2} H_2$$

Since the SHE setup is not convenient for everyday use, other electrodes are typically used. One of these reference electrodes is a reversible hydrogen electrode (RHE) which is like SHE but the electrode can be immersed in a solution with different H^+ activity. Depending on the pH of the solution, the RHE potential differs from that of the SHE (Eq. 2.41) as follows:

$$E = \left[E_{H^+|\frac{1}{2}H_2} \right]_{SHE} + \frac{RT}{F} \ln a_{H^+} = 0\,V \; - \; 0.059\,V.\,pH \tag{2.41}$$

Another commonly used electrode is the silver-silver chloride electrode made of a silver wire, covered with a layer of poorly soluble AgCl and immersed in a solution of sodium or potassium chloride $Ag|AgCl|Cl^-$. At the equilibrium condition, we have

$\mathrm{Ag^+\,(aq) + e^- \rightleftharpoons Ag\,(s)}$

$\mathrm{AgCl\,(s) \rightleftharpoons Ag^+\,(aq) + Cl^-\,(aq)}$

So based on the Nernst equation and

$$K_s^{AgCl} = \frac{a_{Ag^+} \,.\, a_{Cl^-}}{a_{AgCl}} = a_{Ag^+} \,.\, a_{Cl^-} = 1.77 \times 10^{-10} \tag{2.42}$$

We have

$$\left[E_{Ag|AgCl|Cl^-} \right]_{SHE} = \left[E^0_{Ag^+|Ag} \right]_{SHE} + \frac{RT}{F} \ln K_S^{AgCl} + \frac{RT}{F} \ln a_{Cl^-} \tag{2.43}$$

the Nernst equation for the Ag/AgCl cell electrode can also rearranged and written as

$$\left[E_{Ag|AgCl|Cl^-} \right]_{SHE} = \left[E^0_{Ag|AgCl|Cl^-} \right]_{SHE} + \frac{RT}{F} \ln a_{Cl^-} \tag{2.44}$$

Showing that at constant temperature, the electrode potential only depends on the activity of Cl^- in the electrolyte. For instance, the Ag/AgCl with 1 M KCl has a potential of 0.235 V vs SHE [94].

Working electrode: The working electrodes are made of conductive materials, typically metals such as Au and Pt.

Working electrodes can be categorized based on their size into macro- and microelectrodes. The electrode with at least one dimension on the order of microns is called microelectrode or ultramicroelectrode. Besides the single microelectrode, the array of microelectrodes is also used as a working electrode.

2.4.1 Chronoamperometry

In Chronoamperometry (CA), a potential step is instantly applied to the electrode and the current is measured vs time. In CA, the measurement is started from potential E_1 at which no reaction is happening and instantly switches to E_2, generally a potential corresponding to mass transport-limited current (Fig. 2.5-a). As shown in Figure 2.5-b as the potential applied to a macroelectrode switches to E_2, a large (cathodic) current flows and then decays. The decrease of current is related to the depletion of the reactants close to the electrode surface as time progresses. The depletion zone is known as the diffusion layer. The thickness of the diffusion layer becomes thicker during the measurement; therefore, the diffusion rate decreases which consequently leads to the decrease of the current. This is predicted by the Cottrell equation (Eq. 2.45).

$$I = \frac{nFAc_\infty\sqrt{D}}{\sqrt{\pi t}} \tag{2.45}$$

Where c_∞ is the concentration of the electroactive species in the solution (bulk concentration). It shows that the current is inversely proportional to the square root of time ($I \propto \frac{1}{\sqrt{t}}$).

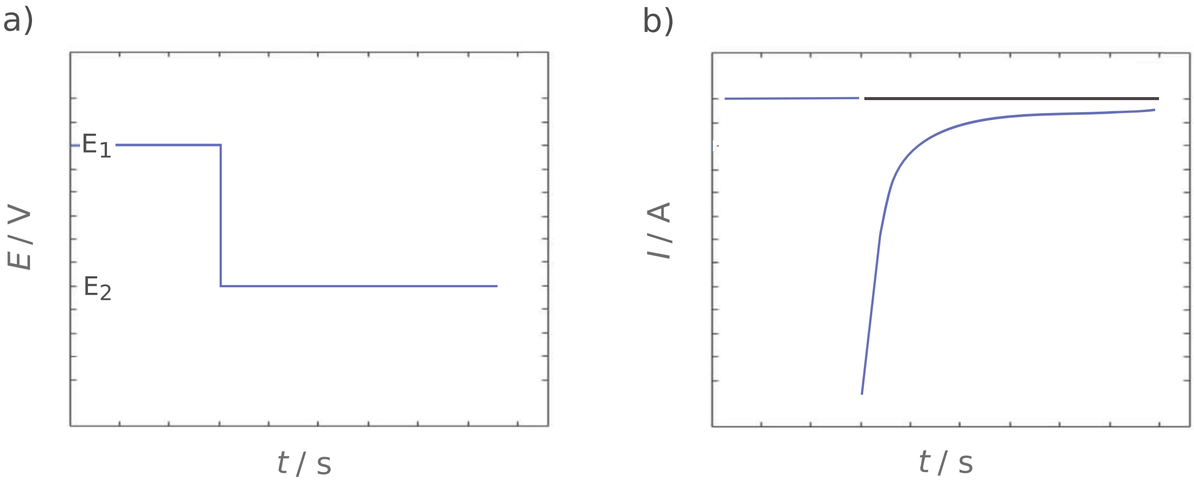

FIGURE 2.5: Step potential applied to the working electrode and b) the resulting current-time transient

2.4.2 Cyclic voltammetry

Voltammetry is a commonly used technique in which a time-dependent potential is applied to an electrochemical cell and the resulting current is recorded as a function of that potential. In cyclic voltammetry (CV) the electrode potential is ramped linearly versus time ($E_t = E_i \pm \nu t$) between two potential limits (vertex potentials) with the scan rate of ν. The potential starts from the initial potential of E_i and when it reaches the vertex potentials (E_1 and E_2) the direction of sweep is reversed (Fig. 2.6-a). The potentials E_1 and E_2 are chosen in a way that the potential interval between these two potentials includes the oxidation or reduction process of interest. The current vs. potential plot is called a voltammogram (Fig. 2.6-b).

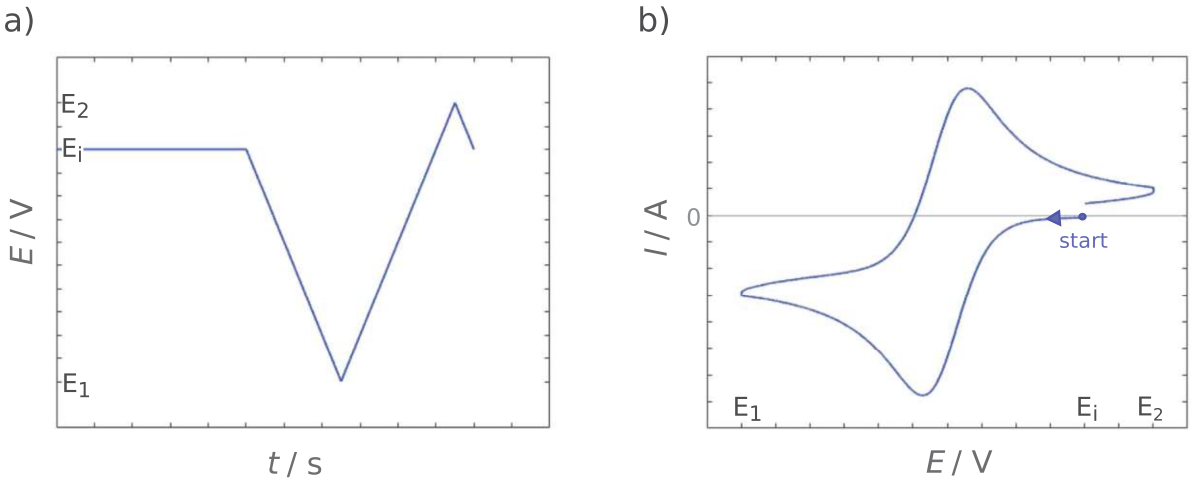

FIGURE 2.6: a) The potential waveform applied to working electrodes with the scan rate of ν. b) The cyclic voltammogram of electroactive species at the electrode surface.

As shown in Figure 2.6 the cyclic voltammetry started from the E_i where the negligible current flows and as the potential gets more negative the reduction current begins to increase based on Butler-Volmer equation and reaches its max amount at a peak cathodic current potential. At yet more negative potentials, the current decreases based on the Cottrell equation (Eq. 2.45) the current decays as a function of $\frac{1}{\sqrt{t}}$ due to the depletion of electroactive species at the electrode's surface (diffusion limitation). As the potential gets to the E_1 the direction of the scan is reversed and potential changes over time from E_1 to E_2 resulting in an oxidation process with a similar behavior as explained for the reduction process.

Linear sweep voltammetry is like cyclic voltammetry. However, in linear sweep voltammetry, when the electrode potential changes from one potential limit to another potential limit (E_1 to E_2) the scan is ended, and the scan is not reversed as cyclic voltammetry. For a microelectrode, at short times, as long as the diffusion layer thickness is smaller than the microelectrode radius (R_e), it follows the Cottrell equation and diffusion is linear. This phase is called the early transient regime or the regime of semi-infinite linear diffusion. At a longer time, where the diffusion layer thickness is larger than R_e, the radial diffusion contributes to the current and it reaches a steady-state limiting current which depends on the size (or radius) of the microelectrode ($i \propto R_e$). This phase is called the steady-state regime [95]. The microelectrodes with smaller radius have greater current density and greater flux of material to/from the surface electrode. The time to reach the steady-state is also shorter for smaller electrodes. The CVs measured on micro and macroelectrodes are shown in Figure 2.7 [96].

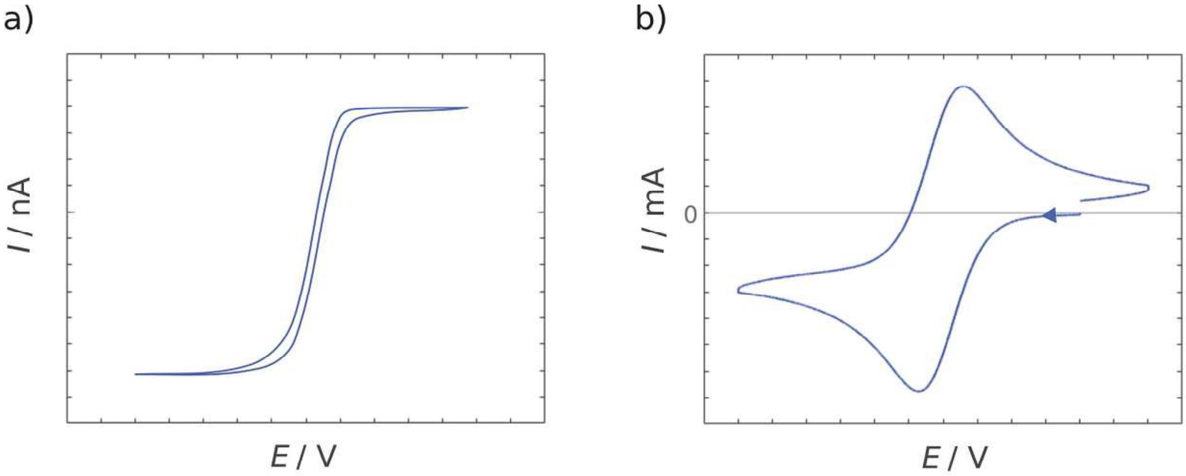

FIGURE 2.7: Cyclic voltammograms of a) micro and b) macroelectrodes.

2.4.3 Peak shape and reversibility

As explained in the electrochemical kinetic sections, when the rate of electron transfer kinetics is faster than the rate of mass transport to the electrode, a reversible voltammetry is observed, and when it is slower, an irreversible voltammetric response is seen. When electron transfer kinetics and mass transport occur on a comparable timescale, it is known as quasi-reversible. For distinguishing the reversibility of electrochemical processes at stationary macroelectrodes, Matsuda and Ayabe introduced a parameter, ζ or Λ

$$\zeta = k^0 \left[\frac{nF\nu D}{RT}\right]^{-1/2} \tag{2.46}$$

where k^0 is the standard electrochemical rate constant. When $\zeta \geq 15$, the electrode kinetics is fast and is considered reversible. A system with ζ in the range of $15 > \zeta > 10^{-3}$ is quasi-reversible and $\zeta \leq 10^{-3}$ is irreversible [97]. A decade later, Nicholson developed a similar parameter, ψ

$$\psi = k^0 \left[D_o \pi \left(\frac{nF\nu}{RT}\right)\right]^{-1/2} \left(\frac{D_o}{D_r}\right)^{\alpha/2} \tag{2.47}$$

where ψ is a kinetic parameter, and D_o and D_r are the diffusion coefficients of the oxidized and reduced species [98]. For most of the cases $\frac{D_o}{D_r} \approx 1$; therefore, Equation 2.47 can be simplified into

$$\psi = k^0 \left[\frac{\pi D n \nu F}{RT}\right]^{-1/2} \tag{2.48}$$

Similar to Matsuda and Ayabe work, depending on ψ value, the reaction with the charge transfer coefficient $\alpha = 0.5$ can be categorized into reversible ($\psi \geq 7$), quasi-reversible ($0.1 \leq \psi < 7$), and irreversible ($\psi < 0.1$) [98].

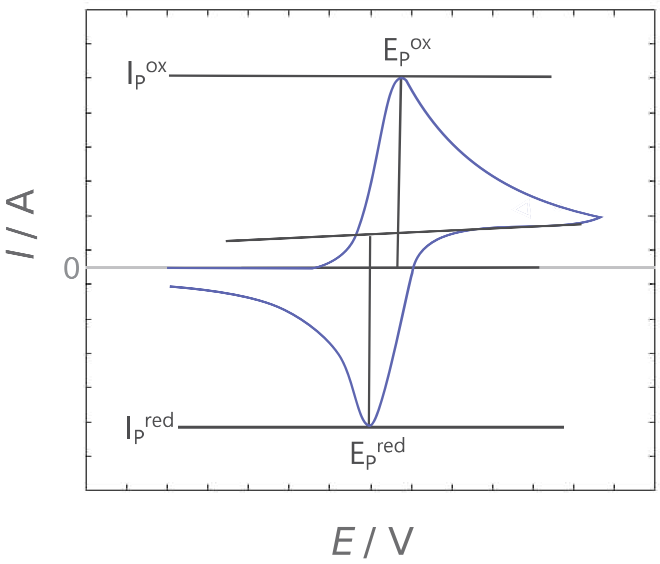

FIGURE 2.8: A cyclic voltammogram illustrating the peak position E_p and peak (current) height I_P.

In an electrochemically reversible process, the difference between the potential of anodic and cathodic peaks or so-called peak-to-peak separation ($\Delta E_p = E_P^{ox} - E_P^{red}$) is equal to $2.218\,\frac{RT}{F} \approx 60\ mV$ which does not depend on scan rate. However, for the irreversible and quasi-reversible processes, ΔE_p changes with scan rate. The E_p and I_P correspond to the oxidation and reduction processes depicted in Figure 2.8.

Besides peak-to-peak separation, the reversibility of the electron transfer can be studied by the relation between peak current (I_P) and the scan rate. For a reversible process at macroelectrodes, I_P increases linearly with the square root of scan rate based on the Randles-Sevcik equation where n is the number of electrons transferred, A (cm^2) the electrode real surface area, D ($\mathrm{cm}^2\,\mathrm{s}^{-1}$) is the diffusion coefficient of the for the redox active species, and c_∞ ($\mathrm{mol\,cm}^{-3}$) is the bulk concentration of the redox species [96].

$$I_P = 0.446\,nFAc_\infty\left(\frac{nF\nu D}{RT}\right)^{1/2} \tag{2.49}$$

At 298 K the equation can be written as

$$I_P = 2.69 \times 10^5 n^{3/2} A c_\infty (D\nu)^{1/2} \tag{2.50}$$

By measuring the CVs at different scan rates for electrochemically quasi-reversible and irreversible systems the relationship between peak current and square root of scan rate is defined as Equation 2.51 and Equation 2.52 where α is the transfer coefficient and n' is the number of electrons transferred before the rate-determining step. [96, 99]

$$I_P^{quasi} = 0.436\,nFAc_\infty\left(\frac{nF\nu D}{RT}\right)^{1/2} \tag{2.51}$$

$$I_P^{irrev} = 0.496\,(\alpha n')^{1/2}\,nFAc_\infty\left(\frac{nF\nu D}{RT}\right)^{1/2} \tag{2.52}$$

Estimation of standard heterogeneous electron transfer rate constant: For a quasi-reversible system, the Nicholson method is commonly used for estimating the observed or apparent standard heterogeneous electron transfer rate constant, k^0 or

${k^0}_{app}$. The method is simple and based on the peak potential separation at different scan rates [98].

$$k^0 = \psi \left[\frac{\pi D n \nu F}{RT}\right]^{1/2} \tag{2.53}$$

For calculating an average k^0, cyclic voltammograms must be measured at different scan rates. Then, ΔE_P at each scan rate needs to be determined. The Nicholson's table provides specific ψ values for each ΔE_P. However, the ψ value can also be calculated based on the empirical equation of [100]

$$\psi = \frac{-0.6288 + 0.0021.(\Delta E_P.n)}{1 - 0.017.(\Delta E_P.n)} \tag{2.54}$$

To estimate ψ for the ΔE_P values bigger than 212 mV the following equation is used [101]

$$\psi = 2.18 \left[\frac{\alpha}{\pi}\right]^{1/2} \exp\left[-\left(\frac{\alpha^2 F}{RT}\right) n \Delta E_P\right] \tag{2.55}$$

By inserting the ψ value and the corresponding ν into Equation 2.53, the k^0 can be calculated. Additionally, it is also possible to obtain k^0 from the slope of ψ vs. $\left[\frac{\pi D n \nu F}{RT}\right]^{-1/2} \nu^{-1/2}$ plot. However, for more accurate determination of k^0, electrochemical simulation packages such as DigiSim, DigiElch KISSA, COMSOL Multiphysics, and MECSim are advised [102].

2.4.4 Voltammetry at partially blocked electrodes

When the surface of a macroelectrode is covered with immobilized inert particles, these particles can significantly modify the diffusion pathway for the electroactive species reaching the surface, as a result, their cyclic voltammograms could be completely different from those of unblocked electrodes. These partially blocked electrodes, depending on the size of particles (blocks), total coverage, and the time scale of the experiment (or scan rate), show different voltammetric responses.

When the size of the blocks and the electroactive sites are under macro size (micrometer-scale), the voltammetric response is different from that of macroelectrodes. Therefore, the voltammetric response of microelectrode arrays needs to be considered. The voltammetric response of microelectrode arrays depends not only on the thickness of the diffusion layer versus the size of the discs but also on the distance between adjacent discs versus diffusion layer thickness.

The thickness of the diffusion layer or the distance that species with the diffusion coefficient D diffuse in the time t is $\delta = \sqrt{\pi D t} = \sqrt{\pi D \frac{\Delta E}{\nu}}$, where ν is scan rate and ΔE is the potential range between start of electrolysis to the peak potential. For an electrochemically reversible voltammogram, ΔE is typically ca. 0.1 to 0.15 V. At a scan rate of 0.1 V/s diffusion layer thickness is around 55 μm. The thickness of the diffusion layer changes with the scan rate. At high scan rates, the diffusion layer becomes thinner, while at low scan rates, it becomes thicker.

The voltammetric responses of the microelectrodes based on their diffusion profile are classified into four categories [96, 103], illustrated in Figure 2.9.

In the first category, the distance between center-to-center of microelectrodes, d, is so large that there is no overlap of diffusion fields ($\delta < d$) and the time scale of the experiment is so short (high scan rate) that $\delta < R_b$, meaning each microdisc experiences isolated linear diffusion. Hence, each microelectrode disc acts like a macroelectrode. As a result, the voltammetric response is similar to macroelectrodes, and the current is proportional to the total electrochemically active area (individual microdisc area × total number of the micodiscs in the array).

In the second category, like the previous category, microelectrodes are so apart that there is no overlap of diffusion fields ($\delta < d$). The condition for this category is $d > 2\sqrt{2D\frac{\Delta E}{\nu}}$. However, in this case the time of voltammetry is so long (low scan rate) that $\delta > R_b$. Thus, every microelectrode in the array would act as an individual microelectrode with radial diffusion field, showing steady-state behaviour with sigmoidal shape voltammogram, scaled by the total number of microdiscs in the array. The limiting current is equal to $I_{lim} = 4nFD[A_{bulk}]R_b$, where n is the number of electrons and $[A_{bulk}]$ the concentration of electroactive species A in electrolyte ($\mathrm{A} \longrightarrow \mathrm{B} + \mathrm{e}$). In this category, the current is independent of the scan rate.

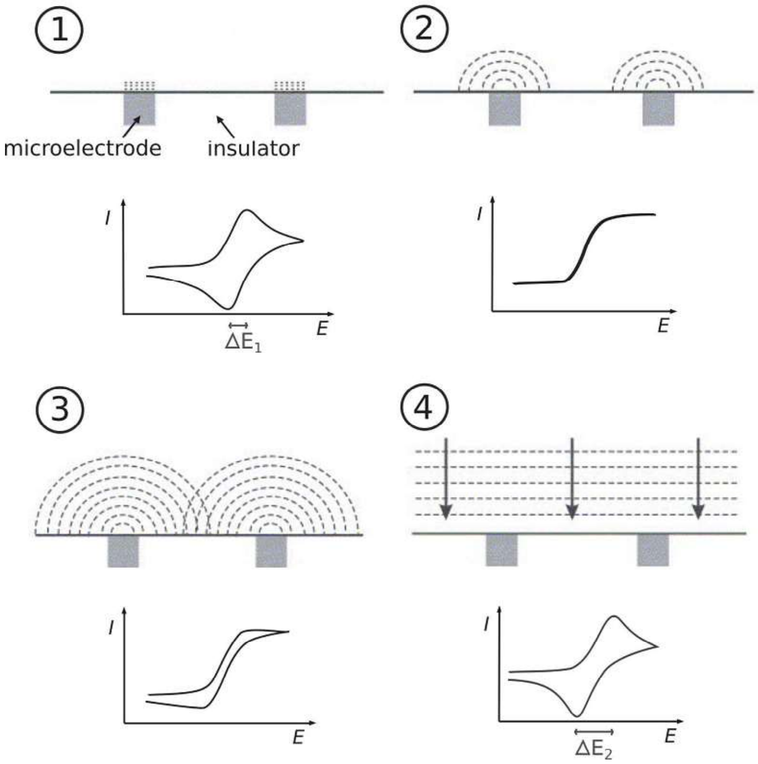

Figure 2.9: Four possible categories of diffusion profile of microelectrode arrays and their corresponding cyclic voltammograms, $\Delta E_1 < \Delta E_2$. Adapted from [103], with permission from Elsevier (2005), and from [104], with permission from the Royal Society of Chemistry (2016).

In the third category, the distance between microelectrodes is small enough that diffusion fields of microelectrodes partially overlap ($\delta > d$) and the voltammetric response would be an intermediate between categories 2 and 4.

In the fourth category, the distance between the microelectrodes is so small that the diffusion fields of the microelectrodes overlap strongly ($\delta >> d$) so the electroactive species above the blocks can be depleted nearly completely through mass transport with linear diffusion characteristics. Therefore, almost complete electrolysis of the species over both blocked and active occurs in the time scale of the experiment, meaning the voltammetric response of such an array is like a single macroelectrode with the total area including microdisc areas plus the insulating area. In turn, this leads to a peak current that is almost equal to unblocked electrodes but with decreased apparent standard (electrochemical) rate constant, k^0_{app}, which is equal to

$$k^0_{app} = (1 - \theta).\, k^0_{bare} \tag{2.56}$$

where θ is the fraction of the surface covered with blocks and the k^0_{bare} is the standard rate constant at the unblocked electrode.

The characteristics of microelectrode arrays distinguished into four categories are summarized in Table 2.1.

TABLE 2.1: The voltammetric characteristics of the four possible categories of microelectrode arrays with different sizes of diffusion zone, δ, microdisk radius, R_b, and center-to-center separation, d. I_{lim} is the limiting current, I_p is the peak current and ν is the scan rate. Reprinted from [103], Copyright (2005), with permission from Elsevier.

Property	Category 1	Category 2	Category 3	Category 4
δ vs. R_b	$\delta < R_b$	$\delta > R_b$	$\delta > R_b$	$\delta > R_b$
δ vs. d	$\delta < d$	$\delta < d$	$\delta > d$	$\delta >> d$
Type of response	clear peak→ I_P	steady state→ I_{lim}	slight peak to clear peak→ I_P	clear peak→ I_P
Scan rate dependence?	yes	no	yes	yes
Current dependence	$I_P \propto \nu^{0.5}$	$I_{lim} \propto R_b$	-	$I_P \propto \nu^{0.5}$

2.4.5 Electrochemical Impedance Spectroscopy

Electrochemical impedance spectroscopy (EIS) is a powerful analytical technique for studying electrode reactions and properties of electrode material. EIS is commonly used in evaluating and studying corrosion, paints and coatings, batteries, fuel cells, and sensors.

In EIS, a small amplitude sinusoidal potential perturbation, E, is applied to an electrochemical system over a wide frequency range (typically from mHz to MHz). The resulting current response, I, is measured, and the impedance, Z, is calculated as the ratio of the potential to the current: $Z = \frac{E}{I}$. Where

$$E(t) = E_0 \sin(\omega t) \tag{2.57}$$

E_0 is the amplitude of the signal and ω is the radial frequency, defined as $\omega = 2\pi f$ where f is a frequency. The signal with a small amplitude gives an approximately linear response. The response signal with the amplitude of I_0 is shown in Equation 2.58 where the phase is shifted by ϕ.

$$I(t) = I_0 \sin(\omega t + \phi) \tag{2.58}$$

The impedance of the system at a frequency f is

$$Z(\omega) = \frac{E}{I} = \big|Z(\omega)\big| e^{j\phi} = \big|Z\big|(\cos\phi + j\ \sin\phi) = Z_{Re}(\omega) - j\ Z_{Im}(\omega) \tag{2.59}$$

The impedance is a complex quantity that has real and imaginary parts in Cartesian coordinates or a magnitude and phase shift in polar coordinates. The $Z(\omega)$ is a vector called impedance where Z_{Re} (or $Z^{'}$) and Z_{Im} (or $Z^{''}$) are real and imaginary parts of the impedance, and $j = \sqrt{-1}$. The magnitude of the Z is shown by $\big|Z(\omega)\big|$ which is equal to

$$\big|Z(\omega)\big|^2 = (Z_{Re})^2 + (Z_{Im})^2 \tag{2.60}$$

ϕ is the phase angle which is given by

$$\tan\phi = \frac{Z_{Im}}{Z_{Re}} \tag{2.61}$$

The impedance data are represented in two ways: Bode and Nyquist plots. The Bode plot consists of two different plots, $\log|Z|$ and ϕ versus $\log(\omega)$. In Nyquist plot Z_{Im} is plotted versus Z_{Re} [95].

While the Nyquist plot is used a lot in the scientific literature, its linear properties carry a substantial risk of compressing a large part of the spectrum (which typically is recorded over many orders of magnitude in frequency) in a corner, making the data effectively invisible and increasing the probability that important parts are overlooked. It is therefore good practice to always plot the same data in both Nyquist and Bode formats.

Table 2.2: Table of equivalent circuit elements with their symbols and impedances

Element	Symbol	Impedance
Resistor	R	$Z_R = R$
Capacitor	C	$Z_C = \frac{1}{j\omega C}$
Inductor	L	$Z_L = j\omega L$
Constant phase element	Q or CPE	$Z_{CPE} = \frac{1}{Q(j\omega)^\alpha}$
Warburg impedance	W	$Z_W = \frac{1}{Q(j\omega)^{\frac{1}{2}}}$

For interpreting the electrochemical impedance spectra, an equivalent circuit is commonly used. An equivalent circuit is a network of elements that represents phenomena and the processes happening at the interface. It can be shown that a unique equivalent circuit to describe the spectrum does not exist. It is possible to combine elements in different ways and get an identical fit to experimental data. Hence, the choice of a certain equivalent circuit must always be based on other information about the system, not on the fact that a good fit is obtained [105]. The elements are divided into two groups: passive elements (such as capacitor, resistor, and inductor) and distributed circuit elements (such as constant phase element (CPE) and Warburg diffusion element).

The impedance of these elements is collected in Table 2.2.

The impedance of a CPE is given by:

$$Z_{CPE} = \frac{1}{Q(j\omega)^\alpha} \tag{2.62}$$

The value of α determines the behavior of the CPE. When $\alpha = 0$ the CPE behaves like a resistor. When $\alpha = 0.5$, it behaves like a Warburg element. When $\alpha = 1$, it behaves like a capacitor, and when $\alpha = -1$, it behaves like an inductor.

The Randles equivalent circuit is the simplest model for an electrified interface in an electrochemical cell (Fig. 2.10).

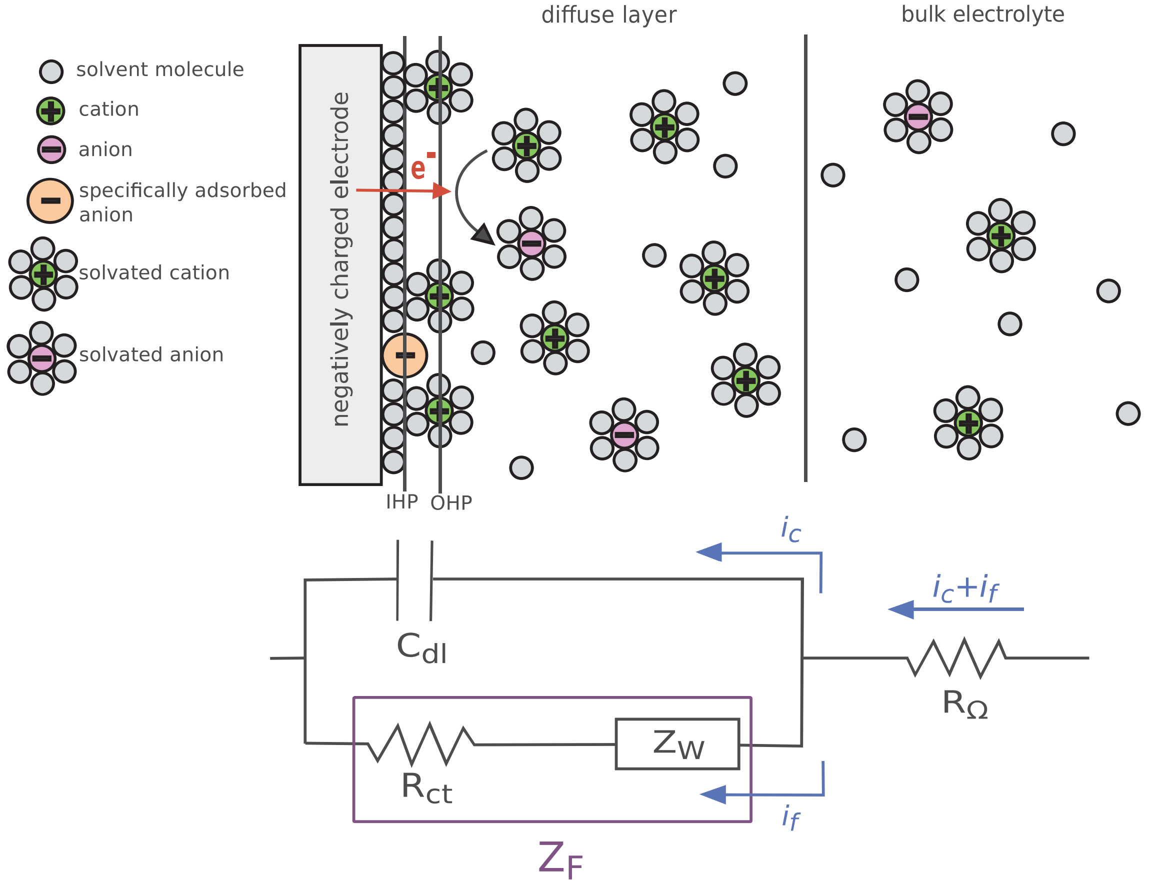

FIGURE 2.10: Schematic of electrode reaction at electrode/electrolyte interface. The electrical double layer on a negatively charged electrode surface includes inner Helmholtz (IHP) and outer Helmholtz plane (OHP). By diffusion of the (solvated) cations to the interface an electron transfer from the electrode to the molecules occurs, resulting in their reduction. The (solvated) anions later diffuse away from the electrode surface into the bulk solution. The Randles equivalent circuit corresponds to a simple electrochemical system with R_Ω (uncompensated resistance of electrolyte solution), C_{dl} (double-layer capacitance), R_{ct} (charge transfer resistance), and Z_W (Warburg impedance). The Z_F can be replaced by R_{ct} in series with Z_W. i_c: double-layer charging current, i_f: faradaic current. Adapted from [106] with permission. Copyright (2003) American Chemical Society.

In an electrochemical cell, the total current is made of both faradaic, i_f and double-layer charging current, i_c, thus the Randles equivalent circuit is made of (at least) two elements in parallel connection: A double-layer capacitance, C_{dl}, in parallel connection with faradaic impedance, Z_F. The Z_F can be subdivided into charge transfer resistance, R_{ct}, in series with Warburg impedance, Z_W, related to the diffusion process.

The uncompensated resistance of electrolyte solution is shown with R_Ω (Fig. 2.10) [95]. A Nyquist plot of the Randles equivalent circuit is shown in Figure 2.11. Due to the surface distribution of certain physical properties, the double layer does not always behave as an ideal capacitor. As a result, it is often represented by a CPE in an equivalent circuit.

Because Equation 2.62 for the CPE does not directly yield capacitance values. An effective capacitance can be estimated based on the equivalent circuit that includes the CPE. For a Randles equivalent circuit which has CPE instead of the capacitor, the effective capacitance is estimated by using Equation 2.63 [107]

$$C_{eff} = Q_0^{\frac{1}{\alpha}} \left(\frac{1}{R_\Omega} + \frac{1}{R_{ct}} \right)^{\frac{\alpha-1}{\alpha}} \tag{2.63}$$

For a surface coated with a film, where the equivalent circuit consists of R_f and CPE connected in parallel, the effective capacitance is estimated using Equation 2.64 [108]

$$C_{eff} = Q_0{}^{\frac{1}{\alpha}}.R^{\frac{1-\alpha}{\alpha}} \tag{2.64}$$

EIS disentangles the different processes (mass transport, charge transfer, etc.) that occur at different rates and contribute to the overall impedance. As shown in the Nyquist plot, Fig. 2.11, the impedance spectrum often consists of a semicircle (at high frequencies) followed by a straight line (at low frequencies) [95, 109].

- High-frequency region (semicircle): This region corresponds to the kinetic control, where R_{ct} dominates. At extremely high frequencies ($\omega \to \infty$), the capacitor C_{dl} has negligible impedance, thus current can easily flow through it, effectively short-circuiting or bypassing the R_{ct} and Z_W. Therefore, only R_Ω is the overall impedance. The R_Ω is constant and does not depend on the frequency and it always contribute equally to impedance.

  At high frequencies, the capacitor has low impedance, but not zero, so it still affects the circuit and R_{ct} remains relatively constant, indicating that the electron transfer reaction kinetics dominate the electrochemical process. In the Nyquist plot, this manifests as a semicircle, which arises from the parallel combination of R_{ct} and C_{dl}. The size of this semicircle is directly proportional to the magnitude of R_{ct}, showing its significant contribution to the overall impedance. A larger

R_{ct} indicates a slower reaction rate or kinetically sluggish system, resulting in a larger semicircle.

- Low-frequency region (straight line): This region corresponds to the mass-transfer control, where diffusion processes limit the reaction rate. At extremely low frequencies ($\omega \to 0$), the impedance is dominated by R_{ct} since C_{dl} behaves like an open circuit (impedance approaches infinity), and Z_W becomes infinitely large. This means Z_W dominates the behavior of the circuit, making diffusion the primary impedance factor.

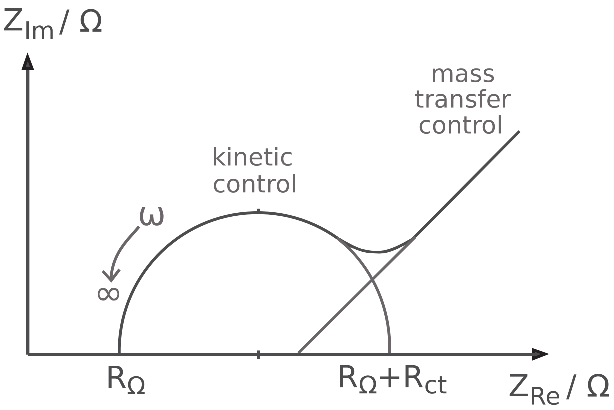

FIGURE 2.11: A Nyquist plot of the Randles equivalent circuit. Reproduced from [95] with permission. Copyright (2001), John Wiley and Sons.

In semi-infinite diffusion, the Warburg impedance (Z_W) is [95]

$$Z_W = \sigma\omega^{-1/2} - j(\sigma\omega^{-1/2}) \tag{2.65}$$

Based on Equation (2.65), Z'_W(real) and $-Z''_W$(imaginary) are equal. Thus, in the Nyquist plot, they form a line with a slope of 1 (45°).

$$|Z'_W| = |Z''_W| \tag{2.66}$$

In Equation (2.65), σ is called the Warburg coefficient [95]

$$\sigma = \frac{RT}{n^2F^2A\sqrt{2}}\left(\frac{1}{\sqrt{D_O}c_O} + \frac{1}{\sqrt{D_R}c_R}\right) \tag{2.67}$$

where R is the gas constant, T the temperature, n the number of electrons, A is the geometric area of an electrode (cm^2), c (mol cm^{-3}) is the bulk concentration of the oxidized and reduced species, and D ($\mathrm{cm^2\,s^{-1}}$) is their corresponding diffusion coefficients. The σ can be extracted from the slope of the Z' and $-Z''$ as a function of $\omega^{-0.5}$. Therefore, by extracting the σ value it is possible to estimate the D value from Equation (2.67).

Not only can D be determined, but it is also possible to estimate the standard electron transfer rate constant, k^0. By combining Equation 2.68 and Equation 2.69,

$$R_{ct} = \frac{RT}{nFI_0} \tag{2.68}$$

$$I_0 = nFAk_0c \tag{2.69}$$

where I_0 represents the exchange current density, k^0 can be estimated by having $c_R = c_O = c$ [110].

$$k^0 = \frac{RT}{n^2F^2AcR_{ct}} \tag{2.70}$$

2.5 Scanning tunneling microscopy

2.5.1 Principle

Scanning tunneling microscopy (STM) is a characterization technique to study metal and semiconductor surfaces at the atomic scale. Scanning tunneling microscope was invented by Gerd Binnig and Heinrich Rohrer in 1981 [111]. STM works based on the quantum mechanical effect called tunneling. In tunneling, electrons from tip/surface penetrate through the impenetrable potential barrier to surface/tip. When the distance between the tip and surface is only a few angstroms, electron wave functions in the tip overlap the electron wave functions in the sample, letting the electrons tunnel. The schematic of the scanning tunneling microscope is shown in Figure 2.12.

The essential parts of the STM are tip, piezoelectric tube, and control electronics. The STM tip is usually made of W or PtIr and it is mounted on the tip holder connected to a piezoelectric tube with three piezoelectric transducers (x piezo, y piezo, and z piezo)

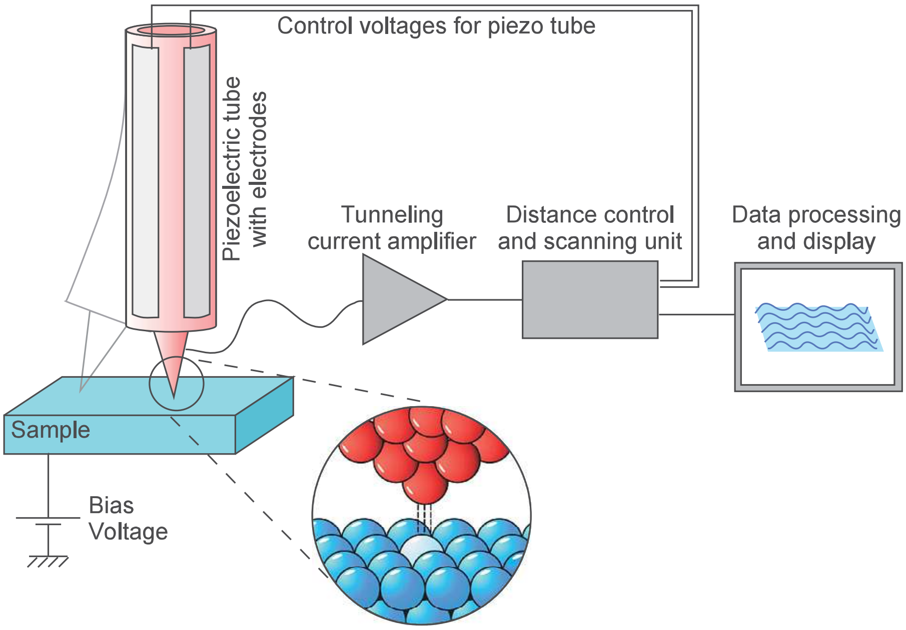

FIGURE 2.12: Schematic of the scanning tunneling microscope. Figure by Michael Schmid, TU Wien.

moves the tip in x, y and z directions. When the tip is approached close enough to the surface and a bias voltage between the sample and tip is applied, the tunneling current starts to flow. While the tip is scanned over the surface, the tunneling current is amplified by the amplifier and converted to a voltage; the voltage is then compared to a reference value. The difference after amplifying again is applied to z piezo. Such a feedback system controls the tip-sample distance so when the measured tunneling current is larger than the reference value, the voltage is applied to z piezo to withdraw a tip from a surface and vice versa [112]. The voltage applied to z piezo via the feedback loop is recorded as an image. This mode of operation is called constant-current mode. Another mode of operation is the constant-height mode. In constant-height mode the distance between the sample and the tip is kept constant and the tunneling current is recorded as an image.

In quantum mechanics, the quantum state of an electron is described by a wave function, Ψ. One dimensional and time-independent Schrodinger equation for an electron with mass of m is

$$-\frac{\hbar^2}{2m}\frac{\partial^2\Psi(z)}{\partial z^2}+U(z)\Psi(z)=E\;\Psi(z) \tag{2.71}$$

Where $\hbar$ is the plank constant, U is the potential barrier and E is the total energy of the electron. The solution of the Schrodinger equation in the potential barrier where $E \leq U$ is

$$\Psi(z) = \Psi(0)\, e^{-\kappa z} \tag{2.72}$$

Where $\kappa = \frac{\sqrt{2m(U-E)}}{\hbar}$

so the electron state decays in z direction with the decay constant of κ. The probability of finding electron in the barrier region is proportional to

$$p = \left|\Psi(0)\right|^2 e^{-2\kappa z} \tag{2.73}$$

In case of STM, the distance between the tip and the sample can be considered as a rectangular potential barrier (Fig. 2.13). A minimum energy required to remove an electron from the bulk metal to vacuum level is the work function, ϕ, with the unit of eV. The highest energy level occupied by the electron is fermi level. Therefore, $E_F = -\phi$.

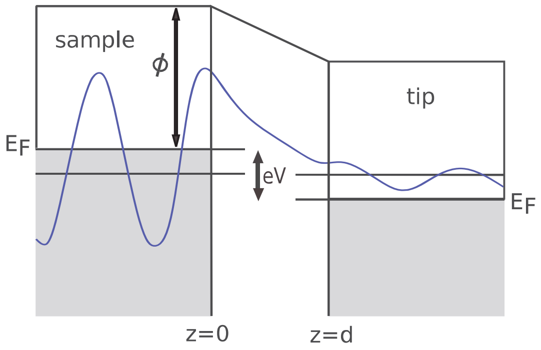

FIGURE 2.13: Energy level diagram for an electron tunneling from the sample to tip with the separation of d. The electron wave function is shown with a black solid line.

When a bias voltage V is applied, tunneling current flows. So, the electrons of the sample with an energy of the E_n and from nth state n present between $E_F - eV$ and E_F can tunnel to the tip. Since the $eV \ll \phi$ and $E_n \approx -\phi$ the decay constant change into

$$\kappa = \frac{\sqrt{2m\phi}}{\hbar} = 0.51\sqrt{\phi} \tag{2.74}$$

The unit of decay constant is $\mathring{A}^{-1}$. Since the tunneling current I is proportional to the probability of finding the electron at the tip surface $z = d$ where d is a separation between tip and sample, we can write

$$I \propto p = \left|\Psi(0)\right|^2 e^{-2\kappa z} \tag{2.75}$$

Besides the separation between the tip and the sample, the number of electronic states in the energy range eV is responsible for the tunneling current. If V is small enough, the tunneling current is directly proportional to the local density of states (LODS) of the sample at the fermi level, $\rho s(0, E_F)$.

$$I \propto V\rho s(0, E_F)e^{-2\kappa d} = V\rho s(0, E_F)e^{-1.025\sqrt{\phi}d} \tag{2.76}$$

Thus, in constant current mode, a topographic image of the surface is the contour of LDOS of the sample surface [112]. The sign of the bias voltage the electrons can tunnel from tip to sample or vice versa. When the sample is positively biased with respect to the tip ($V_{bias} = V_{sample} - V_{tip}$) or the tip is negatively biased with respect to the sample, the electrons tunnel from the tip to empty states of the sample and when the sample is negatively biased, the electrons from the occupied states of the sample tunnel to tip empty states. So depending on the bias voltage empty or occupied states can be imaged by STM. STM is not limited to exploring surfaces in a UHV system. It is also used to probe surfaces in different environments such as in ambient, solvents, and electrolytes.

The self-assembly of the molecules and supramolecules on the surface and the dynamic adsorption and desorption at a solid-liquid interface of them is one the application of the STM in (organic) solvents [113]. The solvents employed for the solid-liquid STM should follow certain criteria such as [114], [115]: 1) The solvents should be non-conductive or electrochemically inert to avoid background current, 2) The solvent should have intermediate degree of solubility to decrease the possibility of molecules already adsorbed at the interface to dissolve again, 3) The adsorption of adsorbates to the surface should be stronger than solvent to make displacement of molecules by solvent impossible, 4) The solvent should have a high boiling point (or low vapor pressure) to have a stable interface during scanning.

2.5.2 Electrochemical scanning tunneling microscopy

The electrochemical scanning tunneling microscope (EC-STM) is a STM that is used in an electrolytic environment. It is a microscopic technique to study the surface structure and the reaction and phenomena happening at the interface. The Schematic of EC-STM is shown in Figure 2.14.

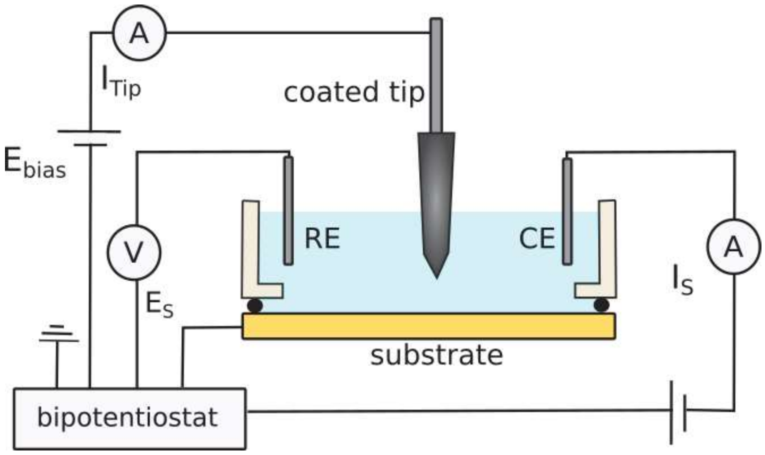

FIGURE 2.14: Schematic of electrochemical scanning tunneling microscope (EC-STM). Adapted from [116] with permission. Copyright (2016), Springer Nature.

There are significant differences between the STM in UHV or solvent and EC-STM. First, the EC-STM is used to study electrochemical phenomena at the surface, so has small-sized electrochemical cells including working, reference, and counter electrodes immersed in the electrolyte. The surface under study is the working electrode. Second, the electrochemical process can also happen at the tip (sometimes called tip electrode), therefore the tip body except the tip apex needs to be coated by insulating material because the current measured at the tip is a combination of the faradaic current and tunneling current that cannot be distinguished by the STM controller. The tip is usually coated by apiezon wax or hot glue.

Third, the potential at the tip and the surface are controlled independently using a bipotentiostat. The potentials are controlled with respect to the reference electrode. Fourth, sample preparation methods such as annealing, and argon-ion sputtering is not possible in commonly used EC-STM. However, there are complex systems that make the direct transfer of samples between the UHV environment and EC-STM possible [117]. Fifth, there is no possibility to modify the EC-STM tip *in situ*, whereas, in the UHV system, tip conditioning by annealing, electron bombardment, and sputtering with noble gas ions are routine procedures [118]. Moreover, in the UHV system, the STM can be improved by modifying the apex with atoms or small molecules like CO molecule [119, 120] or by controllably crashing the tip into Au or Si surface for picking up atoms by tip [112, 121]. In STM in air or organic solvents, applying short voltage pulses between the tip and sample can improve the tip; however, such a procedure is not possible in EC-STM. The only procedure common among STM in all environments is touching the sample with the tip and retracting the tip called 'mini-spot-welding' which was introduced by Binning and Rohrer [122].

2.6 Raman spectroscopy

Raman spectroscopy is an analytical spectroscopic technique for studying the vibrational, rotational, and other low-frequency modes in materials. This technique is based on inelastic scattering of light with sample molecules, known as Raman scattering. The shift in the energy of photons can provide us a fingerprint unique to the molecular structure of the sample. Raman spectroscopy is used for identifying molecules, chemical bonding and the structural properties of a sample.

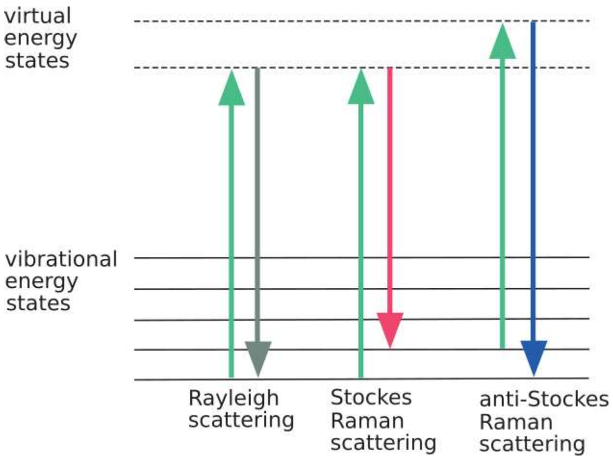

FIGURE 2.15: Energy diagram showing the Rayleigh and Raman (Stockes and anti-Stockes) scattering processes

When a sample is illuminated with a monochromatic laser light, typically in the visible, near-infrared, or near-ultraviolet range, the photons from the laser light interact with the molecules in the sample. These photons can be scattered elastically or inelastically. The majority of the photons are scattered elastically (the energy of scattering photon is unchanged) which is known as Rayleigh scattering. However, a small fraction of the photons are inelastically scattered meaning a transfer of energy between the molecule and the scattered photon occurs. If the molecule gains energy from the photon it ends up in a higher energy state than the initial state, and then the scattered photon loses energy causing its wavelength increases. This is called Stokes Raman scattering. Oppositely, if the molecule loses energy and the scattered photon gains the corresponding energy causing its wavelength to decrease, it is called anti-Stokes Raman scattering (Figure 2.15).

Raman spectra represent scattering intensity as a function of the frequency shifts. There are comprehensive Raman spectral libraries with unique chemical fingerprints to identify different components.

Chapter 3

Experimental Setups and Procedures

This chapter provides a detailed explanation of the experimental setup and procedures used for sample preparation and characterization. The first section covers the general processes, while the subsequent sections describe the specific procedures for each experiment.

3.1 General procedures

3.1.1 Gold samples

In this work, three different Au electrodes were utilized, depending on the characterization techniques. For EC-STM and STM measurements, a flat and smooth surface with a well-defined structure was required, so a gold single-crystal Au(111) electrode was employed. The Au(111) electrode was also used for experiments sensitive to the degree of crystallinity and impurities. For Raman spectroscopy, Au(111)/glass substrates were utilized. For other experiments, polycrystalline Au electrodes were used, referred to as 'Au(poly)' throughout this thesis for convenience.

Preparation of the gold single crystals: The gold surface can be easily cleaned, and the surface can be reconstructed with flame annealing. Before flame annealing, the gold electrodes were rinsed properly with Milli-Q water. The flame annealing was performed in air with a Bunsen burner or butane torch for more than 2 minutes. The annealed gold was also cooled down in the air. The sample in contact with an electrolyte containing the metal ions was first rinsed with nitric acid solution and after rinsing with Milli-Q water, it was flame annealed.

Preparation of the polycrystalline gold electrodes: The Au(poly) electrode was polished with alumina suspensions with sizes of 1 μm and 0.05 μm, respectively. Then it was sonicated in Milli-Q water for 2 minutes. After mechanical polishing, the Au was electropolished by performing 50 to 100 cycles in 0.1 M Na_2SO_4 between $E_2 = -0.1$ V and $E_1 = 0.890$ V vs Ag/AgCl, or in 0.1 M H_2SO_4 between $E_1 = 1.4$ V and $E_2 = -0.4$ V vs Ag/AgCl with 100 mV/s.

Preparation of the Au(111)/glass substrates: For Raman spectroscopy, grafting was performed on $Arrandee^{TM}$ substrates, consisting of a 250 nm thick Au film on borosilicate glass carrying a 2 nm Cr adhesion layer. The sample was cleaned with acetone, isopropanol, and Milli-Q water, followed by brief flame-annealing, although at a lower temperature than that used for gold single crystals.

All glassware and cell compartments were cleaned by boiling in 20% nitric acid and rinsing with ultrapure water. The ultrapure water (Milli-Q, Millipore, 18.2 MOhm cm, $<$ 3 ppb total organic carbon) was used for sample cleaning and preparation of solutions. All electrochemical measurements were performed using the BioLogic SP-30 Potentiostat.

3.1.2 Scanning tunneling microscopy

The Agilent/Keysight 5500 SPM was used to perform the STM and EC-STM. The device has two different scanners for AFM and STM. The microscope has an environmental chamber to perform the microscopy in the Ar environment.

STM in air and organic liquids: STM can be performed in different media, such as UHV, ambient conditions, and solutions. The organic solvents used for STM are liquids with low vapor pressure at room temperature, so it is possible to image the surface without concern about the evaporation of the liquid and changes in the concentration or conductivity during long experiments. They are also electrochemically inert and can be used for a range of molecules that cannot be used in UHV conditions because of their low thermal stability. Also, compared to STM in UHV and EC-STM, the sample preparation and procedures are less complicated. The organic solvents 1-phenyloctane and mesitylene were used.

STM tips for STM in air and organic liquids: The tips for STM in air and organic liquids were prepared by cutting the platinum-iridium (PtIr) wire. The wire, Pt80/Ir20 (temper hard), with a diameter of 0.25 mm was purchased from Advent Research Materials Ltd.

EC-STM electrochemical cell: The electrochemical cell of EC-STM consisted of a Kel-F® cylinder and a Kalrez® O-ring which were pressed onto the surface to create a confined area for holding the electrolyte. Pt wires were used as counter and quasi-reference electrodes (Fig. 3.1). The Pt wire used as a quasi-reference electrode was flame-annealed before use. All cell parts except for the Kalrez O-rings were cleaned, and boiled in 20% nitric acid and rinsed with Milli-Q water. The Kalrez O-ring was cleaned with piranha solution (3:1 conc. H_2SO_4: 30% H_2O_2). This mixture is extremely reactive and requires careful handling. In all our EC-STM studies, the bias voltage refers to the substrate ($V_{bias} = E_{substrate} - E_{tip}$).

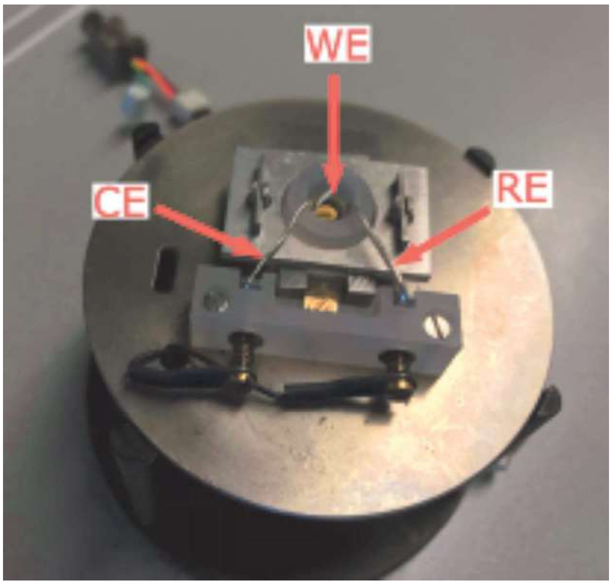

Figure 3.1: Photo of EC-STM cell, including WE: Au(111), quasi-RE: Pt wire and CE: Pt wire

EC-STM tip: The tips were made from the PtIr or tungsten (W) wires. The wires were electrochemically etched and coated before use. The W wire, 99.95% (temper annealed) with a diameter of 0.025 mm, was purchased from Advent Research Materials Ltd. The wire was etched in 2 M NaOH electrolyte by applying a 2.5 V, 50 Hz AC voltage. Then it was coated with hot glue. For PtIr tips, the wire was etched in 2 M KOH/4 M KSCN electrolyte. Then it was coated with Apiezon® wax. Figure 3.2

shows the photos of these two types of tips. The details about the tip etching and coating are explained in Matthias Müllner's PhD thesis [123].

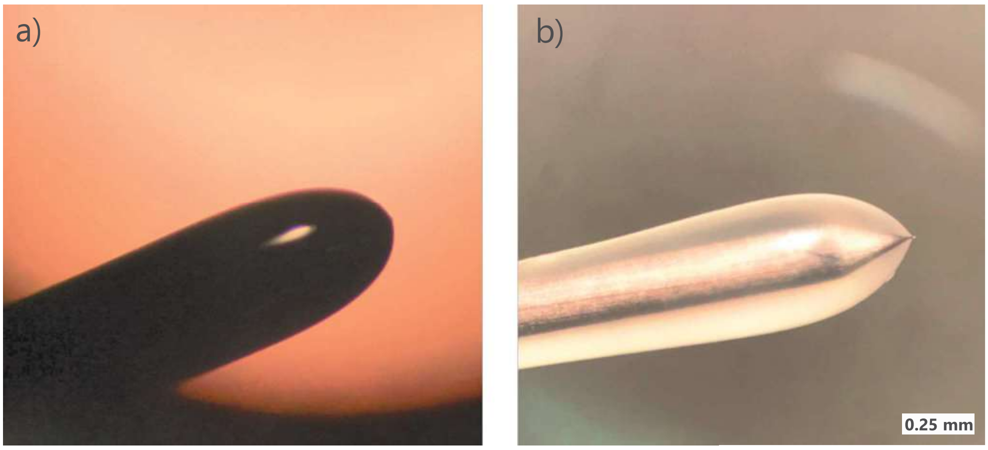

FIGURE 3.2: Magnified photos of the a) Apiezon-coated PtIr tip, and b) hot-glue-coated W tip.

3.2 Characterization of Au(111)/I for studying dynamics of polyiodide chains

Voltammetry in 1 mM KI: The CV of the Au(111) was measured in 5 mM H_2SO_4 + 1 mM KI after removing oxygen from the electrolyte with a scan rate of 10 mV/s. The CV measurement was performed in a three-electrode setup. The Ag/AgCl (3 M NaCl) was used as RE and a polycrystalline Au wire as CE. The OCP of the Pt wire against Ag/AgCl in the same solution was measured. Therefore, for converting the potential measured vs Ag/AgCl to Pt wire the potentials were added to -0.35 V. For converting the potentials measured vs Ag/AgCl to SCE potential, the potentials were added to -0.032 V. For conversion of the potentials measured vs. Pt wire to vs. SCE, the potentials were added to +0.318 V.

EC-STM in 1 mM KI: In Chapter 8, most of the EC-STM images of the Au(111) were measured in the 5 mM H_2SO_4 + 1 mM KI with W tip. However, PtIr tips were also used for further investigation. Two Pt wires were employed as CE and quasi-RE after cleaning with flame.

3.3 Preparation and characterization of bare and grafted gold

Grafting solution and procedure: The grafting solution was prepared in HCl (suprapur), 3,5-bis-*tert*-butylaniline (TBA, 98%, TCI-Tokyo Chemical Industry Ltd.), $NaNO_2$ (99%, Honeywell), NaCl ($\geq$ 99.5%, Thermo Fisher), and Milli-Q. Electrolytes were degassed by bubbling argon (99.999%, Air Liquide) before the electrochemical measurements and it was passed over solutions during measurements unless stated otherwise. For electrochemical grafting, 3,5-bis-*tert*-butylbenzenediazonium (3,5-TBD) was prepared *ex tempore* by mixing 1 or 3 mM TBA in 0.1 M aqueous HCl with a stoichiometric amount of concentrated $NaNO_2$ solution, and magnetic stirring for 10 s. The solutions and the cell used for grafting were kept in an ice-water bath to slow down the decomposition of the diazonium salt. The samples were grafted either by measuring multiple cyclic voltammograms or by chronoamperometry by holding the potential at -0.2 V vs Ag/AgCl for a certain period (the exact grafting time can be found in the result sections for each experiment). The working electrode (or the electrochemical) was tilted at an angle to reduce the chance N_2 bubbles trapped at the surface during the grafting procedure.

After grafting, the samples were first rinsed with Milli-Q water, followed by a generous amount of acetone to remove any physisorbed species, and finally rinsed again with Milli-Q water. This rinsing procedure was applied to all grafted samples; any deviations from this procedure are noted in the text.

Voltammetry in 0.1 M H_2SO_4 solution: The Au(111) electrode for cyclic voltammetry in 0.1 M H_2SO_4 solution (96%, Merck Suprapur) was prepared after flame-annealing procedure. The hanging meniscus configuration was used for the measurements at the single crystal (bare and grafted) electrodes.

The electrolyte was deoxygenated with bubbling argon gas through the electrolyte one hour before electrochemical measurement and flowed above the solution during the measurements. The electrode is immersed in the electrolyte under potential control. The electrode potential was measured against reversible hydrogen electrodes (RHE). For adjusting the meniscus, the potential range of 0.2 V to 0.28 V vs RHE was used. For the main measurements, CV measured between 0.073 and 1.2 V with a scan rate of 10 mV/s with the starting potential 0.25 V. A Pt or Au counter electrode was used.

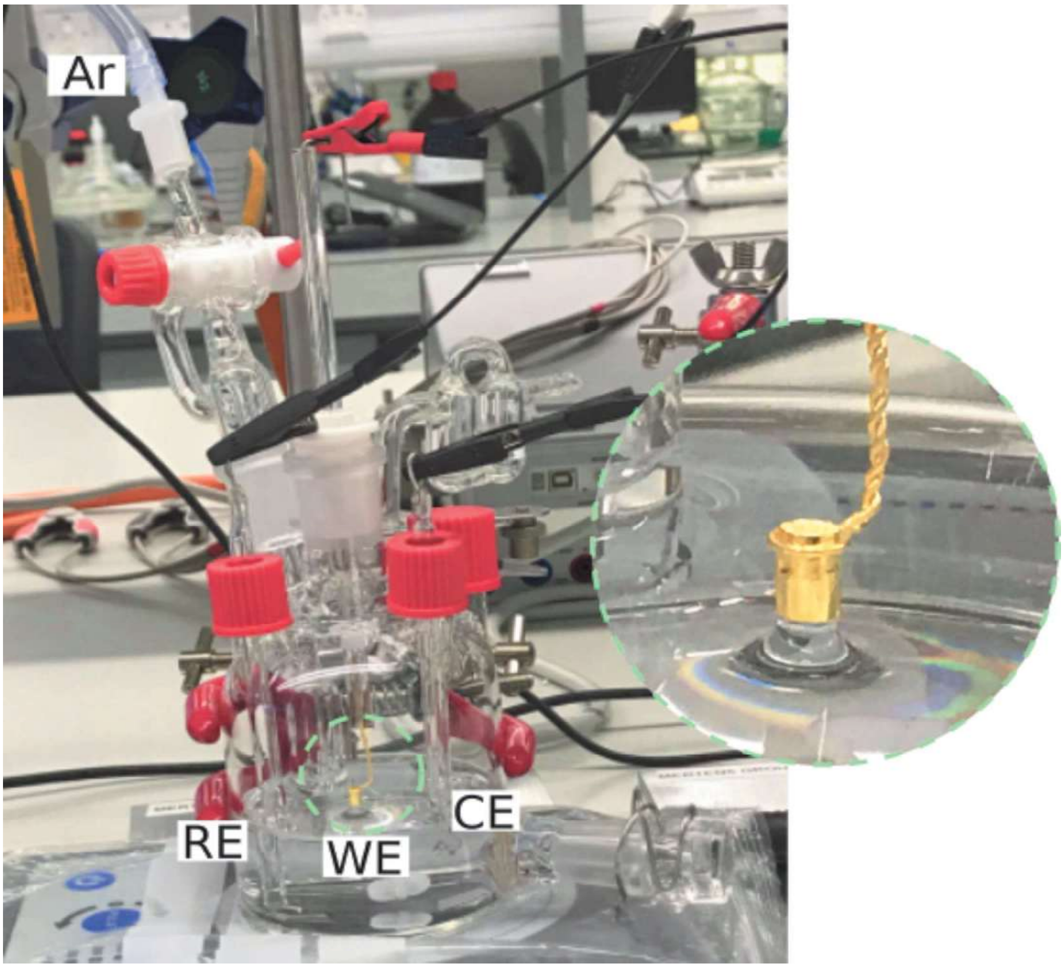

FIGURE 3.3: Photo of the hanging meniscus setup. WE: Au(111), RE: RHE, and CE: Pt wire. Before the start of the measurement, the Ar is purged through the electrolyte, and during the measurement over the electrolyte to remove the oxygen. The magnified image shows an Au cylinder with a flat Au(111) crystal face exposed at the bottom. This flat surface is the only part of the electrode in contact with the electrolyte, interacting through the meniscus at the bottom.

For grafting the Au(111) for studying in 0.1 M H_2SO_4, the freshly annealed electrode was modified by a reduction in a grafting solution containing 1 mM 3,5-TBD. High-coverage grafted Au(111) was prepared by measuring 4 cycles between 0.4 and -0.25 V vs Ag/AgCl in the grafting solution with a scan rate of 50 mV/s, while low-coverage grafting was achieved by extending the negative limit to -0.4 V.

Voltammetry in 1 mM $K_3[Fe(CN)_6]$ in 0.1 M Na_2SO_4 solution: The Au(poly) was mechanically and electrochemically polished. The cyclic voltammetry was performed in 1 mM $K_3[Fe(CN)_6]$ (99%, Merck) in 0.1 M Na_2SO_4 (99.99%, Merck Suprapur) at different scan rates at bare and grafted electrodes. The samples were grafted by CA at -0.2 V vs Ag/AgCl for 400 seconds. Two different concentrations of 1 mM and 3 mM TBD were used.

Cu deposition: The Cu deposition experiments were carried out on bare and modified Au(111) in the hanging meniscus configuration in a glass cell including Au counter electrode and Ag/AgCl/3 M NaCl reference electrode. The $Cu_2(ClO_4)$ (99.999% metals basis, Alfa Aesar), NaCl ($\geq$ 99.5%, Thermo Fisher Scientific), and $HClO_4$ (Merck Suprapur) were used. The copper deposition was performed on the Au(111) in oxygen-free 1 mM $Cu_2(ClO_4)$ + 1 mM NaCl + 0.1 M $HClO_4$ solution with a scan rate of 2 and 10 mV/s for Cu upd and opd, respectively. The flame-annealed Au(111) electrode was grafted by measuring CA at -0.2 V vs Ag/AgCl for 60 seconds in the grafting solution containing 1 mM TBD. After the grafting, the samples were rinsed with Milli-Q water, acetone, and as a final step Milli-Q water.

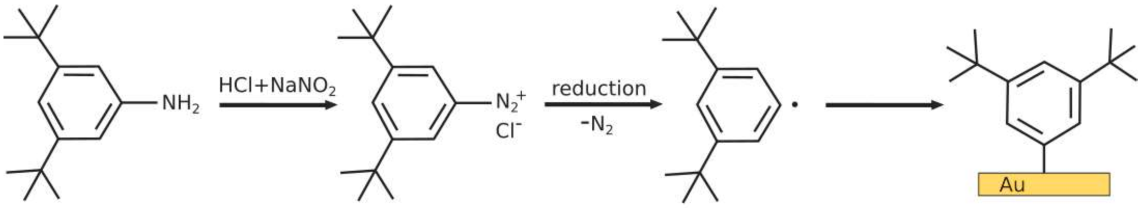

3,5-TBA 3,5-TBD

FIGURE 3.4: The reaction schematic of the grafting process. The process begins with 3,5-bis-*tert*-butylaniline, which is used to produce TBD *in situ*. This is followed by electrochemical reduction to generate aryl radicals. When these radicals form near the gold substrate, they can attack the surface, forming a covalent bond.

Deconvolution of Cu upd peaks: The cathodic segment of the Cu upd voltammogram was deconvoluted into Gaussian peaks using Origin® software. An exponential baseline, accounting for the onset of Cu overpotential deposition, was defined using the software's built-in second derivative anchor points finding method and snapping 12 points on the experimental data, followed by exponential fitting. Nonlinear curve fitting of the peaks relied on the Levenberg-Marquardt algorithm and was considered successful when $\chi^2 \leq 10^{-9}$.

Impedance measurements on Au(poly): Impedance data were measured on bare (poly)Au at OCP (E = 0.196 V vs. Ag/AgCl) in a solution of 1 mM $Fe(CN)_6^{3-/4-}$ and 0.1 M Na_2SO_4. The impedance spectra were recorded using a Metrohm potentiostat in single-sine mode (sinus amplitude = 10 mV) in a frequency range from 100 kHz to 0.1 Hz, consisting of 43 logarithmically spaced frequencies. Data fitting was performed using Nova 2.1 software.

Impedance measurements for studying grafting process: Potassium hexacyanoferrate(III) (99%, Merk), potassium hexacyanoferrate (II) trihydrate (98%, Merk) were used to make 1 mM $[Fe(CN)_6]^{3-}$ and 1 mM $[Fe(CN)_6]^{4-}$ aqueous solutions, separately. The Au(poly) electrode was mechanically polished with alumina suspensions with size of 1 μm and rinsed and sonicated for 30 seconds. The polishing continued with smaller size alumina particles of 0.05 μ m and proceeded with sonication of 2 minutes in Milli-Q water. The Au electrode was further electrochemically polished by measuring 50 cycles in 0.1 M H_2SO_4 between $E_1 = 1.4$ V and $E_2 = -0.4$ V vs Ag/AgCl with a scan rate of 100 mV/s. The Au and Ag/AgCl were used as a counter and reference electrode respectively. The EIS measurements were performed with the cold solution of 1 mM TBA + 0.1 M HCl in the presence of both forms of the Fe(II)/(III) redox couple, 1 mM $[Fe(CN)_6]^{4-}$ and 1 mM $[Fe(CN)_6]^{3-}$, while the three-electrode electrochemical cell was immersed in the ice-water bath. The $NaNO_2$ aqueous solution was added (1.02 mM in the final grafting solution) and stirred for less than 10 seconds before starting the CA and EIS sequence of measurements. The OCP at the beginning of the experiment was about 0.0395 V, equal to the formal potential of the hexacyanoferrate ions, the average of cathodic and anodic peak potential measured by cyclic voltammetry. The sequence started by holding potential at 0.0395 V for 10 seconds and then stepping potential to which electrochemical grafting happens, -0.2 V vs Ag/AgCl for 3 seconds. Then the potential hold for 5 seconds at 0.395 V. After that The EIS measurement was performed by keeping the potential at 0.395 V for 30 seconds in the frequency range between 100 kHz and 100 mHz using a signal sinus amplitude of 10 mV. The sequence of CA and EIS was repeated continuously 10 times in total (Fig. 7.3). In summary, measuring the sequence below was used:

1. Measuring CA at $E_f = 0.395$ V for 10 s
2. Stepping the potential to $E_g =$ -0.2 V for 3 s
3. Stepping back to E_f for 5 s
4. Holding potential to E_f for 30 s before starting the EIS + measuring EIS at E_f
5. Repeating 1 to 4 procedures for 10 times

These EIS measurements were performed with a BioLogic BP-300 potentiostat and the spectra were fitted with EC-Lab software. For fitting, the first two measured points at the highest frequency were excluded.

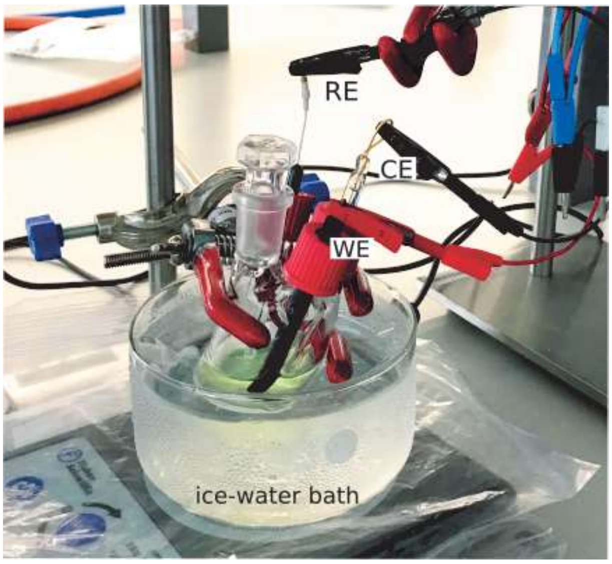

FIGURE 3.5: Experimental setup used in EIS measurement. The cell is placed in an ice-water bath to slow down the chemical decomposition of the diazonium salt and is angled at 45°to allow N_2 produced at the working electrode to escape.

STM and EC-STM of the grafted samples: For both STM and EC-STM, the Au(111) electrodes were flame-annealed before grafting. Grafting was performed using CA at -0.2 V vs Ag/AgCl in the grafting solution, which contained either 1 mM or 3 mM TBD, for 60 seconds. The grafted samples were rinsed with Milli-Q water, acetone, and Milli-Q water after grafting, before mounting on the STM cell.

For the EC-STM in the presence of iodine, a solution of 1 mM KI ($\geq$ 99.99% trace metals basis Merck) + 5 mM H_2SO_4 was prepared (96%, Merck Suprapur).

Raman spectroscopy: Raman Spectroscopy performed on the Au(111)/glass samples. *Ex situ* Raman spectroscopy was carried out in the air with an inVia confocal Raman microscope (Renishaw plc) with a 785 nm laser (20 mW when operating at 100%) and a 50× objective. Data processing was carried out with Spectragryph [1] and baseline correction was performed with an adaptive method and smoothing with triangular moving average of 4 intervals.

---

[1] F. Menges, Spectragryph, Optical spectroscopy software (2023).

Chapter 4

Covalent grafting of gold: voltammetry

In this chapter, we consider the voltammetric aspects of electrochemical grafting on gold substrates, except for copper underpotential and overpotential deposition (Cu UPD and OPD), which are discussed in Chapter 5. To make the information as broadly relevant as possible, we consider both the voltammetric behavior of single crystal electrodes and polycrystalline Au substrates and discuss fundamentals as well as technical aspects. We exclusively focus on the grafting of 3,5-bis-*tert*-butylbenzenediazonium chloride (3,5-TBD), a sterically hindered molecule that is expected to only allow (sub)monolayer formation, and that was studied extensively for grafting on carbonaceous materials in previous work [11, 12, 124]. For stability reasons, the electroactive TBD is formed from its amine precursor 3,5-bis-*tert*-butylaniline (TBA) by adding a small excess of nitrous acid (HCl + $NaNO_2$) immediately before grafting (for details, see Chapter 3).

Sections 4.2.1 and 4.2.2 are published in Azmi et al., *Electrochimica Acta* 500 (2024) 144743. Copyright 2024 by Author(s), published under a Creative Commons Attribution license CC BY-NC 4.0 (see [125]). The information in this chapter has been reformatted and expanded to include additional data and analysis not covered in the original publication.

4.1 Introduction

Among the electrochemical techniques, cyclic voltammetry is the most used technique, performed in the supporting electrolyte with or without the presence of the redox couples. Cyclic voltammetry in an (aqueous or organic) electrolyte provides information about the stability of the film at different potential ranges, the electron transfer, and the estimation of the graft coverage. The determination of surface coverage was reported for graft molecules containing electroactive nitrophenyl groups via the integration of the charge corresponding to the cathodic or anodic processes [42, 48, 49]. The coverage of the grafts can also be estimated by measuring the CVs of the surface in an acidic solution and comparing the integrated charge under the oxide reduction peak before and after modification [126], if the grafts survive these potentials.

Cyclic voltammetry in a solution containing redox species such as hexacyanoferrate (III/II) ($[Fe(CN)_6]^{3-/4-}$) provides valuable information about the electron transfer at the surface of the grafted electrode, as well as its stability and blocking behavior [124, 126–131].

In addition to stability, the barrier properties of the modifying layer can be analyzed using a solution containing redox species. The redox reaction of hexacyanoferrate (III/II) at the gold surface is a reversible electrochemical reaction, as the rate of electron transfer exceeds the rate of mass transport. The apparent or measured electron transfer rate constant is affected whenever the surface electrode is modified. The electron transfer mechanism depends on the nature of the modifying layer, such as a monolayer [132]. Three possible microscopic structures of the monolayer film are illustrated in Figure 4.1. a) For a defect-free, compact, and ordered monolayer uniformly covering the entire surface with constant thickness, the electron transfer occurs through tunneling across the layer. b) If the monolayer is well-ordered and compact but contains microsized pinholes, the electrode acts as a microelectrode array, and these pinholes allow electrons to access the substrate surface directly. c) for a disordered monolayer with microscopic defects and pinholes, the film is thinner at the defect sites than on the rest of the surface (i.e., non-uniform thickness). In this case, the tunneling across the non-uniform layer occurs, where 'average thickness of the whole monolayer' is used for describing the blocking behavior of structurally disordered SAMs on gold electrodes [132–134]. There might be other complex structures that are not discussed here.

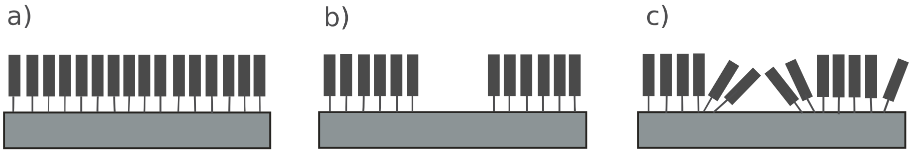

FIGURE 4.1: A monolayer with different microscopic structures.

4.2 Results and discussion

4.2.1 Electrochemical grafting of gold

Figure 4.2 shows the cyclic voltammogram of polycrystalline Au or Au(poly) in the complete grafting solution (0.1 M HCl + 1 mM TBD), red trace, and in the same solution without $NaNO_2$ added, dashed black trace. As TBD is quite unstable once formed, even at low temperatures, any simplification to speed up the procedure is helpful. For this reason, we investigated whether the presence of oxygen from air can be tolerated, as deaeration with an inert gas takes some time. The need to be as fast as possible also explains why we use a polycrystalline Au electrode here, as forming a well-defined hanging meniscus with the Au single crystal is not feasible and is further complicated by the formation of dinitrogen bubbles during grafting. For all single crystal experiments, we show later in the chapter, the grafting itself was performed by immersing the entire Au bead, not just the polished surface. Once grafting was complete, a hanging meniscus could be established as usual, as at that point there was no more time pressure.

In the mixture without $NaNO_2$ (dashed black trace), TBD is not present and therefore cannot be reduced to form aryl radicals. The reduction wave that occurs at -0.3 V vs. Ag/AgCl can therefore be ascribed to either the two-electron or four-electron reduction of dissolved dioxygen:

$$O_2\,(aq) + 2\,e^- + 2\,H^+\,(aq) \longleftrightarrow H_2O_2\,(aq)$$

or

$$O_2\,(aq) + 4\,e^- + 4\,H^+\,(aq) \longleftrightarrow 2\,H_2O\,(aq)$$

Two further processes that can affect covalent grafting must be considered: starting at -0.5 V during the cathodic scan, the onset of the hydrogen evolution reaction (HER) can be observed: $2\,H^+\,(aq) + 2\,e^- \longleftrightarrow H_2\,(g)$

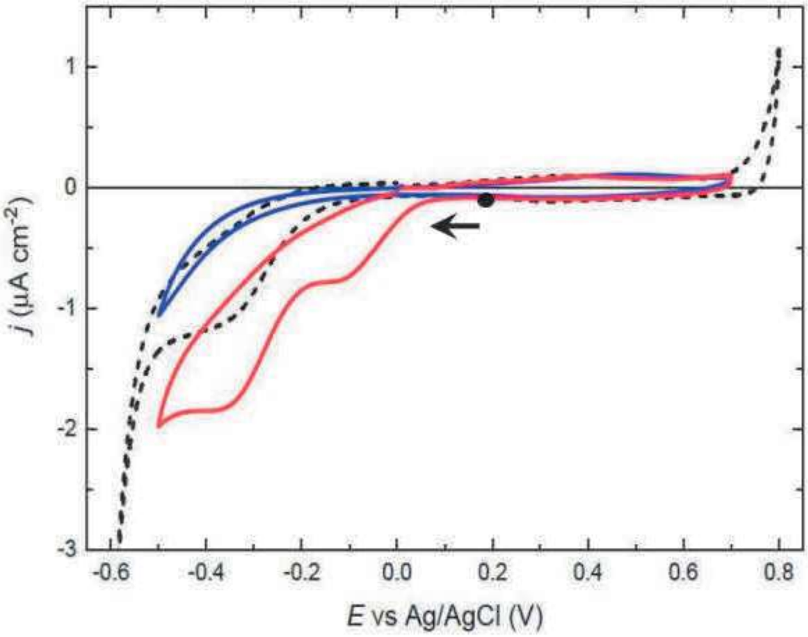

FIGURE 4.2: Cyclic voltammograms (first cycle) of Au(poly) in 1 mM TBD + 0.1 M HCl (1st and 5th cycle, red and blue trace) and in 1 mM TBA + 0.1 HCl (black dashed trace); dissolved dioxygen was not removed. Scan rate: 50 mV/s.

While at +0.8 V during the anodic scan, the oxygen evolution reaction (OER) and/or chloride begins. All these processes are associated with bubble nucleation and growth at the electrode-electrolyte interface. Any bubbles present can act as a mask against grafting and were indeed thought responsible for the formation of nanocorrals ('fairy circles') in previous work [12]. The reduction of dissolved oxygen, however, does not produce bubbles and is therefore not expected to interfere with grafting. So the hydrogen gas evolution at the electrode-electrolyte interface can block radicals from attacking the surface. For increasing the grafting efficiency, the lower vertex potential of the CV for reducing the diazonium salts should be set less negative enough to prevent hydrogen molecule formation. Besides the masking properties of the hydrogen bubbles, the competition of water molecules and diazoniums for reducing at the surface can decrease the grafting efficiency [49].

In the presence of TBD, Fig. 4.2, red (1st cycle), the electrochemical reduction of the diazonium compound (and the generation of aryl radicals) can be seen as an additional wave at ca. 0 V, which is superimposed with the oxygen reduction current at potentials <-0.2 V. Importantly, while the diazonium reduction current is a direct measure of the rate with which the aryl radicals (i.e., the grafting species) are formed, the CV does not provide direct information on the grafting step (that is, the substrate-graft bond formation), which is not electrochemical in nature. Grafting is usually inferred from a decrease in the reduction wave during subsequent cycles, although also the depletion of the electroactive material in the diffusion layer must be considered as well, Fig. 4.2, blue trace.

4.2.2 Grafted Au(111) in supporting electrolyte: stability

As metal single crystals offer a very high microscopic uniformity of binding sites, cyclic voltammetry is often strikingly different from polycrystalline surfaces. Figure 4.3 compares CVs of bare flame-annealed Au(111) in oxygen-free 0.1 M H_2SO_4, black trace, with the same surface with two different degrees of covalent grafting, blue and red trace. The CVs were measured in the double layer potential region, between ca. 0.1 V and 1.2 V vs. RHE. The highly characteristic shape of the bare Au(111) CV is caused by the interaction of (hydrogen)sulfate with the metal surface and is limited by the onset of hydrogen evolution at negative potentials, and gold oxidation starting above 1.3 V.

During the first cycle only, a double peak around 0.6 V indicates the lifting of the thermally induced $(p\times\sqrt{3})$ reconstruction, resulting in a (1×1) surface [135]. The lifting of the reconstruction is accompanied by disordered adsorption of the (hydrogen)sulfate. As the potential increases the density of sulfate adsorbed on the surface increases, leading to a gradual decrease of the interfacial capacitance. The sharp, so-called ‘needle peak’ at 1.1 V, indicates a disorder-to-order phase transition in the (hydrogen)sulfate adlayer, which from STM studies is then known to assume a $(\sqrt{3}\times\sqrt{7})$R19.1° structure. During the cathodic scan, most features observed during the anodic scan are reversed [136–139].

The CVs of the two modified surfaces, low- and high-density grafted Au(111) (blue and red traces, respectively), show several clear differences from bare Au(111), while other features are unexpectedly similar. Intuitively, the easiest to understand is the value of the capacitive current at $E = 0.34$ V, halfway between the onset of hydrogen evolution and the potential region where sulfate starts to adsorb on the surface, and where all three CVs are featureless. From these current values, by considering that $j = C.\,\frac{dE}{dt}$ with current density j and differential capacitance C, the interfacial capacitance can be

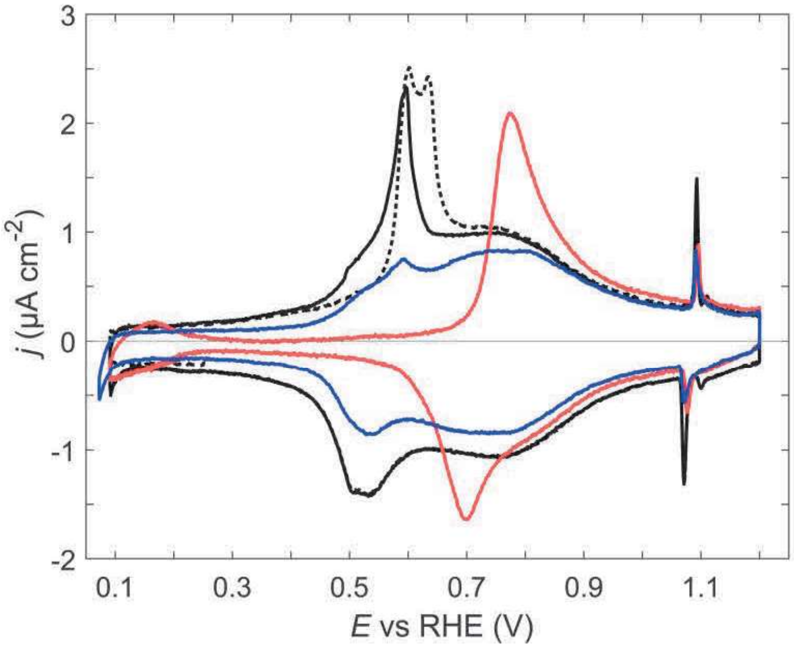

FIGURE 4.3: Cyclic voltammograms of bare (1st and 2nd cycle, black dashed and full trace) and 3,5-TBD modified Au(111) (low and high coverage, blue and red trace) in an oxygen-free 0.1 M H_2SO_4. Scan rate: 10 mV/s

estimated as 27.3 μF cm^{-2} for bare Au(111), which decreases by 44% to 15.2 μF cm^{-2} for low-density grafted Au(111) and by 81% to 5.1 μF cm^{-2} for high-density grafted Au(111), as is expected for an interface that is increasingly covered with low-dielectric organic molecules.

For the low-density (estimated at 30% surface coverage from capacitance and Cu upd, see in Chapter 5) grafted surface (Fig. 4.3, blue trace), this observation persists throughout most of the CV, as all features of the bare Au(111) CV are attenuated to a similar degree. The high-density grafted surface, however, shows some striking differences. Close to the hydrogen evolution onset, at potentials $0.1V < E < 0.2V$ vs. RHE, the capacitance of grafted and bare surface is nearly identical, which may indicate that the grafting fundamentally changes the interaction between solvated protons and the metal surface. Looking at more positive potentials, the characteristic shape associated with (hydrogen)sulfate adsorption on bare Au(111) is qualitatively preserved on the grafted surface, but at potentials that are roughly 200 mV more positive. Once sulfate adsorption has started on the grafted surface, at $E > 0.9$ V, the CV is almost identical to that for bare Au(111). Possibly most surprising is that the needle peak, indicative of the disorder-order transition in the (hydrogen)sulfate adlayer, occurs at the same potential for all three surfaces if attenuated when grafts are present.

Taken together, this behavior may indicate a type of switching in the adlayer, in which the grafts change their configuration on the surface (e.g. between flat-lying and standing up) as a function of interfacial potential, making the adlayer more or less transparent for the species in solution. Theoretical calculations indicate that depending on the details of the metal, upright (yielding a sigma-type bond) and flat-lying (yielding a pi-type bond) orientations of adsorbed aryl radicals are both feasible and energetically clearly qualify as chemisorption [140]. Switching behaviors are often complex and at the basis of many supramolecular phenomena at electrified interfaces, from intricate pattern formation down to single-molecule switching [141–145].

If the total charge in the double layer region is determined by integration of the area under the CVs, the value of 131 $\mu\mathrm{F\,cm^{-2}}$ for bare Au(111) decreases by 30 % to 91.4 $\mu\mathrm{F\,cm^{-2}}$ for low-density grafted Au(111) and by 34% to 85.9 $\mu\mathrm{F\,cm^{-2}}$, only marginally more, for high-density grafted Au(111), which appears to support the switching hypothesis. Alternatively, this may be the effect of physisorbed reaction products (dimers, oligomers) of TBD reduction that accumulate at the electrode surface and block the latter at low potentials but become transparent for (hydrogen)sulfate that may then adsorb at more positive potentials. A definitive answer to the nature of the peak shift will likely require spectroelectrochemical experiments such as surface-enhanced infrared reflection absorption spectroscopy (SEIRAS) [146].

To investigate the possibility of oxidative desorption of the grafts, potentials more positive than those in the previous section were applied. The dotted trace in Figure 4.4 shows the behavior for bare Au(111) in 0.1 M H_2SO_4 up to a potential value of 1.7 V vs. RHE. As the currents are more than an order of magnitude higher than in the double-layer region, the latter is also plotted on a magnified current scale to be able to monitor the effects of oxidation. For bare gold, oxidation starts when $E > 1.3$ V, with a small peak at 1.4 V and a main peak at 1.58 V. The small peak is typically ascribed to the oxidation of step edge atoms, which are more strongly undercoordinated than terrace atoms and hence thermodynamically less stable. The size of this pre-peak can therefore be taken as a measure of the single crystal quality, as a larger miscut leads to a more stepped surface and a larger pre-peak. The main peak accounts for oxidation of the terrace atoms [147]. If the potential is increased beyond the main peak, bulk gold oxidation starts to occur, which is not recommended on high-quality single crystals but may be useful when conditioning mechanically polished single crystals. On reversing the scan direction, the reduction of the Au oxide occurs at 1.18 V [147]. The integrated charge under the oxidation peaks is larger than the reduction charge by 4.6%, which is caused by anodic dissolution of a small amount of gold and contributes to electrochemical polishing of the electrode on continued cycling [148].

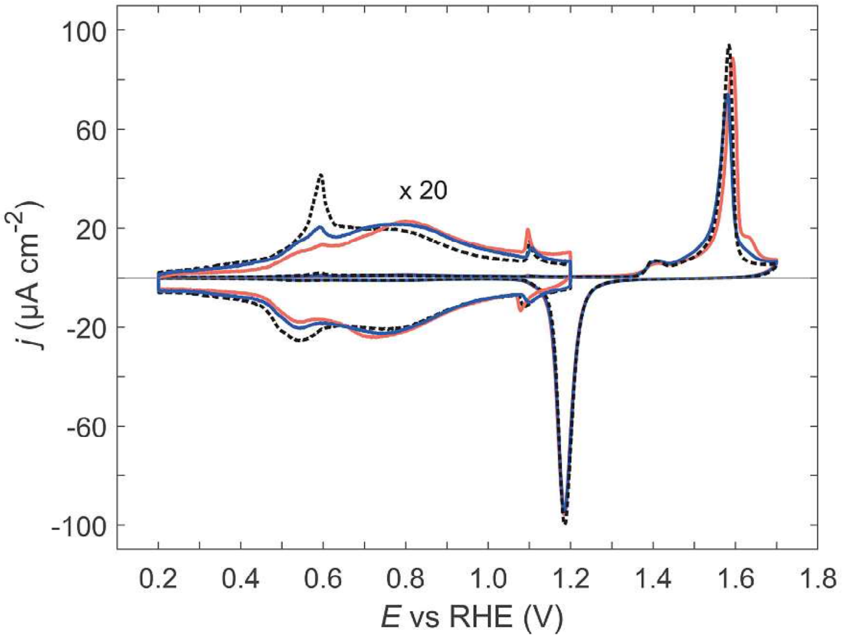

FIGURE 4.4: Cyclic voltammograms of bare (black dashed trace) and grafted (red and blue trace, 2 cycles) Au(111) in oxygen-free 0.1 M H_2SO_4. Scan rate: 10 mV/s.

When the same measurement is performed on grafted Au(111), Figure 4.4, red full trace, an additional peak appears at 1.63 V, but only during the first cycle. This potential value is more positive than the oxidation of Au terrace atoms and suggests that this feature is associated with the oxidative desorption of the covalent grafts. The fact that the extra oxidation feature is observed only once agrees with a chemically irreversible process, or the formation of a soluble species that diffuse away from the surface and does not reabsorb, which matches observations for oxidative desorption of thiols [149]. The gold reduction charge is identical for the three peaks to within 1%. However, the oxidation charge during the first cycle for Au(111)-TBD is 8% larger than during the second cycle, which matches the value for bare Au(111) within the confidence interval of the measurement, strongly suggesting that more charge is consumed than for the oxidation of a monolayer of gold. Even though a full elucidation of the oxidative desorption of the covalent grafts would require a detailed chemical analysis of the electrolyte in the vicinity of the surface and falls outside the scope of this work, this extra charge indicates that the breaking of the Au-C bond is not a homolytic process and may involve the formation of compounds with higher carbon oxidation states.

Additional information is contained in the respective peak positions, which are extremely sensitive to both thermodynamic and kinetic factors that contribute to the overall electrode behavior. During the first oxidation cycle of the grafted surface, the main oxidation peak ascribed to the oxidation of Au terrace atoms occurs 10 mV more positive than for bare gold and returns to this bare Au value during the second cycle. This small but significant increase indicates a stabilization of the surface as a whole by the covalent grafts, even if the surface coverage is much lower than unity. A similar but much more pronounced stabilization against electrochemical oxidation was observed for Rh(111) covered with a corrugated monolayer of hexagonal boron nitride [150].

The oxidative removal of at least part of the covalent grafts is also reflected in the partial return of bare Au(111) behavior in the double-layer region, Figure 4.4, blue trace. The fact that the behavior observed for bare Au(111) is not fully restored also after multiple excursions into the oxidation region for the grafted surface may again point at the role of reaction products that remain physisorbed at the electrode-electrolyte interface.

The exact nature of the Au-C bond is difficult to prove and has been the subject of considerable debate [17]. While Raman spectroscopy is extremely sensitive to the symmetry-breaking during covalent binding of organic radicals to graphitic surfaces, in which an sp^2 carbon assumes at least partial sp^3 character [12, 151], no strong characteristic resonance is associated with a covalent Au-C bond.

Figure 4.5 shows Raman spectra of bare gold (polycrystalline film on glass), and of the same sample after grafting. To maximize comparability of results, both measurements were performed on the same sample that was only half immersed in the solution during grafting, so that a simple repositioning of the sample, without changing focus, yielded both spectra. From the amphiphilic nature of the grafting precursor (hydrophobic bis-*tert*-butylphenyl ring carrying a hydrophilic diazonium chloride group), accumulation of this molecule is expected at the electrolyte-air interface, which explains why higher coverage and a visible line in the optical micrograph occur during grafting, Fig. 4.5, inset. Comparing the Raman spectra of the bare and grafted areas of the sample, peaks

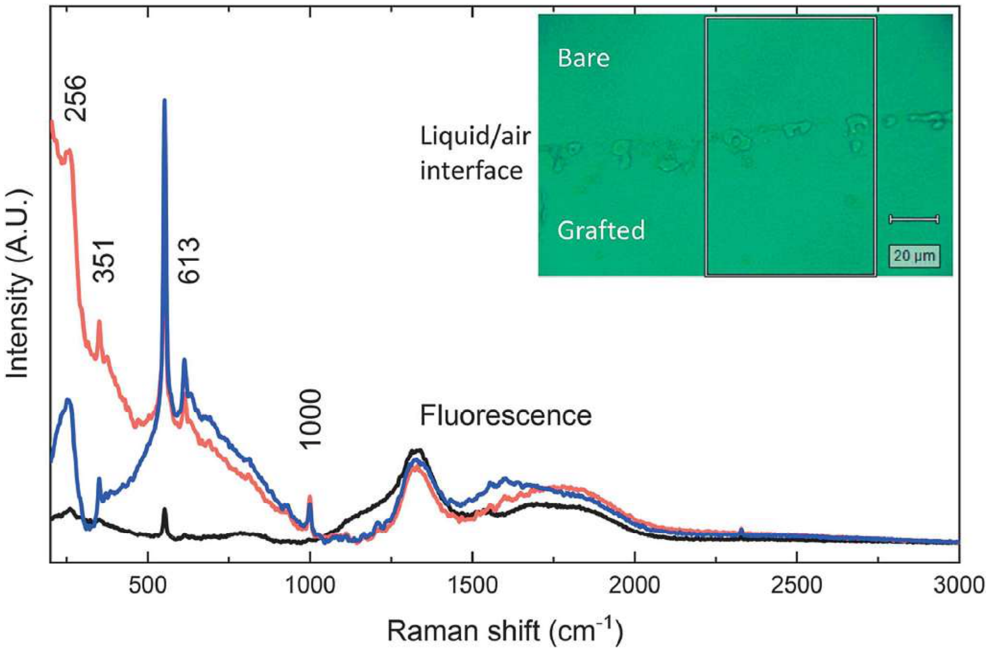

FIGURE 4.5: Raman spectra of bare (black trace) and grafted (red and blue trace) gold (thin film on glass) in air. Laser wavelength 785 nm. The inset shows an optical micrograph of the sample, which was partly immersed in the grafting solution; the water line, where high coverage of grafts is expected, is clearly visible. Performed by Dr. Lorna Ashton.

are found at 613 and at 1000 cm^{-1} on the grafted areas that are absent on bare Au. The bimodal band in the 1300-1700 cm^{-1} region originates from photoluminescence in the Au-on-glass substrate [152, 153]. The peaks in the lowest wavenumber region ($<$ 400 cm^{-1}) may originate from electronic Raman scattering on the substrate roughened by grafting. The peak at 1000 cm^{-1} is tentatively assigned to aromatic in-plane C—H deformation, while the peak at 613 cm^{-1} may indicate a phenyl-metal compound [154]. While the 1000 cm^{-1} peak may arise from any physisorbed aromatic compound on the surface, the 613 cm^{-1} does not and is therefore clearly more significant to demonstrate covalent binding. A recent paper, using ^{13}C cross-polarization/magic angle spinning solid-state NMR spectroscopy combined with isotope substitution provides the to date most conclusive evidence of covalent binding following diazonium-based grafting on gold [155].

4.2.3 Grafted Au(poly) in hexacyanoferrate: blocking behavior

The passivation or blocking of gold surfaces after modification with aryl diazonium salts was studied using potassium ferricyanide as a redox probe.

Figure 4.6 compares CVs of the bare (blue trace) with the grafted Au(poly) followed by rinsing with Milli-Q water (red trace) and later with acetone (green trace). The CVs were measured in 1 mM $K_3Fe(CN)_6$ + 0.1 M Na_2SO_4 with a scan rate of 50 mV/s.

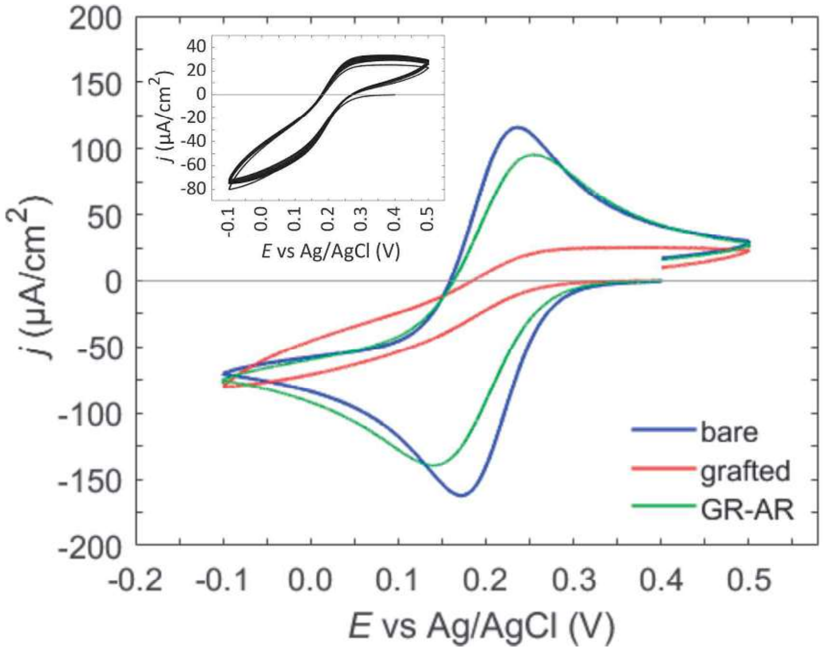

FIGURE 4.6: CVs of bare (blue trace) and grafted Au(poly) (red trace) in 1 mM $K_3Fe(CN)_6$ + 0.1 M Na_2SO_4 at 50 mV/s. The electrode was grafted by CA for 400 sec at -0.2 V vs. Ag/AgCl in 3 mM TBA + 0.5 M HCl + 3 mM $NaNO_2$. After grafting the electrode was rinsed with Milli-Q water (red trace) and then with acetone (green trace). Inset: 20 cycles of grafted Au(poly) in the same electrolyte at 200 mV/s, rinsed with Milli-Q water after grafting.

For the grafted surface (red trace) that has only been rinsed with Milli-Q water, compared to the bare surface (blue trace), the redox reaction is significantly suppressed. However, a complete surface blockage on Au(poly) is not observed and still a faded S-shape or a partially sigmoidal shape CV is observable (see inset). The CV of the grafted Au(poly) before acetone rinse just after rinsing with Milli-Q water, including twenty consecutive cycles with a scan rate of 200 mV/s, is shown in the inset of Figure 4.6. Although some changes are observed after measuring each cycle, they are not significant.

There are dramatic differences between the CVs of the grafted Au(poly) before (Fig. 4.6, red trace) and after rinsing with acetone (green trace). After rinsing the grafted surface with acetone, charge transfer at the Au surface becomes easier; therefore, the current increases to 85% of I_{pc} at the Au bare electrode. In the literature rinsing and sonication of the grafted gold surface in either acetone or acetonitrile have been suggested to remove the physisorbed species from the grafted surface [127, 131, 156]. The physisorbed species, which impede electron transfer, can be removed with a thorough rinse using acetone. The freed Au sites can later contribute to the $K_3Fe(CN)_6$ redox reaction (Fig. 4.6, green trace). Moreover, the figure shows that acetone is a better solvent than water for removing the physisorbed species from the surface.

For studying the barrier properties of the grafted layer, CVs of grafted Au(poly) with 3 mM TBD, before and after acetone rinse, were recorded at scan rates of 5, 10, 25, 50, 100, and 200 mV/s in 1 mM $K_3Fe(CN)_6$ + 0.1 M Na_2SO_4 solution.

For comparison, measurements on bare Au were also included in Figure 4.7. On the bare Au surface, the peak positions remain unchanged with scan rate, Fig 4.7-c, indicating that the $[Fe(CN)_6]^{3-/4-}$ probe exhibits fast electrode kinetics. Thus, we can conclude that it is a reversible process.

In contrast, the peak potentials shift for irreversible and quasi-reversible systems, as observed in Figure 4.7-b, corresponds to grafted Au after acetone rinsing. For CVs of grafted Au before the acetone rinse, there is no peak and it has a partially sigmoidal shape rather than peak-shaped response (Fig. 4.7-a). Therefore, only the data from bare Au and grafted Au after acetone rinse were used for further analysis.

The peak-to-peak separations as a function of scan rate for bare Au and acetone-rinsed grafted Au are shown in Figure 4.8-a, with best-fit lines represented by dashed lines. It shows that the peak-to-peak separation (ΔE_p) of the bare Au (blue asterisk) is constant at different scan rates ($\Delta E = 64 \pm 2$ mV). For a reversible system $\Delta E_p = 2.218\,\frac{RT}{F} = 57$ mV (298 K)[96]. In contrast, for the acetone-rinsed grafted Au (red circle), the peak-to-peak separation increases with increasing scan rate (Fig. 4.7-a).

Besides peak-to-peak separation, the reversibility of the electron transfer can be studied by examining the relation between peak current and the scan rate. For bare Au since the redox process is electrochemically reversible, I_p increases linearly with the square root of the scan rate based on the Randles-Sevcik equation (Eq. 2.49). The peak current values as a function of scan rate are presented in Figure 4.8-b. By analyzing the slope of the I_{pc} vs. $\nu^{1/2}$ plot, the diffusion coefficient of hexacyanoferrate (III) on bare Au can be determined from $D = \left(\frac{slope}{2.7 \times 10^5 \times AC_\infty}\right)^2$ where $A = 0.0201$ cm^2, $C = 1\,\mu\,\mathrm{mol\,cm^{-3}}$ and $T = 295\,K$. The slope corresponding to bare Au is 1.466×10^{-5}

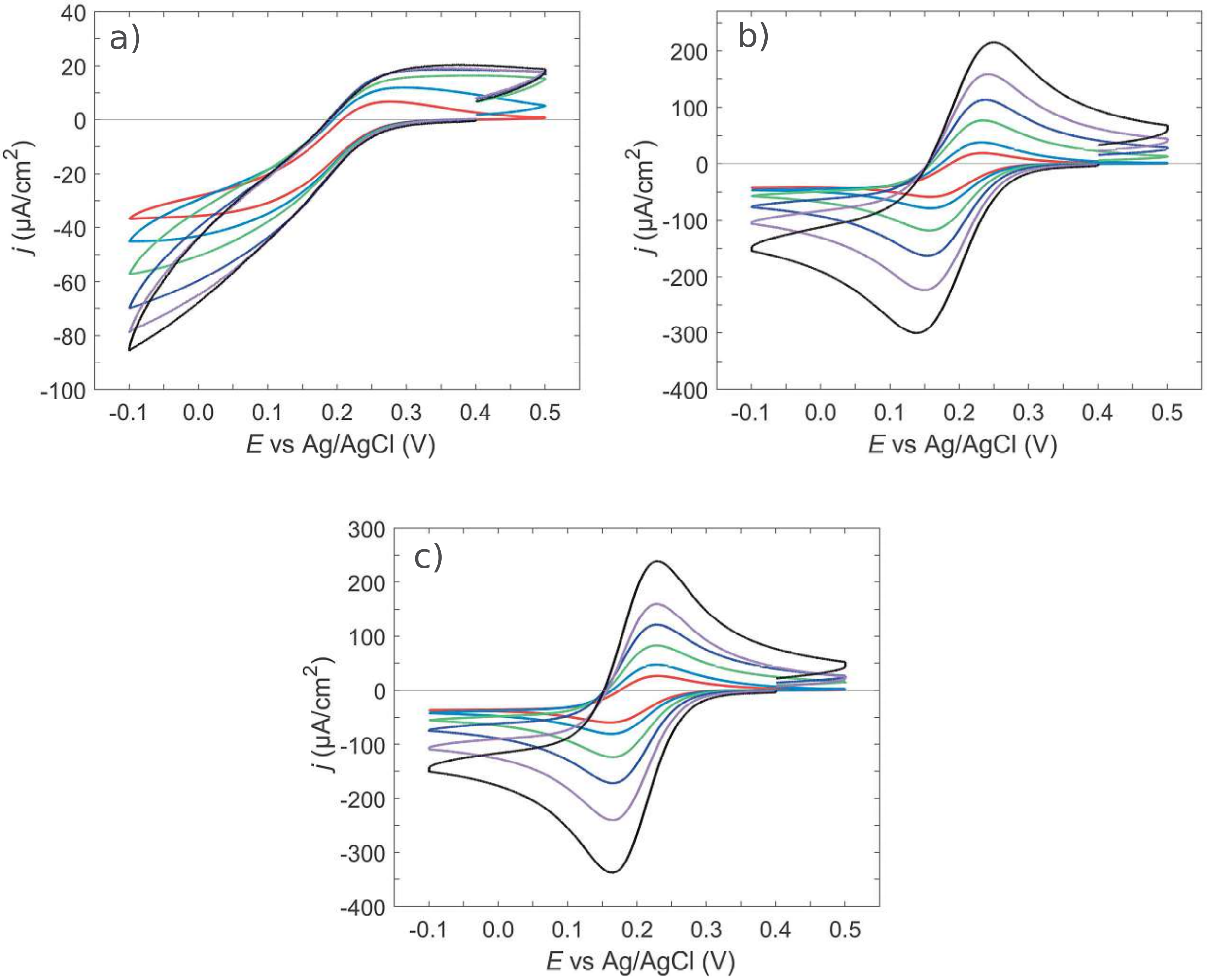

FIGURE 4.7: CVs of a) grafted, b) rinsed with acetone after grafting, and c) bare Au(poly), measured in 1 mM $K_3Fe(CN)_6$ + 0.1 M Na_2SO_4 at different scan rates in the Ar atmosphere. Inner to outer trace: 5, 10, 25, 50, 100 and 200 mVs^{-1}. Au grafted at -0.2 V vs. Ag/AgCl, 400 sec in 3 mM TBA + 0.5 M HCl + 3 mM $NaNO_2$.

$A\,s^{1/2}V^{-1/2}$. The extracted diffusion coefficient of hexacyanoferrate (III) on bare Au is 7.3×10^{-6} $cm^2\,s^{-1}$ which is in good agreement with 7.2×10^{-6} $cm^2\,s^{-1}$ reported in the literature [157, 158].

To extract the heterogeneous electron transfer rate constant, k^0_{app}, a dimensionless parameter ψ was calculated based on Equation 2.54, as more fully discussed in Section 2.4.3.

The actual microscopic rate constant on bare parts of the surface is k^0_{bare} while the apparent rate constant on the whole surface is $k^0_{app-modi}$ which is smaller than k^0_{bare}, ($k^0_{app-modi} < k^0_{bare}$).

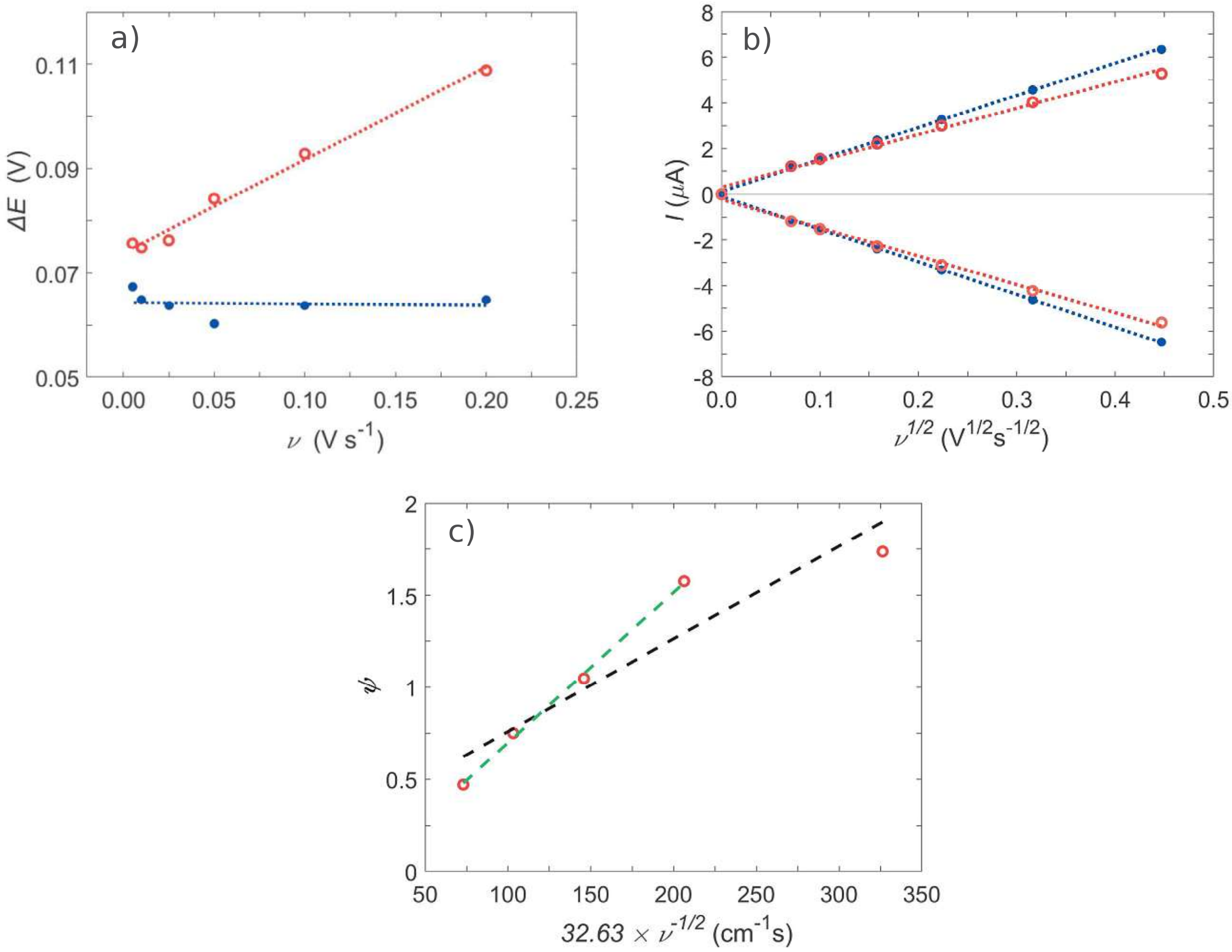

FIGURE 4.8: a) Peak-to-peak separation vs. scan rate for bare (blue *) and acetone-rinsed grafted Au(poly) electrode (red o) as a function of scan rate, b) anodic and cathodic peak currents for bare and acetone-rinsed grafted Au(poly) electrode as a function of the square root of scan rate, c) ψ vs. $\left[\frac{\pi DnF}{RT}\right]^{-1/2}\nu^{-1/2}$ for estimation of the k^0 corresponding to acetone-rinsed grafted electrode ($k^0_{app-modi}$), where $\psi = k^0\left[\frac{\pi DnF}{RT}\right]^{-1/2}\nu^{-1/2} = k^0(32.63 \times \nu^{-1/2})$. The best fitting line is shown with dashed lines. The electrode was grafted with 3 mM TBD.

For the bare electrode, the average ψ value for n=1 is 7.46, since this value is larger than 7, the system is considered reversible. However, for acetone-rinsed grafted Au the peak-to-peak separation changes directly with the scan rate. Therefore, instead of an average value, there is a specific ψ value for each scan rate. The calculated ψ values based on Equation 2.54 are shown on y-axis of Figure 4.8-c where $0.5 \leq \psi < 1.7$ (shown with red circles). It suggests that the acetone-rinsed grafted Au shows a quasi-reversible behavior [98]. Then by inserting the ψ value in Nicholson's equation (Eq. 2.53), k^0_{app} can be calculated. For the bare Au electrode, $k^0_{app-bare}$ is equivalent to k^0_{bare}, with an average value of 0.05 $\mathrm{cm\,s^{-1}}$. This value agrees with the value reported in the literature [159, 160].

For the acetone-rinsed grafted surface, $k^0_{app-modi}$ can be extracted from the slope of ψ vs. $\left[\frac{\pi D n \nu F}{RT}\right]^{-1/2} \nu^{-1/2}$ plot in Figure 4.8-c. The best-fitting lines are indicated with dashed lines in the figure. The black dashed line includes all the experimental points, however, for the green dashed line the highest value of ψ was excluded. The slope of the black line is 0.005 with $R^2 = 0.885$ and the slope of the green line is 0.0082 with $R^2 = 0.997$. Thus, we used the green line to extract the rate constant. Therefore, $k^0_{app-modi}$ extracted from the slope of the green dashed line was 8.2×10^{-3} $\mathrm{cm\,s^{-1}}$.

We assume that rinsing the grafted electrode results in the formation of a submonolayer of molecules on the surface, leading to incomplete and loosely packed coverage. This partial coverage of grafts (blocks) on the electrode surface, categorizing it as a partially blocked electrode. Given that the dimensions of the grafted regions and the electrochemically active areas are on the micrometer scale or smaller, the grafted surface is seen to function as an ultramicroelectrode array, if we assume that the rate constant at the area covered with the grafts is zero (i.e. $k^0_{grafts} = 0$) [161]).

Depending on the fractional coverage of the grafts, or the separation between electroactive zones (pinholes), the system can be classified into four categories [103], as detailed in the experimental methods chapter (Chapter 2).

In the first category, the distance between the electroactive zones is so large and the scan rate so high ($\delta \ll R_b, \delta \leq d$) that every electroactive zone works as an individual macroelectrode with individual linear diffusion, resulting in a peak-shaped voltammogram. This scenario was not observed here.

In the second category, the distance between the electroactive zones is so large and the scan rate is so slow ($\delta \leq d, \delta > R_b$) that every electroactive zone works as an individual (ultra)microelectrode with individual spherical diffusion. Consequently, the voltammogram would exhibit a perfect sigmoidal shape, independent of scan rate, which was also not observed in our case.

In the third category, the separation is short enough that adjacent diffusion layers of the electroactive zones overlap ($\delta > d$); therefore, the voltammogram has slightly to clearly defined peaks that are scan rate dependent. Since the size of the grafts (blocks) is on the order of nanometer, and the thickness of the diffusion layer at the scan rate

$0.005 \leq \nu \leq 0.2$ V/s is $218 \geq \delta \geq 34$ μm, thus the graft size is much smaller than the diffusion layer thickness ($\delta \gg R_b$). The partially sigmoidal CV shown in Figure (4.7-a) related to the grafted surface before acetone rinse falls into this category. We anticipate that CVs at much higher scan rates would demonstrate the transition from category 3 to category 1.

In the fourth category, the separation of electroactive zones is far too small compared to diffusion layer thickness ($\delta \gg d$) thus there are strong overlap diffusion layers leading to linear diffusion. In an ideal situation, the peak current is comparable to that of unblocked electrodes, but with a decreased apparent standard rate constant, based on equation $k^0_{app} = (1 - \theta).\ k^0_{bare}$ (Eq. 2.56). Thus, the CV is expected to resemble the bare surface with increased peak separation [161]. The peak-shaped voltammogram corresponding to the acetone-rinsed grafted surface may belong to this category (Fig. 4.7-c) because rinsing is expected to remove loosely bonded molecules from the surface and increase the number of active zones spaced more closely to each other.

In addition to the shape of the voltammogram and the linear relationship between the peak current and the square root of the scan rate ($I_p \propto \nu^{1/2}$), $k^0_{app-modi} < k^0_{bare}$ meaning it is possible that the acetone-rinsed grafted electrode can be classified as an ultramicroelectrode array belonging to the fourth category.

If we assume that the acetone-rinsed grafted electrode is an ultramicroelectrode array, we can estimate the coverage of the grafts based on equation $k^0_{app} = (1 - \theta).\ k^0_{bare}$ [161]. The obtained values for k^0_{bare} and k^0_{app} from our experiment were 0.05 $\mathrm{cm\,s^{-1}}$ and 8.2×10^{-3} $\mathrm{cm\,s^{-1}}$, respectively. Therefore, the estimated fractional coverage of the grafts on Au prepared with 3 mM TBD is $\theta \approx 0.84$.

The same procedure was applied to the sample grafted with 1 mM TBD, resulting in an estimated $\theta = 0.9$. However, this value is inconsistent with those obtained in other sections. Specifically, the fractional coverage of the grafted surface by 1 mM TBD on Au(111), extracted from the Cu deposition experiment, was approximately 0.3 (see Section 5.2.2). Similarly, the coverage estimated from interfacial capacitance measurements was also 0.3 (see Section 4.2.2).

Although the fractional coverages in other sections were derived from experiments on Au(111) electrodes rather than polycrystalline Au, the coverage of 0.9 appears excessively high. This discrepancy suggests that the $k^0_{app} = (1 - \theta).\ k^0_{bare}$ equation (Eq. 2.56), introduced by Amatore's simulation for regular arrays of microdiscs, may not be suitable for estimating the fractional coverage of grafts in this case. The likely reason is that, unlike regular arrays, the surface here comprises a random array with varying shape, size, and spacing of active areas.

It is worth noting that two decades after Amatore's work, Compton et al. simulated the voltammetric response of partially blocked electrodes, incorporating both random and regular arrays with advanced simulation techniques [103, 162], demonstrating how the voltammetric response of a random array differs from that of a regular array.

4.3 Conclusion

We conducted a detailed study on covalently grafted Au(111) and Au(poly) surfaces. In summary:

- Cyclic voltammetry measurements on the single-crystal Au(111) revealed a significant change in double-layer behavior in dilute sulfuric acid, which we attribute to changes in the interaction between (hydrogen)sulfate and the substrate. The oxidative desorption of the grafts occurred at potentials higher than those required for the oxidation of Au terrace atoms, suggesting that covalent grafting enhanced the structural stability of the surface.

- The blocking properties of the grafts on Au(poly) were investigated by measuring cyclic voltammograms in hexacyanoferrate solution. Rinsing the grafted surface with acetone changes the voltammetric response from a partially sigmoidal shape to a shape typical for quasi-reversible behavior.

- The voltammetric response of the grafted surface was measured in hexacyanoferrate solution, at various scan rates on the grafted surface and after rinsing with acetone. The cyclic voltammogram of the grafted surface before acetone rinse, at scan rates between 0.005 V/s and 0.2 V/s, fell into the third category of ultramicroelectrodes, with a partially sigmoidal shape. However, after rinsing the grafted surface with acetone, it changed to a peak-shaped voltammogram showing quasi-reversible behavior with the extracted $k^0_{app-modi} = 5 \times 10^{-3}$ $\mathrm{cm\,s^{-1}}$. The equation $k^0_{app} = (1-\theta).\ k^0_{bare}$ defined for a regular array of active sites with well-defined size and separations over the inactive surface, could not be used to estimate the fractional coverage of the grafts. Therefore, the voltammetric response of the acetone-rinsed grafted surface does not belong to the fourth category of ultramicroelectrodes.

Chapter 5

Covalent grafting of gold: copper deposition

In this chapter, the grafted Au(111) surface is characterized by copper underpotential deposition. To the best of our knowledge, there has been no published work on the effects of covalent grafting on underpotential deposition. The possibility of copper underpotential deposition as a probing tool for characterizing the surface and quantifying the graft coverage is investigated. Moreover, we compare copper overpotential deposition on a diazonium-modified surface with that on a thiol-modified surface, as the deposition behavior may be similar in both cases.

Section 5.2.2 has been published in Azmi et al., *Electrochimica Acta* 500 (2024) 144743. Copyright 2024 by Author(s), published under a Creative Commons Attribution license CC BY-NC 4.0 (see [125]).

5.1 Introduction

Electrodeposition of a metal (Me) on the same metal substrate through the reduction of metal ions Me^{n+} is predicted by the Nernst equation at the equilibrium potential (E_q) of the Me/Me^{n+} couple:

$$\mathrm{Me}^{n+} + \mathrm{ne}^{-} \longrightarrow \mathrm{Me} \tag{5.1}$$

$$E_q = E_0 + \frac{RT}{nF} \ln \frac{a_{Me^{n+}}}{a_{Me}} \tag{5.2}$$

In Equation 5.2, E_0 is the standard potential, and $a_{Me^{n+}}$ and a_{Me} are the activities of ions in the electrolyte and metal substrate, respectively. However, in practice, a slightly more negative potential than E_q is needed. In the potential range more negative than E_q, known as the overpotential deposition (opd) region, bulk or multilayer metal deposition takes place.

However, when metal Me is deposited on a different metal substrate S, the initial stage of the deposition often occurs at less negative (i.e., less reductive) potentials than predicted by the Nernst equation for deposition on the same metal. For this reason, the phenomenon is called underpotential deposition (upd). In the upd process, only one (rarely two) monolayer of Me is deposited, as after this first step, the (now modified) substrate already has much of the character of bulk Me metal. The monolayer forms because of stronger interaction (binding energy) between the depositing metal ions and the substrate (Me-S) compared to a substrate of their own material [163–165].

Underpotential deposition of metals is one of the well-known electrochemical structure-sensitive techniques. For instance, the sensitivity of this technique to surface structure can be observed in voltammograms for the copper underpotential deposition (Cu upd) on Au single crystal surfaces with different crystallographic orientations (Au(111), Au(110), and Au(100)). As shown in Figure 5.1-(a, b), any differences in Au crystal orientation are reflected on the Cu upd peaks. The cathodic/anodic peaks at different potentials indicate the deposition/dissolution of Cu atoms.

Figure 5.1-a shows the cyclic voltammogram obtained for the Cu upd on Au(111) in H_2SO_4 solution containing copper sulfate. The voltammogram measurement was started at the potential where no adsorption of Cu ions happens on the Au(111). Changing the potential to a more negative value with a slow scan rate of 1 or 2 mV/s leads to the appearance of two cathodic peaks (A, B). The appearance of these two distinctive peaks reveals the presence of different adsorption sites and therefore different structures of the Cu adsorbate on the Au(111) surface. The first peak (A) is assigned to 2/3 adsorption of copper and 1/3 co-adsorption of sulfate and the second peak (B) to the formation of a full monolayer of Cu atoms on a gold surface. The superstructures of Cu adlayer on Au(111) surface at peaks A and B are $(\sqrt{3} \times \sqrt{3})R$ 30° and (1×1), respectively. As the applied potential becomes more negative than the

E_q, the overpotential deposition of Cu begins. In Figure 5.1-a the direction of the scan was reversed before Cu opd occurred, and two anodic peaks A' and B', corresponding to the desorption of Cu atoms, were recorded [163].

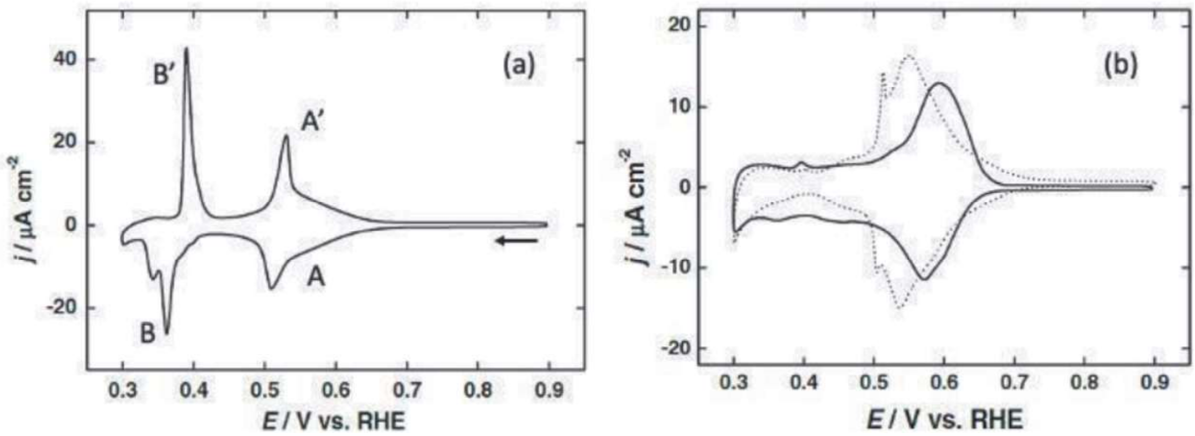

FIGURE 5.1: CVs for the Cu upd on Au surfaces with different crystal orientations: a) Au(111), and b) Au(110) with a solid line and Au(100) with a dotted line, measured in 1 mM $CuSO_4$ + 0.05 M H_2SO_4. Scan rate: 5 mV/s. Reprinted from [166] Copyright (2004), with permission from Elsevier.

Besides the crystal orientation, crystal imperfections at the surface (point defects, kink sites, monoatomic steps, dislocations, grain boundaries, pits, islands, etc.) determine the structure of the upd peaks. The crystal defects strongly affect the initial stage of upd by providing nucleation sites for the growth of deposited metals [166].

Moreover, the presence of halide ions has an impact on the Cu upd process. The addition of halide ions or anions of supporting electrolyte showed a dramatic effect of anions specific adsorption on Cu adlayer formation and therefore the position and number of the upd peaks. The choice of anions not only affects the adlayer structure but also the deposition kinetics. The voltammograms for the Cu upd on Au(111) in four different electrolytes containing the 1 mM Cu^{+2} were collected in Figure 5.2 [167]. Figure 5.2-a shows the cyclic voltammogram for Cu upd in perchloric acid, featuring a broad cathodic peak corresponding to the Cu underpotential deposition and a single sharp anodic peak. Comparing the Cu deposition peak with others in the figure reveals that the perchlorate solution exhibits the slowest deposition rate, as indicated by its broader and less defined cathodic peak. Figure 5.2-b displays the cyclic voltammograms for the Cu upd on Au(111) in a sulfate-containing solution, which is discussed in more detail and included here for better comparison.

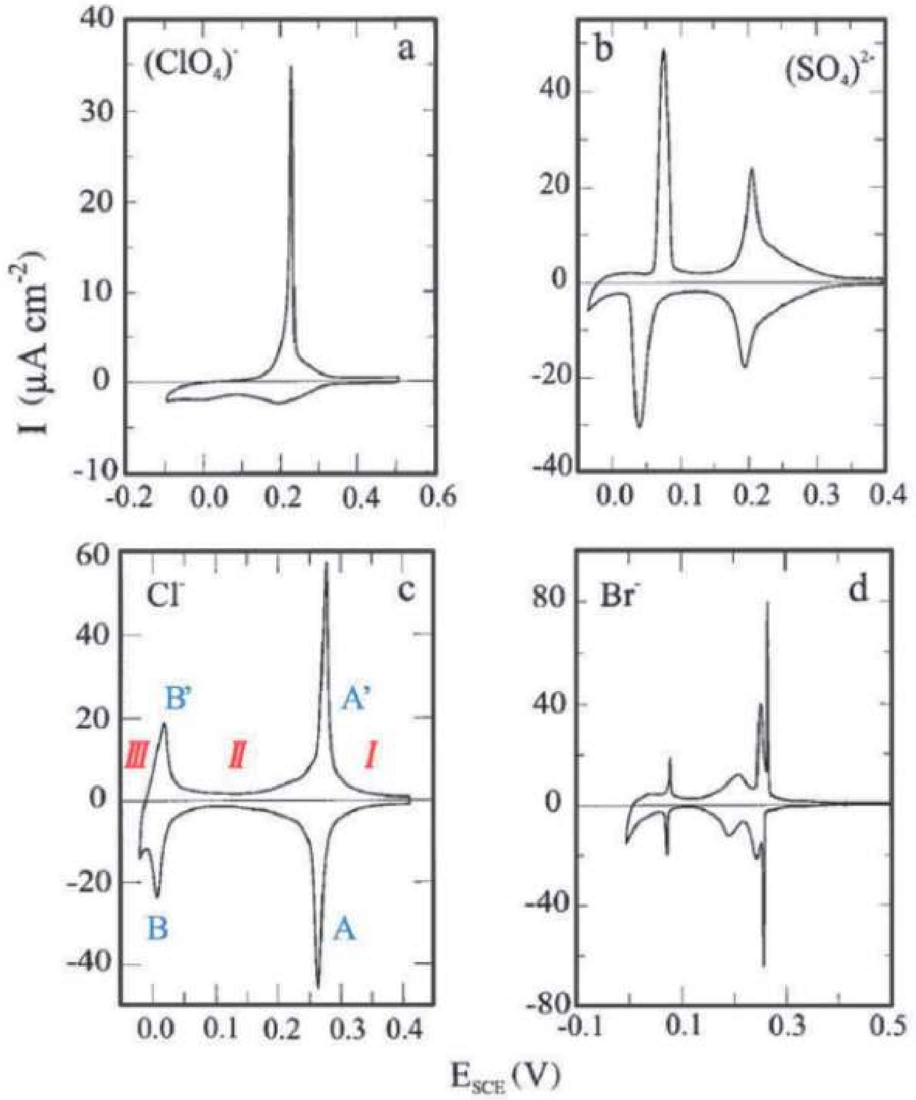

FIGURE 5.2: Effect of different anions on the Cu upd. CVs of Au(111) in 1 mM Cu^{2+} in: a) 0.1 M $HClO_4$, b) 0.05 M H_2SO_4, c) 0.1 M $HClO_4$ + 1 mM NaCl, and d) 0.1 M $HClO_4$ + 1 mM NaBr. Scan rate: 5 mV/s. Adapted from [167] with permission Copyright (1999) Wiley.

The effect of the addition of chloride to a perchloric acid solution on the CV measured on Au(111) for the Cu upd is illustrated in Figure 5.2-c. It shows how chloride can increase the deposition rate and how the strong coadsorption of chlorides with Cu shifts the onset of deposition to more positive potentials. For the electrolyte with chloride, there are two pairs of peaks A/A' and B/B'. The peak B' almost overlaps with the bulk or overpotential deposition of the copper. These peaks show the potential-dependent adsorption and desorption of Cu^{2+} and Cl^- ions on the Au(111). The CV has three potential regions displayed in Figure 5.2-c in red. Based on the STM studies, region I has a disordered structure with Cu^{2+} and Cl^- coadsorbed randomly on the unreconstructed Au(111)-(1×1). Region II is located between A/A' and B/B' peaks, with an incommensurate (5×5)-like structure represented by a bilayer with chlorides on top of copper ions with the same coverage of 0.62 of the monolayer (ML). The structure is more complex than a true (5×5) structure. The distance between maxima on the atomic corrugation pattern is not an integer multiple of four or five of the Au lattice constant [168–170].

In region III at potential more negative than B/B', chlorides are partially desorbed. For low chloride concentration below 10^{-5} M and at potentials below 0.14 V vs SCE a Cu adlayer with quasi-hexagonal structure of (2×2) was imaged that the coverage of the Cu is about 0.75 ML and chloride is about 0.25 ML, while for the higher concentration of the chloride a second (5×5)-like structure with different corrugation height and coverage of 0.62 ML both for Cu and Cl^- were reported [169, 171, 172]. The peak B/B' overlaps almost with the bulk or overpotential deposition of the copper. The difference in voltammograms of different halide anions reflects the difference in coadsorption of halide anions with Cu on the surface at different potentials. For instance, when the superstructure of Cu in perchlorate solution is (2.2×2.2), in chloride solution it is (5×5). For the coadsorption of bromide or chloride with Cu, a bilayer containing a first layer of Cu on gold and a second layer of bromide or chloride on top is formed [167, 173].

5.1.1 Application of copper underpotential deposition

The metal underpotential deposition technique can be applied in various fields, particularly in electrocatalysis. It is commonly used to determine the electrochemically active surface area (ECSA) or the real surface area of metals where Cu upd occurs, such as noble metals and their alloys. In electrocatalysis, a measure of the electrochemical active surface area of the catalysts is necessary. The active surface area is calculated by the equation of $ECSA = \frac{Q}{Q_s}$ where Q is the integration of charges under the Cu upd stripping peaks and Q_s is the charge density equal to the amount of charge transferred per unit surface area by adsorption of a Cu atom on every metal atom. For Cu, Q_s is equal to 420 $\mu\mathrm{C\,cm^{-2}}$ by assuming 2 electrons are transferred per each adsorption $Cu^{2+} + 2\,e^- \longrightarrow Cu_{upd}$ [174–176]. This method can especially be used for ECSA of metallic nanoparticles and nanoporous materials [177]. In more recent studies, because of the sensitivity of Cu upd to surface structure (crystallographic plan), it has been developed to probe the surface structure of nanoparticles with controlled size and shapes quantitatively. In the related study, the percentages of {100}, {111}, and {110} surface domains present at the surface of Pd nanoparticles with Cubic, octahedral, and rhombic dodecahedral shapes were determined in a few steps. First, the CVs for Cu upd on low index Pd single crystals, including Pd(100), Pd(111), and Pd(110) were measured individually, and later, CVs for Cu upd on Pd nanoparticles were measured. Then, the CVs of nanoparticles were deconvoluted and broken down into characteristic peaks of the single crystals. The amount of charge under the corresponding peaks relative to the total charge for the Cu upd was used to quantify the percentages of each domain [178].

The design and control of the shape of nanostructures is another important application of upd in electrocatalysis [179]. The preparation of core-shell noble metal composite through upd, in a variety of compositions, was reported [180–182].

5.1.2 Copper deposition on electrodes modified with organic molecules

Cu deposition is used for diverse purposes, not only on bare metals but also on modified surfaces. A large number of articles are dedicated to metal deposition on SAM-modified electrodes. For instance, a group of thiol-based additives is added to the electroplating solution to affect the metal deposition process [183]. Moreover, the passivating SAM layer can be used as a mold or mask for metal deposition, for the fabrication of micro and nanoscale patterns on the surface [184–186]. The SAM layer can be utilized in the fabrication of organic electronic devices with metal/organic/metal structures [187]. For the surface modified with reduction of diazonium salt, such reasons cannot be applied because the surface cannot be completely and homogeneously covered with organic molecules so the layers of metallic and organic cannot be separated. A less common application is increasing the stability of the SAM layer with deposition of Cu upd on the SAM-modified gold electrodes. This was reported in the case that Cu deposited on self-assembled monolayers of propanethiol intercalates between the SAM and Au surface and increased the stability of the SAM layer toward its reductive desorption [188].

An important application of Cu deposition on modified metal surfaces is using it as a sensitive characterization technique for examining the quality of an insulating film grown or adsorbed on the substrate since Cu only adsorbs on bare areas. For instance, this method was applied to quantify the defect density and nature of 2D h-BN monolayer grown on Rh(111) [150]. The combination of Cu upd and STM for probing and imaging individual defects and porosity of the SAM on the Au surface is another example [189].

The presence of SAM on the metal substrate can strongly affect the nucleation and growth of deposited metal on the surface. There are three possibilities of metal deposition on SAM/metal surfaces based on the location of deposited metal depending on the transport of deposits on the surface and the interaction of adlayer and the deposits [165, 190], illustrated in Figure 5.3: 1) deposition of metal on top of the SAM, which makes either 2D or 3D of Cu clusters, depending on the strength of interaction between deposited metal and SAM, 2) intercalation of deposited material under the SAM layer, which could be a result of stronger interaction between the Cu and the thiol compared to thiol and gold [191], 3) initial metal deposition at the substrate followed by mushroom-like configuration growth [2, 192].

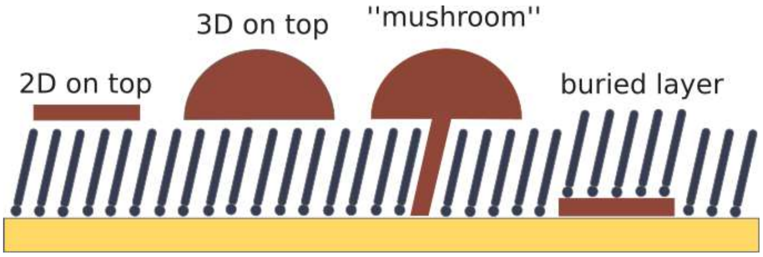

FIGURE 5.3: Possible configurations of deposited metal on SAM-modified surface. Adapted from [190], Copyright (2001), with permission from Wiley.

5.2 Results and discussion

5.2.1 Sensitivity of Cu upd to chlorides

To demonstrate the extreme sensitivity of Cu upd to the presence of halides, Figure 5.4 shows the CV measured on bare Au(111) in a sulfate-based electrolyte (0.1 M H_2SO_4 + 1 mM Cu^{2+}), where small amounts of chloride were added.

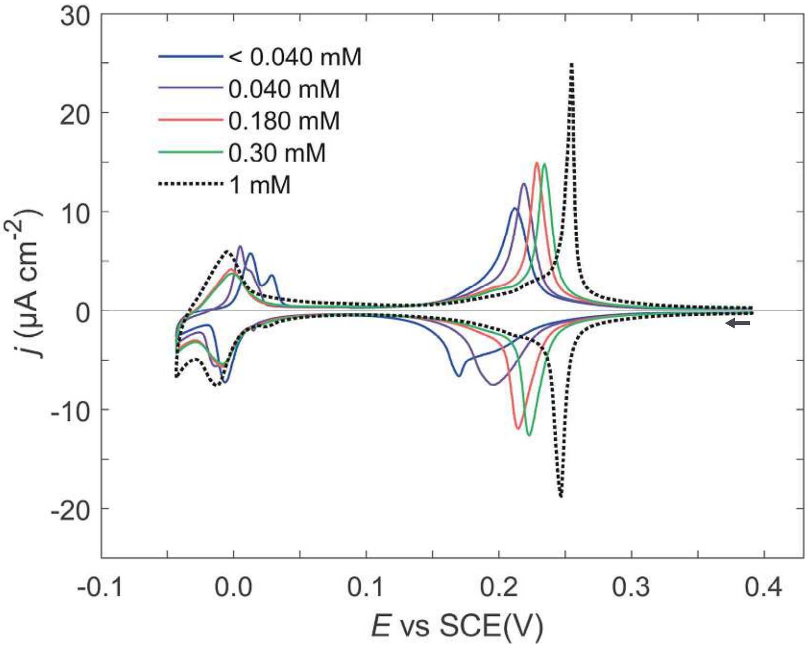

FIGURE 5.4: Effect of increasing chloride concentration on CV of Au(111) in oxygen-free 1 mM Cu^{2+} + 0.1 M H_2SO_4, with NaCl concentrations of <0.04, 0.04, 0.18, 0.3, and 1 mM. The CV (dotted black line) was measured in 1 mM NaCl + 1 mM Cu^{2+} + 0.1 M $HClO_4$. Scan rate: 2 mV/s.

As indicated in the figure, the blue full trace, at low concentrations of the Cl^- ($<$ 0.04 mM), there is adsorption of both ${SO_4}^{2-}$ and Cl^- ions on the Au surface. It was reported that even a trace amount of chloride ($< 10^{-6}$) can diffuse to the surface and adsorb strongly on it, and change the double layer properties by becoming the dominant anions at the interface, which consequently alters the Cu adsorption sites [169].

Considering that the surface density of atoms for Au(111) is 1.39×10^{15} atoms/cm^2 [193] and the surface area of our crystal is 0.0908 cm^2, we estimate that a trace amount of 0.2 nmol chloride is sufficient to produce monolayer adsorption.

As adsorption strength of the ions on Au surfaces follows the sequence: ${ClO_4}^- < {SO_4}^{2-} < Cl^- < Br^- < I^-$ [135], it is expected that the ${SO_4}^{2-}$ is being replaced by Cl^-; however, the concentration of the Cl^- is not high enough to cover the whole surface. Based on the figure, an increase in chloride concentration shifts the A/A' peaks to more positive potentials and increases the height of the peaks. For the B/B' peaks, the multiple peaks merge into a single peak at more negative potentials. Thus, the shape and position of the characteristic upd peaks evolve from the signature behavior observed in sulfates (Fig. 5.2-b) to that in chloride (Fig. 5.4, black dotted-line). At the concentration of 1 mM chloride, we have the characteristic CV for Cu upd on Au(111) in chloride solution. For easier comparison with Fig. 5.2-c, the potentials are illustrated versus SCE reference electrode.

Note that even the voltammogram in nominally chloride-free solution already shows signs of the effects of chloride, which can be ascribed to small amounts originating from the Ag/AgCl electrode that was used (Fig. 5.5). In Figure 5.5, the second cycle, represented with dotted-blue trace, measured 30 min after the first cycle (red-full trace) in the same solution, indicates how the Cl^- can diffuse from the Ag/AgCl reference electrode to the Au surface over time and adsorb, and consequently change the Cu upd process.

Figures 5.4 and 5.5 show the extreme sensitivity of the voltammogram to the concentration of chloride. Therefore, in accurate fundamental studies in halogenide-free electrolytes, Ag/AgCl or similar electrodes should be avoided altogether, or special precautions are required. For our study, we limit ourselves in the following to solutions that are 1 mM in chloride, and the use of a standard Ag/AgCl reference electrode is adequate.

As the solution from which grafting takes place contains a considerable concentration of chloride (0.1 M HCl), it makes sense to also investigate upd on this surface in the presence of chloride, especially as even trace amounts of the halogenides have a pronounced effect on upd characteristics [169].

5.2.2 Cu upd on bare and grafted Au(111)

The Cu upd quasi-steady-state voltammogram of Au(111) in 1 mM Cu^{2+} + 1 mM NaCl + 0.1 M $HClO_4$ is shown in Figure 5.6. In the presence of 1 mM chloride ions in

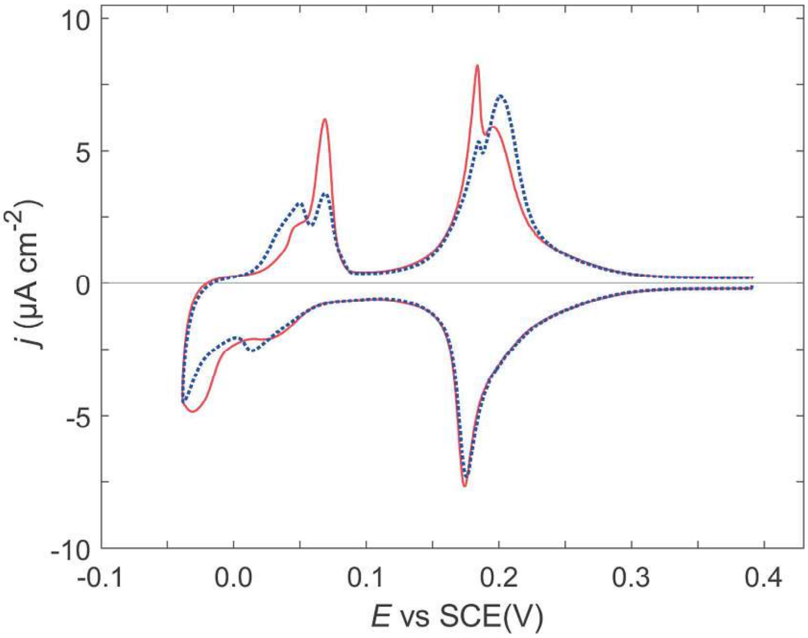

FIGURE 5.5: CV of Au(111) in oxygen free 1 mM Cu^{2+} + 0.1 M H_2SO_4. The 2nd cycle (blue dotted line) was measured 30 minutes after the 1st cycle (red line). RE: Ag/AgCl. Scan rate: 2 mV/s.

the electrolyte, the CV shows two highly symmetrical pairs of peaks, A/A’ and B/B’, that are characteristic of Au(111) in chloride-containing solutions [167].

During the cathodic scan, A is associated with the deposition of approximately 62% of a monolayer of Cu on the substrate, while B is a combination of the rest 38% and the initial part of the bulk deposition [168, 169]. As a side note, the presence of 1 mM chloride ions in solution yields an island-free unreconstructed (1 × 1) surface independent from potential, at variance with a halide-free solution [194]. During the anodic scan, B’ and A’ reverse the earlier deposition, and their potentials are indistinguishable from those of B and A. We note that the minimal current background below A/A’ is flat and therefore capacitive, but starts to increase exponentially on approaching B. Continuation of the cathodic scan, Fig. 5.6, inset reveals that this increase corresponds with the onset of Cu opd. On reversal of the scan, any opd copper undergoes anodic stripping at almost identical potentials as where the peak B’ resides. We also observe that the entire region between the peaks A/A’ and B/B’ is featureless in both the cathodic and anodic scan directions.

The CVs for Cu upd on both bare and grafted Au(111) electrodes measured in oxygen-free 1 mM Cu^{2+} + 1 mM NaCl + 0.1 M $HClO_4$ solution shown in Figure 5.7-a. The

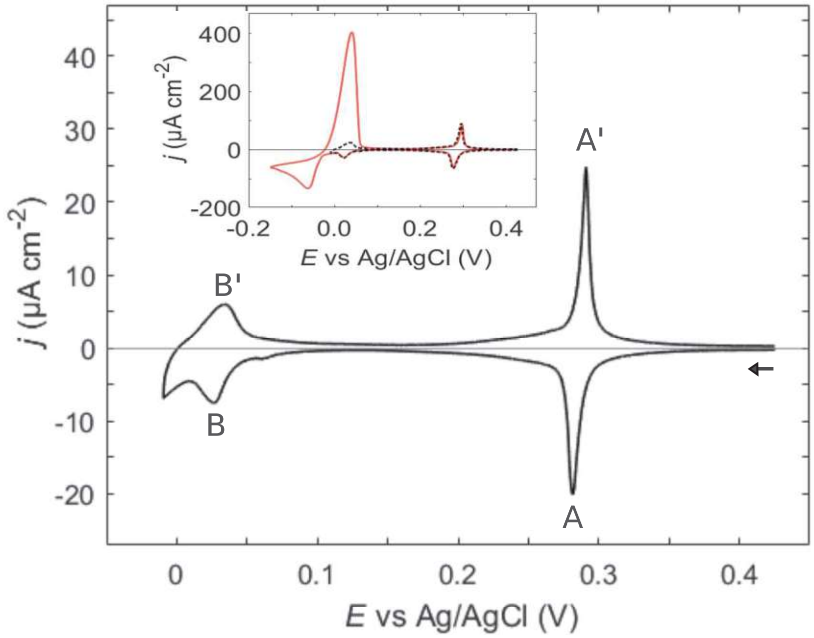

FIGURE 5.6: CV of Au(111) in 1 mM Cu^{2+}+ 1 mM NaCl + 0.1 M $HClO_4$. Inset: Continuation of the CV into the Cu opd region (dashed trace: upd only; full trace: upd + opd).

charges were extracted from the corresponding current density versus time, shown in Figure 5.7-b, because of the complexity of the CV around peak B.

CV for Cu upd on the bare Au(111) shown in Figure 5.7 with black dashed trace in the electrolyte containing chloride anions. When the same Cu upd experiment is carried out on Au(111) carrying TBD grafts on the surface pronounced changes appear, Fig. 5.7-a, red trace. Both peaks A and A' become asymmetrical and tapered towards negative potentials, and peaks B/B' decrease by roughly 50%. In addition, at least very shallow extra peaks C/C' appear in the previously featureless region between A/A' and B/B', and these extra peaks are visible during both the cathodic and anodic scans, but occur at clearly different potentials, unlike the main peaks A/A' and B/B' in the CV.

After electrochemical oxidation of the surface, under the conditions shown in Fig. 5.8, the Cu upd response is in between that of the bare and the grafted Au surface, Fig. 5.7, blue trace: while there is partial restoration of the sharp peak A characteristic of bare Au(111), there remains a pronounced shoulder at more negative potentials, yielding almost bimodal behavior. This behavior suggests again that certain grafts

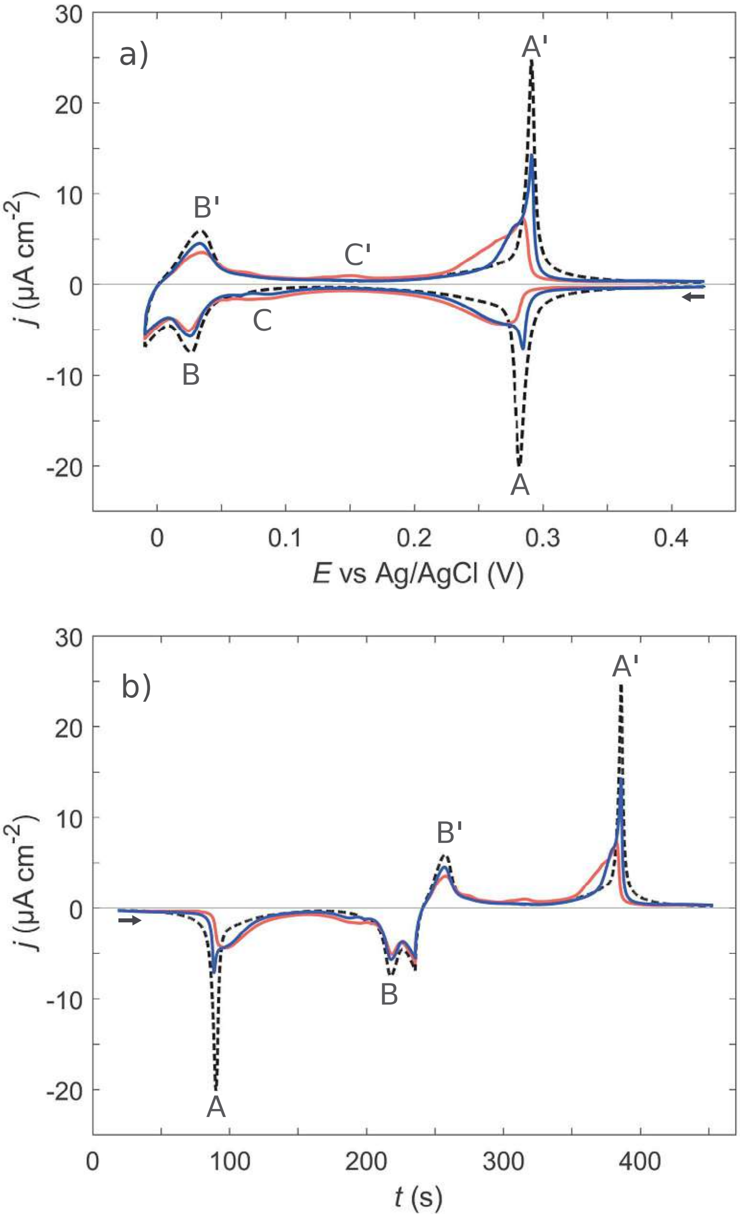

FIGURE 5.7: a) CVs of bare (outer, dashed trace) and grafted Au(111), before (red full trace) and after (blue full trace) excursion into the Au oxidation region, in 1 mM Cu^{2+} + 1 mM Cl^- + 0.1 M $HClO_4$. Scan rate: 2 mV s^{-1}. b) representation of the Cu upd as current density versus time. The Au(111) grafted by CA at -0.2 V vs Ag/AgCl for 60 s in a grafting solution containing 1 mM TBD.

are cleanly removed by electrochemical oxidation, while others resist and are more robustly attached.

In Figure 5.8, the voltammograms measured between -0.01 and 1.4 V vs Ag/AgCl in a solution of 1 mM Cu^{2+} + 1 mM NaCl + 0.1 M $HClO_4$, on bare and grafted Au(111) are

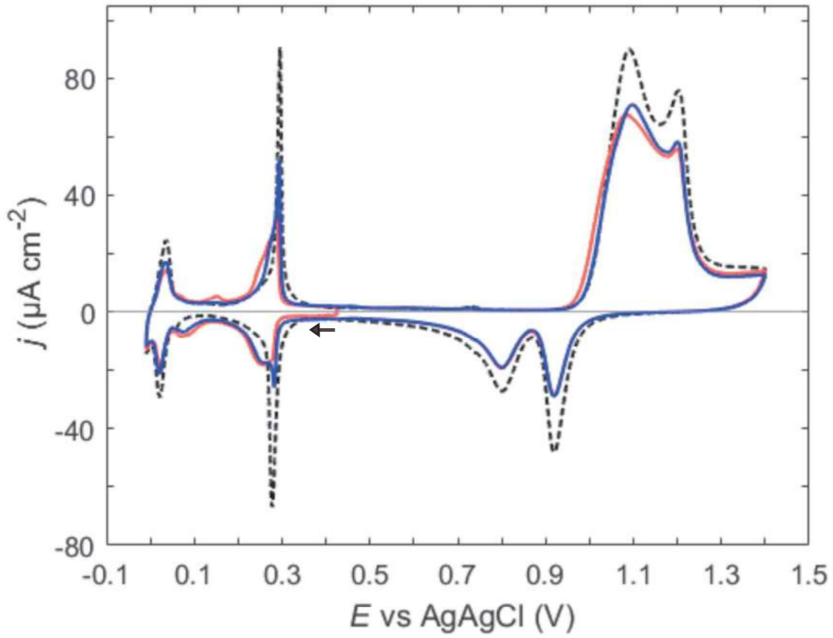

FIGURE 5.8: CVs of bare (black dashed line) and grafted Au(111) (red and blue line, 1st and 2nd cycle) in oxygen-free 1 mM Cu^{2+} + 1 mM Cl^- + 0.1 M $HClO_4$. Scan rate: 10 $mV\,s^{-1}$.

shown with black and red trace, respectively. After measuring a cycle on the grafted surface a second cycle was measured (Fig. 5.8 with blue trace). The starting potential and direction of the CV measurement are indicated with an arrow in the figure.

The shape of the CV of bare gold in the potential region between 0.5 V and 1.4 V is consistent with those reported in the literature for Cu-free 0.1 M $HClO_4$ solution containing 1 mM NaCl (Figure 5.8, dashed black line) [195]. In positive going sweep, there are two anodic peaks at around 1.1 and 1.2 V. Based on reported electrochemical quartz crystal microbalance (EQCM) measurements on a gold electrode in perchloric acid solution containing chloride ions, the anodic peak at 1.1 V is attributed to the $3e^-$ oxidative dissolution of gold due to presence of chlorides. At potentials more positive than 1.1 V, the gold dissolution starts to compete with oxide formation (passivation), and finally at potential around 1.4 V the surface of the gold dissolution is stopped by the formation of a complete gold oxide monolayer [196]. In the negative going sweep, there are two cathodic peaks. The peak at 0.92 V is assigned to the simultaneous oxide reduction and gold dissolution [195]. The second cathodic peak at 0.80 V is related to the re-deposition of dissolved gold. The minor peak anodic peak at 0.74 V is related to an ordered chloride adlayer formed on the Au(111) [135]. In the less positive potential region (E $<$ 0.4 V) of the voltammogram, we observe Cu underpotential deposition, as explained in more detail in the previous paragraphs.

The CV related to grafted and later after measuring the second cycle at a potential larger than 0.8 V has similar peaks to bare Au but with lower current. For quantitative analysis, magnitudes of total anodic and cathodic charges for the bare Au(111), grafted (Grafted-1st cycle), and then after measuring the 2nd cycle (Grafted-2nd cycle) were estimated and were collected in Table 5.1. The oxidation charge was integrated between 0.86 V and 1.4 V and for the reduction process between 1.4 V to 0.5 V, after correcting for capacitive currents.

TABLE 5.1: The total anodic and cathodic charge for the bare Au(111), grafted and after electrochemical oxidation of the surface. The charges are corrected for capacitive current. The oxidation charge was integrated between 0.86 V and 1.4 V and for the reduction process between 1.4 V to 0.5 V.

Sample	Oxidation charge (μC cm^{-2})	Reduction charge (μC cm^{-2})	$\frac{\text{Oxidation charge}}{\text{Reduction charge}}$
Bare-1st cycle	1821	711	2.5
Grafted-1st cycle	1570	482	3.2
Grafted-2nd cycle	1507	479	3.1

Based on the table, the anodic charge for all samples is greater than the cathodic charge. For the bare Au electrode in perchloric acid solution containing Cl^- at concentrations greater than 1 mM, the oxidation charge always exceeds the reduction charge because of gold dissolution [196]. The gold dissolution occurs in the anodic potential region through a $3\,e^-$ oxidation process.

In our study, the presence of Cu upd at potentials more negative than 0.5 V prevented the full integration of the cathodic charge. As a result, the cathodic charges are significantly smaller than the anodic charges. Nevertheless, comparing the total anodic to cathodic current ratio provides valuable insight. For the bare Au, this ratio is 2.5, while for the grafted sample (red trace), it increases to around 3.2. The higher ratio of oxidation to reduction charge for the grafted sample, compared to bare gold, along with the minimal difference in reduction charges between the red and blue traces, indicates that the oxidation of Au(111)-TBD consumes more charge than the oxidation of a gold monolayer. A similar result was observed in Chapter 4, which may be explained by the oxidative desorption of covalent grafts. The additional charge implies that the breaking of the Au-C bond is not a homolytic process and may involve the formation of compounds with higher carbon oxidation states.

To allow for a semi-quantitative analysis, upd peaks were deconvoluted into Gaussian contributions after subtraction of the capacitive and opd background, Fig. 5.9 (for details, see Experimental section). Similar phenomenological deconvolution was successful in rationalizing narrowly spaced quantized charging of metal nanoparticles [197] and in separating overlapping peaks in electroanalytical procedures [198–200]. A more rigorous treatment that considers mechanistic details is beyond the scope of the present paper.

Full numerical details of the deconvolution, including peak position (both in terms of time and of potential), peak full width at half maximum (FWHM, in volt), and charge under each peak component are collated in Table 5.2 for the three surfaces we compare. The labeling of the different components follows that of the experimentally observed peaks A, B, and C, with a number added to indicate up to 4 Gaussian contributions.

The sharper any of the Gaussian components appears (i.e., the smaller its FWHM), the more well-defined and uniform we consider the the underlying physicochemical process to be across the surface, both in terms of thermodynamics and kinetics. Starting with the simplest situation, we find that the bare Au(111) Cu upd voltammogram can be fully described by considering just two components under peak A. For the grafted Au(111)-TBD surface, before and after electrochemical oxidation, a good quality fit of peak A requires 4 components, while peak B can be modeled satisfactorily with only two components for all three surfaces. The intermediate peak C is minimally present for bare Au(111), but emerges clearly for grafted Au(111)-TBD, to decrease again after electrochemical oxidation. The (doubtlessly still oversimplified) model that emerges is shown in Fig. 5.10: covalent grafts change the microscopic structural, thermodynamic, and kinetic landscape of the surface, and the upd process samples all these variations. These may include grafts adsorbing in on-top, bridge and threefold hollow sites of Au(111), while proximity of neighbouring grafts or of step edges will add further complexity.

In the scheme, the footprint of each graft is shown as commensurate with the Au lattice itself, but this may be in fact quite different and include both electronic (i.e., changing the local density of states of the substrate atoms) and topological (i.e., the

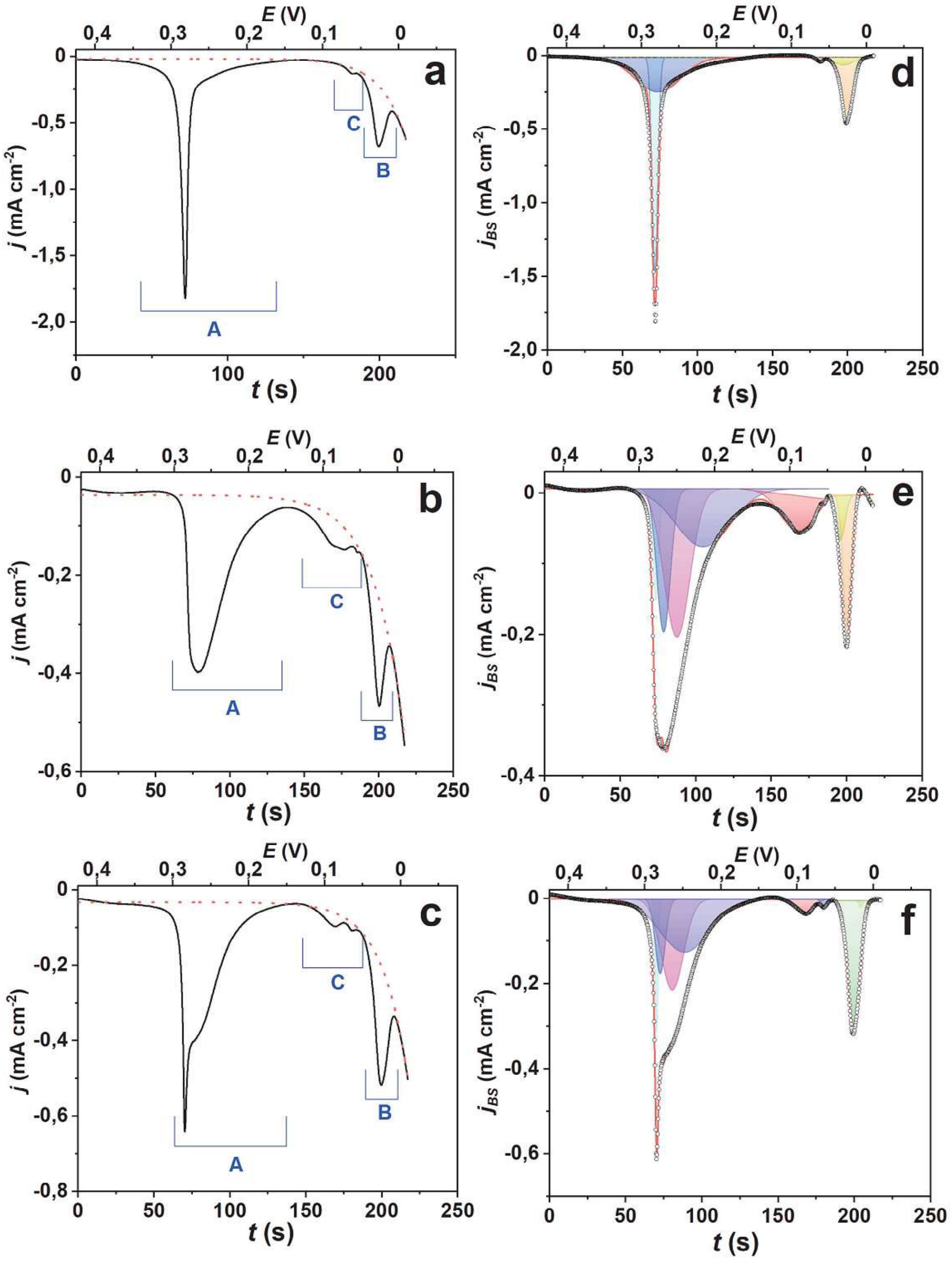

FIGURE 5.9: Cathodic branch of Cu upd CVs shown in Fig. 5.7 for a) bare Au(111), b) grafted Au(111), and c) grafted Au(111) after electrochemical oxidation, in 1 mM Cu_2^+ + 1 mM Cl^- + 0.1 M $HClO_4$. The exponentially increasing baseline (dashed) reflects the onset of Cu opd. Scan rate: 2 mV s^{-1}. (d-f) Deconvolution into Gaussian peaks after baseline subtraction. The details of the peaks are provided in Table 5.2.

Table 5.2: Deconvolution parameters for Cu upd voltammograms.

Electrode	Peak component	t_{max}(s)	E_{max}(V)	FWHM(V)	Q_{fit} (mC cm^{-2})
Bare Au(111)	**A1**	71.6	0.282	0.009	-7.05
	A2	73.5	0.278	0.071	-8.91
	C1	181.5	0.062	0.009	-0.13
	B1	197.1	0.031	0.030	-0.85
	B2	199.7	0.026	0.017	-3.50
Grafted Au(111)	**A1**	73.5	0.278	0.009	-0.79
	A2	78.7	0.267	0.021	-2.30
	A3	87.5	0.250	0.041	-4.55
	A4	104.7	0.215	0.085	-3.74
	C1	168.2	0.088	0.056	-1.80
	B1	195.9	0.033	0.014	-0.49
	B2	200.3	0.024	0.013	-1.34
Grafted post oxidation	**A1**	70.2	0.284	0.005	-0.79
	A2	72.6	0.280	0.015	-1.45
	A3	80.5	0.264	0.035	-3.99
	A4	88.6	0.248	0.076	-5.09
	C1	167.5	0.090	0.026	-0.48
	C2	180.3	0.064	0.010	-0.09
	B1	199.4	0.026	0.006	-2.94
	B2	204.1	0.017	0.018	-0.05

presence of the grafts changing the local geometry, similar to the emergence of partial sp^3 character when grafting on sp^2 carbons) effects.

Computational work points at different adsorption geometries on different metals (on-top/bridge/three-fold hollow) [140], but these are thermodynamic minima, and real bonds may be kinetically trapped [143]. While our initial experiments demonstrate high sensitivity of upd to the changing landscape during covalent grafting of the metal surface and any following treatment (e.g., electrochemical oxidation), careful further experimentation (for example, on surfaces with controlled step density) and theoretical modeling will be required to provide a direct link between any microscopic model and the upd behavior.

In addition to extracting information regarding the energy landscape of the gold surface and the effect of grafting and electrochemical oxidation, we can also use the upd charges to determine the microscopic the surface area of the different electrodes. If we limit ourselves to the first the main peak, and thus avoid any ambiguity that

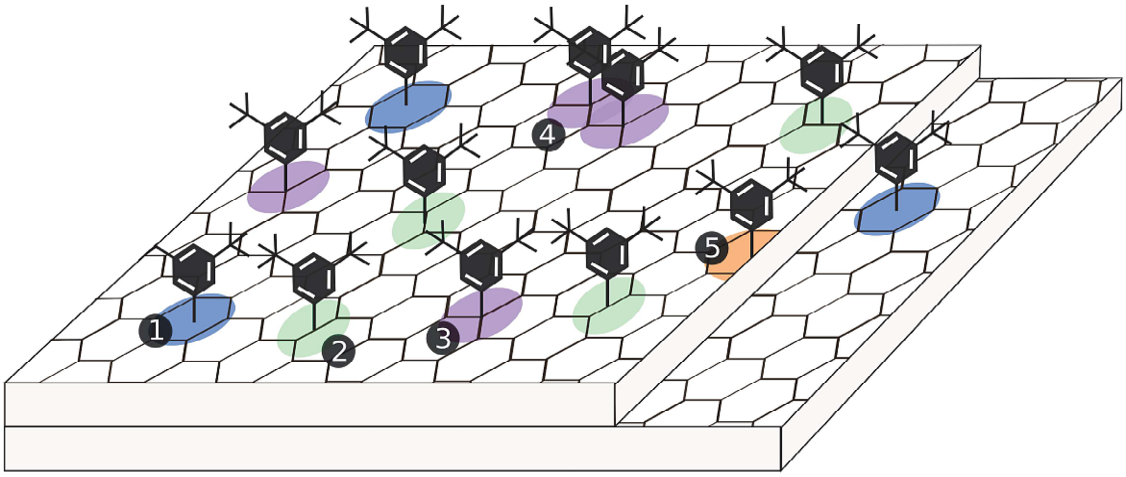

Figure 5.10: Schematic microscopic landscape with different binding motifs for covalent grafts, including adsorption in on-top (blue (1)), bridge (green (2)) and threefold hollow (pink (3)) sites of Au(111). The effects of graft proximity (overlapping footprints (4)) and undercoordinated edge sites (orange (5)) are also shown. Grafts and substrate atoms are not drawn to scale.

may arise from the exponential background subtraction under peaks B and C discussed earlier, the bare unreconstructed Au(111) surface yields a total charge under A-peak components $\Sigma Q_{A,\,bare} = 15.96\ \mathrm{mC\,cm^{-2}}$. For the grafted surface, the same exercise yields $\Sigma Q_{A,\,grafted} = 11.38\ \mathrm{mC\,cm^{-2}}$, which equals 71.3% of the bare surface value and closely matches the charge in interfacial capacitance we extracted from the cyclic voltammograms in sulfuric acid (see Fig. 4.3). More surprisingly, however, is that the equivalent charge after electrochemical oxidation of the grafted surface equals $\Sigma Q_{A,\,post-oxidation} = 11.32\ \mathrm{mC\,cm^{-2}}$, or 99.5% of the Cu upd charge required for the grafted surface. Whereas a reorganization of the surface and its multiple microscopic contributions are obvious from the change between Fig. 5.9-b and Fig. 5.9-c, we, therefore, conclude that most of the grafts that are responsible for the decrease in microscopic surface area during grafting are not removed by electrochemical oxidation.

5.2.3 Configuration of bulk Cu deposited on grafted Au(111)

To evaluate the possible configuration of Cu deposition on our modified Au(111) surface, we employed electrochemical voltammetry techniques similar to those used for SAM-modified surfaces. As shown in Fig. 5.3, in the introduction section of this chapter, there are three possibilities of Cu deposition on grafts/Au surface: 1) formation of

2D or 3D Cu clusters on top grafts, 2) intercalation of deposited Cu under the grafts layer, and 3) initial Cu deposition at the Au substrate followed by mushroom-like configuration growth.

As the first step, we measured the CV for Cu opd on bare and grafted Au(111) performed in oxygen-free 1 mM Cu^{2+} + 1 mM NaCl + 0.1 M $HClO_4$ solution with a scan rate of 10 mV/s (Fig. 5.11). The shape of the CV measured on the grafted Au (red) is very similar to the bare Au. As explained in this chapter, when potentials more negative than those used for Cu upd are applied, opd occurs on the surface, resulting in the deposition of multilayers of Cu on the Au surface rather than a monolayer. A cathodic peak at -0.06 V and an anodic peak at 0.04 V are assigned to bulk copper deposition and stripping, respectively.

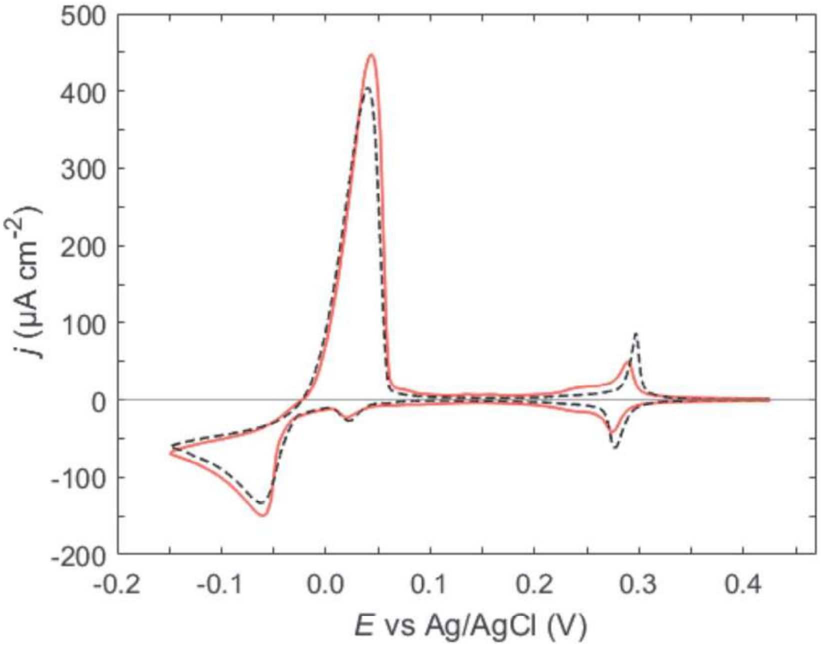

FIGURE 5.11: CVs for Cu opd on bare (black dashed trace) and grafted (red trace) Au(111) in oxygen-free 1 mM Cu^{2+} + 1 mM NaCl + 0.1 M $HClO_4$ solution. Scan rate: 10 mV/s. The Au(111) was grafted by CA at -0.2 V for 60 s in 1 mM 3,5-TBD solution.

The oxidation and reduction charges corresponding to the Cu upd and opd peaks for both bare and grafted Au(111) were calculated and are summarized in Table 5.3.

The ratios of the total charge including Cu opd charge to the Cu upd charge for both bare and grafted samples during Cu deposition and stripping are also presented in Table 5.3. These ratios, expressed as $\frac{\textit{total recution charge including opd}}{\textit{upd reduction charge}}$ and $\frac{\textit{total oxidation charge including opd}}{\textit{upd oxidation charge}}$,

TABLE 5.3: Oxidation and reduction charges corresponding to Cu upd and opd on bare and grafted Au(111), without correction for double-layer charging.

	Reduction charge (μC cm^{-2})			Oxidation charge (μC cm^{-2})		
Sample	upd	opd	upd+opd/upd	upd	opd	upd+opd/upd
Bare	368	1879	5.1	360	1836	5.1
Grafted Au(111)	374	2086	5.5	378	2044	5.4

are denoted as opd+upd/upd. For the reduction process, the opd+upd/upd ratio for the bare sample is approximately 5.1, while for the grafted sample, it is around 5.5. This indicates that bulk deposition on the grafted surface is slightly more favorable compared to the bare Au surface.

Three potential explanations can account for the higher opd+upd/upd ratio observed for grafted Au.

The first is that the gold crystal electrode used in hanging meniscus configuration has edges that do not have perfect (111) crystallographic planes. The edges of the grafted gold single-crystal electrode may contain a greater number of defects and step edges. As reported in the literature for Au electrodes the higher density of defects and step edges can increase the rate of nucleation [201].

The second possibility is that the grafts themselves contribute to the increased opd charge compared to bare Au. This is supported by comparisons with Cu deposition in the presence of thiourea on Au. Thiourea, commonly used as an additive in plating solutions, is known to enhance deposition rates. STM studies have shown that thiourea strongly adsorbs onto the surface, hindering Cu upd and altering its behavior [202]. Notably, in sulfate-containing solutions, thiourea adsorption changes the shape of the Cu upd curve from two distinct peaks (as seen on bare Au) to a single adsorption peak, indicating a significant modification of the surface interactions. The charge under the Cu upd peaks in the presence of thiourea is smaller than that corresponding to a full Cu monolayer. During Cu upd, small monoatomic Cu islands form on the surface, and the edges of these islands later serve as nucleation sites for bulk deposition. Since bulk deposition is not restricted to the step edges of the Au substrate, the presence of thiourea enhances the deposition process [202]. Based on this observation, we hypothesize that the grafts on the Au surface play a comparable role, influencing both Cu upd and bulk deposition like thiourea.

The third possible explanation could be that the grafts themselves act as artificial nuclei, facilitating Cu growth by providing additional nucleation sites. Alternatively, the grafts may induce a subtle reconstruction of the Au surface, creating a more favorable environment for bulk deposition. To find out which explanation is the real cause, further characterization techniques such as STM would be necessary, which are not performed as part of this thesis, leaving this question open for future research.

Depending on film and substrate, opd measurements could have permanent and irreversible effects on the surface which is reflected on the Cu upd measured afterward. For instance, measuring repetitive cycles of opd on the Au(111) modified via chemisorbed heterocyclic thiols, such as 2-mercaptobenzimidazole and 2-mercaptobenzothiazole, leads to a change of Cu upd CV or Cu adsorption and desorption processes that cannot be restored by limiting the cycling to upd region potential range [203]. They suggested that the organic adlayer is significantly disrupted by bulk deposition and/or stripping. Another example is measuring a Cu opd on hexagonal boron nitride grown on Rh(111) before upd which increases the upd peaks clearly. It was conjectured that the Cu can penetrate the hBN film through initial defects which intercalates between hBN and Rh(111) and leads to delamination of the hBN layer [150].

We investigated the effect of an excursion into the Cu opd region on upd. After measuring the first CV of Cu upd on the grafted surface (Fig. 5.12, red trace), the sample was exposed to the negative potential where the bulk deposition happens, then another Cu upd was measured (blue dashed trace), the same procedure was repeated. The inset shows the two opd measured on the surface. Figure 5.12 presents three identical upd CVs, meaning that the opd process does not affect the upd process (at the time scale of the two measurements).

Intercalation of Cu or Ag between SAM and Au substrate during Cu upd has been reported repeatedly [165, 204, 205]. In this process, metal ions penetrate a SAM layer through defects and a layer of metal grows laterally between the SAM and an Au substrate. To investigate whether Cu intercalates or creeps under the grafts, the sample was held at a potential more negative than the second peak of Cu deposition for varying durations, followed by anodic stripping CV measurements or Linear sweep voltammetry (LSV) [205, 206].

For instance, one reported study investigated Cu upd deposition on Au(111) modified with a butanethiol self-assembled monolayer (BT-SAM) [206]. LSV recorded for a

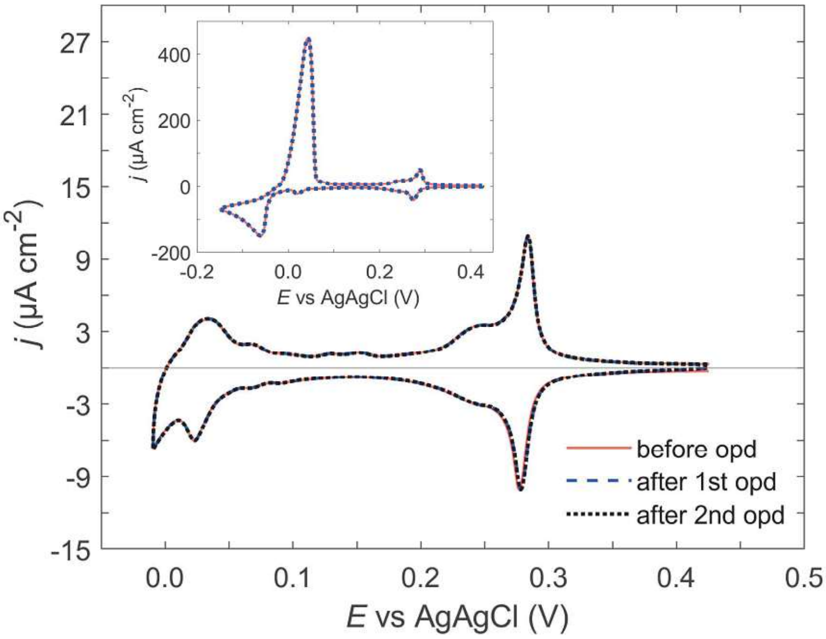

FIGURE 5.12: Effect of measuring Cu opd on the Cu upd behavior. The inset provides the opd cyclic voltammograms acquired before the upd measurements on Au(111). The Cu upd and opd are measured at 2 and 10 mV/s, respectively. Solution: oxygen-free 1 mM Cu^{2+} + 1 mM NaCl + 0.1 M $HClO_4$.

BT-SAM-modified electrode, following polarization for 20 minutes at -75 mV vs. SCE, revealed two prominent peaks corresponding to the desorption of the Cu adlayer. These peaks appeared at potentials different from those observed for a freshly prepared BT-SAM/Au(111) sample (non-polarized). Furthermore, the integrated charge under Cu upd desorption peaks measured after 20 minutes of polarization was more than twice that of the non-polarized sample. They also used X-ray absorption spectroscopy as a complementary technique to characterize the system.

Therefore, to study whether Cu intercalates into grafts/Au(111) interface, the electrode potential was kept at 0.01 V for durations of 1, 3, 30, and 60 min and then LSV was measured between -0.01 and 0.425 V with a scan rate of 2 mV/s. Figure 5.13 shows the LSVs after holding potential for different times. There is almost no difference between the LSV after 1 min and after 60 min so we can conclude that the Cu cannot creep between graft and gold surface.

The presence of SAM on the metal substrate can strongly affect the nucleation and growth of deposited metal on the surface and there are different possibilities of metal

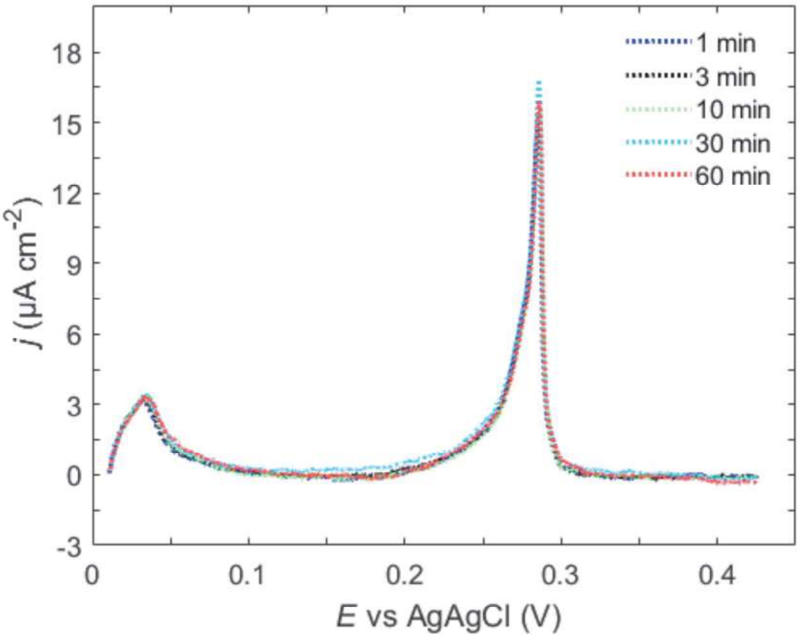

FIGURE 5.13: Effect of holding potential at 0.01 V vs. Ag/AgCl for 1 to 60 minutes on LSV in oxygen-free 1 mM Cu^{2+} + 1 mM NaCl + 0.1 M $HClO_4$ solution. Scan rate: 2 mV/s.

deposition on SAM/metal surface depending on the location of deposited metal (explained in Section 5.1.2) [190]. Based on the experiment performed in this chapter we can suggest the possible configuration of the Cu/grafts/Au(111). First, the deposition of metal on top of grafts would not be possible because the amount of Cu charge deposited on the grafted surface is less than bare gold and the CH_3 moiety of the bonded graft molecules is considered as hydrophobic and the CH_3 does not react with Cu adatoms [192]. The voltammograms of LSV CVs after holding potential and repetitive opd showed that Cu cannot intercalate between the Au and grafts. A dramatic increase in the amount of charge at opd at more negative potential was not seen. The mushroom-like growth suggested for some SAMs is unlikely because the graft coverage on the gold surface, which equals 28.7% (section 5.2.2), indicates a low surface concentration. Additionally, the grafts cannot form a compact monolayer on the surface like SAMs typically do.

The most likely model involves the deposition of Cu atoms solely on the Au areas not covered by grafts. On bare Au(111), during bulk deposition, the nucleation and growth of Cu clusters occur exclusively at monoatomic-high steps [190, 207, 208]. These copper clusters grow into three-dimensional structures resembling mountains [190]. Figure

5.14 illustrates the proposed model for Cu upd and opd on the grafted surface. During Cu upd on grafted gold, the entire surface, except for the regions covered by grafts, is coated with a monoatomic layer of Cu. Subsequently, bulk deposition proceeds similarly to bare Au(111), forming copper mountains at defect sites not occupied by grafts.

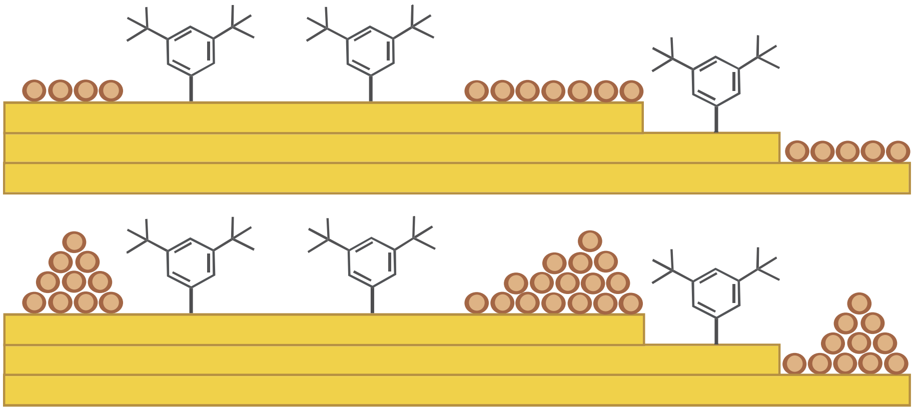

FIGURE 5.14: Cu upd vs opd on the grafted surface of gold

5.3 Conclusions

In summary, copper underpotential and overpotential deposition on grafted Au(111) was studied and the following results were obtained:

- The electrochemical deposition of copper was performed in a solution containing 1 mM NaCl because any trace of chloride from the reference electrode or grafting procedure could significantly change the voltammograms.
- The comparison between the copper underpotential deposition voltammogram of the grafted surface and the bare Au(111) reveals the presence of extra peaks. Our study showed that after electrochemical oxidation of the grafted surface, the Cu upd voltammogram exhibits the characteristics of both bare Au (111) and robustly attached grafts at the same time.
- The peaks of Cu upd voltammogram on grafted Au(111) were deconvoluted. This highlighted an energetically complex landscape, which may reflect different binding geometries of the grafts and proximity effects between nearest neighbors.

- The estimated coverage of the grafts, based on the data extracted from the deconvolution of the peaks, was around 0.3, which agrees well with the coverage extracted from the interfacial capacitance charge from cyclic voltammograms in sulfuric acid.

- To suggest the possible configuration of the deposited copper on grafted Au(111), we first measured the copper overpotential deposition voltammogram which was very similar to that of bare Au(111). Second, the multiple copper overpotential voltammograms were measured before the underpotential voltammogram, which had no effect on it. Third, holding the sample potential at 0.01 V for a duration of up to 60 min had no impact on the underpotential voltammogram. Therefore, we suggest that during copper underpotential deposition on grafted gold, a monolayer of copper covers the bare parts of Au(111) not covered by any grafts and during the overpotential deposition procedure, the nucleation and growth of Cu clusters follow the same mechanism observed on bare Au.

Chapter 6

Covalent grafting of gold: scanning tunneling microscopy

In this chapter, Au surfaces grafted with radicals derived from the reduction of 3,5-bis-*tert*-butylbenzenediazonium were imaged and studied with the scanning tunneling microscope in different environments. Our goal was to achieve molecular resolution.

Figure 6.10 is published in Azmi et al., *Electrochimica Acta* 500 (2024) 144743. Copyright 2024 by Author(s), published under a Creative Commons Attribution license CC BY-NC 4.0 (see [125]).

6.1 Introduction

The scanning tunneling microscopy images of the individual grafts by reduction of 3,5-bis-*tert*-butylbenzenediazonium (3,5-TBD) and 4-nitrobenzenediazonium (4-NBD) on HOPG in ambient condition were reported for the first time in 2015 (Fig. 6.1). The height profile obtained from STM images revealed that for HOPG grafted with 3,5-TBD, the apparent height of the particles ranged from 0.7 to 1 nm, suggesting that each measured particle was a single molecule. In contrast, for surfaces modified by 4-NBD, the particle height was 2.1 ± 0.1 nm, indicating these particles were clusters of molecules rather than single molecules [11]

The authors also performed Raman spectroscopy to estimate the degree of covalent grafting. The covalent attachment of graft molecules to the carbon surfaces leads to

sp^3 hybridization, considered as lattice defects that can appear as a D-peak in Raman spectra. The G-Peak corresponds to sp^2 pristine carbon. Therefore, the integrated intensity ratio of D and G peaks (I_D/I_G) can be used to quantify the degree of covalent grafting [209–211].

The I_D/I_G for the surfaces grafted with 1 mM 3,5-TBD was significantly larger than for 4-NBD at the same concentration, which was attributed to multilayer formation in 4-NBD. This difference is also evident in the STM images, where the graft density of 3,5-TBD appears higher than that of 4-NBD [11].

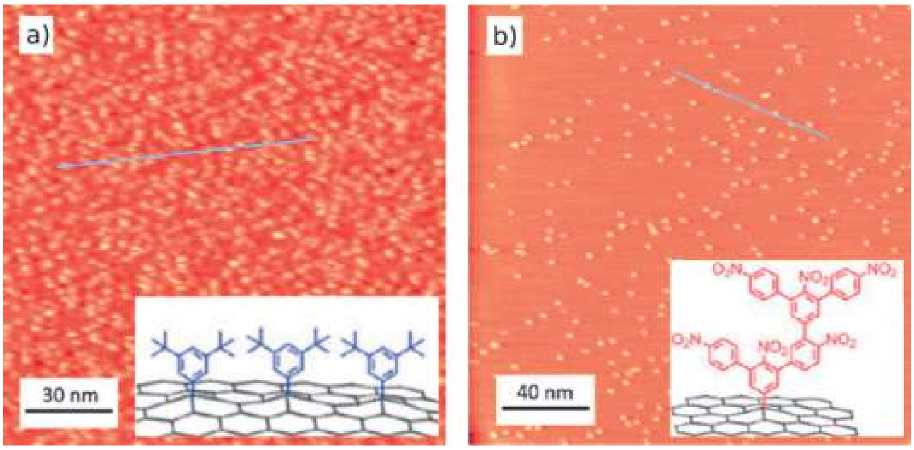

FIGURE 6.1: STM images of HOPG grafted by electrochemical reduction of a) 4-NBD, b) 3,5-TBD. The concentration of both diazonium salts is 1 mM. Adapted with permission from [11], Copyright (2015) American Chemical Society.

They also demonstrated that by using a high tunneling current and low bias during STM on the grafted surface it is possible to locally remove grafted molecules or clusters from the surface or perform so-called nanoshaving or tip-induced nanolithography. Figure 6.2 illustrates the nanoshaving on the grafted HOPG. By combining Raman spectroscopy with nanoshaving they proved that the removal of the grafts restores the pristine carbon surface with sp^2 hybridization. Additional evidence of surface restoration is seen in the self-assembly of the n-pentacontane only in the nanoshaved areas, where characteristic lamellae can be seen (Fig. 6.2-c). Besides the nanoshaving, the fast and easy fabrication of nanometer-sized pristine nanocorrals over macroscopic areas of graphite and graphene is also reported [12].

In another STM study, Au(111) surface was exposed to 4-bromobenzenediazonium tetrafluoroborate (BBD) in two different media: acetonitrile (MeCN) and 0.1 M $HClO_4$. The STM images are shown in Figure 6.3-a,b where it reveals two different structures

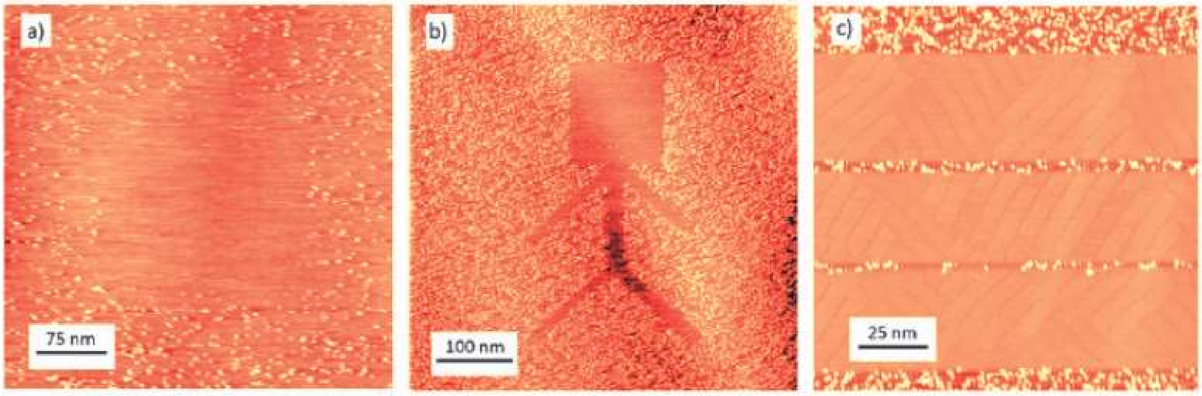

FIGURE 6.2: STM images, after nanoshaving on the HOPG grafted via a) 4-NBD and b) 3,5-TBD. The tunneling parameters: I_t = 0.08-0.1 nA and V_{bias} = -0.4 V. C) Self-assembly of the n-pentacontane (n-$C_{50}H_{102}$) in the nanoshaved areas. The nanoshaving in (a) was performed by several times scanning 200 × 200 nm with I_t = 0.5 nA. Adapted with permission from [11]. Copyright (2015) American Chemical Society.

on the surface depending on the grafting media. Figure 6.3-a shows that the MeCN grafting medium forms a disordered thin layer of grafts on the surface, while the surface modified via $HClO_4$ solution shows an ordered monolayer of 4,4'-dibromobiphenyl on the surface, attributed to a radical-radical coupling reaction, meaning the surface was not grafted in $HClO_4$ medium [212].

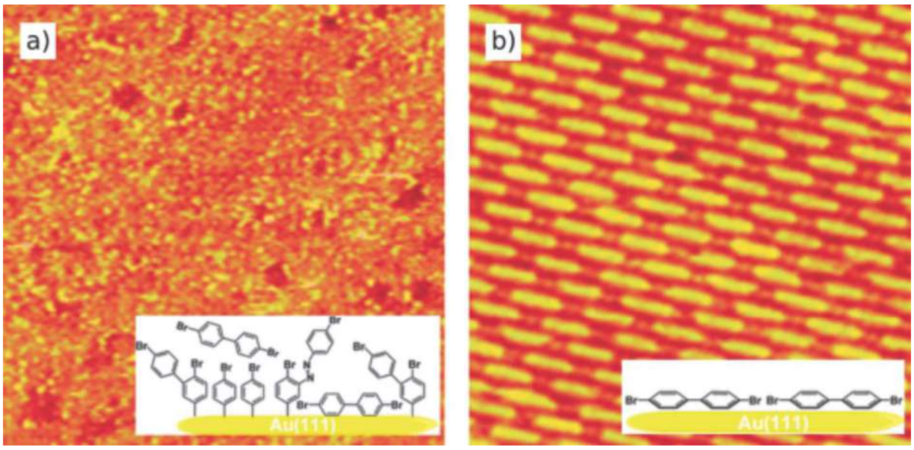

FIGURE 6.3: EC-STM images of Au(111) surface after exposing to 4-BBD in: a) acetonitrile and b) 0.1 M $HClO_4$. Reprinted with permission from [212]. Copyright (2013) American Chemical Society.

6.2 Results and discussion

6.2.1 STM of grafted Au(111) in air

Figure 6.4 shows the STM images of Au(111) surface grafted by 1 mM 3,5-TBD. The Au (111) surface was grafted by measuring three cycles between -0.4 V and 0.4 V vs. Ag/AgCl in the grafting solution of 1 mM 3,5-TBA in 0.5 M HCl + 1 mM $NaNO_2$, without removing oxygen. The electrode was rinsed with Milli-Q water and dried with Ar flow. Imaging was performed in constant-current mode with a low tunneling current of $I_t = 0.04$ nA and sample bias of $V_{\text{sample bias}} = 0.9$ V.

The STM image Figure 6.4-a reveals flat Au terraces with particles of various sizes on the surface. The particles observed on the surface may represent grafted molecules, along with contamination from air exposure and the grafting process. The effect of continuous scanning led to the modification or etching of the gold and enlargement of the pits on the surface (Fig. 6.4-b). More dramatic changes were observed at the center of the image, where larger pits formed after decreasing the sample bias to 0.4 V and continuously scanning the same area.

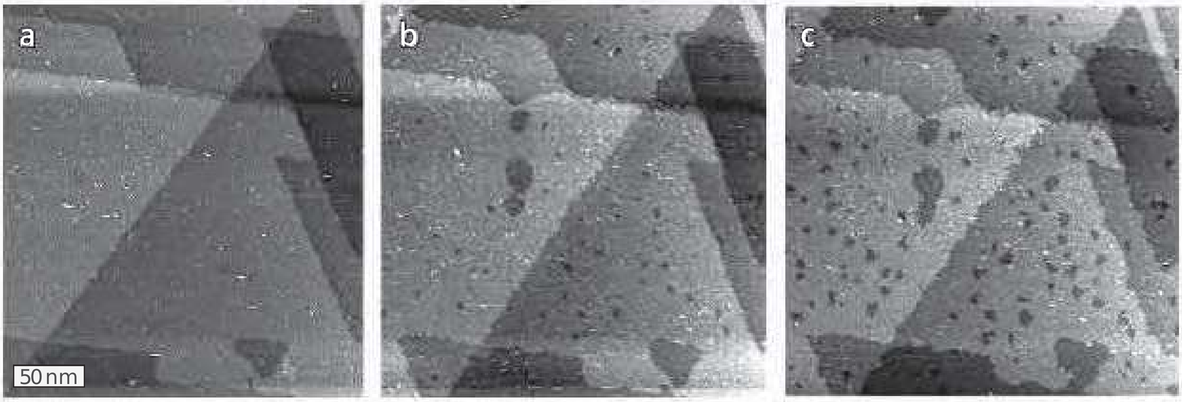

FIGURE 6.4: STM images of the grafted Au(111), in air with PtIr tip, a) the surface before interaction of the tip with the surface (etching) b) after etching, and c) after longer scanning (etching). $V_{\text{sample bias}} = 0.9$ V and $I_t = 0.04$ nA. The image c was taken after 1.5 hours after image b. Au(111) was grafted by measuring a few cycles in the grafting solution of 1 mM 3,5-TBA in 0.1 M HCl + 1 mM $NaNO_2$ between -0.4 and 0.4 V vs. Ag/AgCl. Scan size: 250 nm × 250 nm.

In addition to pit enlargement, etched and jagged step edges were also visible (Fig. 6.4-c). These changes on the surface are similar to those reported in a study on self-assembled n-octadecanethiol layers on Au(111), where scanning the surface with I_t

= 1 nA and V_{bias} = 1 V caused the pit expansion, suggesting significant tip-surface interactions [213]. They also showed that continuous scanning under similar tunneling conditions does not alter bare Au(111) surfaces. Therefore, such modifications are specific to Au surfaces modified with alkanethiols, where the sulfur atoms of the alkanethiol molecules form strong chemical bonds with the Au substrate surface [213]. The STM images related to field-enhanced diffusion/deposition of the material from the STM tip to the same surface can be found in the Appendix (Chapter A, Section A.1).

6.2.2 STM of grafted Au(111) in organic solvent

To image the grafted Au(111) surface in phenyloctane, we first performed STM on the bare Au(111) and then proceeded to image the grafted surface.

The bare Au(111) was imaged in the organic solvent phenyloctane. The STM images of the freshly annealed Au(111) are presented in Figure 6.5, where 6.5-a displays (111) terraces with herringbone reconstruction at a sample bias voltage of $V_{\text{sample bias}}$ = -0.6 V [214]. When the sample bias was changed to +0.6 V, some patterns and structures appeared on the surface (Fig. 6.5-b). Changing the potential to +0.6 V did not recover the surface to its initial state, indicating that the changes on the surface are irreversible. The tip was then moved to a different position on the surface and imaged at -0.5 V, which showed the surface to be free of any particles (Fig. 6.5-d). Since the changes on the surface were local, we suggest that at $V_{\text{sample bias}}$= +0.6 V there is an interaction between the tip and the organic solvent (or surface), which should be avoided when imaging the surface itself.

Besides phenyloctane, mesitylene was also used for imaging the bare gold. The STM images of the bare Au(111) in mesitylene can be found in the Appendix (Chapter A, Section A.2).

Figure 6.6 shows the STM images of the grafted Au(111) with 3 mM TBD, after rinsing with acetone and Milli-Q water, in phenyloctane. Imaging the surface without rinsing with acetone was almost impossible for the sample electrografted via CA at -0.2 V vs. Ag/AgCl for 400 s with 3 mM TBD. Careful rinsing with acetone to remove physisorbed by-products from the surface, and imaging in phenyloctane, improved the situation somewhat. Without achieving high resolution, this image reveals both grafts

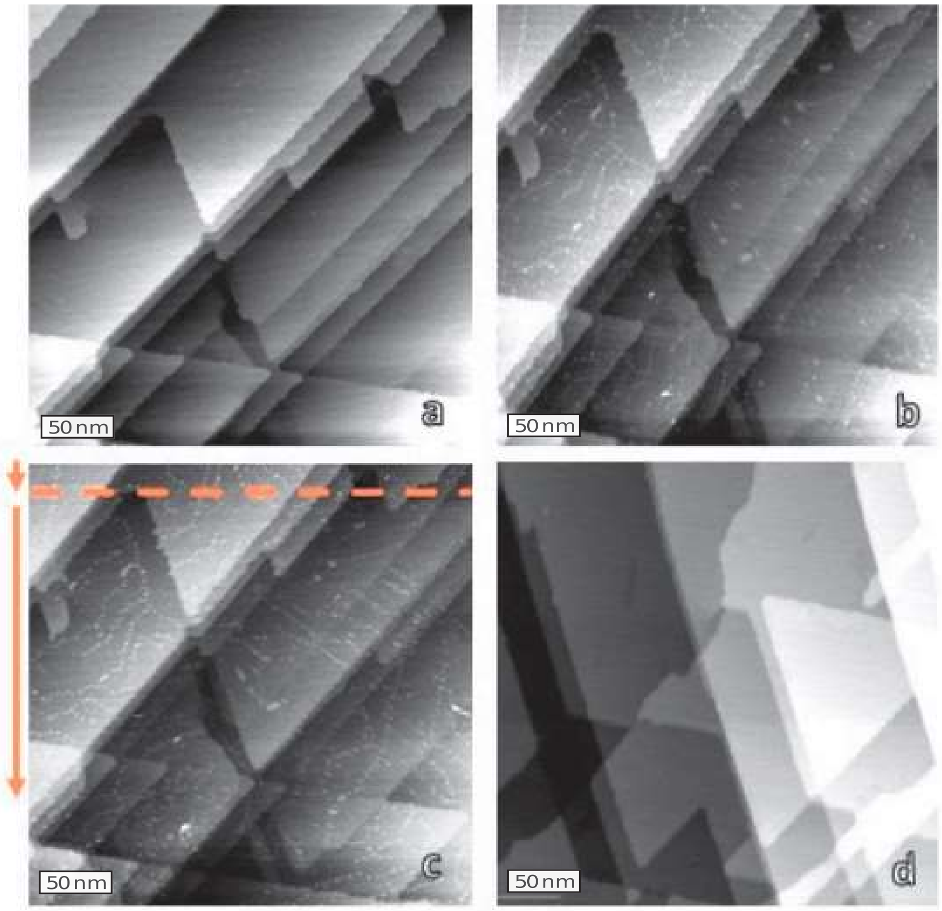

FIGURE 6.5: STM images of the bare Au(111) measured in phenyloctane with I_t = 20 to 50 pA with a PtIr tip. a) the reconstructed surface of Au(111), $V_{\text{sample bias}}$ = -0.6 V, b) the formation of chains on the surface, $V_{\text{sample bias}}$ = +0.6 V, c) change of $V_{\text{sample bias}}$ = +0.6 V to $V_{\text{sample bias}}$ = -0.6 V, showing the irreversible change of the surface, d) moving tip to another area and imaging the surface with $V_{\text{sample bias}}$ = -0.5 V. Scan size: 300 nm × 300 nm.

(bright features) and vacancy islands (dark) in addition to areas with unperturbed apparent height. This observation strongly suggests that the covalent binding of the aryl radicals on the Au surface is structurally not innocent, but accompanied by the formation of 'etch pits', potentially quite similar to observations of thiols on gold [3].

The apparent height of the big particles is 0.374 ± 0.119 nm, and the apparent height of the smaller particles or protrusions is 0.089 ± 0.038 nm. The nature of all particles is not clear to us. We have some other species together with grafts present on the surface. Distinguishing the grafts from contaminants originating from the air and the grafting procedure was challenging.

It is established that upon exposure of the clean gold to ambient air the surface is

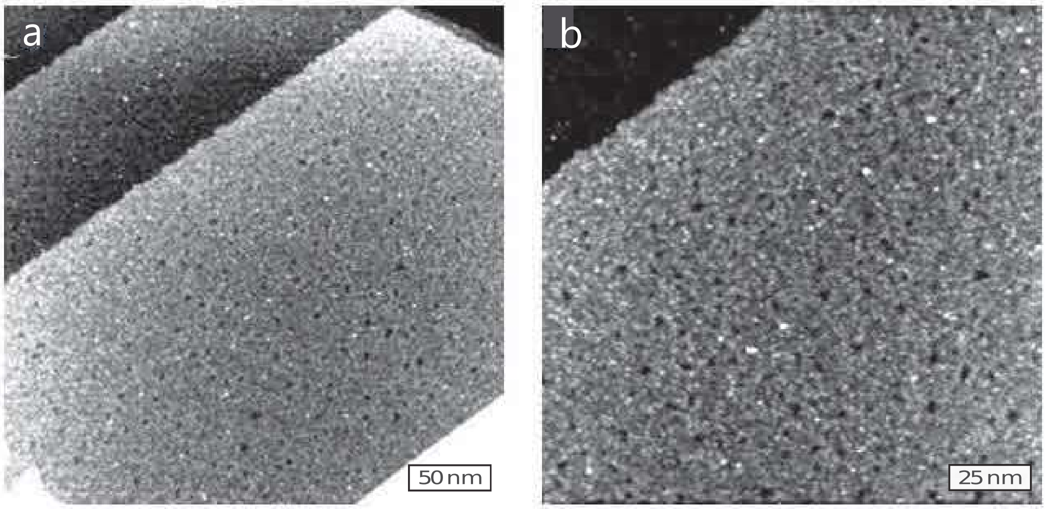

FIGURE 6.6: STM of the grafted Au(111) in phenyloctane measured at $V_{\text{sample bias}}$ = -0.5 V with and I_t = 18 pA, with scan size of a) 300 nm × 300 nm and b) 150 nm × 150 nm. The surface was grafted via CA at -0.2 V vs. Ag/AgCl for 400 s with 3 mM TBD and rinsed with acetone and Milli-Q water after grafting.

contaminated by organic molecules, so-called adventitious carbon [215–219]. Thus, in a UHV environment, the gold surface is cleaned by repeating the cycles of Ar^+ sputtering and thermal annealing before attempting any experiment [220–222]. Aside from adventitious carbon, during the grafting procedure, there are by-products that form on the surface and can be physisorbed on the surface [42, 127].

6.2.3 EC-STM of grafted Au(111) in iodide solution

The EC-STM images of the grafted surface, 1 mM 3,5-TBD, were also measured in 0.1 M $HClO_4$ (Fig. 6.7). The image shows the presence of particles, pits, and other species on the surface, similar to STM images obtained in phenyloctane.

We need an electrolyte containing anions that adsorb more strongly on the surface than the contamination. The adsorption strength of the ions to adsorb on the Au surface follows the sequence: $ClO_4{}^- < SO_4{}^{2-} < Cl^- < Br^- < I^-$ [135]. Therefore, we used an iodide solution of 1 mM KI + 5 mM H_2SO_4. By exposing the grafted surface to the iodide solution, we benefit from the fact that iodide adsorbs on the surface strongly; hence, physisorbed species formed during grafting and exposure to air can be replaced by iodide.

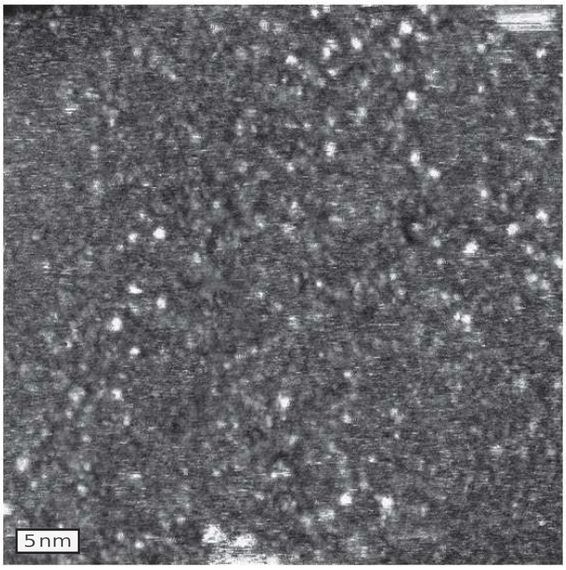

FIGURE 6.7: EC-STM of the grafted Au(111) by 1 mM 3,5-TBD, recorded in 0.1 M $HClO_4$. V_{sample} = -0.18 V vs. Pt wire, V_{tip} = -0.7 V , I_t= 50 pA ($V_{sample\ bias}$ = 0.52 V). Scan size: 43 nm × 43 nm.

The use of an iodide solution to clean the gold substrate for a SERS study was reported [223]. In their approach, the gold surface was cleaned through a two-step process: chemical adsorption of iodide, followed by electrochemical oxidation before measurements, ensuring a clean and homogeneous Au substrate.

Figure 6.8 shows the CVs of the grafted Au measured in 5 mM H_2SO_4 + 1 mM KI. Figure 6.8-a presents a voltammogram (two cycles) of the grafted Au(111) electrode, recorded within the potential range of -0.72 V to -0.074 V vs. Pt wire. A tiny cathodic peak at -0.63 V is due to reductive desorption of the adsorbed iodine [90]. At nearly the same potential, there is a more visible anodic peak corresponding to the readsorption of iodide. At potentials less negative than -0.63 V vs. Pt wire, an ordered adlayer of the iodine forms on Au(111) surface. This adlayer in the potential range between -0.63 V and -0.07 V vs. Pt wire has two phases. The first phase is the centered-rectangular phase with $c(p \times \sqrt{3}R - 30°)$, where, at around -0.63 V,the $p = 3$ and $c(p \times \sqrt{3}R - 30°) \equiv (\sqrt{3} \times \sqrt{3})30°$ (more details can be found in Chapter 8). By making the potential more positive, the value of p decreases to 2.49 [89]. At -0.13 V, where a small anodic spike can be seen, there is a transition to a rotated-hexagonal phase, forming a moiré pattern on the surface. The transitions between these two phases lead to the formation of two spikes around -0.15 V [90].

Figure 6.8-b shows the CV of the grafted surface measured over the range -0.76 V to 0.35 V. At potentials more positive than +0.01 V vs. Pt wire, the Au starts to oxidize to Au(I) and iodide (I^-) to tri-iodide ($I_3{}^-$). The big anodic peak at 0.16 V is assigned to the direct oxidation of iodide to iodine (I_2). The decrease in current at a potential higher than 0.16 V is because of the passivating solid iodine film formed on the electrode surface [224]. Our CV in Figure 6.8-b is identical to CV of Ir(111) at 50 mV/s in 1 mM KI + 0.1 M $HClO_4$, where they also observed sharp reversible redox peaks around 0.07 V, which they assigned to the I^-/I_2 redox couple [225].

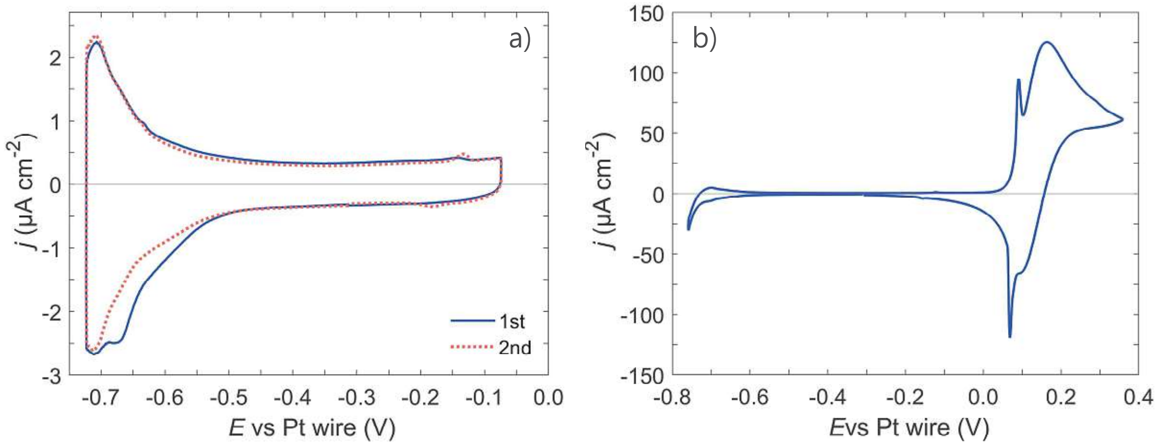

FIGURE 6.8: CVs of the grafted Au(111) measured in the 5 mM H_2SO_4 + 1 mM KI measured in different potential ranges after removing oxygen by purging Ar. The Au was grafted by CA at -0.2 V vs. Ag/AgCl for 60 s in 1 mM 3,5-TBD. Starting from 0.31 V vs. Pt wire to negative going scan. The scan rate a) 10 mVs (including 1st and 2nd cycles), and b) 20 mVs.

Figure 6.9-a and 6.9-c, shows the EC-STM images of the grafted Au(111) in iodide solution (1 mM KI + 5 mM H_2SO_4). At the potential used in Fig.6.9-a and 6.9-c, the iodide adlayer is known to assume a moiré structure whose periodic nature is visible in the image. Figure 6.9-b shows the fast Fourier transform (FFT) of the image in 6.9-a, revealing two sets of spots: the central hexagonal set represents the superlattice (moiré pattern). In contrast, the less discernible outer spots correspond to the iodine ad-lattice or atomic structure.

Compared to Figure 6.6 imaged in phenyloctane, the etch pits or holes vanished from the surface which can be explained by the enhancement of gold step atoms mobility due to iodine adsorption or (or rather, iodine-gold complexes) [81, 226]. The strong adsorption of iodide on gold removes any remaining physisorbed material from the surface. Still, it may also remove grafts that are less robustly adsorbed, which may

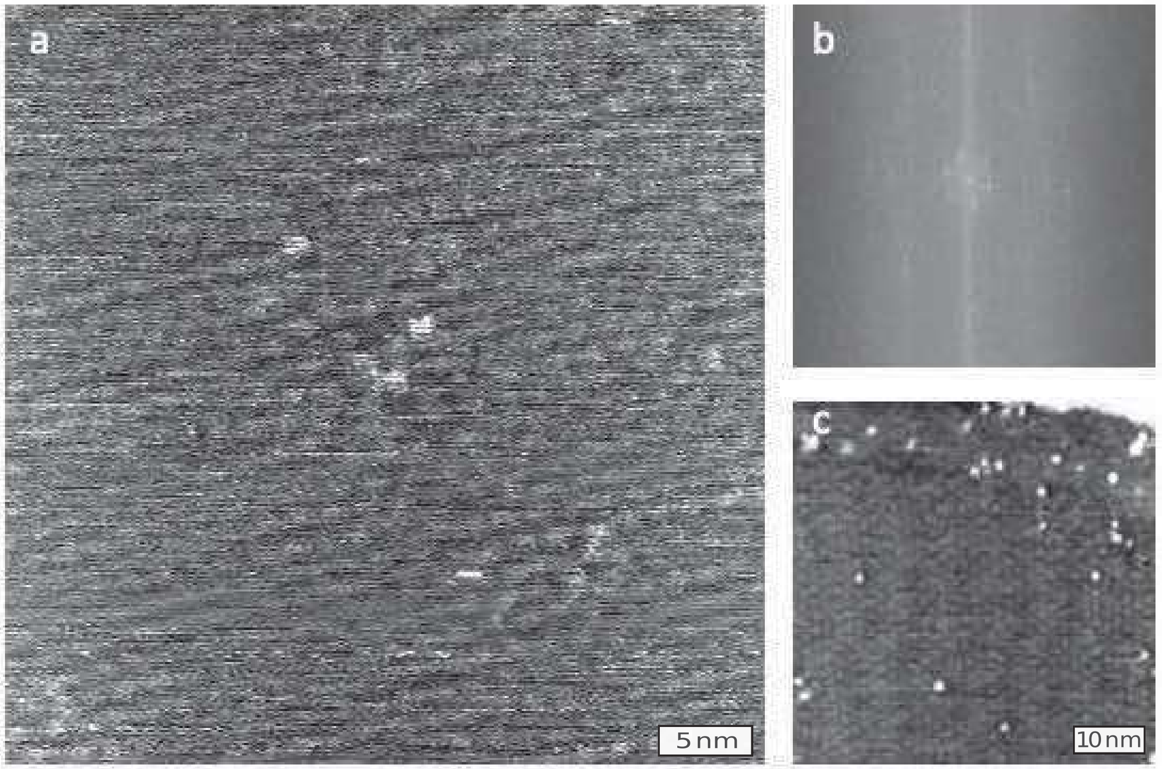

FIGURE 6.9: EC-STM images of the grafted Au(111) measured in the 1 mM KI + 5 mM H_2SO_4 with a W tip. a) scan size: 40 nm × 40 nm, V_{sample} = -0.08 V, V_{tip} = -0.47 V, $I_{tunneling}$ = 0.140 nA, $V_{sample\ bias}$ = +0.39 V, b) FFT of the (a), c) scan size: 50 nm × 50 nm, V_{sample} = -0.113 V, V_{tip} = -0.42 V, I_t = 20 pA, $V_{sample\ bias}$ = +0.307 V.

explain the low coverage with bright features, because the (reported) calculated adsorption energy of the iodine on Au(111) is in the same range as the grafts on Au [227, 228]. The adsorption energy of I (iodine) on Au(111) calculated via DFT is 2.14 eV (206.45 kJ/mol) [227] and for the aromatic carbon is 133 kJ/mol [228].

The average height of white particles is 0.344±0.072 nm. The DFT calculations on the bonding and structures of phenyl groups on the Au (111) surface reported the higher adsorption energy for the upright configuration compared to the tilted configuration where C_6H_5 molecular plane is tilted with an angle of 38° with respect to surface normal [140]. Therefore, we can conclude that the apparent height of the grafts on the surface in an upright configuration is 0.344 ± 0.072 nm.

STM images of covalently 3,5-TBD grafted Au(111) in different environments are shown in Figure 6.10.

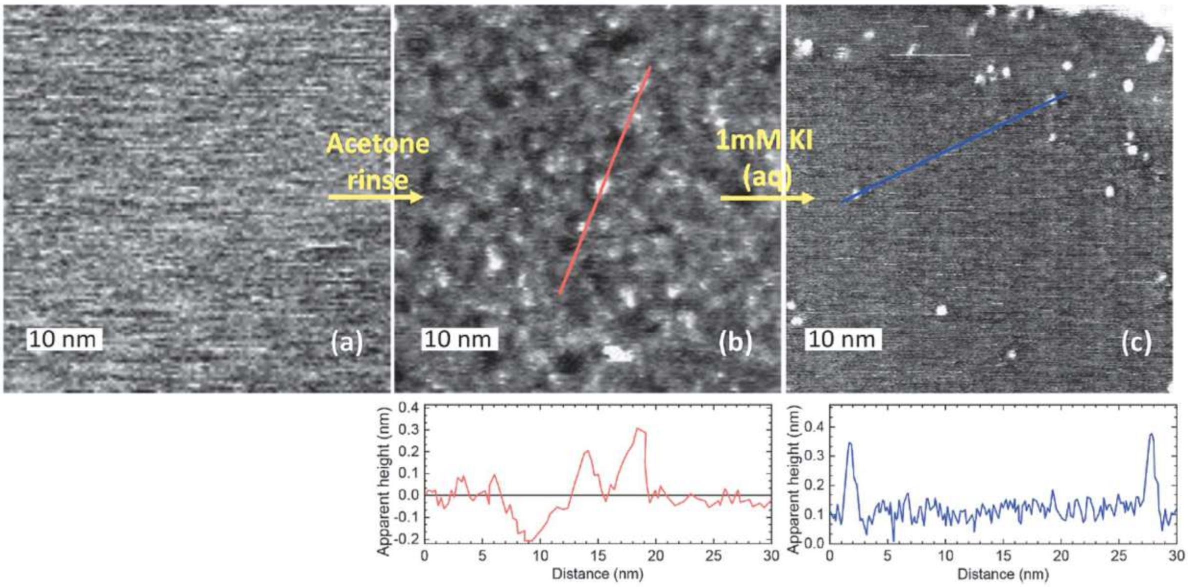

FIGURE 6.10: STM images of covalently 3,5-TBD grafted Au(111): a) in the air after rinsing with Milli-Q water; b) in phenyloctane after rinsing with acetone, revealing grafts (bright) and vacancy islands (dark); c) in 5 mM H_2SO_4 + 1 mM KI (aq), revealing high-contrast grafts and a moiré pattern of iodine on Au(111). Apparent height profiles along red (panel b) and blue (panel c) lines as shown. Tunneling parameters: I_t = 20 pA (all images); $V_{\text{sample bias}}$ = +2 V (a), -0.5 V (b), -0.07 V (c); V_{sample}= +2 V -0.113 V vs. Pt quasi-reference (c).

Figure 6.11 presents EC-STM images of the grafted Au(111) in 1 mM KI + 5 mM H_2SO_4, recorded at various sample potentials between -0.1 and -0.4 V vs. Pt wire. Figure 6.11-a, imaged at the sample potential of -0.1 V, shows a moiré pattern accompanied by visible particles (grafts). When the sample potential changes from -0.1 V to -0.25 V (Fig. 6.11-b) the moiré structure transitions to a non-moiré. Additionally, the effect of noise on the STM images becomes evident as the tunneling current increases. Although the particles appear less distinct compared to earlier images, faint chain-like structures are discernible on the surface. With a further increase in the tunneling current to 0.8 nA, these chain structures become more pronounced (Fig. 6.11-c).

We propose that these observed chains correspond to those previously identified on the bare Au(111) surface (Chapter 8). Notably, the concentration of these chains appears higher in regions where particles are located. This observation suggests two possibilities: either the particles serve as nucleation sites for the growth of these chains, or both particles and chains exhibit a stronger affinity for substrate regions with higher defect densities (e.g., grain boundaries). The arrows in Figure 6.11-a and 6.11-d indicate the same two particles imaged at different potentials. More EC-STM images of the grafted

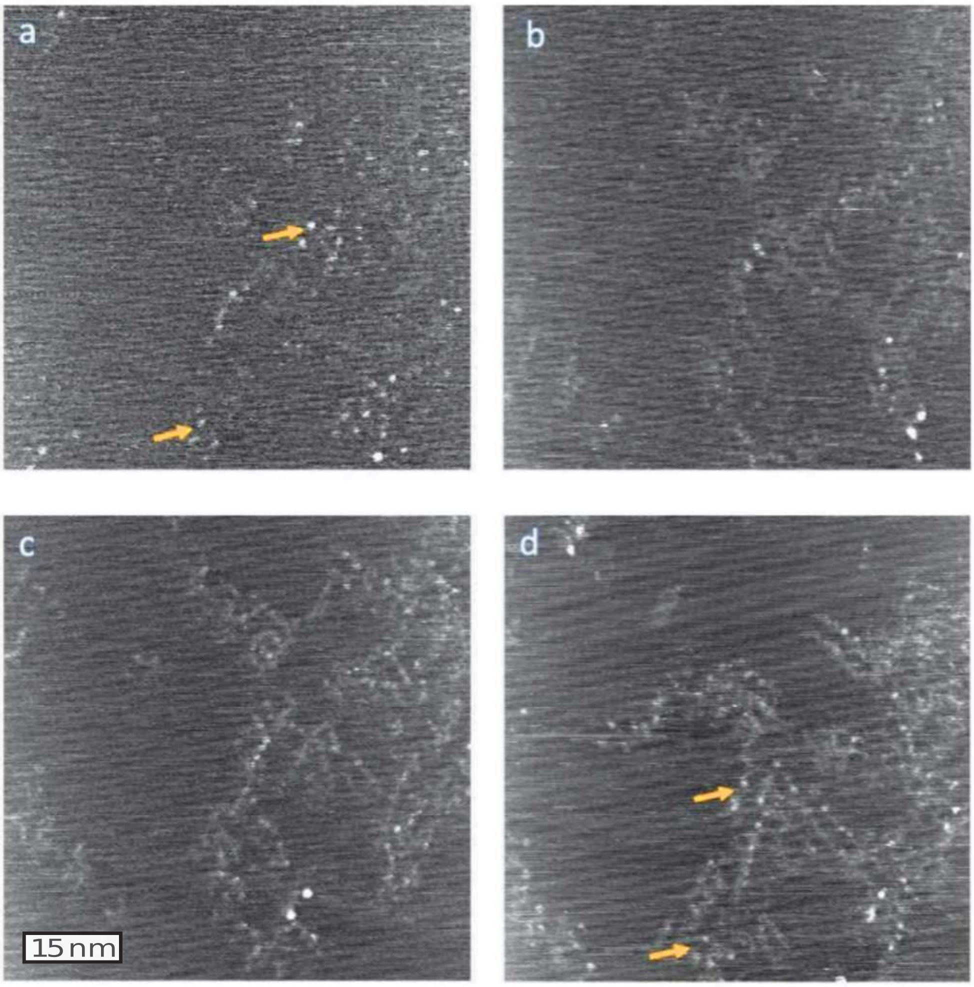

FIGURE 6.11: EC-STM images of the grafted Au(111) in the 1 mM KI + 5 mM H_2SO_4 at different sample potentials: a) V_{sample} = -0.1 V, I_t = 0.1 nA, b) V_{sample} = -0.25 V, with I_t = 0.4 nA, c) V_{sample} = -0.28 V, I_t = 0.8 nA, d) V_{sample} = -0.4 V, I_t = 1.12 nA, measured by a W tip with V_{tip}= -0.47 V vs. Pt wire. The yellow arrows mark the same two particles observed at different potentials in (a) and (d). Scan size: 70 nm × 70 nm.

Au(111) at different sample potentials can be seen in Appendix (Chapter A, Section A.3).

6.3 Conclusion

Scanning tunneling microscopy (STM) was performed on grafted Au(111) surfaces in various environments to achieve molecular resolution.

- Initial attempts at STM in air especially for the samples grafted with 3 mM 3,5-TBD, were not successful (see Fig. 6.10-a). However, by careful rinsing with acetone to remove physisorbed by-products from the surface, we managed to image the grafted surface in phenyloctane (Fig. 6.10-b). This image reveals both grafts (bright particles) and etch pits (dark ones) in addition to areas with unperturbed apparent height.

- High-contrast observation of the covalent grafts is first possible by using EC-STM in a solution containing iodide, as shown in Fig. 6.10-c. At the potential used in Fig. 6.10-c, the iodide adlayer is known to assume a moiré structure, whose periodic nature is visible in the image. The strong adsorption of iodide on gold removes any remaining physisorbed material from the surface and promotes high mobility of individual gold atoms (or rather, iodine-gold complexes), but may also remove grafts that are less robustly adsorbed, which may explain the low coverage with bright features. In the present case, this enhanced surface mobility heals the etch pits that are visible in Fig. 6.10-b. To our knowledge, this is the first high-resolution visualization of covalent grafts on a metal surface.

Chapter 7

Covalent grafting of gold: electrochemical impedance spectroscopy

EIS is a widely used technique to unveil the electrochemical properties of the modified surface. The blocking or barrier effect of the film before and after grafting onto carbon or gold in the solution containing the ferri/ferrocyanide redox couple has been reported [29, 127, 128]. Here, we utilized EIS as an *operando* technique to monitor the grafting process in real time. To the best of our knowledge, in all reported studies thus far, EIS has only been used to characterize the surface before and after modification via the reduction of diazonium salt. Additionally, the impedance data measured at the grafting potential and without applying the potential (spontaneous grafting) were compared.

7.1 Introduction

During the reduction of the 3,5-TBD diazonium salt aryl radicals are formed. The radicals near the surface can form covalent bonds to the surface. However, based on our previous chapters, the grafting is not the only process happening during the grafting and the surface is being covered by by-products such as dimers that are formed via radical-radical coupling [156, 229]. These by-products can be physisorbed on the surface. Therefore, during the diazonium salt reduction, we have a surface that is being partly covered by the grafted molecules and partly by the by-products physisorbed on the surface (Figure 7.1).

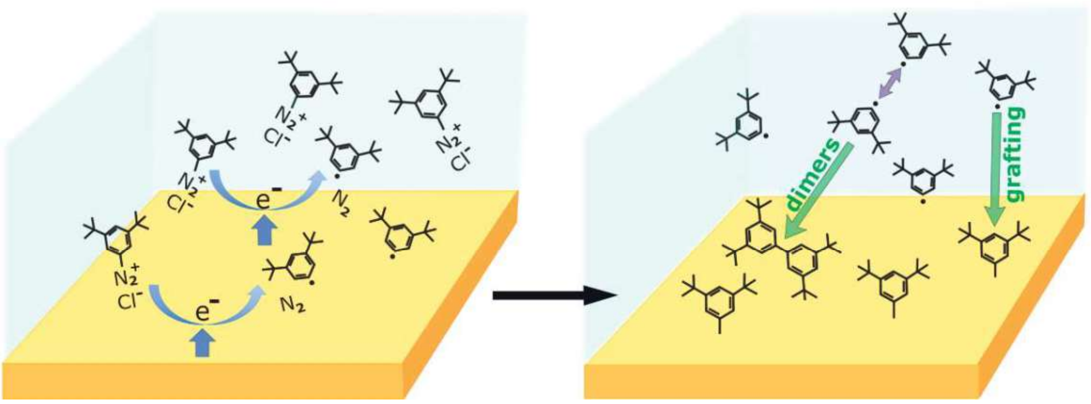

FIGURE 7.1: The reduction of the diazonium salt at the gold surface results in the formation of free radicals. These radicals can either bind to the surface or produce other products such as dimers, that may be physisorbed on the surface.

There are significant similarities between our grafted surface and a metal surface covered by a defective coating, despite their opposing formation processes. In our case, we start with a bare surface, and with each grafting step, a portion of the surface becomes progressively covered. We assume this process continues until the surface is almost fully covered by the grafts.

For the metal surface coated with an insulating film, it is initially more or less fully covered. However, due to the pores in the coating, electrolyte ions reach the metal surface. Over time, as the coating deteriorates, more areas of the metal become exposed to the electrolyte.

Four possible equivalent circuits for metal surfaces covered by a non-conductive coating are shown in Figure 7.2 [105]. Figure 7.2-a shows an ideal, undamaged non-conductive coating, covering the whole surface without any pores. In Figure 7.2-b there is a coating that only partially covers the surface. In Figure 7.2-c the surface is covered by a non-conductive layer containing pores exposing the electrode to the electrolyte. Figure 7.2-c can be viewed as an extension of the scenario depicted in Figure 7.2-b, where the film becomes thicker and the fractional surface coverage nears unity. In Figure 7.2-d electrode is coated by two porous layers containing pores exposing the electrode to the electrolyte.

The final two models will later be used in the results section to analyze data from a surface under operando grafting conditions.

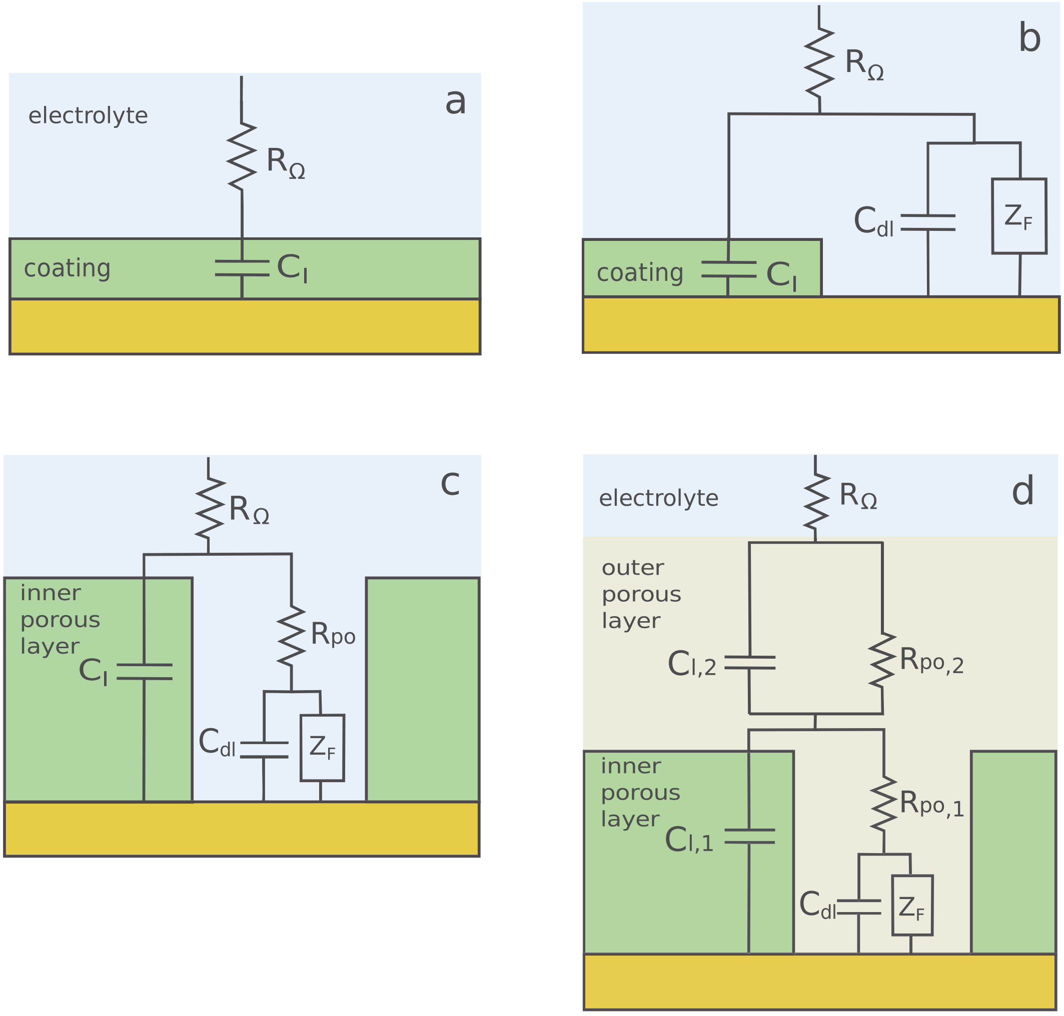

FIGURE 7.2: Equivalent electrical circuit for: a) Ideal non-conductive coating on a metal electrode, b) Partially covered electrode by non-conductive coating, c) Surface covered by a non-conductive layer containing pores exposing the electrode to the electrolyte, d) Electrode coated by two porous layers containing pores exposing the electrode to the electrolyte. Adapted from [105] with permission. Copyright (2017), John Wiley and Sons.

7.2 Results and discussion

In designing our experiments to use EIS as an *operando* technique, for monitoring the grafting process, we considered several key factors: First, the decomposition of diazonium precursor happens relatively fast, so the EIS experiment was conducted in an electrochemical cell immersed in an ice-water bath to slow down the decomposition. To prepare the grafting solution, all components were mixed immediately before the experiment, while previously they were kept in a fridge. Second, the working electrode and the electrochemical cell were tilted at an angle of approximately 45° to allow N_2

bubbles to escape during grafting. Third, to keep the experimental time short and to approach a time-invariant system during the measurement period, only 3 points per decade were measured, providing a compromise between level of detail and time required to complete a spectrum [230]. In our EIS measurements, we selected a 3-second grafting step, which was short enough to keep the overall experiment brief but long enough to observe the effect of grafting on the impedance spectrum.

Figure 7.3 shows the sequence of electrochemical measurements including CA and EIS for studying electrochemical grafting of Au with 3,5-TBD at potential -0.2 V vs. Ag/AgCl.

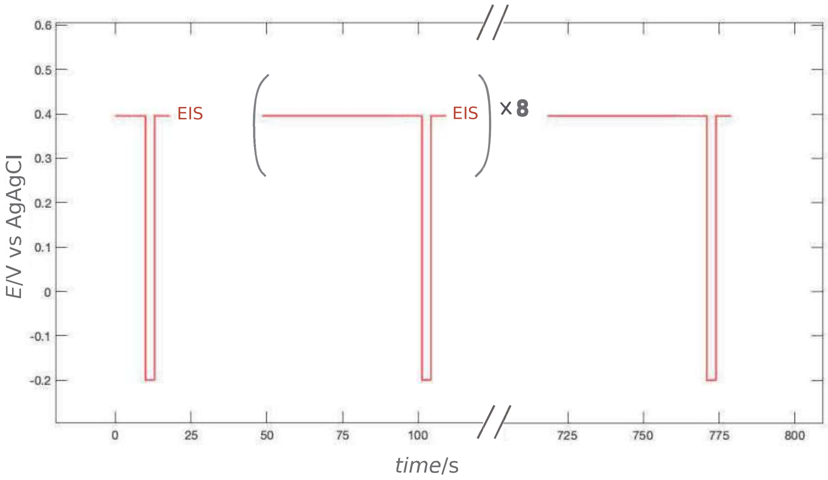

FIGURE 7.3: Sequence of electrochemical measurements, including CA and EIS, for studying the electrochemical grafting of Au with 3,5-TBD in real-time. Each grafting step was performed by holding the potential at -0.2 V for 3 s in a grafting solution containing 1 mM $[Fe(CN)_6]^{4-}$ and 1 mM $[Fe(CN)_6]^{3-}$. After each grafting step, EIS was measured, and the process was repeated 10 times.

7.2.1 Bare Au in hexacyanoferrate solution

Impedance data measured on bare Au(poly) are presented in Nyquist and Bode representations in Figures 7.4-a and 7.4-b, respectively. The EIS measurement was performed at OCP (E = 0.196 V vs. Ag/AgCl) in a solution of 1 mM $Fe(CN)_6{}^{3-}$ + 1 mM $Fe(CN)_6{}^{4-}$ + 0.1 M Na_2SO_4. The system's impedance response was modeled using the Randles circuit, which represents a single redox reaction coupled with mass transfer. The experimental data are indicated by markers, while the fit is shown with lines in Figure 7.4.

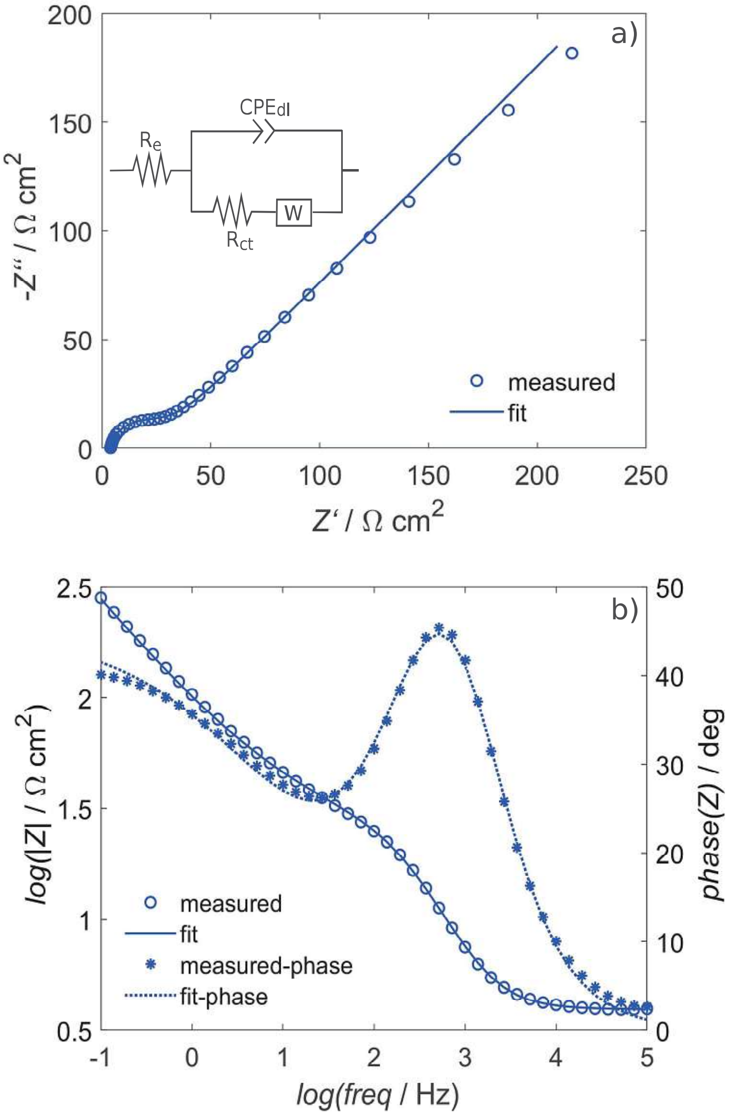

FIGURE 7.4: a) Nyquist and b) Bode plots obtained at Au(poly) electrode, at open circuit potential (E = 0.196 V vs. Ag/AgCl) in 1 mM $Fe(CN)_6^{3-/4-}$ + 0.1 M Na_2SO_4 in frequency range from 100 kHz to 0.1 Hz. The experimental data: circle and asterisk, fitting: full and dotted line. The Randles equivalent circuit shown in (a).

The Nyquist plot, Fig 7.4-a, displays a semicircle at high frequencies followed by a straight line at low frequencies. The semicircle represents an RC equivalent circuit that combines the charge-transfer resistance and the double-layer capacitance of the electrode. The diameter of the semicircle is equal to $R_{ct} = 23\ \Omega\,\mathrm{cm}^2$. The R_{ct} on the bare Au electrode is small, indicating fast electron transfer. The uncompensated resistance $R_\Omega = 3.92\ \Omega\,\mathrm{cm}^2$ was obtained from the intersection of the leftmost side of the semicircle with the x-axis, representing the resistance of the electrolyte solution

TABLE 7.1: Parameters of the equivalent circuit resulting from the fitting of impedance spectra, measured on bare Au in 0.1 M Na_2SO_4 solution containing 1 mM $Fe(CN)_6{}^{3-/4-}$, with $\chi^2 = 0.0378$.

	Values	Estimated Error (%)
$R_\Omega(\Omega\,\mathrm{cm}^2)$	3.92	0.98
$R_{ct}(\Omega\,\mathrm{cm}^2)$	23	2.72
$Q_{0-dl}(\mathrm{s}^\alpha/\Omega\,\mathrm{cm}^2)$	5.92×10^{-5}	9.781
α	0.915	1.25
$Q_{0-W}(\mathrm{s}^{0.5}/\Omega\,\mathrm{cm}^2)$	4.83×10^{-3}	0.81

between WE and RE. As explained in Chapter 2 in Section 2.4.5, at low frequencies, a 45° Warburg line emerges, signifying the diffusion processes of hexacyanoferrate ions to the electrode surface. Since the diffusion of the hexacyanoferrate ions to the electrode surface is slower than the electron transfer rate, the impedance response is dominated by diffusion, causing the straight line corresponding to the diffusion-limited Warburg impedance to appear longer [95, 109]. In our case, the slope of the Warburg in the Nyquist plot is 0.93; therefore, $tan^{-1}(0.93) = 43°$.

The Bode plot is shown in Fig 7.4-b. From the impedance magnitude vs. frequency (logarithmic scale) plot, the value of $R_\Omega = 3.92\ \Omega\,\mathrm{cm}^2$ can be extracted at very high frequencies, while at low frequencies, the total resistance $R_\Omega + R_{ct}$ is observed. In the phase angle vs. frequency plot, the phase angle approaches 0° at high frequencies, indicating purely resistive behavior dominated by R_Ω. At low frequencies, the phase angle approaches 45°, reflecting diffusion-controlled processes (Warburg impedance). In the mid-frequency range, a peak is observed, highlighting the dominance of capacitive behavior attributed to C_{dl} [109].

The extracted parameters are collected in Table 7.1.

To estimate the effective capacitance we used Equation 2.63 introduced in Chapter 2, Section 2.4.5. The calculated C_{dl} was $26.8 \times 10^{-6}\ \mathrm{F\,cm}^{-2}$. The C_{dl} and R_{ct} are close to those reported [231].

Assuming semi-infinite diffusion, the diffusion coefficient D can be obtained from the EIS data based on Equation 2.67 corresponding to the Warburg coefficient, σ.

In our case the $c_R = c_O = c = 1\mu\,\text{mol}\,\text{cm}^{-3}$ and A = 0.0201 cm^2. We also assume that $D_R = D_O = D$ [232, 233]. Therefore, Equation 2.67 reduces to

$$\sigma = \frac{2RT}{n^2F^2Ac\sqrt{2D}} \tag{7.1}$$

The value of σ can be extracted from the slope of the Z'_W(real) and $-Z''_W$(imaginary) as a function of $\omega^{-0.5}$ [232–234], shown in Figure 7.5. The $-Z'$ and Z'' data recorded at low frequencies are Z'_W and $-Z''_W$, respectively.

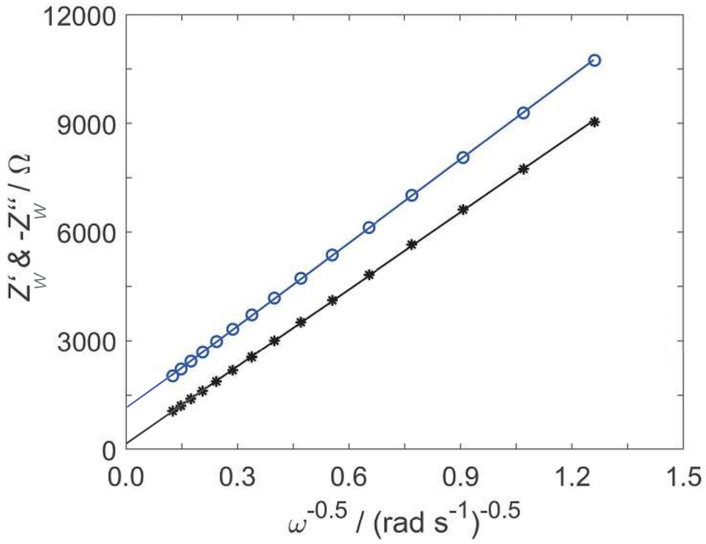

FIGURE 7.5: Plot of Z'_W (o, blue) and $-Z''_W$ (*, black) as a function of $\omega^{-0.5}$ to extract the σ.

The slopes of the Z'_W and $-Z''_W$ are 7.66×10^3 and 7.08×10^3, respectively. The averaged slope of 7.37×10^3 yields a value of D equal to 6.45×10^{-6} cm^{2}s^{-1}. This value is close to the value (7.2×10^{-6} cm^{2}s^{-1}) reported in the literature [157, 158].

It is also possible to estimate the standard electron transfer rate constant, k^0, based on Equation 2.70 [110]. The calculated k^0 was 0.0115 cm s^{-1}. For bare gold electrodes, the k^0 value has been reported to range between 0.01 and 0.1 cm s^{-1} [159, 235, 236].

7.2.2 Operando monitoring of electrochemical grafting

Figure 7.6 shows the fourth EIS measurement in the sequence shown in Figure 7.3 performed in the grafting solution in the presence of $\mathrm{Fe(CN)_6}^{3-/4-}$. The Nyquist plot shows the presence of two semicircles. Among the equivalent circuits suggested in Figure 7.2, the equivalent circuit 7.2-c with two semicircles has been chosen. However, because there is the diffusion of hexacyanoferrate ions to the surface, the Warburg element must be added to the circuit.

In the frequency range used in this experiment, only for the first step of EIS, the tail can be seen. The tail is quite short, and the angle 45° cannot be seen, it is also possible that the tail is due to the presence of another phenomenon. However, because of keeping the total time of the experiment short, we had to limit our measurement to low frequencies. Moreover, the semicircles in the Nyquist plot are relatively depressed, which indicates the presence of CPE instead of ideal capacitive behavior. The distribution of grafted molecules on the surface can lead to microscopic surface roughness and inhomogeneity in both surface characteristics and kinetics, which is represented by the CPE [29]. Moreover, the faradaic impedance Z_F was replaced by the charge transfer resistance R_{ct} in series with the Warburg element W. In the equivalent circuit, R_Ω is the uncompensated solution resistance, and R_{po} is the coating pore resistance. The equivalent circuit to obtain a fit to the experimental data is shown in Figure 7.7.

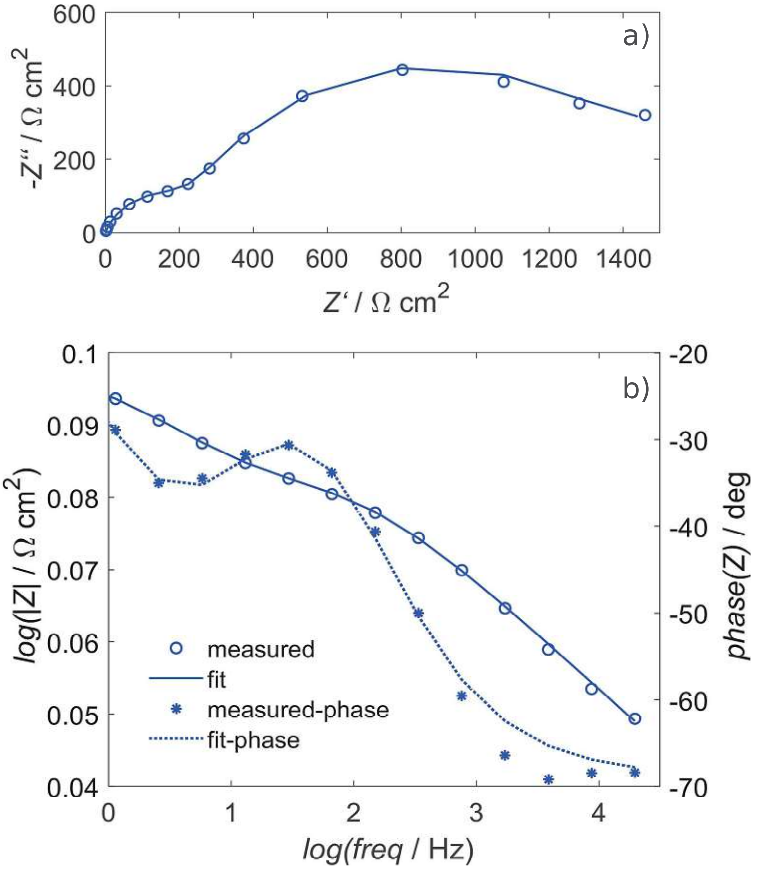

FIGURE 7.6: a) Nyquist plot, b) Bode plot of impedance data measured on Au(poly) after 4th step of diazonium reduction (12 s) at -0.2 V vs. Ag/AgCl in 1 mM 3,5-TBA + 0.1 M HCl + 1.2 mM $NaNO_2$ + 1 mM $[Fe(CN)_6]^{4-}$ + 1 mM $[Fe(CN)_6]^{3-}$. Each step of grafting was 3 s. The experimental data: circle and asterisk, fitting: full and dotted line. The experimental data were fit to the equivalent circuit in Figure 7.7.

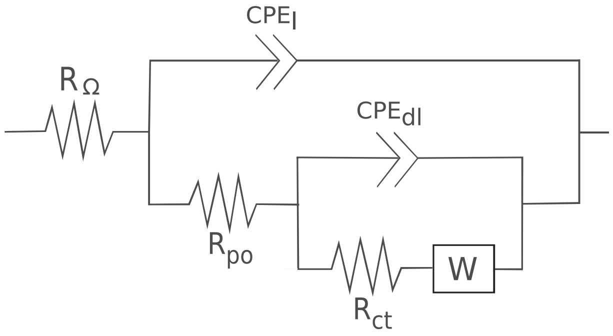

FIGURE 7.7: Equivalent circuit used for fitting the EIS response of the system.

The changes of measured electrochemical impedance spectra with time are shown in Figure 7.8. The Nyquist representation of these spectra is shown in Figure 7.8-a, and the corresponding Bode plots are presented in Figures 7.8-b,c. The arrows in the figure display the change of the plots with time. The electrochemical parameters were extracted and presented in Figure 7.9. Since Q values do not have any physical meaning, they were converted to the effective capacitance value with Equation 2.64 [108].

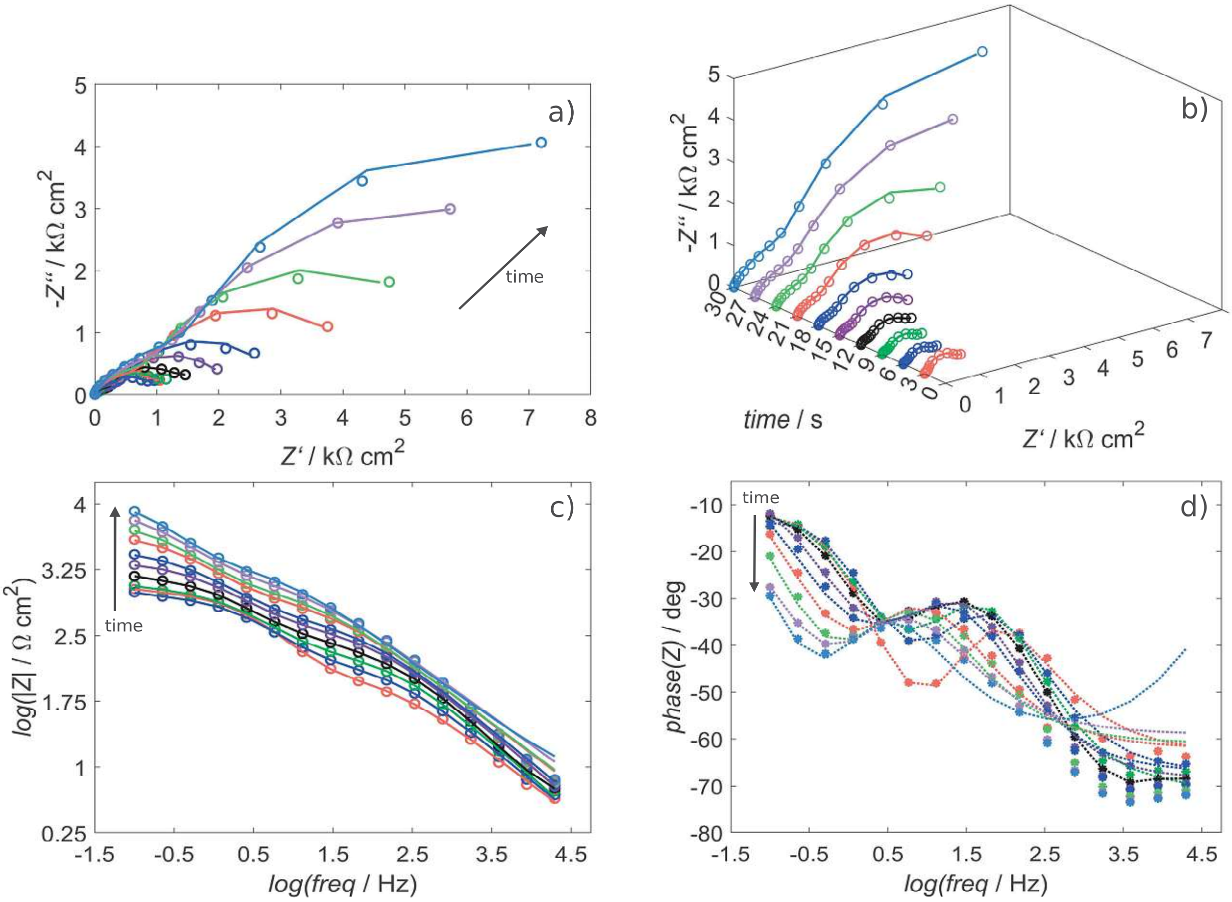

FIGURE 7.8: a) Nyquist plot, b) Nyquist plot vs. time c) Bode magnitude plot, and d) Bode phase angle plot for grafting Au(poly) after each step of diazonium reduction at -0.2 V vs AgAgCl for a duration of 3 s, repeated for 10 times. The EIS performed in 1 mM 3,5-TBA + 0.1 M HCl + 1.2 mM $NaNO_2$ in the presence of 1 mM $[Fe(CN)_6]^{4-}$ and 1 mM $[Fe(CN)_6]^{3-}$. The experimental data are shown with markers and fit with lines. The black arrows show the change over time.

To understand the effect of repeating grafting steps on the gold electrode, we focused on the changes in the resistances and capacitances of the system after each step of grafting.

The capacitance, C, of a capacitor, made of two parallel conducting plates with a surface area A separated by a dielectric material with a thickness d and (absolute) permittivity ϵ, is given by Eq. 7.2, where $\epsilon = \epsilon_r \epsilon_0$. The ϵ_0 is the electrical permittivity in vacuum and ϵ_r denotes the relative permittivity of the dielectric material.

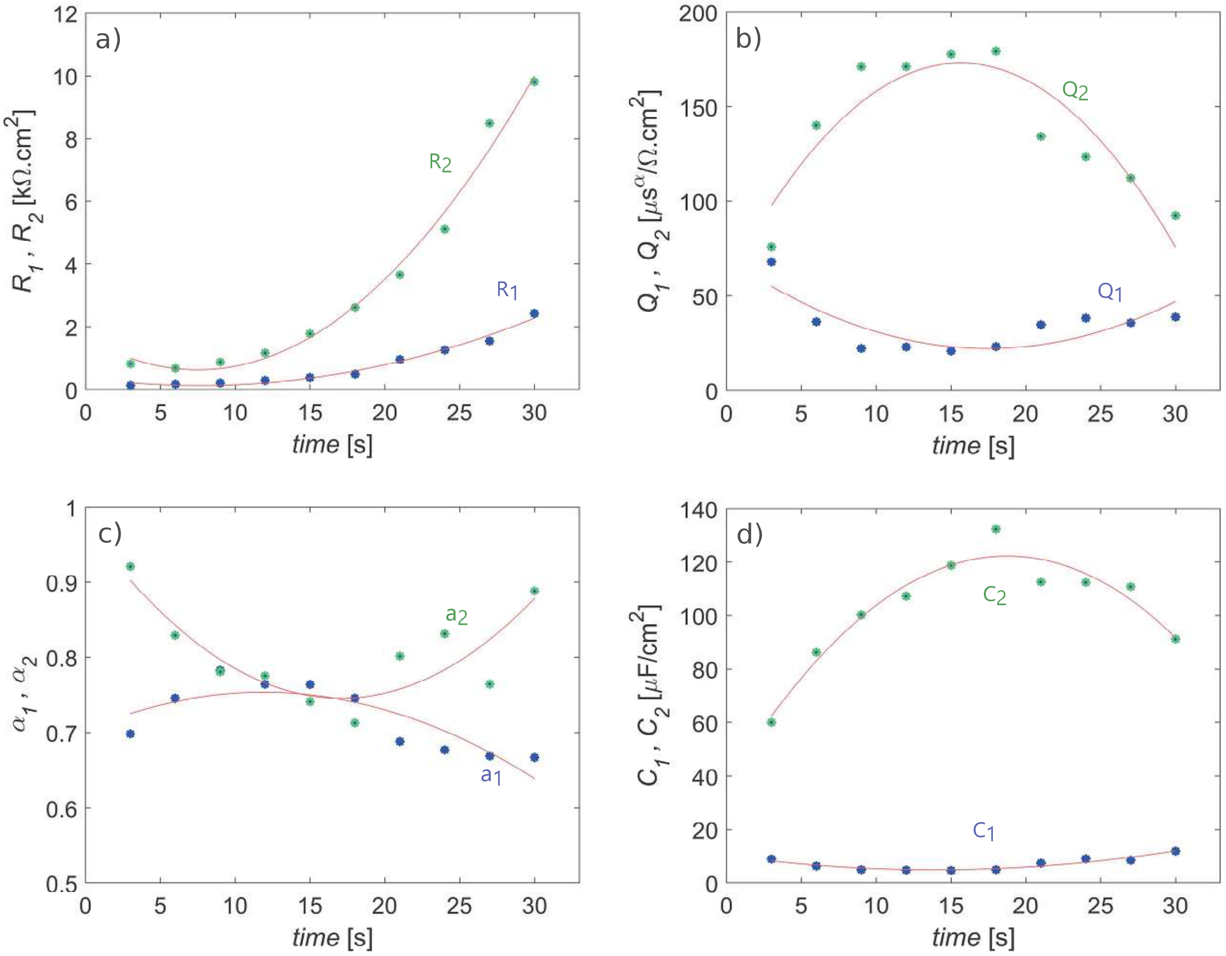

FIGURE 7.9: The values of $R_1 = R_{pore}$, $R_2 = R_{ct}$, $Q_1 = Q_l$, $Q_2 = Q_{dl}$, α_1, α_2 and effective capacitance $C_1 = C_l$ and $C_2 = C_{dl}$ (calculated via Equation 2.64) versus time, for the sample grafted at -0.2 V vs. Ag/AgCl.

$$C = \epsilon \frac{A}{d} \tag{7.2}$$

The electrical resistance of the layer, R, with the cross-sectional area, A and the length of the layer in the direction of current flow, l, and the electrical resistivity, ρ, is written as:

$$R = \rho \frac{l}{A} \tag{7.3}$$

When the current flow is perpendicular to the film's surface, l in the resistance formula (Eq. 7.3) can be considered the thickness of the film, d.

Changes in material properties (dielectric constant, ion permeability, etc.) will be reflected in changes in C and R. In our case, the coating layer is made of both grafts and physisorbed species on the surface.

As shown in Figure 7.9-a, the $R_{ct}(= R_2)$ increases over time initially slowly and then faster. The increase of R_{ct} indicates the electron transfer kinetics of redox couples at the surface become more difficult because more area of the bare electrode is being blocked by the formation of the non-conductive (or less conductive) layer of species (physisorbed and chemisorbed) on the surface. The coating pore resistance $R_{pore}(= R_1)$ shows the anti-penetrating ability of the layer to the electrolyte solution. So as the number of species on the surface becomes larger, the penetration of the electrolyte ions becomes more difficult.

One of the striking observations in Figure 7.9-d is that $C_{dl}(= C_2)$ increases in the first total 15 s of grafting, while $C_l(= C_1)$ decreases, and in the next 15 s they behave oppositely. If we assume that by further measuring the EIS more surface area of the electrode is being blocked by species, then C_{dl} needs to decrease especially in the first 15 s. Moreover, following the direct relationship between the covered area and C_l, during the first 15 s of the grafting, C_l should increase instead of decreasing.

If we assume that during grafting, the microscopic properties of the uncovered metal-electrolyte interface remain unchanged, we can introduce the parameter $\theta = \frac{A_l}{A}$ to account for the change in surface coverage, where A_l is the area covered by the layer and A is the total area of the electrode before coverage. A bare surface corresponds to $\theta = 0$, while a fully covered surface corresponds to $\theta = 1$. In Figure 7.10-a schematic of the surface with $0 < \theta < 1$ is shown. In Figure 7.10-b the equivalent circuit is shown where the electrical parameters have coefficients containing θ, which indicates their dependence on the θ value [237].

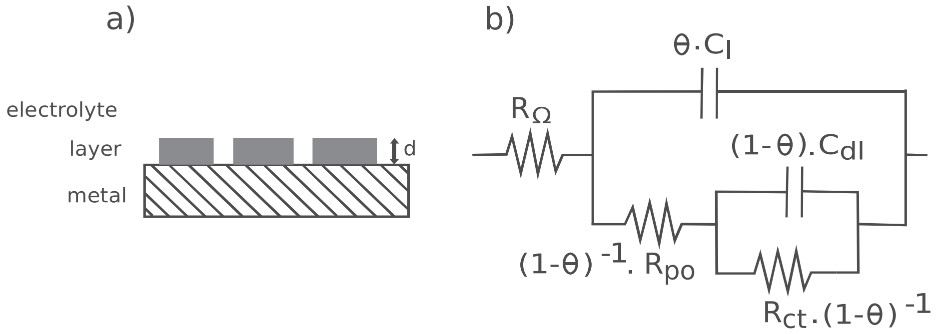

FIGURE 7.10: a) Schematic of metal surface covered by a layer of insulating material containing electrolyte-filled pores. d: the thickness of the layer. b) The equivalent circuit, where θ is the degree of coverage ($0 < \theta < 1$). Adapted from [237], Copyright (2001) with permission from Elsevier.

Using this simple model, we assume that during grafting, a portion of the surface becomes covered with a discontinuous layer composed of non-conductive or (electro)chemically inert material, which can block the electrochemical reaction, while the remaining surface remains exposed. We can consider the uncovered areas as pores in the insulating layer, where the electrochemical reaction can happen at the metal-electrolyte interface through these pores.

We also assume that a dielectric material covers part of the surface during the grafting process. In these covered areas, the combination of the metal electrode and dielectric layer functions as a capacitor. Thus, $C = \epsilon\frac{A\theta}{d}$, where ϵ is the permittivity of the dielectric. $A\theta$ is the electrode area covered by the layer with a thickness of d. We assumed that on the coated parts of the electrode, the layer adheres to the surface so strongly that there is no electrolyte between the layer and the metal electrode. Moreover, layer pore resistance ρ_{pore} is related to the resistance to ions reaching the electrode surface within the pores, $R_{pore} = \rho\frac{d}{A(1-\theta)}$.

We further assume that ϵ and ρ are constant values, which means that the electrolyte resistivity (ρ), is a constant value and does not change with time (meaning the concentration of electrolyte does not change inside the pores over time), and the dielectric constant of the film (ϵ) does not change over time. If $\epsilon\rho = constant$, we have $R_{pore} \times C_l = \rho\frac{d}{A(1-\theta)} \times \epsilon\frac{A\theta}{d} = \epsilon\rho\frac{\theta}{1-\theta} = constant$. Figure 7.11-a shows the change of the $R_{pore} \times C_l$ over time or better to say change of $\frac{\theta}{1-\theta}$ over time. Qualitatively, the evolution of $R_{pore} \times C_l$ obeys the expected change of $\frac{\theta}{1-\theta}$, assuming very small and slowly increasing values for degrees of coverage close to zero, and assuming a monotonously increasing slope for theta approaching unity.

To estimate a value of $\epsilon\rho$, we consider in the first instance that $\rho \approx 0.03$ Ωcm based on the electrical resistivity of a 0.1 M HCl solution at 4°C. ϵ_r for phenyl layers is around 2.3 [238]. Therefore, $\epsilon_r \approx 2$, yielding $\epsilon\rho = \epsilon_0\epsilon_r\rho = 8.85 \times 10^{-14}\ \mathrm{F\,cm^{-1}} \times 2 \times 0.03\ \Omega\mathrm{cm} \approx 5 \times 10^{-15}\ \mathrm{F\,\Omega}$. As can be seen in Figure 7.11-b with dark blue △ for the value $\epsilon\rho = 5 \times 10^{-15}\ \mathrm{F\,\Omega}$, this would lead to a value of θ close to unity already after the first grafting step, and is clearly not valid. In order to investigate valid options for the $\epsilon\rho$ value, we plotted the θ as a function of time by assuming different values of the $\epsilon\rho$. Treating $\epsilon\rho$ instead as a parameter that we allow to vary, Fig. 7.11-b shows different profiles as a function of time that are more realistic, and that in particular show a sigmoidal approach to unit coverage. The lower values of the product may have their origin in the non-uniform structure and composition of the surface film, and pores in which the composition of the electrolyte is quite different from the bulk. Based on these calculations, the assumption that ϵ and ρ are constant values is incorrect. The lower values of the product may have their origin in the non-uniform structure and composition of the surface film (e.g., including pockets of water), and pores in which the composition of the electrolyte is quite different from the bulk. The latter is unsurprising as the electrochemical double layer itself is of the same order of thickness and can vary widely in structure and composition, depending on microscopic details [239]. Hence, the concentration of the ions in the pores is not constant over time, and/or the ϵ is not a constant value throughout the experiments.

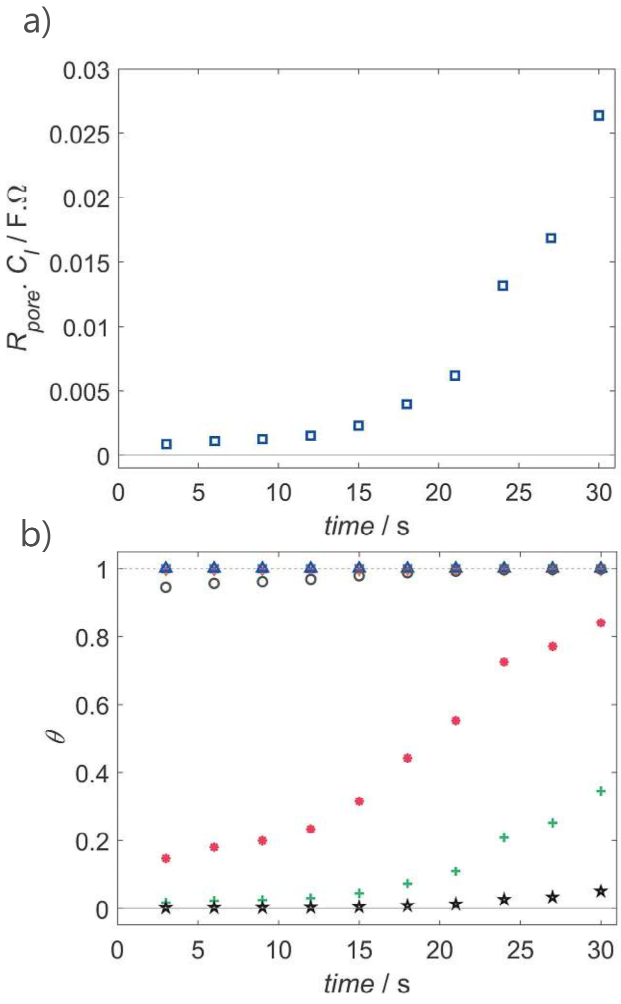

FIGURE 7.11: Plots of a) Product of pore resistance and the layer capacitance ($R_{pore} \times C_l$) as a function of time, and b) Estimated surface coverage θ as a function of time for varying $\epsilon\rho$ values: 5×10^{-15} (dark blue $\triangle$), 5×10^{-13} (yellow $+$), 5×10^{-12} (orange $\diamond$), 5×10^{-10} (purple $\times$), 5×10^{-8} (blue $\Box$), 5×10^{-5} (grey $\circ$), 5×10^{-3} (red $\bullet$), 5×10^{-2} (green $+$), and 5×10^{-1} (black $\star$) in F Ω.

It is also important to acknowledge that the model we employed assumes a metal surface with insulating coatings containing pores. However, the voltammetry data (Chapter 4) suggests the grafted molecules cannot completely block electron tunneling. Therefore, electron tunneling might also occur in areas outside of those pores, questioning the model's assumption of complete insulation by the grafted molecules in those regions.

We assume that during the grafting procedure, more than just the formation of covalent bonds (grafting) occurs on the surface, and other species are formed as by-products that can be physisorbed onto the surface. Thus, the equivalent circuit should have additional C and R parameters. Figure 7.12-a, b shows a model that can be used for a system containing two surface layers, L_1 and L_2. This model was introduced for metal surfaces with two partially insulating layers, in which only an extreme degree of adhesion between the metal surface is considered (perfectly adhering and non-adhering) [240]. Thus, we assumed that the first layer adheres strongly to the metal surface (grafts) and the second layer is made of physisorbed species (physisorbed layer) forming a non-adhering layer, meaning the electrolyte is present between L_2 and the metal surface.

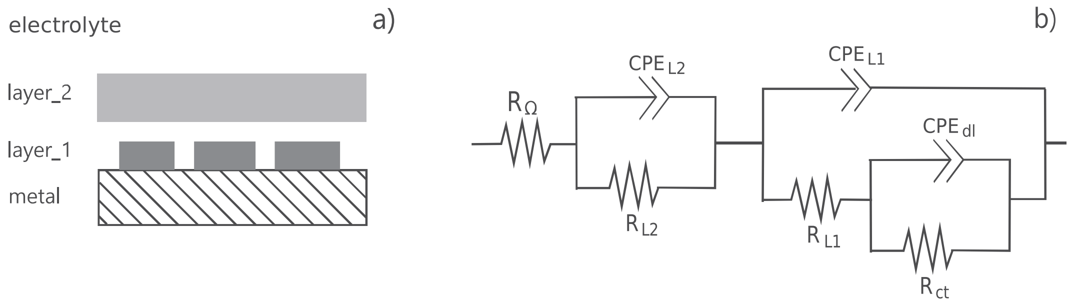

FIGURE 7.12: a) Schematic of metal surface covered by a layer of insulating material containing electrolyte-filled pores (L_1) and extra layer due to physisorption of the species (L_2). b) Equivalent circuit with three time constants.

Figure 7.13 shows the Nyquist and Bode plots of experimental data (red circle), fitting an equivalent circuit with two time constants (black line and markers), and simulated data with three time constants (blue line) introduced in 7.12-b. The data corresponds to the first EIS measurement (after the initial 3 s of grafting at -0.2 V). As explained in previous sections, because the frequency range used in these experiments was short, we could not certainly say whether we have two or three time constants. As in Figure 7.13-a,b, there is good agreement at lower frequencies between the experiment, the fit, and the simulation. For the first EIS measurement, the small tail at the lowest frequency is visible but for the rest of the sequence, the tail is not clearly visible. We used the fitting tool to fit the equivalent circuit with three time constants for fitting to experimental data. Here we used an option in EC-Lab (BioLogic potentiostat) software to sequentially fit the impedance data from EIS steps (cycles). The fitting tool can automatically fit the data for each cycle without any action by the user.

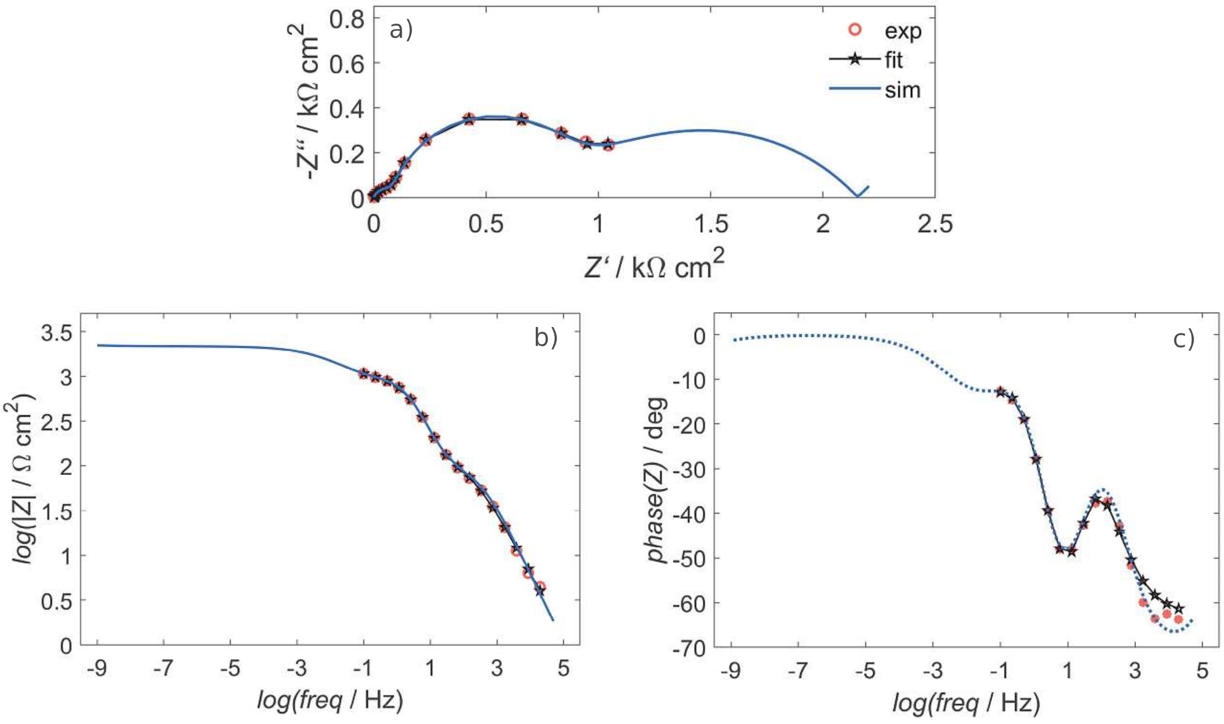

FIGURE 7.13: Electrochemical impedance spectroscopy data: a) Nyquist plot, b) Bode magnitude plot, and c) Bode phase angle plot. Experimental data (red markers) are compared with a two time constants equivalent circuit fit (black -⋆-) and a three time constants equivalent circuit simulation (blue line).

The extracted values from the fitting process are collected in Figure 7.14. The last data point (at 30 s) was removed because the margin of error was too large, making the data unreliable.

To interpret the data we have assumed again that the only parameter that can change during the measurements is the coverage of the species and other parameters like the ρ and ϵ do not change. Based on Figure 7.14-a, the R_{L2}, R_{L1}, and R_{ct} show an increasing trend over time. The increase in R_{L2} means the surface is becoming more covered by the physisorbed species. The R_{L1} is the pore resistance in the first layer of the coating adhering strongly to the surface or the layer made of grafts. The increase in the R_{L1} means the anti-penetration ability of this layer against the electrolyte solution is

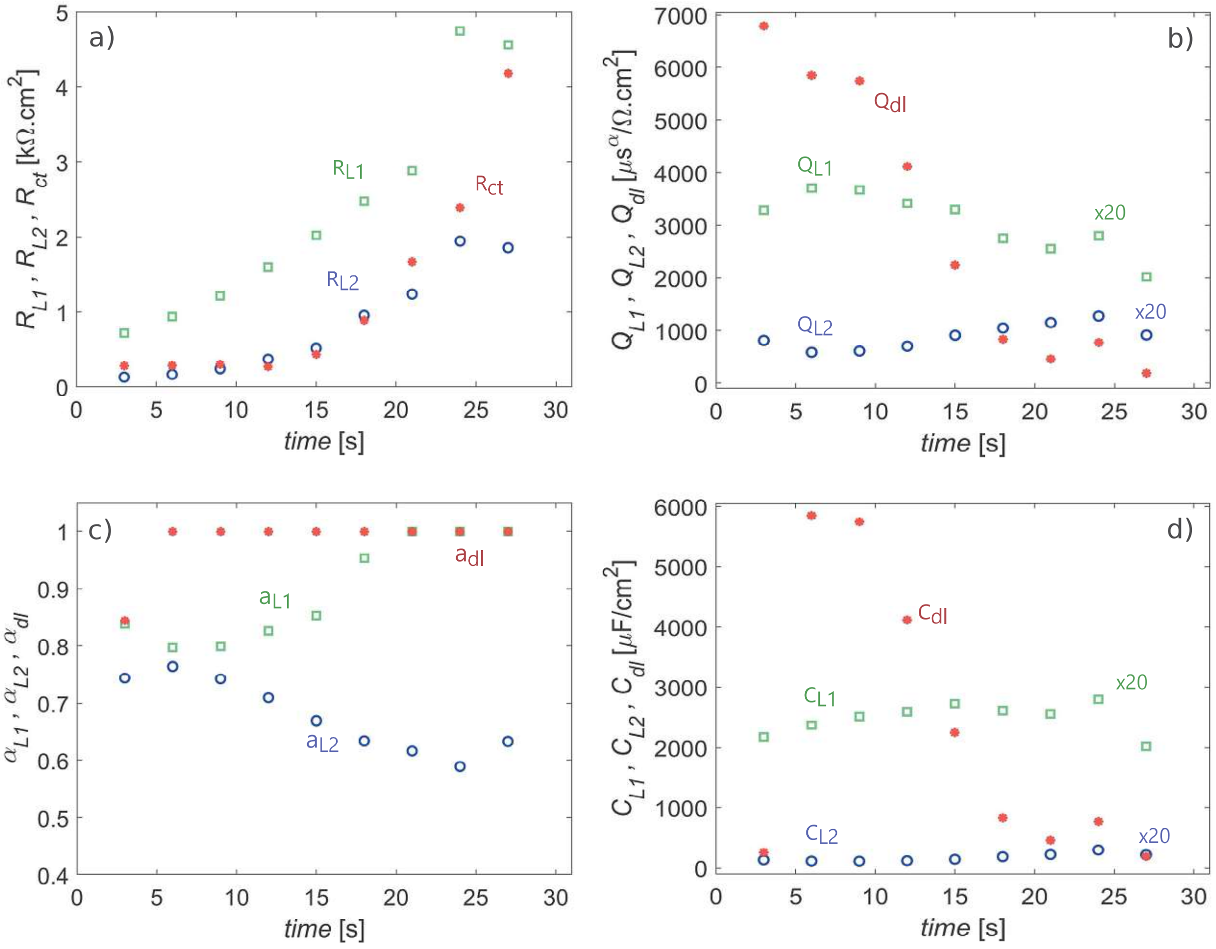

FIGURE 7.14: The values of R_{L2}, R_{L1}, R_{ct}, Q_{L2}, Q_{L1}, Q_{dl}, α_1, α_2, and α_3 and effective capacitance C_{L2}, C_{L1} and, C_{dl} were calculated via Equation 2.64 versus time. The sample grafted at -0.2 V vs. Ag/AgCl.

increasing over time, or, in other words, the surface is gradually being covered by the grafts. The trend that R_{ct} follows is very similar to that of the R_{ct} in 7.9-a. It slightly decreases and then noticeably rises again. This increase indicates that the electron transfer kinetics of $[Fe(CN)_6]^{4-/3-}$ at the surface become more difficult because more area of the bare electrode is gradually getting covered.

The change of the Q_{L2}, Q_{L1}, and Q_{dl} and their corresponding α values over time, can be seen in Figure 7.9-b,c. The insets in Figure 7.9-b,d show the change of the Q and C values of layers 1 and 2 more clearly. Figure 7.9-d shows effective capacitances C_{L2}, C_{L1} and, C_{dl} over time. The C_{L1} and C_{L2} show opposite behaviors from the beginning until the half way through the whole measurement, while the C_{L1} is increasing over time, the C_{L2} is decreasing over time, and then it seems that the C_{L2} is increasing over time, the C_{L1} is decreasing over time, Figure 7.9-d, inset. The increase of C_{L1} in the first 15 s of the measurements may mean that the number of grafts on the surface increases over time. However, for the C_{L2} the changes are not as obvious, and it seems relatively constant. This may mean that the number of the physisorbed species is more or less constant throughout the experiment, meaning the overall number of the physisorbed species adsorbing and leaving the surface is constant. For the C_{dl} except the first value after the first 3 s grafting, the rest of the data shows the decrease of the C_{dl}. The decrease of C_{dl} means that because of the grafting process, there is less active surface area of the gold electrode available for the ions to form a double layer. Although the decrease of the C_{dl} over time can be expected, the values of the C_{dl} in Figure 7.9-d are unrealistically high, suggesting the inability of this model to fully explain the data.

7.2.3 Spontaneous grafting

Even without applying an external potential that reduces the 3,5-TBD, this substance decomposes spontaneously with a certain rate and produces aryl radicals that can graft onto the gold surface. In this section, we aim to quantify this process, using the same measurement sequence shown in Figure 7.3, but leaving out the electrochemical activation step.

To study the grafting procedure at OCP over time, we repeated the experiment in Figure 7.8 and, instead of a grafting potential of -0.2 V we used the OCP. The surface potential was held at OCP for 3 s. We used the same settings except the grafting potential to have a proper comparison, however, the number of sequences measured for spontaneous grafting was increased to monitor the surface for a longer time. The impedance data are presented in Nyquist and Bode plots in Figure 7.15. The parameters were extracted via the equivalent circuit in Figure 7.16.

The shape of the R_1 and R_2 and also the C_1 and C_2 is very similar to those parameters corresponding to grafting at -200 mV, Fig. 7.9.

Apart from changing the rate with which radicals are formed close to the electrode surface, also the possibility of fundamentally different mechanisms for spontaneous and electrochemical grafting have been considered. There is a proposed mechanism for grafting of p-nitrobenzenediazonium (pNBD) onto the gold surface [241]. In this

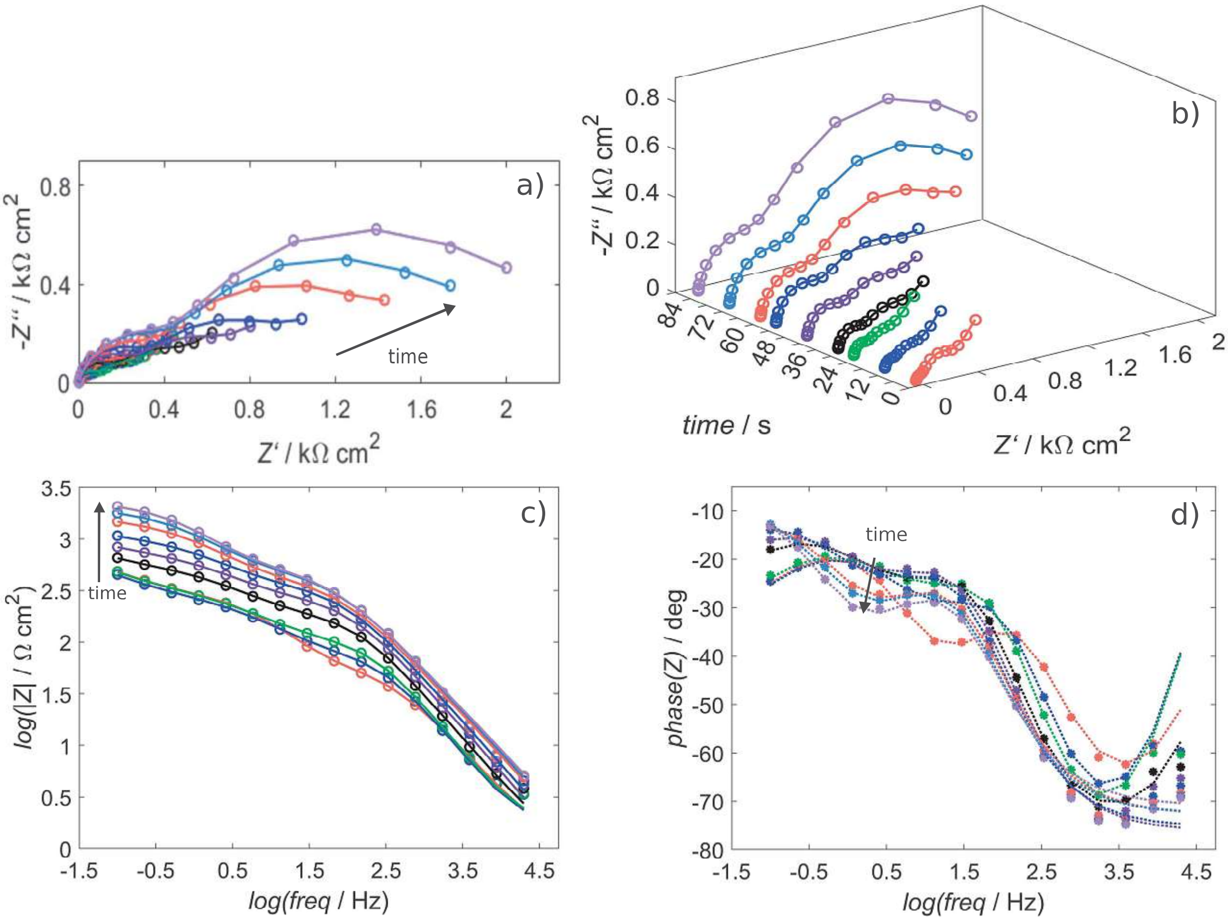

FIGURE 7.15: a) Nyquist plot, b) Nyquist plot vs. time c) Bode magnitude plot, and d) Bode phase angle plot, for grafting the Au(poly) after each step of diazonium reduction at OCP for a duration of 3 s repeated 30 times. The EIS performed in 1 mM 3,5-TBA + 0.1 M HCl + 1.2 mM $NaNO_2$ in the presence of 1 mM $[Fe(CN)_6]^{4-}$ and 1 mM $[Fe(CN)_6]^{3-}$. The experimental data are shown with markers (circle and asterisk) and the fit with line (dotted and full). Only some of the measured EIS steps are shown here.

hypothesized mechanism the first step is adsorption of the aryl diazonium cations on the gold surface. The adsorption is a charge mediated reversible process in which the attached molecule accepts electrons from the surface. In the second step the nitrogen is eliminated and a covalent bond forms between the molecule and the surface. The summary of the mechanisms of covalent grafting for pNBD (M) is shown in Figure 7.17.

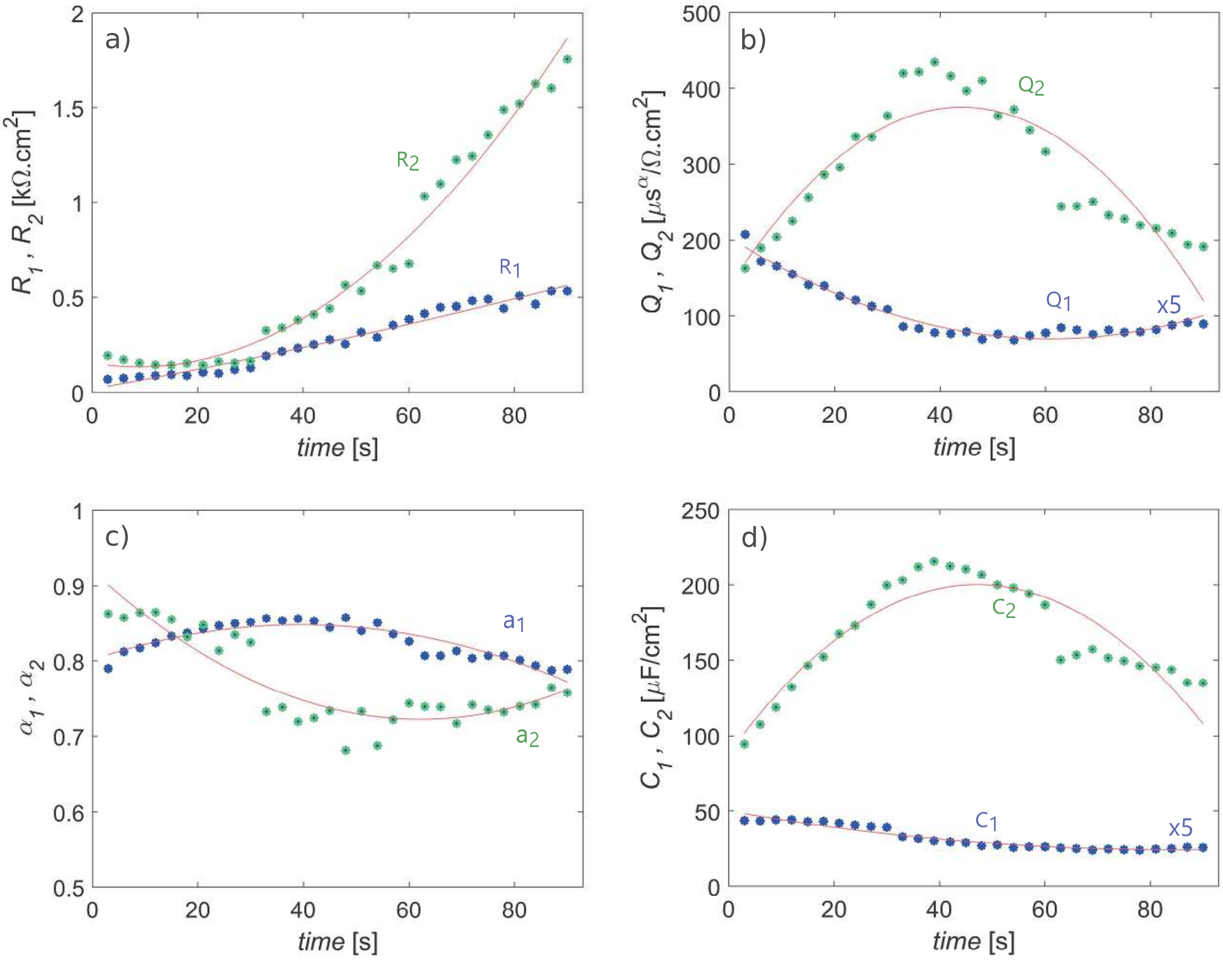

FIGURE 7.16: The values of $R_1 = R_{po}$, $R_2 = R_{ct}$, $Q_1 = Q_l$, $Q_2 = Q_{dl}$, α_1, α_2 and effective capacitance $C_1 = C_l$ and $C_2 = C_{dl}$ (calculated via Equation 2.64) versus time, for the sample grafted at OCP.

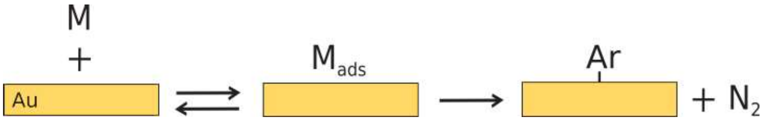

FIGURE 7.17: Summary of the mechanisms of covalent grafting for pNBD (M) on Au surface. Adapted from [241]. Copyright (2011) with permission from American Chemical Society.

The adsorption of the diazonium cations as the first step of the spontaneous grafting onto the carbon surface has been proposed [242–246]. The mechanism of spontaneous grafting onto the gold surfaces is not fully understood yet; however, in a later paper published by Jean Pinson and his colleagues, the possibility of the grafting through aryl carbocations was studied [247]. Their DFT calculations showed that spontaneous grafting through a carbocation is more favorable than through a radical, and their experiments showed that the carbocations obtained by heterolytic dediazoniation can also react with and graft onto gold surfaces, depending on the medium. For electrolytes with pH=1, grafting of carbocations onto gold is more favorable [247].

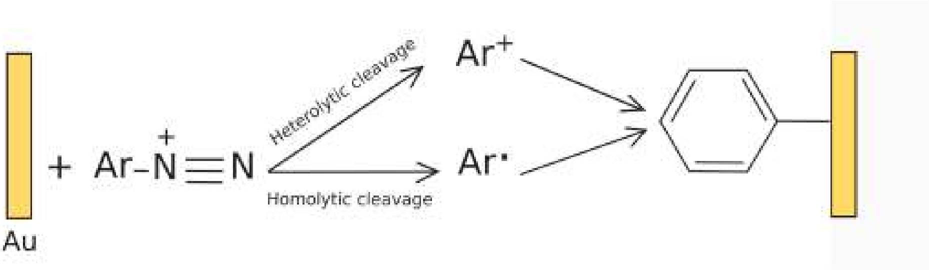

FIGURE 7.18: Possible mechanism of spontaneous grafting of the surface by an aryl carbocation or an aryl radical. Adapted from [247]. Copyright (2017) with permission from American Chemical Society.

If we assume that the grafting process is happening through this mechanism, we need an equivalent circuit with two time constants, as shown in Figure 7.19. The difference between this equivalent circuit and the equivalent circuit in Figure 7.7 is the position of the CPE_{dl} and the R_{ct} relative to other R and CPE elements. Thus, in Figure 7.16 the $C_1 = C_{dl}$ and $C_2 = C_{ad}$ and $R_1 = R_{ct}$ and $R_2 = R_{ad}$. Consequently, the interpretation of the data in Figure 7.16 would be completely different. The increase of R_{ad} means that the adsorption of the species or intermediates becomes more difficult. The figure shows in the first half of the measurement the C_{dl} decreases over time, while the more carbocations are adsorbed on the surface blocking more active area of the surface. As a result C_{ad} is also increased.

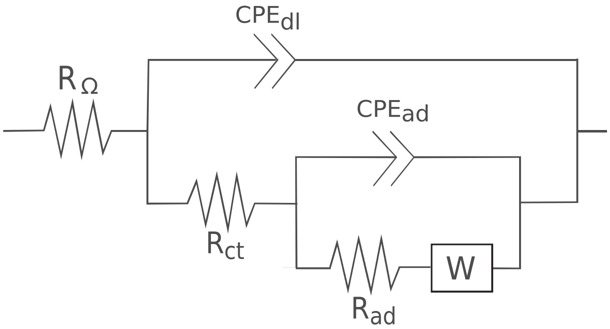

FIGURE 7.19: Equivalent circuit used for fitting the EIS response considering adsorption of the species or intermediates.

Based on Figure 7.16, we observe a change in behavior at 40 s. One possible explanation is the formation of covalent bonds via those carbocations adsorbed on the surface, and therefore, a change in their identity can be reflected in the capacitance value.

It is important to note that the nucleation, growth, and departure of bubbles on the surface may affect the EIS results [248]. The reduction of diazonium molecule is accompanied by release of N_2. During the electrografting, bubbles have been seen on the electrode surface. Although, to avoid the accumulation of these bubbles, our electrode was positioned at an angle to avoid trapping, it could not be avoided completely. As the diazonium reduction starts, the concentration of N_2 molecules increases near the surface and reaches the supersaturation level where bubbles start to nucleate. We expect that the concentration of the nitrogen molecules would be higher than the number of grafts on the surface, because not every radical bonds to the surface. After the accumulation of nitrogen at the surface, the bubbles attached to the surface can combine together to form bigger bubbles, known as bubble coalescence. The bubbles attached to the surface can block a part of the electrode surface area. Therefore, attachment and detachment of the bubbles on the surface can highly affect the measured data.

The wetting characteristics of the surface affect the adhesion and dynamics of a bubble on the surface [249]. While the bubbles tend to adhere and spread over hydrophobic surfaces, they can easily detach and slide from hydrophilic surfaces. Based on the hydrophobicity of the grafts on the surface, we can suggest that the bubbles tend to attach to areas where the concentration of the grafts is higher.

Not only the wetting characteristics of the bubble but also the orientation and inclination of the surface can affect the bubble adhesion and dynamics (i.e., sliding). In a study on an inclined hydrophobic surface in water, the air bubble movement was compared on the upward- and downward-facing sides of the surface [250]. Their results showed that for the same given volume of the bubble, on the downward-facing surface, the bubble spreads over a larger area compared to the upward-facing surface, which is explained by the greater hydrostatic pressure imposed on the bubble on the downward-facing surface. Consequently, the bubble's lateral adhesion force is greater, and therefore, a larger inclination angle is needed for sliding a bubble on a downward-facing surface.

The dramatic change in the EIS data at 15 s for the surface grafted at -0.2 V, and at 40 s grafted at OCP might be related to the point where bubbles are big enough to depart from the surface and leave an area of the electrode free.

To gain a deeper understanding of what is happening on the surface, further experiments are required. However, conducting these experiments was not possible within the timeframe of this thesis and will be suggested in more detail in the following section.

7.3 Summary and outlook

In the first section of this chapter, the impedance measurements on bare (poly)Au in $\mathrm{Fe(CN)_6}^{3-/4-}$ + 0.1 M Na_2SO_4 were performed at OCP ($E = 0.196$ V vs. Ag/AgCl). The calculated value of the diffusion coefficient and the standard electron transfer rate constant from this measurement agreed with the values reported in the literature.

In the second section of the chapter, EIS was used for *operando* monitoring of the electrochemical grafting process in a grafting solution containing $\mathrm{Fe(CN)_6}^{3-/4-}$. The experiment was conducted using short grafting sequences (CA at -200 mV vs, Ag/AgCl for 3 s) and after each grafting step, the EIS was measured at the formal potential of the hexacyanoferrate ions, and this process was repeated to study the surface over time. The measured impedance data were fitted to the nested model with two time constants to model a metal surface covered by a defective insulating coating, through whose defects (pores) the electrolyte can reach the metal surface. Besides, the equivalent circuit model with two time constants, an equivalent circuit with three time constants was used.

Although the model with two time constants provided the best fit for our system, it could not explain the change in surface coverage over time. Our further investigations showed that the assumption that the concentration of the ions in the pores is constant over time and/or the ϵ is a constant value during the experiments was not correct.

In addition, to investigate the potential's effect, the sequences from the second section were replicated, this time using a CA at the OCP instead of -200 mV. The measured data were fitted to the same equivalent circuit with two time constants. The change of the R and C values over time was similar to those EIS data after applying -200 mV.

Although the equivalent circuit used in this work provided the best fit for our system, we cannot neglect the limited number of experimental points. This limitation was due to the need to maintain our system time-invariant during the EIS measurement. It was more serious at low-frequency regions, where the error margin was too high to rely on fit data to extract the R and C parameters at this region. For the later EIS sequences measured, the issue of not having enough data points makes the fitting process more problematic, so we cannot confidently say whether the fitted data are reliable to work with.

Another point that should be considered is that we used the model that is used for a metal surface covered by a defective insulating coating, however, our result in Chapter 4 revealed the possibility that grafting molecules do not completely block electron tunneling, allowing some electron tunneling across them.

Aside from the inherent challenges, certain considerations need to be addressed in future studies when using EIS as an *operando* technique to investigate the grafting process. First, the reduction of every diazonium molecule is accompanied by release of N_2. Therefore, in performing a set of experiments, positioning the working electrode upwards and saturating the solution with N_2 gas should be considered.

Further experiments are required to improve our understanding of the grafting process and to track surface changes over time. Ideally, these experiments would combine EIS with complementary *in situ* techniques, such as spectroscopy (e.g., sum frequency generation spectroscopy) or quartz crystal microbalance with dissipation monitoring.

Chapter 8

Dynamics of polyiodide chains in Au(111)/I adlayers

Adlayers of halides on metal surfaces are among the most extensively studied systems using EC-STM [74]. This chapter investigates the surface structure of iodine on Au(111) under varying surface potentials using the EC-STM technique. The focus is on the dynamics of bright chains or strings, previously identified as iodide oligomers/polymers, or polyiodides [78]. Despite earlier studies, more detailed information about these chains is needed because they are observed at potentials different from those previously reported, and the resolution of modern STM far surpasses that of three decades ago. Here, we explore Au(111) in an electrolyte containing 5 mM H_2SO_4 and 1 mM KI at different potentials, aiming to elucidate the possible identity of these chains.

8.1 Introduction

Iodine adsorption on Au(111) has been studied intensively with different surface techniques. Determination of iodine structure by STM under various conditions such as UHV, air, organic solvent, and electrolyte has been ongoing since the early 1990s [72, 77–80, 80–85]. The strong adsorption of iodine to the surface of metal electrodes such as platinum and gold, together with the dependence of the iodine coverage on the electrode potential, has made such a system an interesting topic for *in situ* scanning microscopy or EC-STM [64, 67, 69, 72, 79, 90]. The detailed *in situ* STM study of the iodine adlayer on Au(111) in 0.5 mM KI + 0.1 M $HClO_4$ solution at different surface potentials was performed by Gao and Weaver. They reported different iodine adlayer structures in the potential range between -0.3 to 0.4 V vs. SCE below the electrooxidation potential of the iodide solution [78].

At potentials between -0.6 and -0.3 V, the iodide adlayer is distorted and mobile; therefore, it cannot be imaged and only STM images of the underlying substrate (i.e. Au) can be achieved. At -0.3 V vs. SCE, iodides are chemisorbed on the surface, forming essentially uncharged iodine adatoms [76]. At this potential, an ordered hexagonal $(\sqrt{3} \times \sqrt{3})R30°$ structure relative to Au(111) substrate with a coverage of 0.33 was observed [89, 90], as shown in Figure 8.1-a. In general, this phase is the starting point for a centered-rectangular phase denoted as $c(p \times \sqrt{3}R - 30°)$ with coverages ranging from 36.6% to 40.9% [89, 91]. At -0.3 V, the p value is equal to 3 ($p = 3$), hence $c(p \times \sqrt{3}R - 30°) \equiv (\sqrt{3} \times \sqrt{3})R30°$ while at more positive potentials, the p value decreases to 2.49 [89]. Figure 8.1-b shows the structure of $c(2.6 \times \sqrt{3}R - 30°)$. At 0.1 V vs. SCE, $(5 \times \sqrt{3})$ adlayer with the coverage of around 0.4 was observed [78], although it has not been reported in a similar STM measurement [79].

Above +0.2 V the distance between the I adatoms decreases to 4.35 ±0.1 Å and the coverage reaches the value of 0.44. This phase is a rotated-hexagonal and has long-range z corrugation (moiré pattern). The moiré originates from the non-commensurate structure of the iodine adlayer to underlying gold. A superstructure of $(7 \times 7)R21.8°$ is assigned to this phase [78]. The *in situ* STM or EC-STM image of the iodine adlayer with the moiré structure can be found in Figure 8.1-c.

In the two phases, the centered-rectangular and rotated-hexagonal, the iodine adlayer structures compress as the potential increases, a phenomenon known as electrocompression. Above 0.3 V the polyiodide chains are observed (Fig. 8.2). The formation of multilayers of iodine starts above a 0.4 V potential [78].

Figure 8.2 shows the early electroanalytical experiments on the electrooxidation of the iodide at Au. The study of the electrooxidation of iodide by Gao and Weaver was not limited to the EC-STM technique. They studied the oxidation of iodide (1 mM NaI + 0.1 M $HClO_4$) at Au by combining rotating disk voltammetry with Surface-enhanced Raman spectroscopy (SERS) [87]. They showed that during the

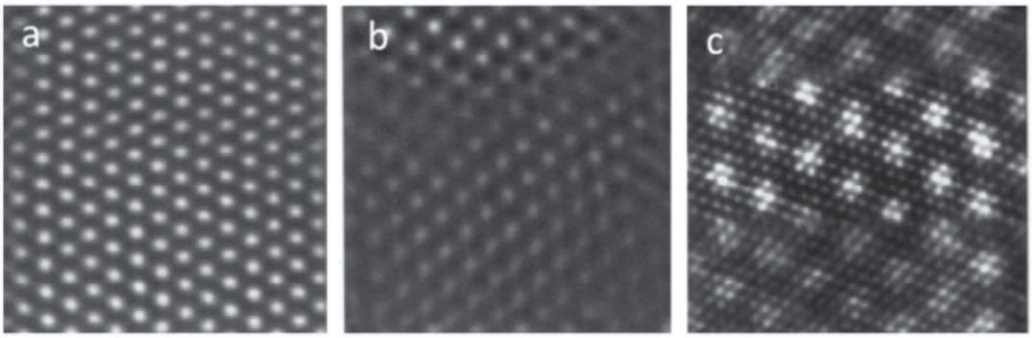

FIGURE 8.1: *In situ* STM images of Au(111) in 1 mM KI at a) -0.28 V vs. SCE with the structure of $(\sqrt{3} \times \sqrt{3})R30°$, and b) -0.01 V with the structure of $c(2.6 \times \sqrt{3}R - 30°)$ with tunneling current of 2 and 3 nA and scan size of $5\,\mathrm{nm} \times 5\,\mathrm{nm}$, c) at 0.33 V with rotated hexagonal or the moiré structure imaged at 28.5 nA with the size of $10\,\mathrm{nm} \times 10\,\mathrm{nm}$. Reprinted with permission [89]. Copyright (1995) American Chemical Society.

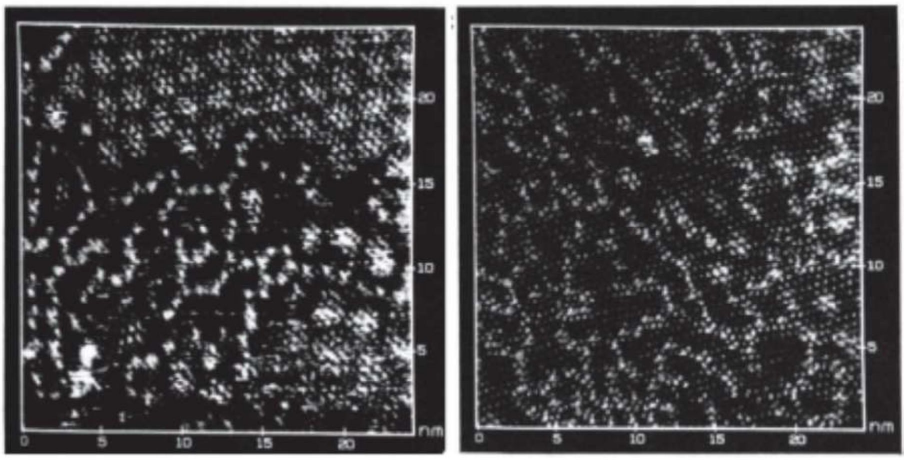

FIGURE 8.2: *In situ* STM images of the polyiodide chains measured at 0.3 to 0.4 V vs. SCE with $V_{bias} = -200$ mV and $I_t = 10$ nA with tungsten tip in 0.1 M $HClO_4$ + 0.5 mM KI. Reprinted with permission [78]. Copyright (1992) American Chemical Society.

electrooxidation process, both triiodide (I_3^-) and molecular iodine (I_2) are formed [87]. In the following reactions 'ads' refers to an adsorbed species:

$$2\,I^- + I^-\,(ads) - 2\,e^- \longrightarrow I_3^-\,(ads) \tag{8.1}$$

$$2\,I^- + I_3^-\,(ads) - 2\,e^- \longrightarrow I_5^-\,(ads) \tag{8.2}$$

and /or

$$2\,I^- + I^-\,(ads) - 2\,e^- \longrightarrow I_2 \ldots I^-\,(ads) \tag{8.3}$$

followed by

$$I_5{}^- \text{ (ads)} \longrightarrow I_2 + I_3{}^- \text{ (ads)} \tag{8.4}$$

and or

$$I_2 \ldots I^- \text{ (ads)} \longrightarrow I_2 + I^- \text{ (ads)} \tag{8.5}$$

The $I_3{}^-$ or I^- and I_2 are considered the 'building blocks' of polyiodides. The possible combinations that can be made from the building blocks [88] are

$$mI_2 + nI^- \longrightarrow I\ {}_{2m+n}{}^{n-} \quad (m \text{ and } n \text{ integers}{>}0,\ \ n{=}1\text{-}4) \tag{8.6}$$

$I_3{}^-$ is the only isolated polyiodide in solution with an almost linear structure while other species need H^+ ions for stabilization [251].

8.2 Results and discussion

A cyclic voltammogram of Au(111) in oxygen free 5 mM H_2SO_4 + 1 mM KI is shown in Figure 8.3. The shape of the CV is in good agreement with a CV measured in 0.1 M $NaClO_4$ + 5 mM NaI reported in the literature [90]. The CV measurements were conducted using a hanging meniscus setup with an Ag/AgCl reference electrode. However, since the literature data discussed here was reported using an SCE reference electrode and a Pt wire in the EC-STM cell as a quasi-reference electrode, the potentials are presented relative to both SCE and Pt wire for consistency.

The surface structure of iodine was investigated by EC-STM on an Au(111) in 5 mM H_2SO_4 + 1 mM KI, in air. The scanning of the surface was started at the OCP, shown by the STM device. The OCP of the sample immediately after connecting the cell was -0.15 V vs. Pt wire (+0.168 V vs. SCE). A W tip was used to image the adlayer at different potentials. Figure 8.4-a shows the EC-STM images of the iodine on gold at -0.3 V vs. Pt wire with $(5 \times \sqrt{3})$ structure and Figure 8.4-b shows the EC-STM images of the moiré pattern at -0.067 V vs. Pt wire. The insets in the figures show the FFT of the corresponding EC-STM images, showing the surface periodicity. The distances in the slow scan direction are smaller, which is probably due to thermal drift.

While imaging the surface at -0.3 V vs. Pt wire, chains of molecules are observed on the surface alongside the ordered iodide adlayer (Fig. 8.5). The appearance of these

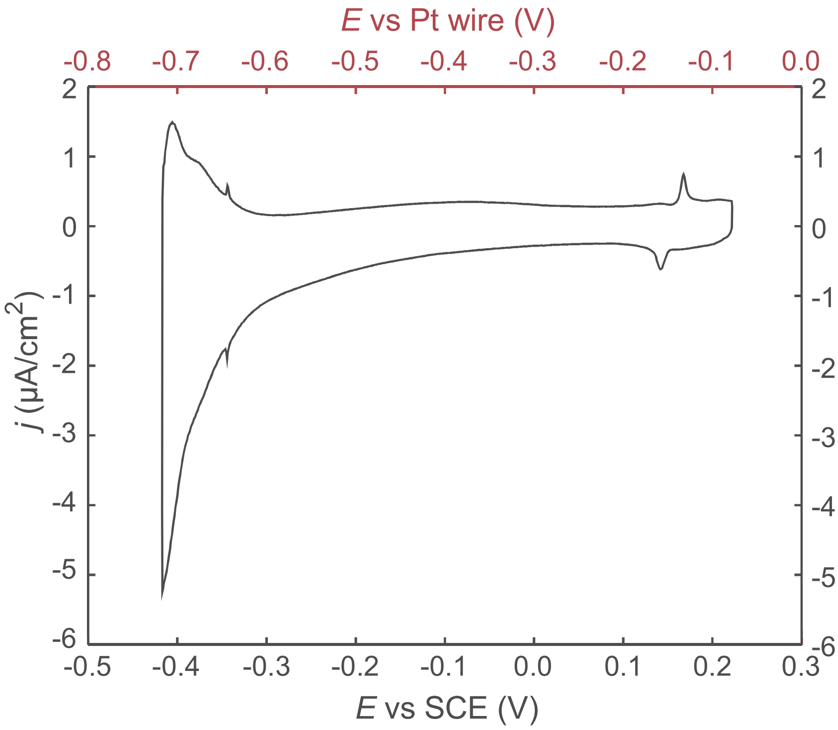

FIGURE 8.3: CV of Au(111) in oxygen free 5 mM H_2SO_4 + 1 mM KI. Potentials are presented vs. SCE and Pt wire ($E_{vs.\,SCE} = E_{vs.\,Pt} + 0.318\,V$). Scan rate: 10 mV/s.

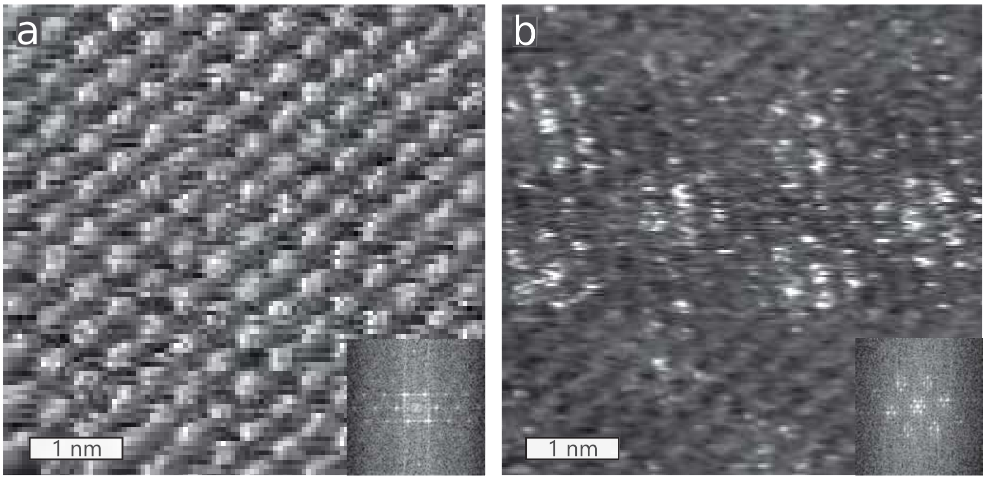

FIGURE 8.4: EC-STM images of Au(111) in 5 mM H_2SO_4 + 1 mM KI with a W tip at -0.42 V and scan size of 5 nm × 5 nm at sample potentials: a) -0.3 V vs. Pt wire with structure of $(5 \times \sqrt{3})$, V_{bias} = 120 mV, I_t = 4.3 nA, b) -0.067 V vs. Pt wire, V_{bias} = 0.34 V, I_t = 3.9 nA with a moiré pattern.scan size of 6.5 nm × 6.5 nm. Insets show the FFT of the images.

chains resembles the polyiodide chains reported in the literature [78] shown in Figure 8.2. The max positive potential applied to the sample before imaging them was equal to -0.15 V vs. Pt wire (OCP). So it seems that these chains were formed on the surface even without applying any potential to the surface.

Our images reveal that changing the potential from -0.15 V vs. Pt wire to a more negative potential of -0.3 V does not lead to the reduction of them or desorption of them from the surface. Although they seem to be kinetically trapped on the surface, interestingly, these chains are not completely static on the surface, some of them change to some degree over time. The change in the chains' arrangement over time has been shown in Figure 8.6, in which the same area of the sample was imaged after every 151 s without changing any scanning parameters. A dramatic change of the surface after 151 s can be found in the Appendix (Chapter A, Fig. 5).

It is important to point out that due to limitations of the conventional EC-STM, the observation of highly dynamic processes such as the adsorption/desorption and diffusion of the species on the surface at room temperature is not possible, because those processes are happening faster than the scanning rate of STM [252]. However, our EC-STM images revealed that chain rearrangement occurs more frequently in regions where the chains are less confined by neighboring chains, allowing greater freedom for reorganization. For example, in the upper part of Figure 8.6, where fewer chains are present and fewer closed loops or confined areas are formed, chains with free ends exhibit greater flexibility to rearrange and change over time.

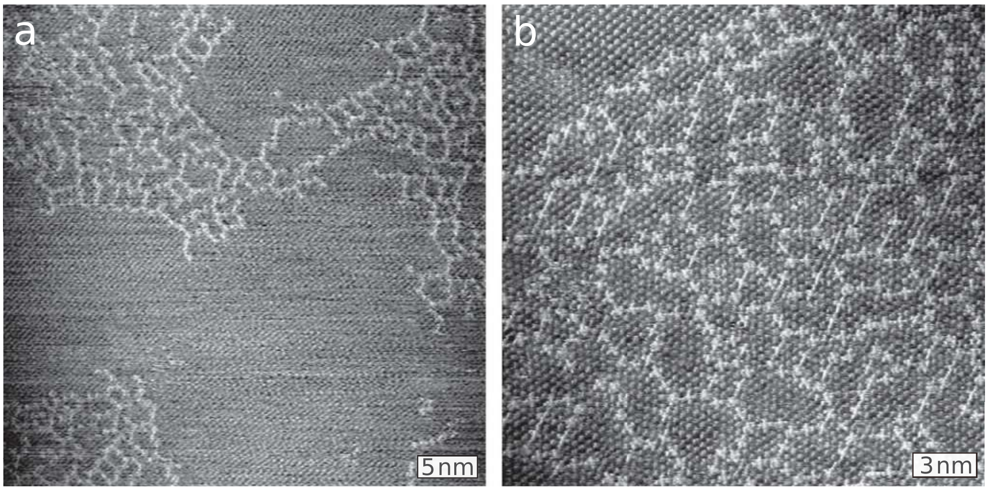

FIGURE 8.5: EC-STM images of Au(111) in 5 mM H_2SO_4 + 1 mM KI showing presence of chains on the surface. $V_{sample} = -0.3$ V vs. Pt wire, $V_{tip} = -0.42$ V, $I_t = 4.30$ nA, $V_{bias} = 120$ mV, $I_t = 4.3$ nA, with scan size of a) 39.5 nm × 39.5 nm and b) 22 nm × 22 nm.

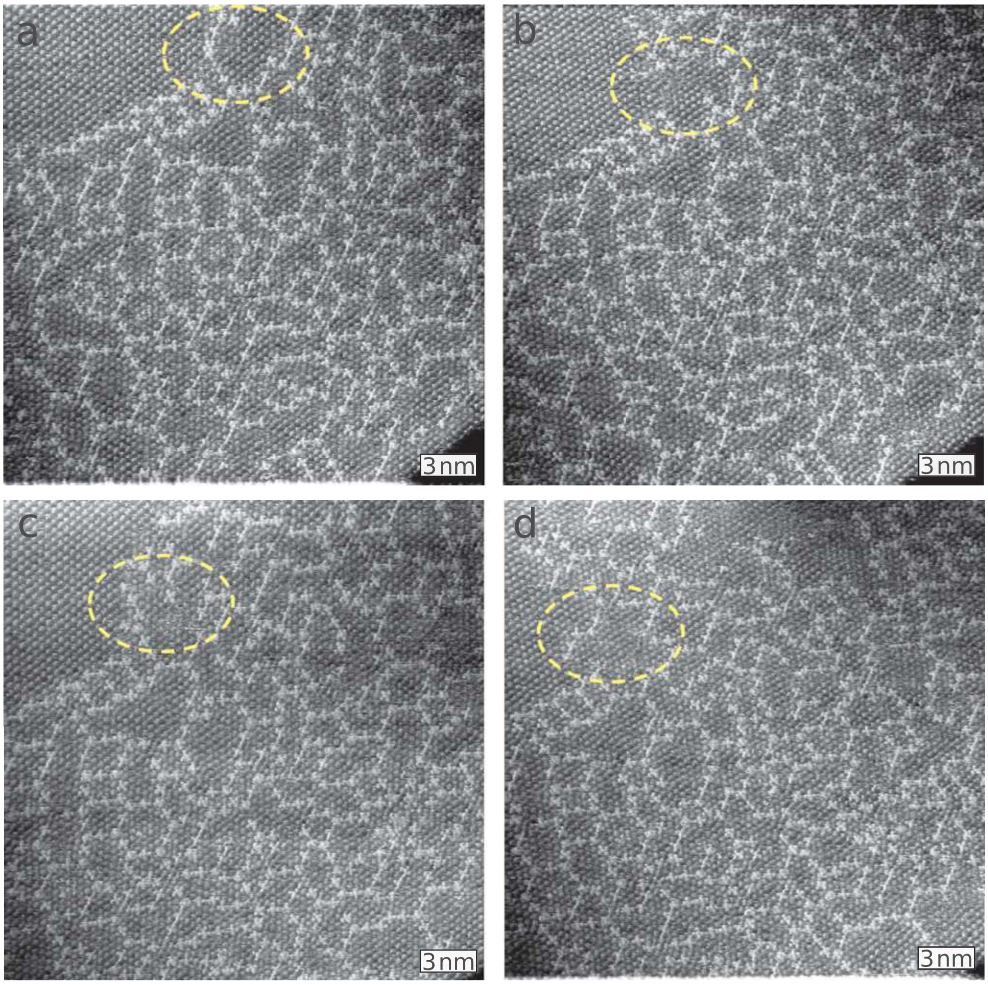

FIGURE 8.6: EC-STM images of Au(111) in 5 mM H_2SO_4 + 1 mM KI showing the change of chains imaged after every 151 s. $V_{sample} = -0.3$ V, $V_{tip} = -0.42$ V vs. Pt wire, $I_t = 4.30$ nA, $V_{bias} = 120$ mV, $I_t = 4.3$ nA. Scan size: 25 nm × 25 nm, W tip.

The presence of these closed chains not only limits on-surface diffusion but also their presence can distort the structure of the iodine adlayer on the Au surface. This was shown more clearly in the FFT of the areas confined between the chains in Figure 8.7. The dashed circles show the area where the FFT patterns were obtained. The FFT shown in the inset corresponds to the whole image. The l_1, l_2, and the angle between these two parameters (θ) were used for comparing the FFT patterns (see Appendix, Chapter A, Table 1). The change in l_1, l_2, and θ from one area to another indicates the distortion of the iodine adlayer confined by the chains.

The significant impact of chains on the distortion of the adlayer is evident in Figure 8.7, particularly at the centers of circles 5 and 6. Here, the confinement of a large number of atoms induces a vertical distortion, which appears as a lighter contrast in the STM image.

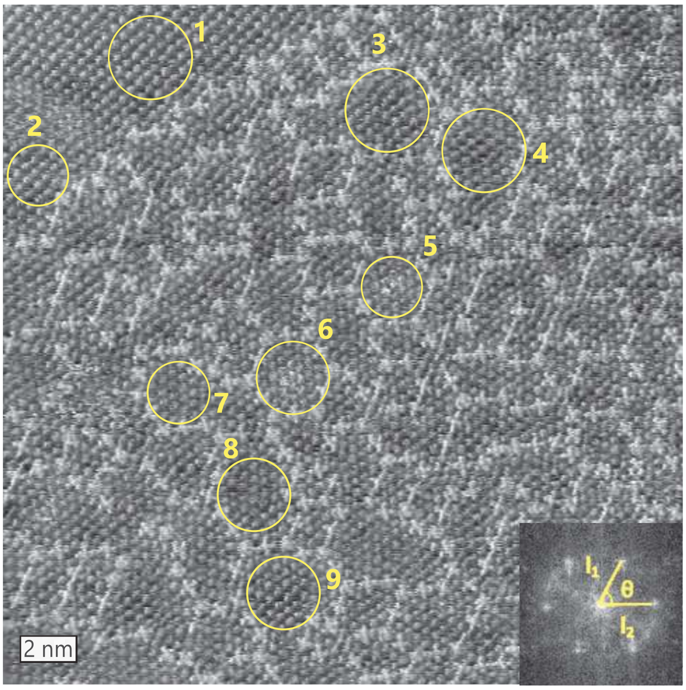

FIGURE 8.7: Possible distortion of enclosed iodide adlayer sections. Inset: FFT of the whole image. Imaging condition: $V_{sample} = -0.3$ V, $V_{tip} = -0.42$ V vs. Pt wire, $I_t = 4.30$ nA, $V_{bias} = 120$ mV, $I_t = 4.3$ nA.

A closer look at the EC-STM images shows how the structures confined by the chains are vertically distorted. So it looks like the bright lines are domain boundaries.

Figure 8.8 shows the line profile taken along the yellow lines on an EC-STM image. The apparent height of the particles in the upper left corner of the image, where there are no chains, is 1.37 ± 0.20 Å; however, in some of the areas confined among the chains, the height seems to decrease to 0.99 ± 0.22 Å.

There are two distinct molecular shapes on the surface: cross-shaped and circular-shaped. The heights of cross-shaped and circular-shaped units are 2.42 ± 0.19 Å and 2.36 ± 0.23 Å, respectively. Linear strings consisting of two or three cross-shaped units are connected at an angle of 180°. The circular-shaped units are seen where three linear strings intersect, always at an angle of 120° (Fig. 8.9). The distance from the center of the cross-shaped units to the center of the neighboring cross-shaped units is 7.65 ± 0.03 Å equal to the distance measured from the center of the circular-shaped units to the cross-shaped units. The long diagonal of the hexagon as shown in Fig 8.9, is 29.48 ± 1.00 Å which is consistent with the 30 Å value reported in the literature [78].

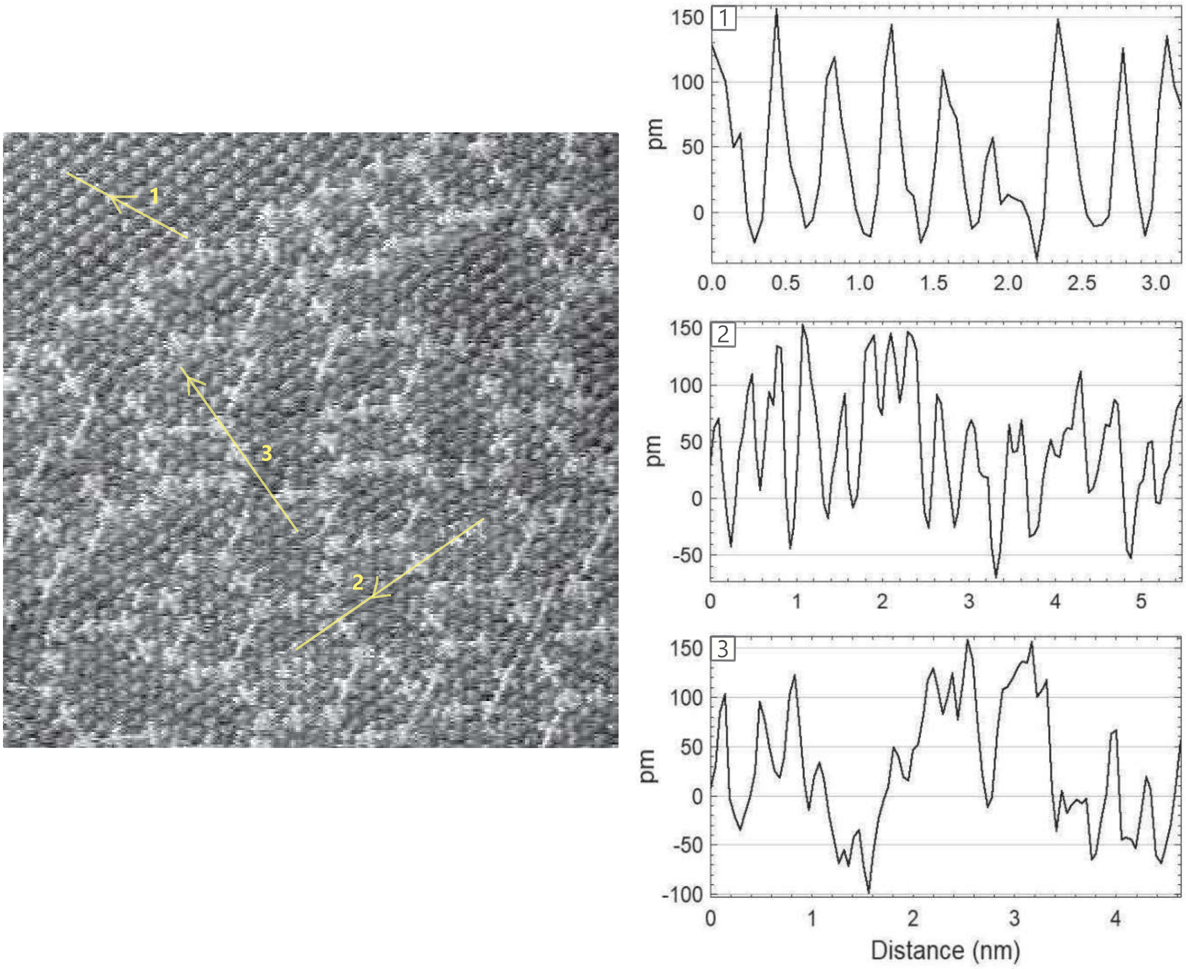

FIGURE 8.8: EC-STM image of the surface with apparent heights (in pm) along the yellow lines. Arrows indicate the direction in which the line profiles were measured. Imaging condition: $V_{sample} = -0.3$ V, $V_{tip} = -0.42$ V vs. Pt wire, $I_t = 4.30$ nA, $V_{bias} = 120$ mV, $I_t = 4.3$ nA.

The connection of the linear strings can lead to either a (hexagonal) closed area or a non-confined area with cross-shaped units forming linear features with loose ends. The analysis of the EC-STM images showed that the number of cross-shaped units between two circular-shaped units is in 95% of all cases, one cross-shaped unit, and in 5% of all cases, two cross-shaped units. The number of cross-shaped units confined by a circular-shaped unit from one side and a loose end from the other side is one and two, with probabilities of 56% and 44%, respectively.

The EC-STM images showed that the number of loose-end chains is higher in the area where the concentration of chains is lower. This can be seen in the upper area of the STM image in Figure 8.7. As reported in [78] in contrast to the ordered iodine adlayers, the strings predominantly align with the direction of the gold substrate rows.

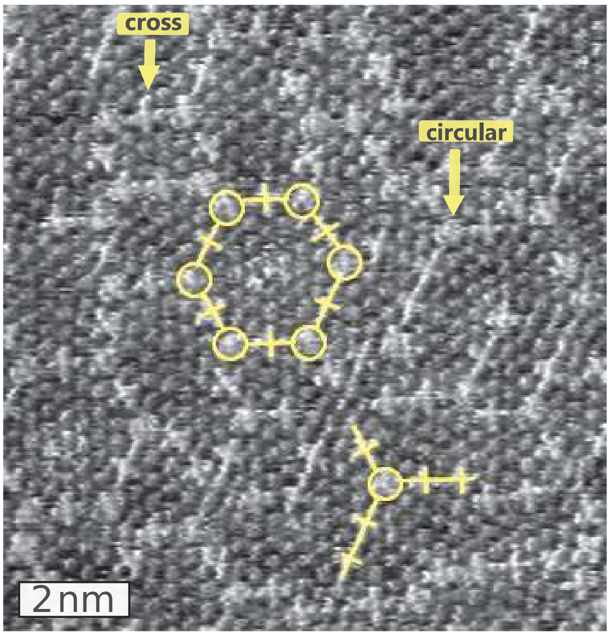

FIGURE 8.9: Cross-shaped (+) and circular (o) units, with some highlighted in yellow.

The potential dependent structures of the iodine on gold are shown in Figure 8.10. The scanning started at a potential of -0.3 V vs. Pt wire in Figure 8.10-a, with the structure of $(5 \times \sqrt{3})$, and then the potential changed to -0.2 V vs. Pt wire in Figure 8.10-b. By making the potential more positive, the structure appearing on the area free of chains but close to chains seems like the moiré pattern otherwise occurring at more positive potentials. The same phenomenon was seen in Figure 8.11-a. The compression of the iodine adlayer in the vicinity of those chains, providing a rigid wall, might be an explanation for this phenomenon.

In Figure 8.10-c, the potential was changed from -0.3 V vs. Pt wire to -0.35 V. The dashed line shows where the potential changed in the upward scan. We may have $(5 \times \sqrt{3})R30°$ structure. As it appears, the chains on the surface disappeared, which may be explained by tip and surface interaction. The tip was so close to the surface that the chains distorted mechanically. Figure 8.10-d shows the surface imaged at -0.35 V. In the next images, Fig. 8.10-e, imaged at -0.15 V vs. Pt wire, the terraces imaged in Figure 8.10-c,d seem to have less chains. It is also possible that by making the surface more negative, these chains were disintegrated or desorbed from the surface.

In Figure 8.10-e,f the moiré pattern and chains are both present on the surface.

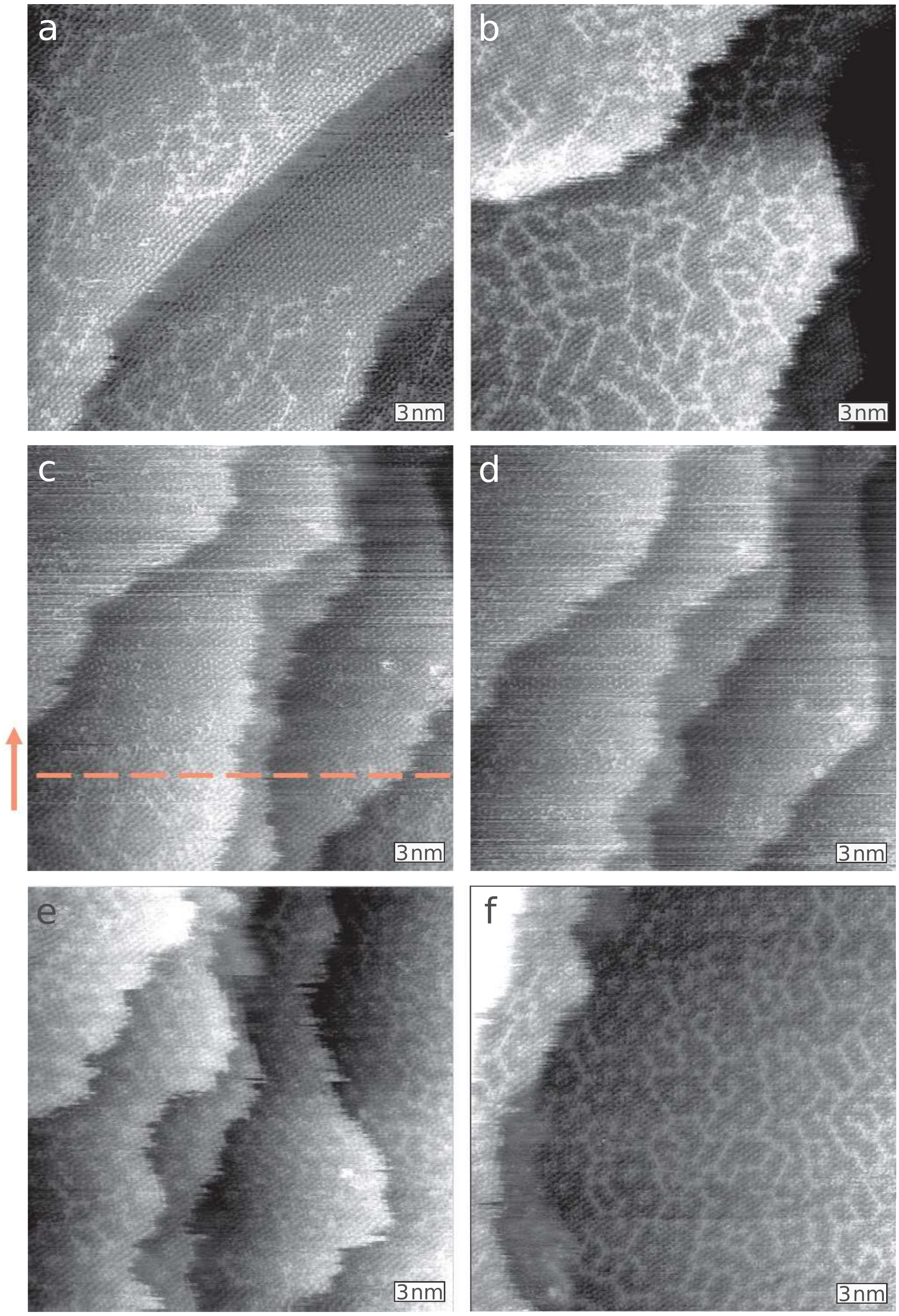

FIGURE 8.10: EC-STM images of Au(111) in 5 mM H_2SO_4 + 1 mM KI at different sample potentials: a) -0.3 V, b) -0.2 V, c) -0.3 to -0.35 V, d) -0.35 V, e) -0.15 V, and f) -0.11 V vs. Pt wire. $I_t = 4.3$ nA, $V_{bias} = 120$ mV. W tip with $V_{tip} = -0.42$ V. Scan size: 25 nm × 25 nm.

The structure change from moiré to non-moiré is clearly shown in Figure 8.11.

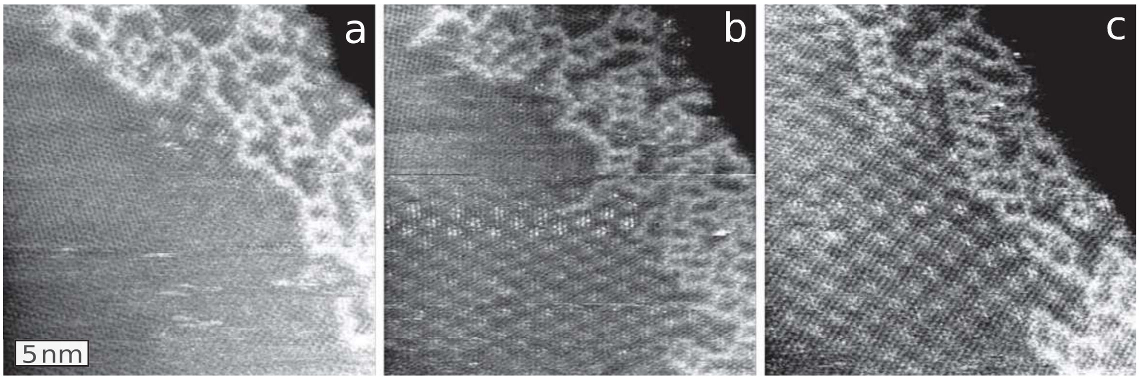

FIGURE 8.11: EC-STM images of Au(111) in 5 mM $HClO_4$ + 1 mM KI at different sample potentials a) -0.167 V, b) -0.167 to -0.067 V, and c) -0.067 V with $V_{tip} = -0.41$ V vs. Pt wire, $I_t = 3.9$ nA, $V_{bias} = 120$ mV, $I_t = 4.3$ nA. Scan size: 25 nm × 25 nm, W tip.

8.2.1 Possible origin of the bright chains

Gao and Weaver proposed that these chains seen in EC-STM images are polyiodides produced by the electrooxidation of iodide, supporting their idea with surface-enhanced Raman spectroscopy. Their SERS study on electrooxidation of iodide in 1 mM NaI + 0.1 M $HClO_4$ at Au revealed that the start of surface changes with two bands at 110 cm^{-1} and 145 cm^{-1} at a potential of 0.225 to 0.250 V vs. SCE, is located at a potential much more negative than 0.4 V, where the considerable faradaic current of iodide oxidation starts occurring. These peaks were assigned to the adsorbed polyiodide [87]. Interestingly, our EC-STM images recorded from -0.3 to -0.11 V vs. Pt wire (0.018 to 0.208 V vs. SCE), already showed the presence of similar linear or chain-like structures on the surface.

Given the limited information about their identity and formation, we decided to explore alternative possibilities that could explain the formation of the bright chains on the surface. After discovering that the tungsten oxide present at the surface of tungsten EC-STM tip can be dissolved in an acidic solution and form 1D adsorbates on the surface by our group [253], the possibility of tungsten oxide being responsible for these chains increased. In Gao and Weaver's work where they reported the polyiodide chains, a W tip was used as the EC-STM tip [78]. Therefore, for further investigation, we used PtIr tips. Figure 8.12 shows the surfaces imaged with a PtIr tip at the OCP potential where we can see the presence of the chains. The experiments were performed on two different Au samples with two different EC-STM setups. The sample imaged in Fig. 8.12-b was electropolished and annealed before the scanning, and a relatively low tunneling current of 0.67 nA was used, compared to the 10 nA employed in Gao and Weaver's work [78]. Imaging these structures with PtIr tips on freshly annealed surfaces ruled out the possibility that these chains are composed of tungsten oxides.

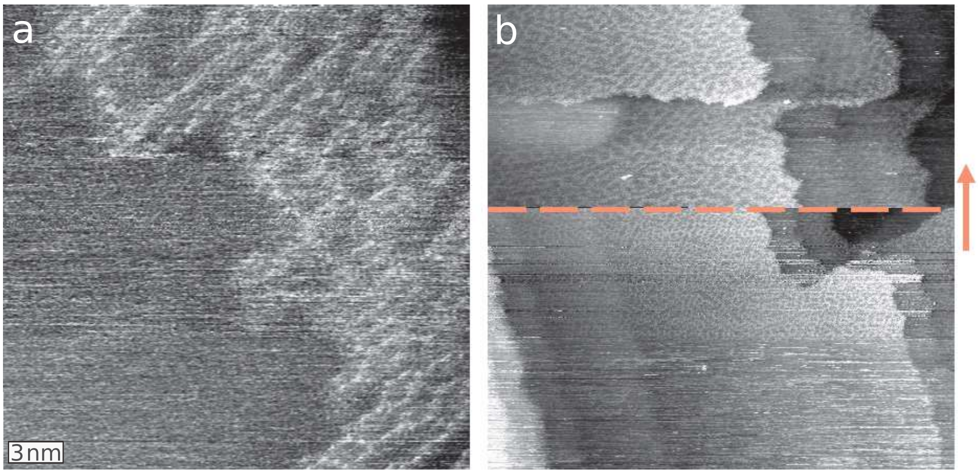

FIGURE 8.12: EC-STM images measured with a PtIr tip on Au(111) in 5 mM H_2SO_4 + 1 mM KI at sample potential -0.15 V vs. Pt wire. With sizes of a) 25 nm × 25 nm and b) 95 nm × 95 nm changed into 50 nm × 50 nm.

The other possibility could be the presence of some impurities. We prepared solutions with high-purity (99.99%) KI salt and acids for these experiments. By considering that other halogen ions are the most likely impurities, iodide adsorbs the strongest on gold among other halogen ions such as Cl^- and Br^-, decreasing the possibility of a large group of impurities.

Another candidate as an impurity is sulfur. Based on the reported DFT calculations, the adsorption energy of sulfur on Au(111) is between -2.59 and -3.94 eV [254] which is stronger than the adsorption of iodine on gold, -0.98 to -2.3 eV [255]. The sulfide electrooxidation on Au(111) with EC-STM in 0.1 M $NaClO_4$ + 4 mM $HClO_4$ + 0.5 mM Na_2S aqueous solution was reported. They showed that at relatively low electrode potential, from -0.4 to -0.1 V vs. SCE, a sulfur adlayer has $(\sqrt{3} \times \sqrt{3})R30°$ structure relative to Au(111) substrate, whereas at a more positive potential above ca. -0.1 V, arrays of quasi-rectangular rings, S_8 arrays, are formed on the surface [256]. The formation of these S_8 rings is not limited to acidic media and has also been observed in alkaline solution [257].

Although adsorption and electrooxidation of the sulfide in the potential range measured by STM in our experiments are possible, there is a big difference between the shape of the S_8 rectangular rings and the chains observed in our experiment. The interatomic

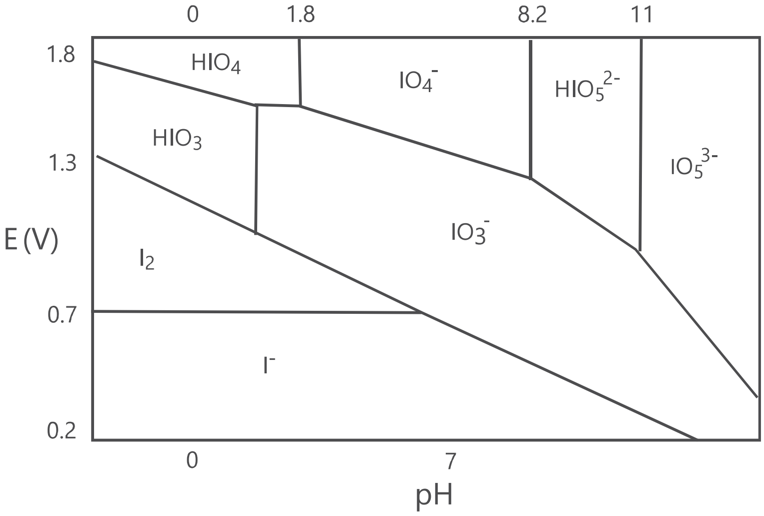

FIGURE 8.13: Pourbaix diagram showing chemical states of iodine species. Reproduced from [258], Copyright (2022) with permission from John Wiley and Sons.

distance between the sulfur adatoms in the ring is $2.9 \leq d \leq 3.1$ Å which means the width of quasi-rectangular rings is $(6.2 \pm 0.3) \times (5.8 \pm 0.3)$ Å^2 [259]. By comparing our EC-STM images and those of S_8, the structures on the our surface are not S_8 arrays. However, the possibility of complex compounds containing sulfur and iodine was not considered.

Another possible element in the solution is oxygen. Based on the Pourbaix diagram shown in Figure 8.13, the oxyanions such as $IO_3{}^-$, $IO_4{}^-$ and $IO_5{}^-$ are only stable in alkaline media. Therefore, at pH=2, the formation of oxyanions is not favorable. Moreover, at the potential range used in this study, the possibility of HIO_3 and HIO_4 being formed is very low, because a potential more positive than 1.24 V vs SCE is needed.

Another possible candidate for forming chains or strings is the reaction of the iodine adsorbed on the surface and the Au atoms from the surface. Figure 8.14 shows the Pourbaix diagram of the Au and iodide system with 10^{-2} M I^- in aqueous solution, showing that at pH=2 the metallic Au can be oxidized into $AuI_2{}^-$ and $AuI_4{}^-$, whereas at potentials lower than 0.5 V, Au is the predominant species [224]. Cyclic voltammetry of the gold in $1\,M\,HClO_4 + 10^{-2}\,M\,NaI$ (pH=0) by rotating disk electrode and chronoamperometry techniques showed that the oxidation of Au to Au(I) and I^- to $I_3{}^-$ at the same time in the potential range between 0.35 and 0.5 V vs. SCE [224].

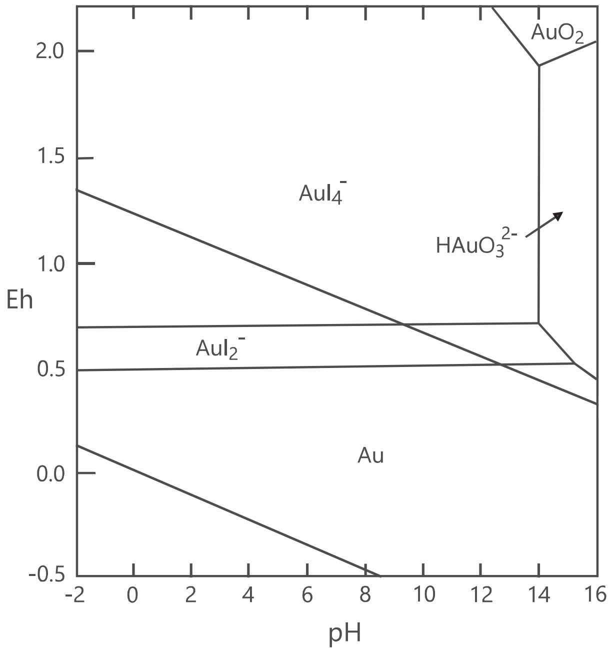

FIGURE 8.14: Pourbaix (Eh-pH) diagram of Au and iodide system with 10^{-2} M I^- in aqueous solution. The dashed lines illustrate the stability limits of water. Reproduced from [224], Copyright (1993) with permission from Elsevier.

The proximity in the standard reduction potential for iodide and gold-iodine species can be seen in Table 8.1.

TABLE 8.1: Table of standard reduction potential for iodide and gold species. Adapted from [224], Copyright (1993) with permission from Elsevier.

	Anodic reaction	E^0 (V) vs. SHE
a	$I_3^- + 2e^- \longrightarrow 3I^-$	0.535
b	$I_2(aq) + 2e^- \longrightarrow 2I^-$	0.619
c	$I_2(s) + 2e^- \longrightarrow 2I^-$	0.534
d	$3I_2(aq) + 2e^- \longrightarrow 2I_3^-$	0.784
e	$3I_2(s) + 2e^- \longrightarrow 2I_3^-$	0.533
f	$AuI_2^- + e^- \longrightarrow Au + 2I^-$	0.578
g	$AuI_4^- + 3e^- \longrightarrow Au + 4I^-$	0.560
h	$AuI_4^- + 2e^- \longrightarrow AuI_2^- + 2I^-$	0.551
i	$3AuI_4^- + e^- \longrightarrow 3Au + 4I_3^-$	0.757

In addition to the similar standard reduction potentials, there are geometric similarities between gold halides and polyiodides [88]. For example, both I_3^- and AuI_2^- ions have linear configuration, and I_5^- and AuI_4^- can have square planar or linear or V/L-shaped geometry, of which the V/L-shape is the most stable geometry. For distinguishing gold halides from polyiodides, spectroscopy techniques are needed. Future work may therefore elucidate these possibilities conclusively.

A closer look at the large-size images can help us to estimate the starting point of the chains on the surface. Based on the images in Figure 8.15 the presence of the chains is not only limited to regions that emanate from steps but also occurs on the terraces. As shown in Figure 8.15-d, there are some nucleation points located on the terraces. The presence of some defects on the surface may work as nucleation points on terraces. By going to more positive potentials, these chains probably grow larger and stop by the edges. However, for the sulfur atoms (without presence of iodide in solution), the nucleation of the sulfur on Au(111) surface started only at the step edges [259, 260].

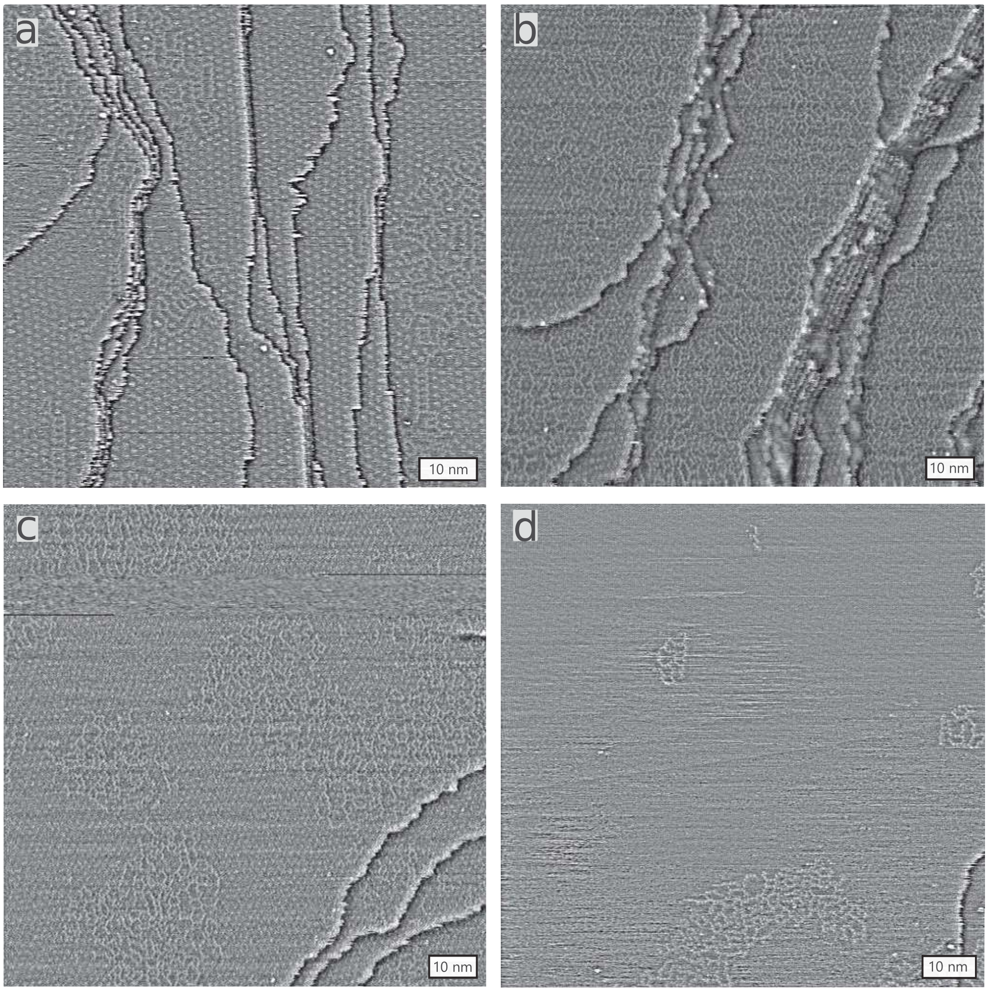

FIGURE 8.15: EC-STM images of Au(111) in 5 mM H_2SO_4 + 1 mM KI after high pass filtering process imaged at a) -0.06 V, b) -0.11 V, c) -0.11 V and d) -0.024 V with $V_{tip} = -0.41$ V vs. Pt wire, imaged with W tip in different scan size width from 83 nm to 102 nm.

8.3 Conclusion

We investigated the structure of iodine using electrochemical scanning tunneling microscopy at different potentials in a 1 mM KI solution. Our high-resolution EC-STM images revealed the presence of chains on the surface. While the structure of the iodine adlayer on gold (Au) has been extensively studied, information regarding these chains is limited. Over 30 years ago, Gao and Weaver identified these chains as polyiodides using EC-STM and surface-enhanced Raman spectroscopy [78]. However, our STM images showed that these chains can also form at less positive potentials than previously reported. Consequently, we reassessed the possibility of these structures being polyiodides and explored alternative explanations. Based on our findings, these chains may not be polyiodides; however, further electrochemical scanning microscopy combined with spectroscopic techniques are needed for definitive identification.

Additionally, larger-scale STM images demonstrated that the formation of these chains is not restricted to step edges; any surface imperfections can serve as nucleation points for their development.

Chapter 9

Conclusion

In conclusion, this thesis studied the adsorption behaviors of graft and iodine molecules on gold surfaces, providing insights into their binding affinities and surface dynamics. These findings contribute to a deeper understanding of molecule-surface interactions, with implications for catalysis, sensors, and surface modification applications.

Adsorption of grafts:

- In this work, Au surfaces were grafted via the reduction of 3,5-TBD. The cyclic voltammetry on grafted Au(111) reveals a significant change in the double-layer behavior in dilute sulfuric acid, which we attribute to alterations in (hydrogen)sulfate interactions with the substrate. It also showed that the oxidative desorption of the grafts occurs at potentials higher than those required for the oxidation of Au terrace atoms, suggesting that covalent grafts provide structural stabilization. The blocking behavior of grafts was studied in 1 mM $K_3Fe(CN)_6$ and the results were compared to partially blocked electrodes. While the grafted electrode after rinsing with water shows the CV corresponding to the ultra microelectrodes arrays, the CV of the grafted electrode rinsed with acetone does show any response related ultra microelectrodes arrays.
- To gain a better real-time understanding of the grafting process occurring on the surface, EIS measurements were performed in the grafting solution in the presence of a redox couple. However, due to the limitations required to maintain time invariance, EIS alone did not provide a clear picture of the surface events

during grafting. Combining complementary methods with EIS could offer deeper insights into the surface processes taking place.

- The copper upd and its deconvolution reveal a complex energetic landscape, potentially indicating varying binding geometries of the grafts and proximity effects between neighboring sites. The copper opd voltammogram suggests the bulk deposition of Cu atoms only on the Au area free of any graft molecules which is mountain-like similar to that of bare Au.
- STM in phenyloctane suggests that grafting produces shallow etch pits on the surface. Exposure to strongly adsorbing iodide restores an atomically flat Au(111) surface and enables high-contrast EC-STM observation of individual covalent grafts.

Adsorption of iodine:

- We studied Au(111) in 5 mM H_2SO_4 + 1 mM KI using the EC-STM technique at various potentials and investigated the possible identity of the observed chains. These chains may not be polyiodides.

Outlook: The experiments could be further refined and expanded to enhance the systematic comparison of surface characterization methods to estimate, for example, the surface coverage of grafts. A key improvement would involve using the same Au(111) electrode for all experiments, grafted consistently with fixed parameters, to allow more accurate cross-comparisons between techniques. However, practical challenges with the hanging meniscus setup such as maintaining a fixed surface area in contact with the electrolyte and achieving a stable meniscus during CV measurements on a hydrophobic grafted surface-limited our ability to use this approach in all experiments. With an Au surface grafted under consistent conditions, it would be valuable to compare surface coverage obtained from CV measurements across different electrolytes: (1) H_2SO_4, (2) Cu^{2+}, and (3) hexacyanoferrate. Additionally, advanced techniques like AFM and STM could provide visual insights into graft distribution, although they would require extensive imaging across various surface points. EIS in non-grafting solutions could further inform on graft coverage.

Combining complementary methods, such as sum frequency generation spectroscopy and quartz crystal microbalance with dissipation monitoring, with EIS could offer deeper insights into the surface processes taking place. More considerations in the design of an EIS experiment are mentioned in the outlook section of Chapter 7.

As outlined in Chapter 4, the grafted Au surface behaves as an ultramicroelectrode array with four distinct response categories. Studying different graft concentrations and adjusting scan rates could reveal transitions between these categories.

The proposed configuration of overpotentially deposited Cu on the grafted surface could also be verified through STM or AFM.

Finally, to determine whetherthe observed chains are polyiodides, further electrochemical scanning microscopy combined with spectroscopic techniques is needed. Extending the potential range to more positive and negative limits would provide additional insights into formation, dynamics, and stability of them.

Appendix A

Appendix

A Extra results and details

A.1 Field-enhanced diffusion/deposition

Figure 1 shows the STM images on the grafted Au(111), imaged in an ambient air environment. In Figure 1-a, during the scan, the sample potential changed from 0.3 V to -0.8 V. The deposition and formation of the mounds can be seen in Fig. 1-b imaged with the potential of -0.5 V. By zooming in on the area with the size of 70 nm × 70 and changing the potential from -0.5 V to -0.66 V mounds formed on the surface again which can be seen by zooming out and scanning the surface with a potential of -0.66 V. The same procedure of mound formation continued by changing scanning size and scanning in a smaller size area (50 nm × 50 nm) and changing the potential from -0.66 V to -1.2 V (Fig. 1-d). The quality of the image scanned with a potential of -1.2 V was not good enough so it was changed to -0.3 V for imaging (Fig. 1-e).

Applying large voltage pulses, typically a few volts is a common method for cleaning STM tips or for renewing the apex of a damaged tip in vacuum or air [261–263]. In the literature, the formation of the mounds and pits by applying the large voltage pulses between sample and tip was reported [213, 262–264]. During scanning the surface the molecules present on the surface can stick to the tip and deposit back on the surface by applying voltage pulses. Two processes can lead to local modification of the surface under the tip: field evaporation and field-enhanced diffusion. In the field

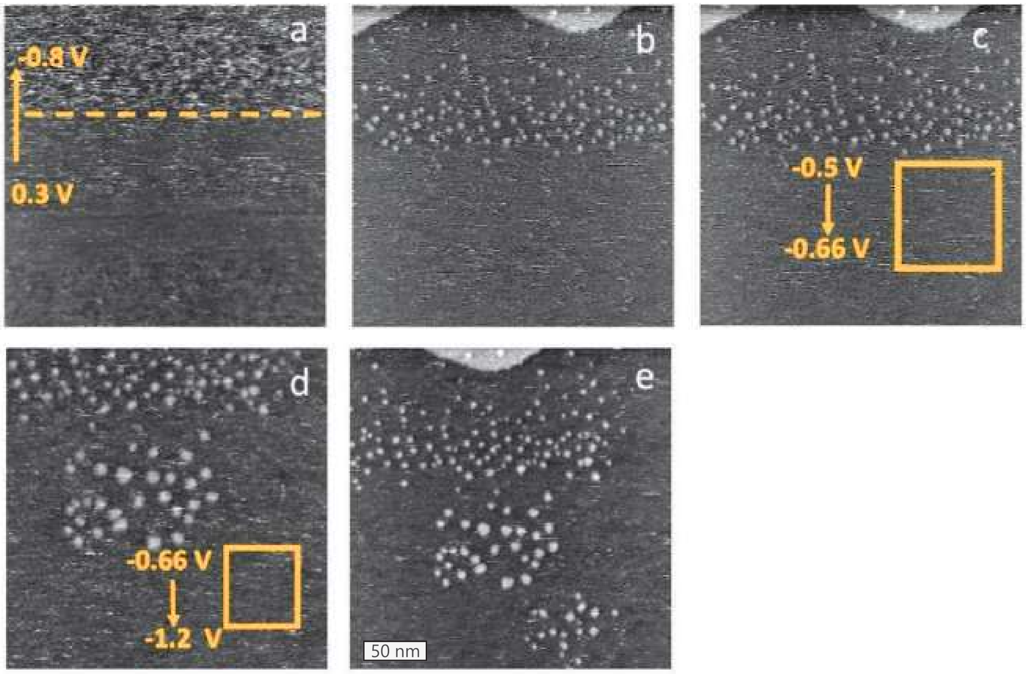

FIGURE 1: STM images of the grafted Au(111) in air with a PtIr tip. Au(111) grafted by measuring a few CVs in the grafting solution of 1 mM 3,5-TBA in 0.1 M HCl + 1 mM $NaNO_2$. The surface is decorated via the deposition of material from the tip. Scan size between 200 nm × 200 nm and 250 nm × 250 nm and tunneling current of 0.05 nA.

evaporation process, a higher voltage amplitude range (higher than 3 V) than field-enhanced diffusion is applied to that surface [261]. Although we did not apply voltage pulses, a sudden change in the sample potential (or sample bias) led to a similar effect on the surface.

In our study, the STM tip scans the surface at an extremely close range, likely closer than necessary. This proximity causes some material from the surface to be adsorbed onto the tip, either through direct mechanical contact or field-enhanced diffusion. Whenever the sample bias becomes more negative, these adsorbed species are redeposited back onto the surface. The field-enhanced diffusion/deposition of the material from the tip to surface at negative tip potential has been reported [261]. However, we cannot certainly say the mound formation is due to field-enhanced diffusion because the change of potential in our case is not comparable with high-voltage pulses of a few volts (typically 1.5-3 V) reported in the literature [213, 261, 264, 265].

Another explanation could be that at short distances and low electric fields, the van der Waals force contributes to mound formation [265, 266]. In an investigation of the force between a gold-coated AFM tip and a gold surface at short distances and under low electric fields, using an AFM cantilever placed inside a transmission electron microscope (TEM), the measurements revealed an unusually high jump-to-contact distance, suggesting a stronger force than would be expected based on the van der Waals force alone. They reported the formation of a thin neck of material between the tip and the sample. They interpreted that the van der Waals force triggered a field-induced surface diffusion leading to the decrease in the gap distance, which consequently increased the van der Waals force, and this avalanche of adatoms quickly formed the neck. The gap rapidly fills until reaching the typical jump-to-contact distance [266]. Further experiments would be required to explore these surface phenomena in detail, but this was beyond the scope of our current study.

A.2 STM images of Au(111) in mesitylene

Besides phenyloctane, mesitylene was also used for imaging the bare gold. Figure 2 shows the STM images of the bare Au(111). Figure 2-a shows that applying the large sample bias of 2 V can modify the surface. By decreasing the sample bias to 0.4 V and moving to a new location, a bare area without any chain of particles can be imaged.

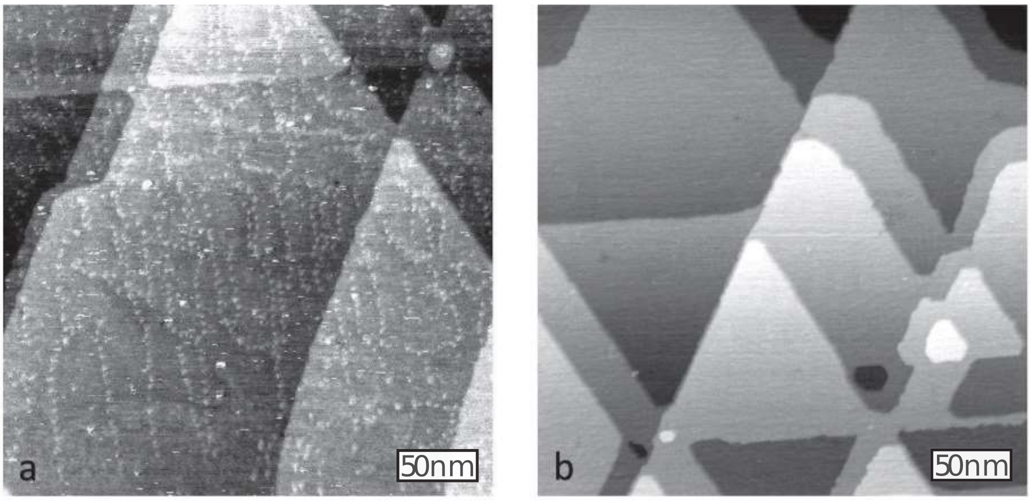

FIGURE 2: STM images of the bare Au(111) measured in mesitylene with a PtIr tip. The interaction of tip with mesitylene depends on the same potential. a) presence of a chain of particles on the surface at $V_{\text{sample bias}} = 2$ V, $I_t = 20$ pA, b) $V_{\text{sample bias}} = 0.4$ V, $I_t = 90$ pA.

A.3 EC-STM of grafted Au(111) in 1 mM KI

The surface of the grafted gold was studied in 5 mM H_2SO_4 + 1 mM KI at different surface potentials ranging from -0.42 V to 0.4 V, as shown in Figure 3. Image Figure 3-a shows how the surface image changes by changing the potential from -0.42 V to 0.07 V with $I_t = 0.190$ nA. The direction of the arrow indicates the slow scan direction, while a new arrow marks the change in sample potential. At -0.42 V, no particles are visible on the surface. However, upon increasing the potential to 0.07 V, the particles (grafts) can be imaged. One possible explanation for this behavior is that the particles are organic molecules with a band gap, which prevents them from being imaged at all sample biases. Consequently, at -0.42 V, the imaging conditions are unsuitable for detecting the particles.

For the area imaged at -0.42 V, the step edges have a ‘frizzy’ appearance. Often, frizzy steps originate from the faster diffusion of step-edge atoms compared to the scan rate. This phenomenon was reported during *in situ* STM on iodine-modified Au(111) surfaces [81]. Although one could expect to see the frizzy steps, even at 0.07 V, in our case this might be due to the interaction of the STM tip with the substrate. Because at 0.07 V, the sample bias was too small so to reach to tunneling current of 0.190 nA, the tip may have had to get too close to the surface. Since the particles are not conducive, the tip could not image the particles and imaged the substrate only, which can lead to tip moving the step atoms laterally. It would be better if we could image the same area in Figure 3-a once with sample potential 0.07 V and then with -0.42 V and again switching to 0.07 V.

The sample imaged at the -0.07, 0, 0.05, 0.1, and 0.3 V (Fig. 3-b to 3-f) appears identical, with no visible surface changes. Although changes were anticipated based on the CV shown in Figure 6.8, the lack of observable differences can be attributed to insufficient resolution to detect surface modifications. Figure 3-g imaged at a sample potential of 0.3 V, is similar to previous images. However, the particles look slightly bigger in width reflecting the change of tip apex during the scanning. By increasing the sample potential to 0.4 V, the surface changes dramatically close to this potential the oxidation for Au to Au (III) and I_3^- to I_2 [224] take place which makes imaging the surface almost impossible.

Figure 4 illustrates the EC-STM images of the grafted Au(111) in 1 mM KI + 5 mM H_2SO_4 at various sample potentials ranging from -0.1 to -0.5 V versus a Pt wire,

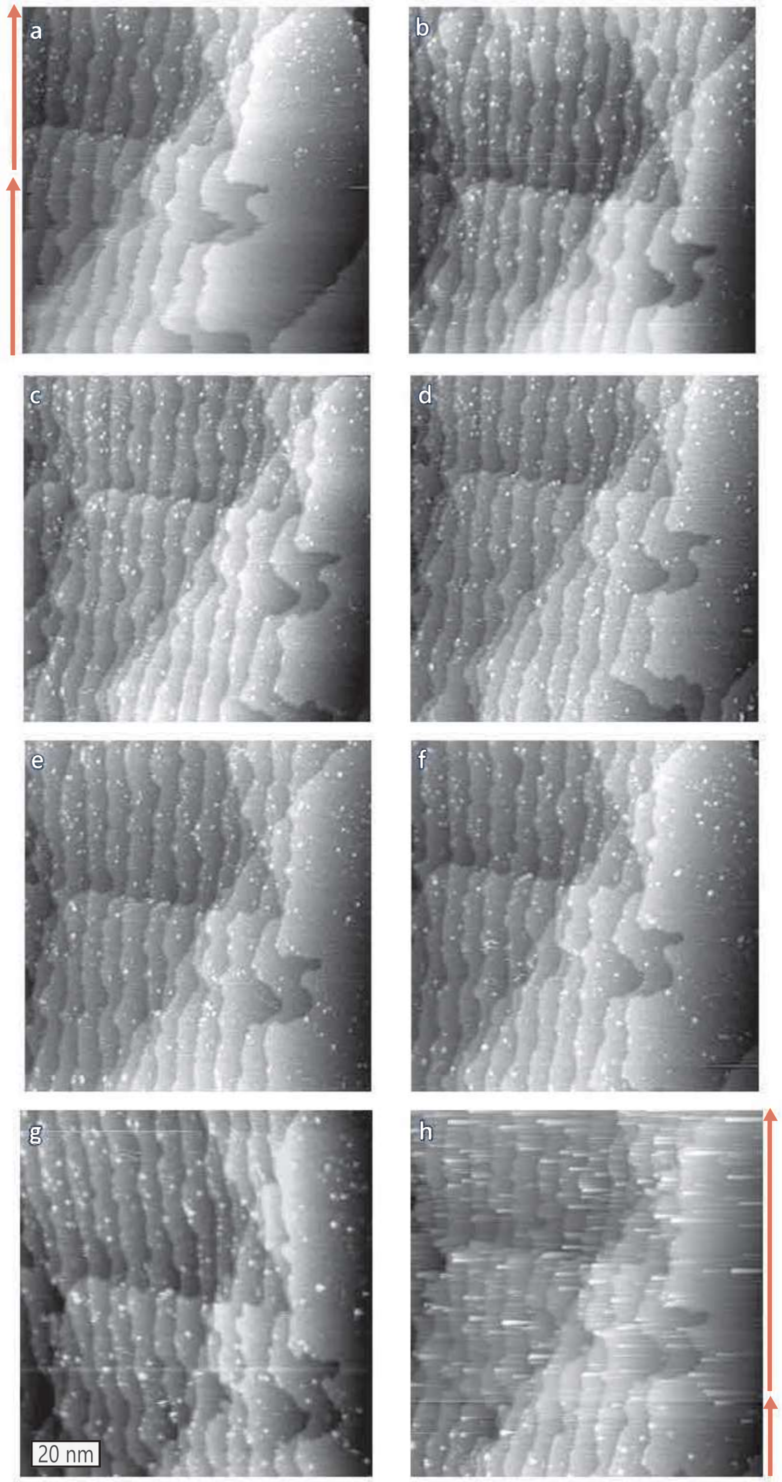

FIGURE 3: EC-STM images of the grafted Au(111) at different sample potentials a) from -0.42 V to 0.07 V, b) -0.07 V, c) 0 V, d) 0.05 V, e) 0.1 V, f) 0.2 V, g) 0.3 V, and h) 0.4 V, measured in the 1 mM KI + 5 mM H_2SO_4 with a W tip with V_{tip} = -0.45 V vs. Pt wire, I_t = 0.190 nA. The arrows indicate the direction of the slow scan and the change of sample potentials during the scan. Scan size: 100 nm × 100 nm.

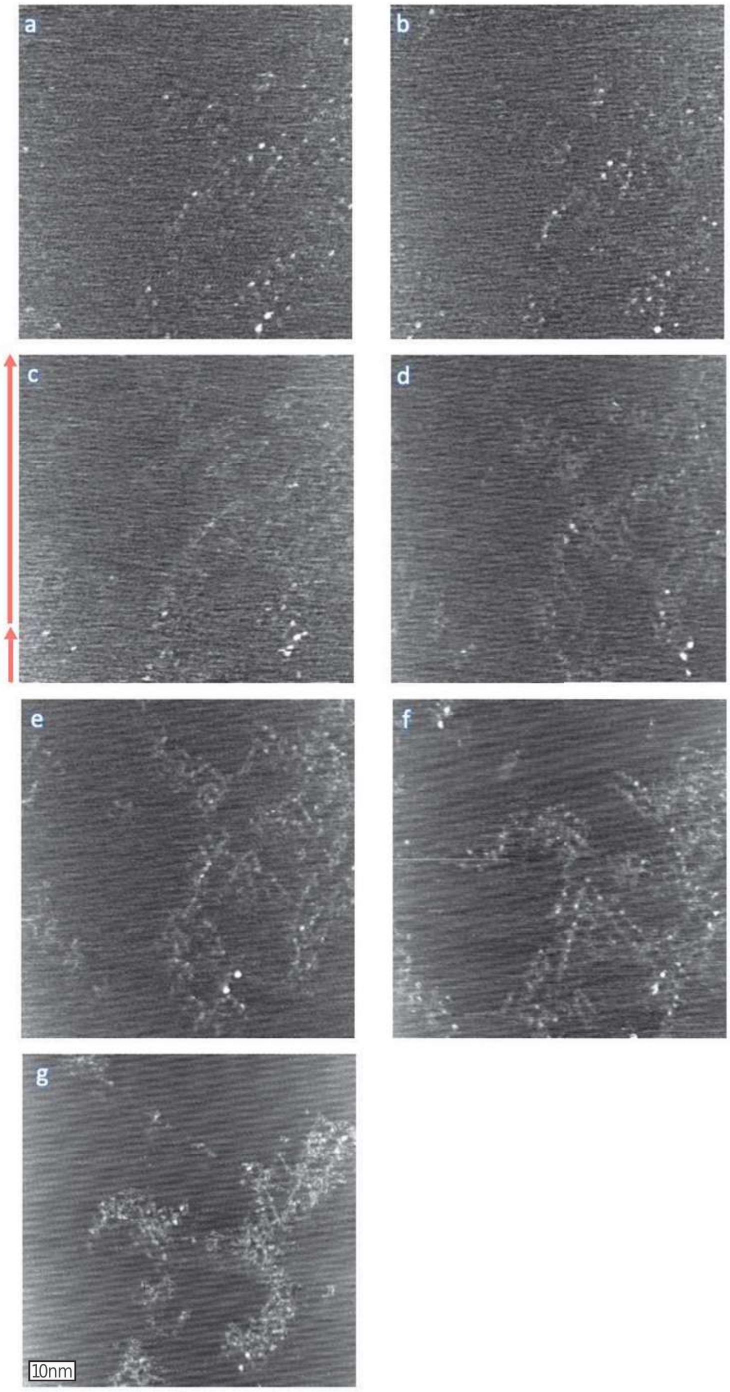

FIGURE 4: EC-STM images of the grafted Au(111) in the 1 mM KI + 5 mM H_2SO_4 at different sample potentials imaging condition a) V_{sample} = -0.08 V, I_t = 0.05 nA, b) V_{sample} = -0.1 V, I_t = 0.1 nA, c) V_{sample} = -0.1 V to -0.2 V, I_t= 0.3 nA, d) V_{sample} = -0.25 V, I_t = 0.4 nA, e) V_{sample} = -0.28 V, I_t = 0.8 nA, f) V_{sample} = -0.4 V, I_t = 1.12 nA, g) V_{sample} = -0.45 V, I_t = 1.3 nA, and h) V_{sample} = 0.51 V, I_t = 1.2 nA. A W tip with V_{tip} = -0.47 V vs. Pt wire. Scan size: 70 nm × 70 nm.

with the tungsten tip potential held at -0.47 V. In Figure 4-a and 4-b, imaged at a sample potential of -0.08 V and -0.1 V, both a moiré pattern and distinct particles (grafts) are visible. In Figure 4-c the direction of the arrow indicates the slow scan direction, while a new arrow marks the change in sample potential from -0.1 V to -0.2 V, showing the change from moiré structure to non-moiré. Figure 4-d recorded at a sample potential of -0.25 V shows the non-moiré structure. The effect of noise on STM images as the tunneling current increases can be seen (Fig. 4-e). While the particles appear less well-defined than in earlier figures, faint chain-like features are noticeable on the surface. Further increases in tunneling current and shifts to more negative sample potentials enhance the clarity of these chain structures (Fig. 4-f and Fig. 4-g). We hypothesize that these chains are the same as those previously observed on the bare Au(111) surface. A higher density of chains in regions where particles are located suggests two possibilities: either the particles act as nucleation sites for chain formation, or both the particles and chains preferentially adhere to substrate regions with a higher defect density, such as grain boundaries.

A.4 Change of chains over time

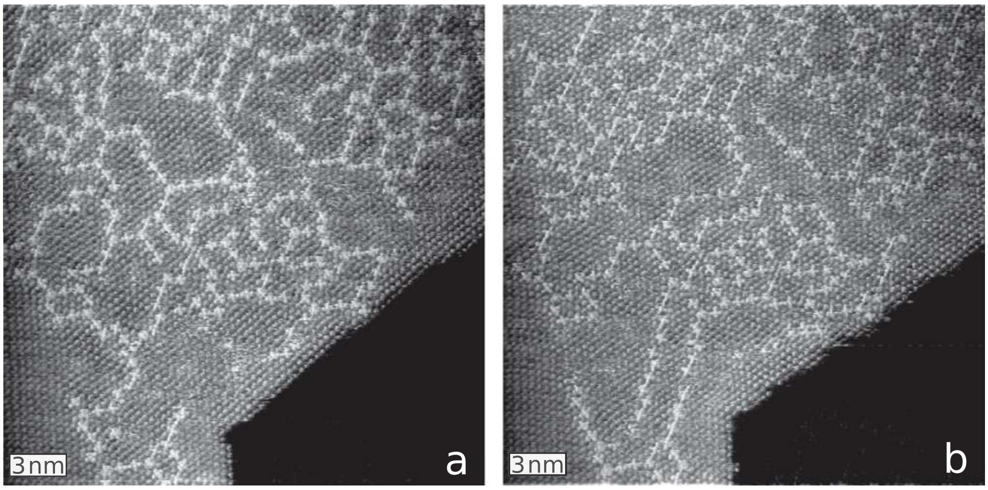

FIGURE 5: EC-STM images of Au(111) in 5 mM H_2SO_4 + 1 mM KI showing more dramatic change of the surface after 151 s. $V_{sample} = -0.3$ V vs. Pt wire, $V_{tip} = -0.42$ V, $I_t = 4.30$ nA, $V_{bias} = 120$ mV, with a scan size of $25\,\text{nm} \times 25\,\text{nm}$, W tip.

TABLE 1: The parameters l_1, l_2, and θ extracted from the image 8.7.

Area	l_1 (nm)	l_2 (nm)	Angle degree
1	0.4859	0.4098	128.20
2	0.4716	0.4352	124.87
3	0.4003	0.3827	121.61
4	0.4391	0.4308	128.91
5	0.4085	0.3661	122.95
6	0.3971	0.3844	121.20
7	0.3893	0.3851	111.72
8	0.4169	0.3975	115.84
9	0.4415	0.3804	123.45

A.5 FFT of the confined areas

ImageJ software was used to perform the FFT within each circle shown on the STM image, to extract values of l_1 and l_2 in real space. The values of l_1 and l_2 in real space are collected in Table 1.

B Copyright permissions

Contents lists available at ScienceDirect

Electrochimica Acta

journal homepage: www.journals.elsevier.com/electrochimica-acta

A new look at metal–carbon hybrids: Molecular-scale study of covalently grafted gold

Mandana Azmi [a,b], Enrico De Bonis [a], Saurav K. Guin [c], Lorna Ashton [a], Stijn F.L. Mertens [a,b,*]

[a] *Department of Chemistry, Energy Lancaster and Materials Science Institute, Lancaster University, Bailrigg, Lancaster LA1 4YB, United Kingdom*
[b] *Institute of Applied Physics, TU Wien, Vienna, Austria*
[c] *National University of Ireland Maynooth, Maynooth, Kildare, Ireland*

ARTICLE INFO

Keywords:
Gold-carbon hybrids
Grafting
Diazonium
Underpotential deposition
Scanning tunnelling microscopy

ABSTRACT

The reliable integration of new nanocarbons in future molecular and hybrid electronics requires mastery of chemical binding between dissimilar materials down to the individual bond. Here, we present a detailed study of covalent grafting of aryl radicals on single crystal Au(111), and investigate their electrochemical stability and oxidative desorption. Copper underpotential deposition and Gaussian deconvolution of its current–potential trace are used to map the thermodynamic and kinetic landscape of the modified Au surface. Scanning tunnelling microscopy in a high-boiling organic solvent suggests that grafting is accompanied by vacancy island formation on the Au surface, while iodide adsorption heals these vacancies and allows high-contrast imaging of individual covalent grafts.

1. Introduction

With the increasing importance of on-surface synthesis of nanographenes and related carbon structures with atomic precision [1,2], also the important question of addressability of such compounds and their covalent or non-covalent connection to the 'outside world' moves into renewed focus. Over the past decades, a variety of binding motifs for molecular electronics has been studied in detail [3]. The most studied have been thiols on Au, but many other chemistries (e.g. N-containing heterocycles on Pt group metals) have been explored.

In this context, direct covalent carbon–metal bonds have been relatively less studied, although an extensive literature exists [4] around covalent grafting on various surfaces, including those of nanoparticles [5]. Starting with the serendipitous discovery [6] of metal passivation by electrochemically generated aryl radicals, mostly different forms of carbon and polycrystalline metals have been in focus, but conclusions regarding structure and binding were typically based on voltammetric behaviour combined with spectroscopy [7,8]. Direct imaging of grafts using scanning probe microscopy was attempted previously [9], but not achieved until 2015 [10], when a detailed study of diazonium based grafting of highly oriented pyrolytic graphite (HOPG) and graphene revealed several surprising phenomena, including tip-induced nanolithography that returns heavily modified carbon to pristine graphene, and the fast and easy fabrication of nanometre-sized pristine nanocorrals over macroscopic areas [11]. An often-encountered challenge in the grafting literature is the formation of multilayers by radical attack to already grafted molecules. This can be avoided by using precursors that because of steric hindrance lead to strict (sub)monolayer formation, Scheme 1, even though more sophisticated approaches have been developed to achieve a similar goal [12].

In this paper, we combine single crystal voltammetry of grafted Au (111) with copper underpotential deposition (upd) to pursue a molecular-scale understanding of grafting. While clearly an ensemble-averaging technique, upd shows exceptional sensitivity for surface crystallography and other features, and has the advantage of scalability over scanning probe techniques of investigation, allowing integration over macroscopic areas and curved structures that elude microscopies [13]. We also present scanning tunnelling microscopy results that show, for the first time, individual covalent grafts on a single-crystal metal surface.

2. Experimental

Voltammetry was performed using a BioLogic SP-30 potentiostat. Au (111) single-crystal (miscut $< 0.1°$) measurements were performed in hanging-meniscus configuration in a standard two-compartment glass

---

[*] Corresponding author.
E-mail addresses: s.mertens@lancaster.ac.uk, stmerten@gmail.com (S.F.L. Mertens).

https://doi.org/10.1016/j.electacta.2024.144743
Received 31 March 2024; Received in revised form 26 June 2024; Accepted 17 July 2024

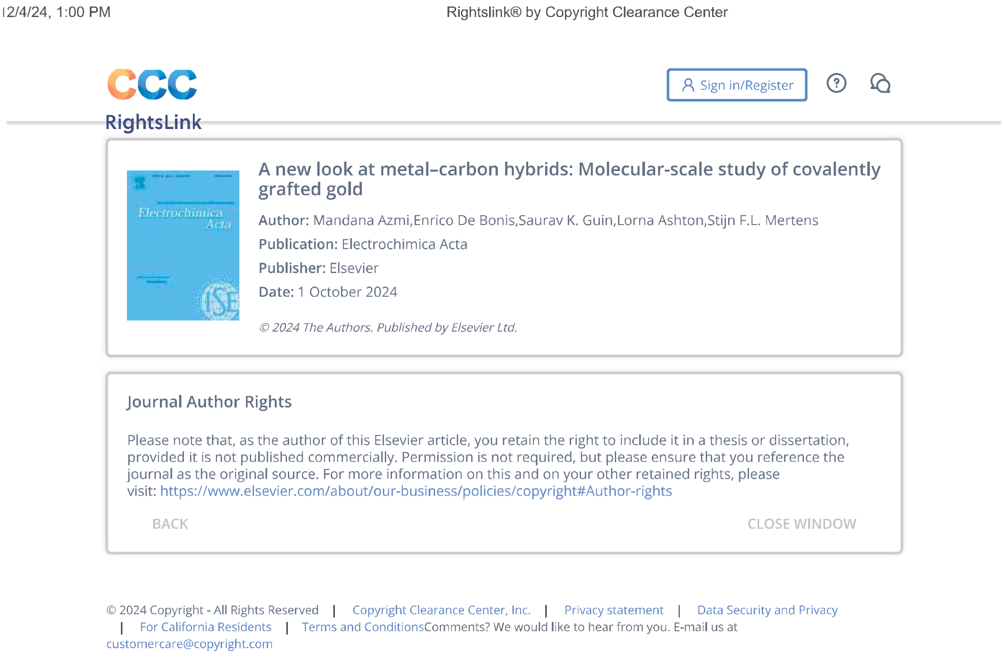

12/4/24, 1:00 PM Rightslink® by Copyright Clearance Center

A new look at metal–carbon hybrids: Molecular-scale study of covalently grafted gold

Author: Mandana Azmi,Enrico De Bonis,Saurav K. Guin,Lorna Ashton,Stijn F.L. Mertens
Publication: Electrochimica Acta
Publisher: Elsevier
Date: 1 October 2024

© 2024 The Authors. Published by Elsevier Ltd.

Journal Author Rights

Please note that, as the author of this Elsevier article, you retain the right to include it in a thesis or dissertation, provided it is not published commercially. Permission is not required, but please ensure that you reference the journal as the original source. For more information on this and on your other retained rights, please visit: https://www.elsevier.com/about/our-business/policies/copyright#Author-rights

© 2024 Copyright - All Rights Reserved | Copyright Clearance Center, Inc. | Privacy statement | Data Security and Privacy | For California Residents | Terms and ConditionsComments? We would like to hear from you. E-mail us at customercare@copyright.com

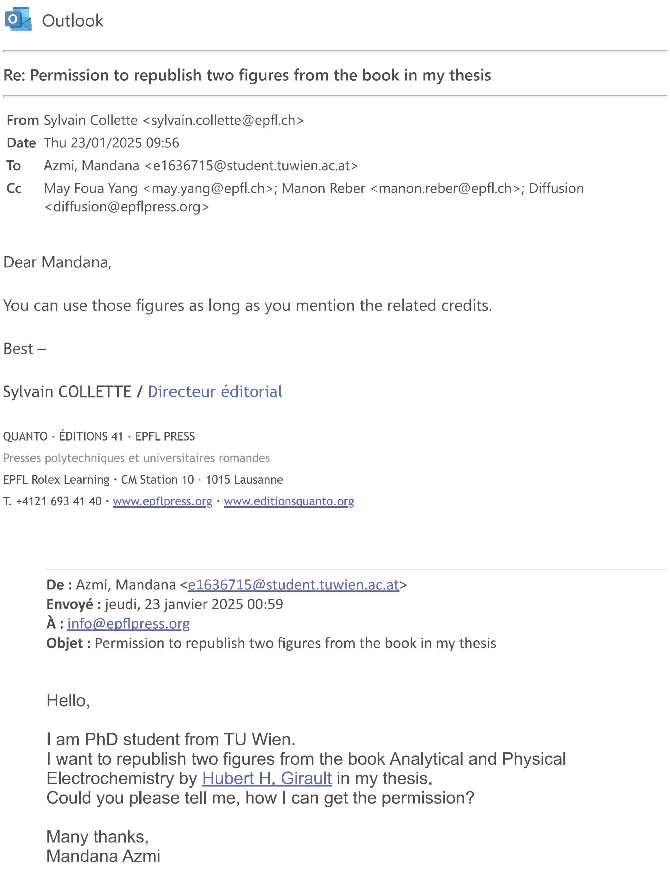

Outlook

Re: Permission to republish two figures from the book in my thesis

From Sylvain Collette <sylvain.collette@epfl.ch>
Date Thu 23/01/2025 09:56
To Azmi, Mandana <e1636715@student.tuwien.ac.at>
Cc May Foua Yang <may.yang@epfl.ch>; Manon Reber <manon.reber@epfl.ch>; Diffusion <diffusion@epflpress.org>

Dear Mandana,

You can use those figures as long as you mention the related credits.

Best –

Sylvain COLLETTE / Directeur éditorial

QUANTO · ÉDITIONS 41 · EPFL PRESS
Presses polytechniques et universitaires romandes
EPFL Rolex Learning · CM Station 10 · 1015 Lausanne
T. +4121 693 41 40 · www.epflpress.org · www.editionsquanto.org

De : Azmi, Mandana <e1636715@student.tuwien.ac.at>
Envoyé : jeudi, 23 janvier 2025 00:59
À : info@epflpress.org
Objet : Permission to republish two figures from the book in my thesis

Hello,

I am PhD student from TU Wien.
I want to republish two figures from the book Analytical and Physical Electrochemistry by Hubert H. Girault in my thesis.
Could you please tell me, how I can get the permission?

Many thanks,
Mandana Azmi

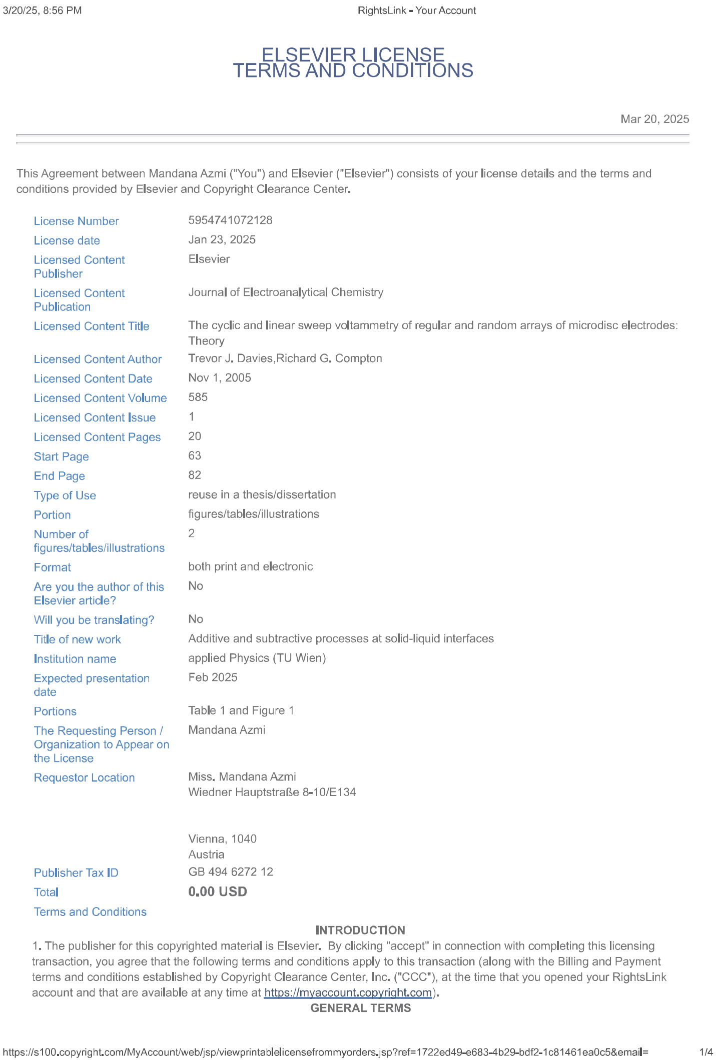

3/20/25, 8:56 PM RightsLink - Your Account

ELSEVIER LICENSE
TERMS AND CONDITIONS

Mar 20, 2025

This Agreement between Mandana Azmi ("You") and Elsevier ("Elsevier") consists of your license details and the terms and conditions provided by Elsevier and Copyright Clearance Center.

License Number	5954741072128
License date	Jan 23, 2025
Licensed Content Publisher	Elsevier
Licensed Content Publication	Journal of Electroanalytical Chemistry
Licensed Content Title	The cyclic and linear sweep voltammetry of regular and random arrays of microdisc electrodes: Theory
Licensed Content Author	Trevor J. Davies,Richard G. Compton
Licensed Content Date	Nov 1, 2005
Licensed Content Volume	585
Licensed Content Issue	1
Licensed Content Pages	20
Start Page	63
End Page	82
Type of Use	reuse in a thesis/dissertation
Portion	figures/tables/illustrations
Number of figures/tables/illustrations	2
Format	both print and electronic
Are you the author of this Elsevier article?	No
Will you be translating?	No
Title of new work	Additive and subtractive processes at solid-liquid interfaces
Institution name	applied Physics (TU Wien)
Expected presentation date	Feb 2025
Portions	Table 1 and Figure 1
The Requesting Person / Organization to Appear on the License	Mandana Azmi
Requestor Location	Miss. Mandana Azmi Wiedner Hauptstraße 8-10/E134 Vienna, 1040 Austria
Publisher Tax ID	GB 494 6272 12
Total	**0.00 USD**
Terms and Conditions	

INTRODUCTION

1. The publisher for this copyrighted material is Elsevier. By clicking "accept" in connection with completing this licensing transaction, you agree that the following terms and conditions apply to this transaction (along with the Billing and Payment terms and conditions established by Copyright Clearance Center, Inc. ("CCC"), at the time that you opened your RightsLink account and that are available at any time at https://myaccount.copyright.com).

GENERAL TERMS

https://s100.copyright.com/MyAccount/web/jsp/viewprintablelicensefrommyorders.jsp?ref=1722ed49-e683-4b29-bdf2-1c81461ea0c5&email= 1/4

1/23/25, 11:45 AM Rightslink® by Copyright Clearance Center

Numerical Simulation of the Diffusion Processes in Nanoelectrode Arrays Using an Axial Neighbor Symmetry Approximation

Author: Ana Sol Peinetti, Rodrigo S. Gilardoni, Martín Mizrahi, et al
Publication: Analytical Chemistry
Publisher: American Chemical Society
Date: Jun 1, 2016

Copyright © 2016, American Chemical Society

PERMISSION/LICENSE IS GRANTED FOR YOUR ORDER AT NO CHARGE

This type of permission/license, instead of the standard Terms and Conditions, is sent to you because no fee is being charged for your order. Please note the following:

- Permission is granted for your request in both print and electronic formats, and translations.
- If figures and/or tables were requested, they may be adapted or used in part.
- Please print this page for your records and send a copy of it to your publisher/graduate school.
- Appropriate credit for the requested material should be given as follows: "Reprinted (adapted) with permission from {COMPLETE REFERENCE CITATION}. Copyright {YEAR} American Chemical Society." Insert appropriate information in place of the capitalized words.
- One-time permission is granted only for the use specified in your RightsLink request. No additional uses are granted (such as derivative works or other editions). For any uses, please submit a new request.

If credit is given to another source for the material you requested from RightsLink, permission must be obtained from that source.

© 2025 Copyright - All Rights Reserved | Copyright Clearance Center, Inc. | Privacy statement | Data Security and Privacy | For California Residents | Terms and ConditionsComments? We would like to hear from you. E-mail us at customercare@copyright.com

---

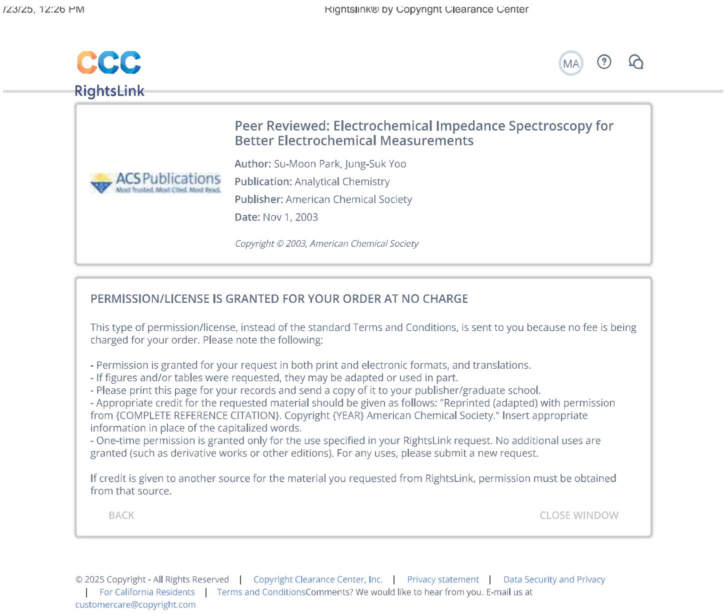

/23/25, 12:26 PM Rightslink® by Copyright Clearance Center

Peer Reviewed: Electrochemical Impedance Spectroscopy for Better Electrochemical Measurements

Author: Su-Moon Park, Jung-Suk Yoo
Publication: Analytical Chemistry
Publisher: American Chemical Society
Date: Nov 1, 2003

Copyright © 2003, American Chemical Society

PERMISSION/LICENSE IS GRANTED FOR YOUR ORDER AT NO CHARGE

This type of permission/license, instead of the standard Terms and Conditions, is sent to you because no fee is being charged for your order. Please note the following:

- Permission is granted for your request in both print and electronic formats, and translations.
- If figures and/or tables were requested, they may be adapted or used in part.
- Please print this page for your records and send a copy of it to your publisher/graduate school.
- Appropriate credit for the requested material should be given as follows: "Reprinted (adapted) with permission from {COMPLETE REFERENCE CITATION}. Copyright {YEAR} American Chemical Society." Insert appropriate information in place of the capitalized words.
- One-time permission is granted only for the use specified in your RightsLink request. No additional uses are granted (such as derivative works or other editions). For any uses, please submit a new request.

If credit is given to another source for the material you requested from RightsLink, permission must be obtained from that source.

© 2025 Copyright - All Rights Reserved | Copyright Clearance Center, Inc. | Privacy statement | Data Security and Privacy | For California Residents | Terms and ConditionsComments? We would like to hear from you. E-mail us at customercare@copyright.com

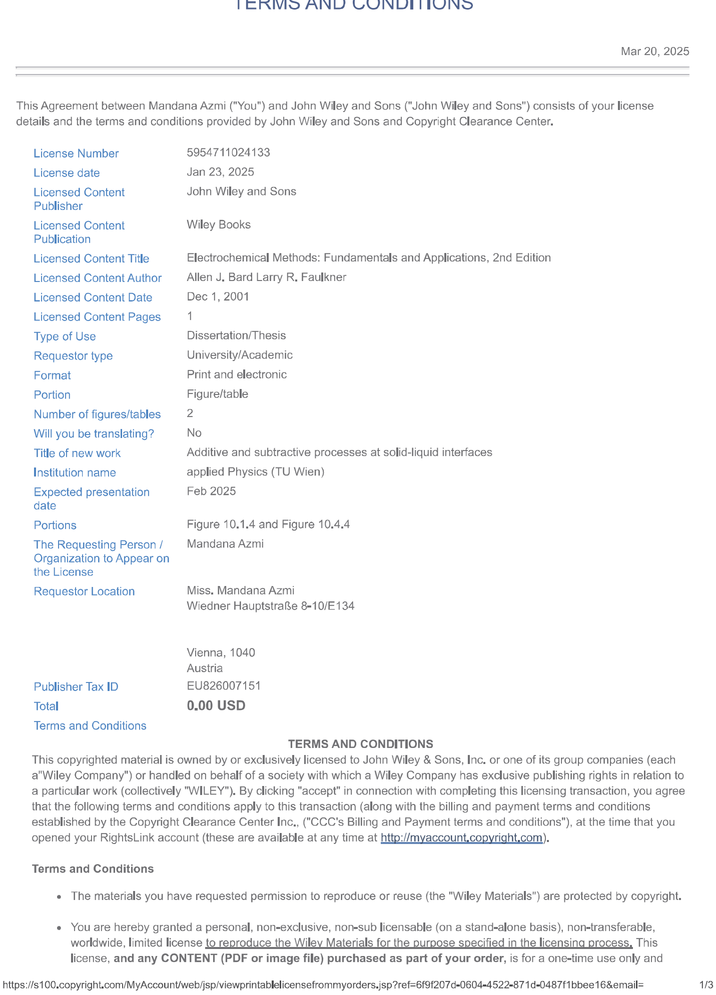

TERMS AND CONDITIONS

Mar 20, 2025

This Agreement between Mandana Azmi ("You") and John Wiley and Sons ("John Wiley and Sons") consists of your license details and the terms and conditions provided by John Wiley and Sons and Copyright Clearance Center.

License Number	5954711024133
License date	Jan 23, 2025
Licensed Content Publisher	John Wiley and Sons
Licensed Content Publication	Wiley Books
Licensed Content Title	Electrochemical Methods: Fundamentals and Applications, 2nd Edition
Licensed Content Author	Allen J. Bard Larry R. Faulkner
Licensed Content Date	Dec 1, 2001
Licensed Content Pages	1
Type of Use	Dissertation/Thesis
Requestor type	University/Academic
Format	Print and electronic
Portion	Figure/table
Number of figures/tables	2
Will you be translating?	No
Title of new work	Additive and subtractive processes at solid-liquid interfaces
Institution name	applied Physics (TU Wien)
Expected presentation date	Feb 2025
Portions	Figure 10.1.4 and Figure 10.4.4
The Requesting Person / Organization to Appear on the License	Mandana Azmi
Requestor Location	Miss. Mandana Azmi Wiedner Hauptstraße 8-10/E134 Vienna, 1040 Austria
Publisher Tax ID	EU826007151
Total	**0.00 USD**
Terms and Conditions	

TERMS AND CONDITIONS

This copyrighted material is owned by or exclusively licensed to John Wiley & Sons, Inc. or one of its group companies (each a"Wiley Company") or handled on behalf of a society with which a Wiley Company has exclusive publishing rights in relation to a particular work (collectively "WILEY"). By clicking "accept" in connection with completing this licensing transaction, you agree that the following terms and conditions apply to this transaction (along with the billing and payment terms and conditions established by the Copyright Clearance Center Inc., ("CCC's Billing and Payment terms and conditions"), at the time that you opened your RightsLink account (these are available at any time at http://myaccount.copyright.com).

Terms and Conditions

- The materials you have requested permission to reproduce or reuse (the "Wiley Materials") are protected by copyright.
- You are hereby granted a personal, non-exclusive, non-sub licensable (on a stand-alone basis), non-transferable, worldwide, limited license to reproduce the Wiley Materials for the purpose specified in the licensing process. This license, **and any CONTENT (PDF or image file) purchased as part of your order**, is for a one-time use only and

https://s100.copyright.com/MyAccount/web/jsp/viewprintablelicensefrommyorders.jsp?ref=6f9f207d-0604-4522-871d-0487f1bbee16&email= 1/3

TERMS AND CONDITIONS

Mar 20, 2025

This Agreement between Mandana Azmi ("You") and Springer Nature ("Springer Nature") consists of your license details and the terms and conditions provided by Springer Nature and Copyright Clearance Center.

License Number	5954760157923
License date	Jan 23, 2025
Licensed Content Publisher	Springer Nature
Licensed Content Publication	Springer eBook
Licensed Content Title	Electrochemical Scanning Tunneling Microscopy
Licensed Content Author	Ilya V. Pobelov, Chen Li, Thomas Wandlowski
Licensed Content Date	Jan 1, 2016
Type of Use	Thesis/Dissertation
Requestor type	academic/university or research institute
Format	print and electronic
Portion	figures/tables/illustrations
Number of figures/tables/illustrations	1
Will you be translating?	no
Circulation/distribution	1 - 29
Author of this Springer Nature content	no
Title of new work	Additive and subtractive processes at solid-liquid interfaces
Institution name	applied Physics (TU Wien)
Expected presentation date	Feb 2025
Portions	Figure related to electrochemical scanning tunneling microscope schematic
The Requesting Person / Organization to Appear on the License	Mandana Azmi
Requestor Location	Miss. Mandana Azmi Wiedner Hauptstraße 8-10/E134 Vienna, 1040 Austria
Billing Type	Invoice
Billing Address	Vienna University of Technology Wiedner Hauptstraße 8-10/E134 Vienna, Austria 1040
Total	**0.00 USD**
Terms and Conditions	

Springer Nature Customer Service Centre GmbH Terms and Conditions

The following terms and conditions ("Terms and Conditions") together with the terms specified in your [RightsLink] constitute the License ("License") between you as Licensee and Springer Nature Customer Service Centre GmbH as Licensor. By clicking 'accept' and completing the transaction for your use of the material ("Licensed Material"), you confirm your acceptance of and obligation to be bound by these Terms and Conditions.

https://s100.copyright.com/MyAccount/web/jsp/viewprintablelicensefrommyorders.jsp?ref=24b3932c-7734-4c5a-b705-d89b7a2637d4&email= 1/4

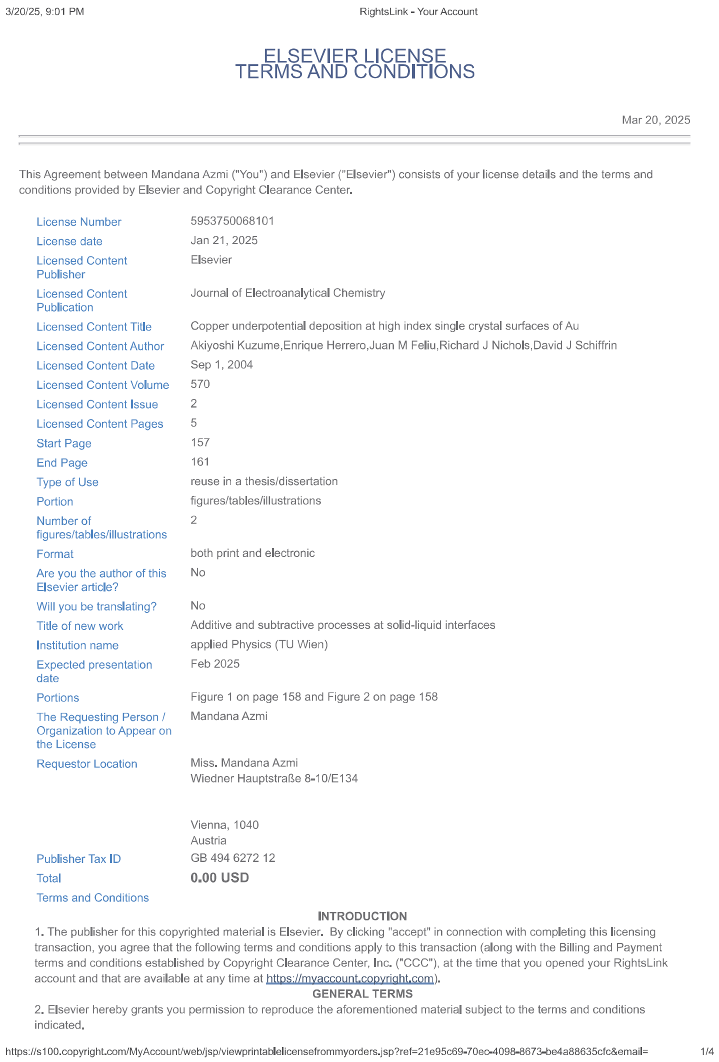

3/20/25, 9:01 PM RightsLink - Your Account

ELSEVIER LICENSE
TERMS AND CONDITIONS

Mar 20, 2025

This Agreement between Mandana Azmi ("You") and Elsevier ("Elsevier") consists of your license details and the terms and conditions provided by Elsevier and Copyright Clearance Center.

License Number	5953750068101
License date	Jan 21, 2025
Licensed Content Publisher	Elsevier
Licensed Content Publication	Journal of Electroanalytical Chemistry
Licensed Content Title	Copper underpotential deposition at high index single crystal surfaces of Au
Licensed Content Author	Akiyoshi Kuzume,Enrique Herrero,Juan M Feliu,Richard J Nichols,David J Schiffrin
Licensed Content Date	Sep 1, 2004
Licensed Content Volume	570
Licensed Content Issue	2
Licensed Content Pages	5
Start Page	157
End Page	161
Type of Use	reuse in a thesis/dissertation
Portion	figures/tables/illustrations
Number of figures/tables/illustrations	2
Format	both print and electronic
Are you the author of this Elsevier article?	No
Will you be translating?	No
Title of new work	Additive and subtractive processes at solid-liquid interfaces
Institution name	applied Physics (TU Wien)
Expected presentation date	Feb 2025
Portions	Figure 1 on page 158 and Figure 2 on page 158
The Requesting Person / Organization to Appear on the License	Mandana Azmi
Requestor Location	Miss. Mandana Azmi Wiedner Hauptstraße 8-10/E134 Vienna, 1040 Austria
Publisher Tax ID	GB 494 6272 12
Total	**0.00 USD**
Terms and Conditions	

INTRODUCTION

1. The publisher for this copyrighted material is Elsevier. By clicking "accept" in connection with completing this licensing transaction, you agree that the following terms and conditions apply to this transaction (along with the Billing and Payment terms and conditions established by Copyright Clearance Center, Inc. ("CCC"), at the time that you opened your RightsLink account and that are available at any time at https://myaccount.copyright.com).

GENERAL TERMS

2. Elsevier hereby grants you permission to reproduce the aforementioned material subject to the terms and conditions indicated.

https://s100.copyright.com/MyAccount/web/jsp/viewprintablelicensefrommyorders.jsp?ref=21e95c69-70ec-4098-8673-be4a88635cfc&email= 1/4

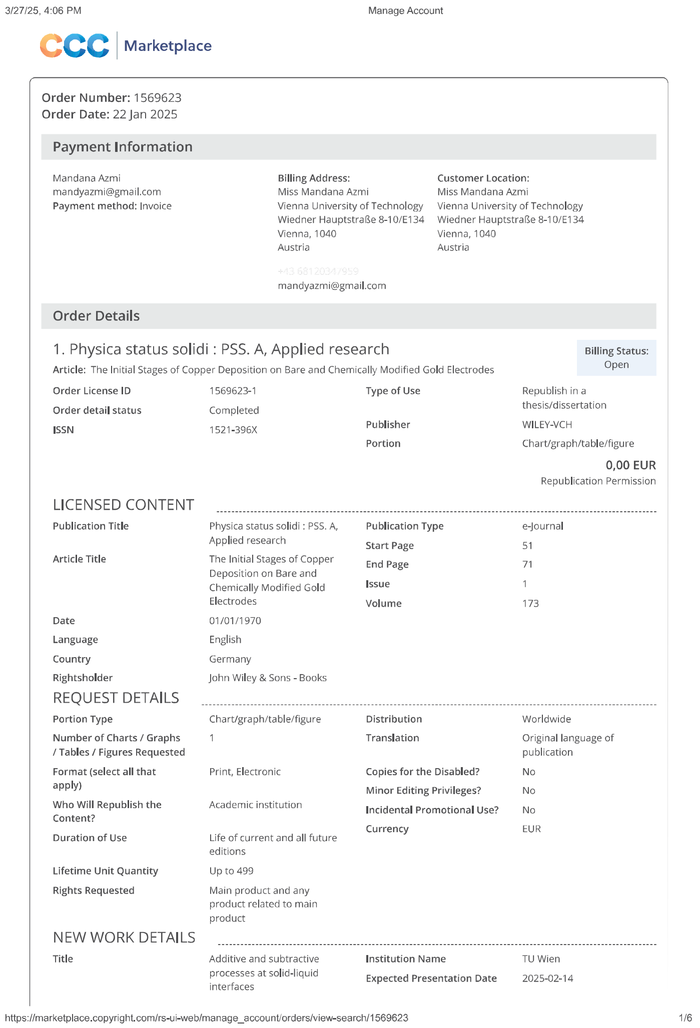

3/27/25, 4:06 PM Manage Account

CCC | Marketplace

Order Number: 1569623
Order Date: 22 Jan 2025

Payment Information

Mandana Azmi
mandyazmi@gmail.com
Payment method: Invoice

Billing Address:
Miss Mandana Azmi
Vienna University of Technology
Wiedner Hauptstraße 8-10/E134
Vienna, 1040
Austria

+43 68120347959
mandyazmi@gmail.com

Customer Location:
Miss Mandana Azmi
Vienna University of Technology
Wiedner Hauptstraße 8-10/E134
Vienna, 1040
Austria

Order Details

1. Physica status solidi : PSS. A, Applied research

Billing Status: Open

Article: The Initial Stages of Copper Deposition on Bare and Chemically Modified Gold Electrodes

Order License ID	1569623-1	**Type of Use**	Republish in a thesis/dissertation
Order detail status	Completed	**Publisher**	WILEY-VCH
ISSN	1521-396X	**Portion**	Chart/graph/table/figure

0,00 EUR
Republication Permission

LICENSED CONTENT

Publication Title	Physica status solidi : PSS. A, Applied research	**Publication Type**	e-Journal
Article Title	The Initial Stages of Copper Deposition on Bare and Chemically Modified Gold Electrodes	**Start Page**	51
		End Page	71
		Issue	1
		Volume	173
Date	01/01/1970		
Language	English		
Country	Germany		
Rightsholder	John Wiley & Sons - Books		

REQUEST DETAILS

Portion Type	Chart/graph/table/figure	**Distribution**	Worldwide
Number of Charts / Graphs / Tables / Figures Requested	1	**Translation**	Original language of publication
Format (select all that apply)	Print, Electronic	**Copies for the Disabled?**	No
		Minor Editing Privileges?	No
Who Will Republish the Content?	Academic institution	**Incidental Promotional Use?**	No
		Currency	EUR
Duration of Use	Life of current and all future editions		
Lifetime Unit Quantity	Up to 499		
Rights Requested	Main product and any product related to main product		

NEW WORK DETAILS

Title	Additive and subtractive processes at solid-liquid interfaces	**Institution Name**	TU Wien
		Expected Presentation Date	2025-02-14

https://marketplace.copyright.com/rs-ui-web/manage_account/orders/view-search/1569623 1/6

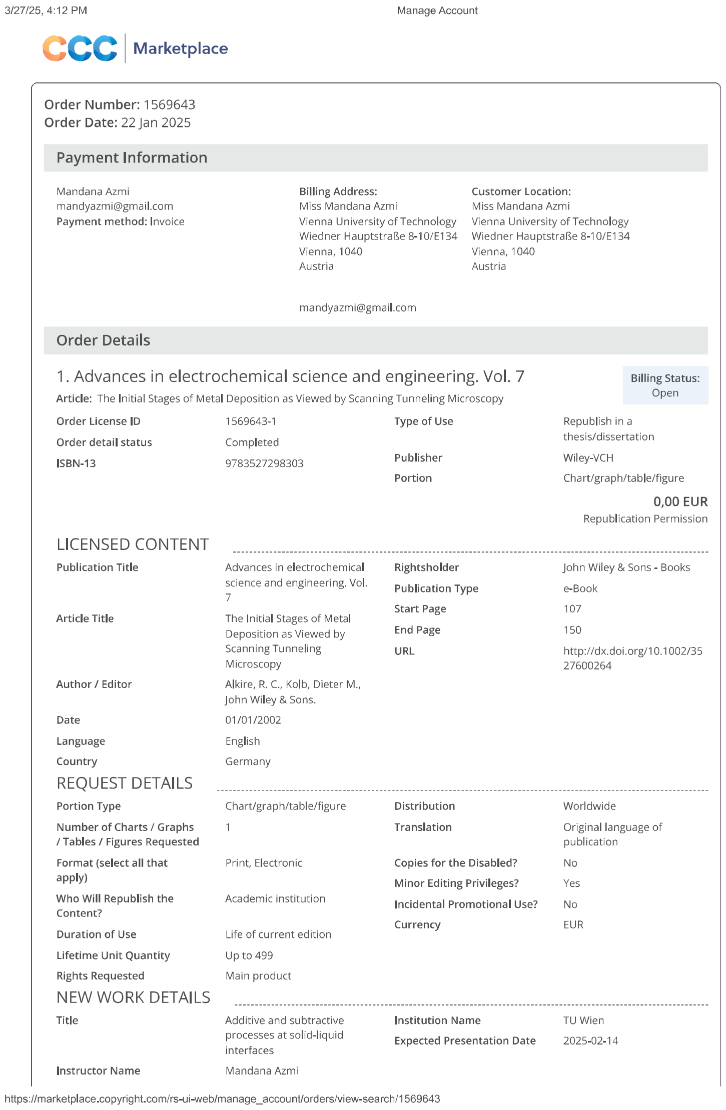

3/27/25, 4:12 PM Manage Account

Marketplace

Order Number: 1569643
Order Date: 22 Jan 2025

Payment Information

Mandana Azmi
mandyazmi@gmail.com
Payment method: Invoice

Billing Address:
Miss Mandana Azmi
Vienna University of Technology
Wiedner Hauptstraße 8-10/E134
Vienna, 1040
Austria

mandyazmi@gmail.com

Customer Location:
Miss Mandana Azmi
Vienna University of Technology
Wiedner Hauptstraße 8-10/E134
Vienna, 1040
Austria

Order Details

1. Advances in electrochemical science and engineering. Vol. 7

Billing Status: Open

Article: The Initial Stages of Metal Deposition as Viewed by Scanning Tunneling Microscopy

Order License ID	1569643-1	**Type of Use**	Republish in a thesis/dissertation
Order detail status	Completed	**Publisher**	Wiley-VCH
ISBN-13	9783527298303	**Portion**	Chart/graph/table/figure

0,00 EUR
Republication Permission

LICENSED CONTENT

Publication Title	Advances in electrochemical science and engineering. Vol. 7	**Rightsholder**	John Wiley & Sons - Books
		Publication Type	e-Book
Article Title	The Initial Stages of Metal Deposition as Viewed by Scanning Tunneling Microscopy	**Start Page**	107
		End Page	150
		URL	http://dx.doi.org/10.1002/3527600264
Author / Editor	Alkire, R. C., Kolb, Dieter M., John Wiley & Sons.		
Date	01/01/2002		
Language	English		
Country	Germany		

REQUEST DETAILS

Portion Type	Chart/graph/table/figure	**Distribution**	Worldwide
Number of Charts / Graphs / Tables / Figures Requested	1	**Translation**	Original language of publication
Format (select all that apply)	Print, Electronic	**Copies for the Disabled?**	No
		Minor Editing Privileges?	Yes
Who Will Republish the Content?	Academic institution	**Incidental Promotional Use?**	No
		Currency	EUR
Duration of Use	Life of current edition		
Lifetime Unit Quantity	Up to 499		
Rights Requested	Main product		

NEW WORK DETAILS

Title	Additive and subtractive processes at solid-liquid interfaces	**Institution Name**	TU Wien
		Expected Presentation Date	2025-02-14
Instructor Name	Mandana Azmi		

https://marketplace.copyright.com/rs-ui-web/manage_account/orders/view-search/1569643 1/6

1/21/25, 7:48 PM Rightslink® by Copyright Clearance Center

Covalent Modification of Graphene and Graphite Using Diazonium Chemistry: Tunable Grafting and Nanomanipulation

Author: John Greenwood, Thanh Hai Phan, Yasuhiko Fujita, et al
Publication: ACS Nano
Publisher: American Chemical Society
Date: May 1, 2015

Copyright © 2015, American Chemical Society

PERMISSION/LICENSE IS GRANTED FOR YOUR ORDER AT NO CHARGE

This type of permission/license, instead of the standard Terms and Conditions, is sent to you because no fee is being charged for your order. Please note the following:

- Permission is granted for your request in both print and electronic formats, and translations.
- If figures and/or tables were requested, they may be adapted or used in part.
- Please print this page for your records and send a copy of it to your publisher/graduate school.
- Appropriate credit for the requested material should be given as follows: "Reprinted (adapted) with permission from {COMPLETE REFERENCE CITATION}. Copyright {YEAR} American Chemical Society." Insert appropriate information in place of the capitalized words.
- One-time permission is granted only for the use specified in your RightsLink request. No additional uses are granted (such as derivative works or other editions). For any uses, please submit a new request.

If credit is given to another source for the material you requested from RightsLink, permission must be obtained from that source.

© 2025 Copyright - All Rights Reserved | Copyright Clearance Center, Inc. | Privacy statement | Data Security and Privacy | For California Residents | Terms and ConditionsComments? We would like to hear from you. E-mail us at customercare@copyright.com

---

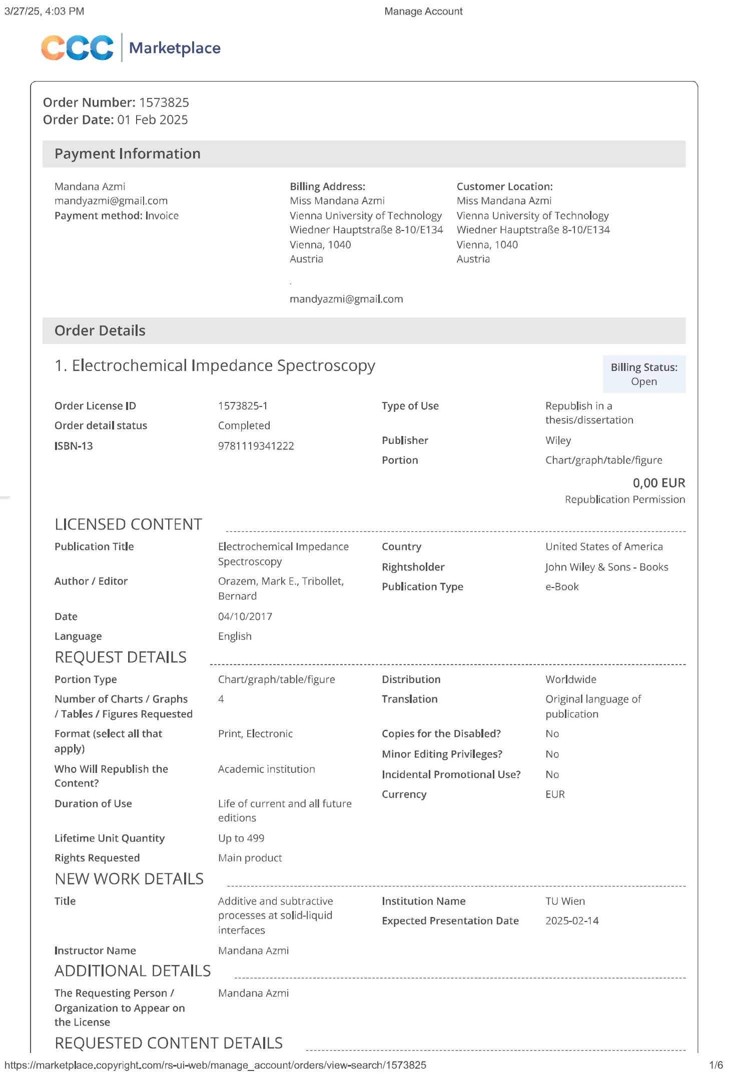

3/27/25, 4:03 PM Manage Account

Marketplace

Order Number: 1573825
Order Date: 01 Feb 2025

Payment Information

Mandana Azmi
mandyazmi@gmail.com
Payment method: Invoice

Billing Address:
Miss Mandana Azmi
Vienna University of Technology
Wiedner Hauptstraße 8-10/E134
Vienna, 1040
Austria

mandyazmi@gmail.com

Customer Location:
Miss Mandana Azmi
Vienna University of Technology
Wiedner Hauptstraße 8-10/E134
Vienna, 1040
Austria

Order Details

1. Electrochemical Impedance Spectroscopy

Billing Status: Open

Order License ID	1573825-1	**Type of Use**	Republish in a thesis/dissertation
Order detail status	Completed	**Publisher**	Wiley
ISBN-13	9781119341222	**Portion**	Chart/graph/table/figure

0,00 EUR
Republication Permission

LICENSED CONTENT

Publication Title	Electrochemical Impedance Spectroscopy	**Country**	United States of America
		Rightsholder	John Wiley & Sons - Books
Author / Editor	Orazem, Mark E., Tribollet, Bernard	**Publication Type**	e-Book
Date	04/10/2017		
Language	English		

REQUEST DETAILS

Portion Type	Chart/graph/table/figure	**Distribution**	Worldwide
Number of Charts / Graphs / Tables / Figures Requested	4	**Translation**	Original language of publication
Format (select all that apply)	Print, Electronic	**Copies for the Disabled?**	No
		Minor Editing Privileges?	No
Who Will Republish the Content?	Academic institution	**Incidental Promotional Use?**	No
		Currency	EUR
Duration of Use	Life of current and all future editions		
Lifetime Unit Quantity	Up to 499		
Rights Requested	Main product		

NEW WORK DETAILS

Title	Additive and subtractive processes at solid-liquid interfaces	**Institution Name**	TU Wien
		Expected Presentation Date	2025-02-14
Instructor Name	Mandana Azmi		

ADDITIONAL DETAILS

The Requesting Person / Organization to Appear on the License	Mandana Azmi

REQUESTED CONTENT DETAILS

https://marketplace.copyright.com/rs-ui-web/manage_account/orders/view-search/1573825 1/6

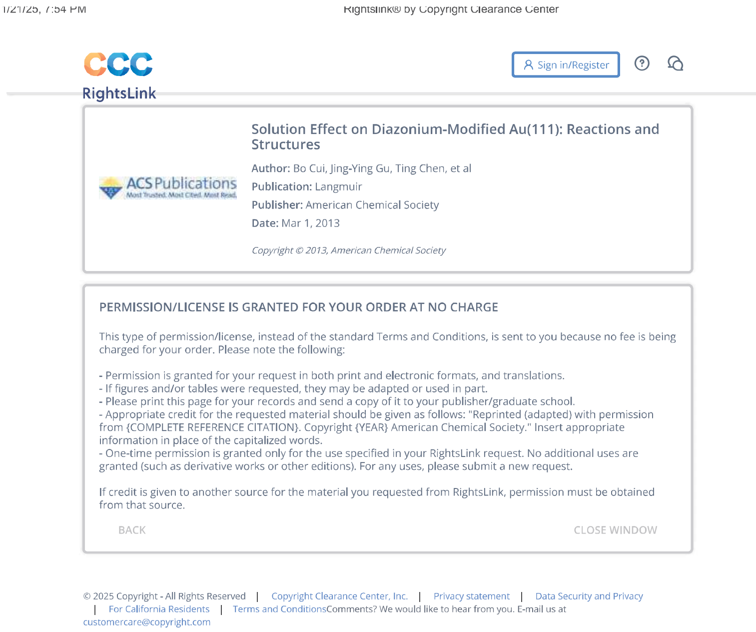

1/21/25, 7:54 PM Rightslink® by Copyright Clearance Center

Solution Effect on Diazonium-Modified Au(111): Reactions and Structures

Author: Bo Cui, Jing-Ying Gu, Ting Chen, et al
Publication: Langmuir
Publisher: American Chemical Society
Date: Mar 1, 2013

Copyright © 2013, American Chemical Society

PERMISSION/LICENSE IS GRANTED FOR YOUR ORDER AT NO CHARGE

This type of permission/license, instead of the standard Terms and Conditions, is sent to you because no fee is being charged for your order. Please note the following:

- Permission is granted for your request in both print and electronic formats, and translations.
- If figures and/or tables were requested, they may be adapted or used in part.
- Please print this page for your records and send a copy of it to your publisher/graduate school.
- Appropriate credit for the requested material should be given as follows: "Reprinted (adapted) with permission from {COMPLETE REFERENCE CITATION}. Copyright {YEAR} American Chemical Society." Insert appropriate information in place of the capitalized words.
- One-time permission is granted only for the use specified in your RightsLink request. No additional uses are granted (such as derivative works or other editions). For any uses, please submit a new request.

If credit is given to another source for the material you requested from RightsLink, permission must be obtained from that source.

© 2025 Copyright - All Rights Reserved | Copyright Clearance Center, Inc. | Privacy statement | Data Security and Privacy | For California Residents | Terms and ConditionsComments? We would like to hear from you. E-mail us at customercare@copyright.com

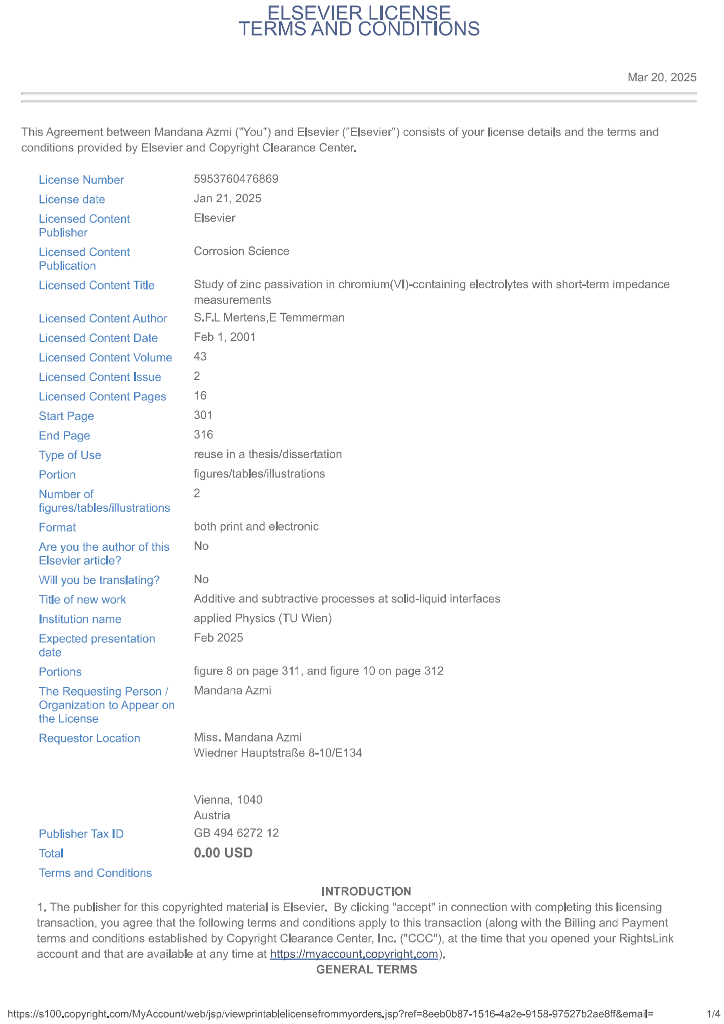

ELSEVIER LICENSE TERMS AND CONDITIONS

Mar 20, 2025

This Agreement between Mandana Azmi ("You") and Elsevier ("Elsevier") consists of your license details and the terms and conditions provided by Elsevier and Copyright Clearance Center.

License Number	5953760476869
License date	Jan 21, 2025
Licensed Content Publisher	Elsevier
Licensed Content Publication	Corrosion Science
Licensed Content Title	Study of zinc passivation in chromium(VI)-containing electrolytes with short-term impedance measurements
Licensed Content Author	S.F.L Mertens,E Temmerman
Licensed Content Date	Feb 1, 2001
Licensed Content Volume	43
Licensed Content Issue	2
Licensed Content Pages	16
Start Page	301
End Page	316
Type of Use	reuse in a thesis/dissertation
Portion	figures/tables/illustrations
Number of figures/tables/illustrations	2
Format	both print and electronic
Are you the author of this Elsevier article?	No
Will you be translating?	No
Title of new work	Additive and subtractive processes at solid-liquid interfaces
Institution name	applied Physics (TU Wien)
Expected presentation date	Feb 2025
Portions	figure 8 on page 311, and figure 10 on page 312
The Requesting Person / Organization to Appear on the License	Mandana Azmi
Requestor Location	Miss. Mandana Azmi Wiedner Hauptstraße 8-10/E134 Vienna, 1040 Austria
Publisher Tax ID	GB 494 6272 12
Total	**0.00 USD**
Terms and Conditions	

INTRODUCTION

1. The publisher for this copyrighted material is Elsevier. By clicking "accept" in connection with completing this licensing transaction, you agree that the following terms and conditions apply to this transaction (along with the Billing and Payment terms and conditions established by Copyright Clearance Center, Inc. ("CCC"), at the time that you opened your RightsLink account and that are available at any time at https://myaccount.copyright.com).

GENERAL TERMS

https://s100.copyright.com/MyAccount/web/jsp/viewprintablelicensefrommyorders.jsp?ref=8eeb0b87-1516-4a2e-9158-97527b2ae8ff&email= 1/4

1/21/25, 6:26 PM Rightslink® by Copyright Clearance Center

RightsLink

Structure of Electrochemically Deposited Iodine Adlayer on Au(111) Studied by Ultrahigh-Vacuum Instrumentation and in Situ STM

Author: Taro Yamada, Nikola Batina, Kingo Itaya
Publication: The Journal of Physical Chemistry A
Publisher: American Chemical Society
Date: May 1, 1995

Copyright © 1995, American Chemical Society

PERMISSION/LICENSE IS GRANTED FOR YOUR ORDER AT NO CHARGE

This type of permission/license, instead of the standard Terms and Conditions, is sent to you because no fee is being charged for your order. Please note the following:

- Permission is granted for your request in both print and electronic formats, and translations.
- If figures and/or tables were requested, they may be adapted or used in part.
- Please print this page for your records and send a copy of it to your publisher/graduate school.
- Appropriate credit for the requested material should be given as follows: "Reprinted (adapted) with permission from {COMPLETE REFERENCE CITATION}. Copyright {YEAR} American Chemical Society." Insert appropriate information in place of the capitalized words.
- One-time permission is granted only for the use specified in your RightsLink request. No additional uses are granted (such as derivative works or other editions). For any uses, please submit a new request.

If credit is given to another source for the material you requested from RightsLink, permission must be obtained from that source.

© 2025 Copyright - All Rights Reserved | Copyright Clearance Center, Inc. | Privacy statement | Data Security and Privacy | For California Residents | Terms and ConditionsComments? We would like to hear from you. E-mail us at customercare@copyright.com

---

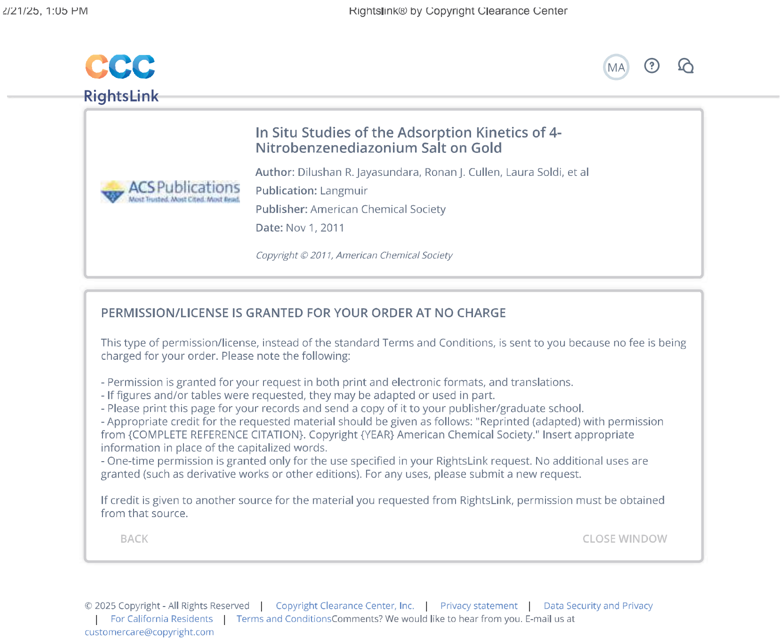

2/21/25, 1:05 PM Rightslink® by Copyright Clearance Center

RightsLink

In Situ Studies of the Adsorption Kinetics of 4-Nitrobenzenediazonium Salt on Gold

Author: Dilushan R. Jayasundara, Ronan J. Cullen, Laura Soldi, et al
Publication: Langmuir
Publisher: American Chemical Society
Date: Nov 1, 2011

Copyright © 2011, American Chemical Society

PERMISSION/LICENSE IS GRANTED FOR YOUR ORDER AT NO CHARGE

This type of permission/license, instead of the standard Terms and Conditions, is sent to you because no fee is being charged for your order. Please note the following:

- Permission is granted for your request in both print and electronic formats, and translations.
- If figures and/or tables were requested, they may be adapted or used in part.
- Please print this page for your records and send a copy of it to your publisher/graduate school.
- Appropriate credit for the requested material should be given as follows: "Reprinted (adapted) with permission from {COMPLETE REFERENCE CITATION}. Copyright {YEAR} American Chemical Society." Insert appropriate information in place of the capitalized words.
- One-time permission is granted only for the use specified in your RightsLink request. No additional uses are granted (such as derivative works or other editions). For any uses, please submit a new request.

If credit is given to another source for the material you requested from RightsLink, permission must be obtained from that source.

© 2025 Copyright - All Rights Reserved | Copyright Clearance Center, Inc. | Privacy statement | Data Security and Privacy | For California Residents | Terms and ConditionsComments? We would like to hear from you. E-mail us at customercare@copyright.com

---

2/21/25, 1:36 PM Rightslink® by Copyright Clearance Center

RightsLink

Some Theoretical and Experimental Insights on the Mechanistic Routes Leading to the Spontaneous Grafting of Gold Surfaces by Diazonium Salts

Author: Avni Berisha, Catherine Combellas, Frédéric Kanoufi, et al
Publication: Langmuir
Publisher: American Chemical Society
Date: Sep 1, 2017

Copyright © 2017, American Chemical Society

PERMISSION/LICENSE IS GRANTED FOR YOUR ORDER AT NO CHARGE

This type of permission/license, instead of the standard Terms and Conditions, is sent to you because no fee is being charged for your order. Please note the following:

- Permission is granted for your request in both print and electronic formats, and translations.
- If figures and/or tables were requested, they may be adapted or used in part.
- Please print this page for your records and send a copy of it to your publisher/graduate school.
- Appropriate credit for the requested material should be given as follows: "Reprinted (adapted) with permission from {COMPLETE REFERENCE CITATION}. Copyright {YEAR} American Chemical Society." Insert appropriate information in place of the capitalized words.
- One-time permission is granted only for the use specified in your RightsLink request. No additional uses are granted (such as derivative works or other editions). For any uses, please submit a new request.

If credit is given to another source for the material you requested from RightsLink, permission must be obtained from that source.

© 2025 Copyright - All Rights Reserved | Copyright Clearance Center, Inc. | Privacy statement | Data Security and Privacy | For California Residents | Terms and ConditionsComments? We would like to hear from you. E-mail us at customercare@copyright.com

---

1/21/25, 6:30 PM Rightslink® by Copyright Clearance Center

RightsLink

Probing redox-induced molecular transformations by atomic-resolution scanning tunneling microscopy: iodide adsorption and electrooxidation on gold(111) in aqueous solution

Author: Xiaoping Gao, Michael J. Weaver
Publication: Journal of the American Chemical Society
Publisher: American Chemical Society
Date: Oct 1, 1992

Copyright © 1992, American Chemical Society

PERMISSION/LICENSE IS GRANTED FOR YOUR ORDER AT NO CHARGE

This type of permission/license, instead of the standard Terms and Conditions, is sent to you because no fee is being charged for your order. Please note the following:

- Permission is granted for your request in both print and electronic formats, and translations.
- If figures and/or tables were requested, they may be adapted or used in part.
- Please print this page for your records and send a copy of it to your publisher/graduate school.
- Appropriate credit for the requested material should be given as follows: "Reprinted (adapted) with permission from {COMPLETE REFERENCE CITATION}. Copyright {YEAR} American Chemical Society." Insert appropriate information in place of the capitalized words.
- One-time permission is granted only for the use specified in your RightsLink request. No additional uses are granted (such as derivative works or other editions). For any uses, please submit a new request.

If credit is given to another source for the material you requested from RightsLink, permission must be obtained from that source.

© 2025 Copyright - All Rights Reserved | Copyright Clearance Center, Inc. | Privacy statement | Data Security and Privacy | For California Residents | Terms and ConditionsComments? We would like to hear from you. E-mail us at customercare@copyright.com

JOHN WILEY AND SONS LICENSE TERMS AND CONDITIONS

Mar 20, 2025

This Agreement between Mandana Azmi ("You") and John Wiley and Sons ("John Wiley and Sons") consists of your license details and the terms and conditions provided by John Wiley and Sons and Copyright Clearance Center.

License Number	5960281263722
License date	Feb 01, 2025
Licensed Content Publisher	John Wiley and Sons
Licensed Content Publication	Advanced Materials Technologies
Licensed Content Title	Inorganic Aqueous Anionic Redox Liquid Electrolyte for Supercapacitors
Licensed Content Author	Hongxia Wang, Le Pang
Licensed Content Date	Sep 12, 2021
Licensed Content Volume	7
Licensed Content Issue	4
Licensed Content Pages	25
Type of Use	Dissertation/Thesis
Requestor type	University/Academic
Format	Print and electronic
Portion	Figure/table
Number of figures/tables	1
Will you be translating?	No
Title of new work	Additive and subtractive processes at solid-liquid interfaces
Institution name	applied Physics (TU Wien)
Expected presentation date	Feb 2025
Portions	Pourbaix diagram (fig. 5)
The Requesting Person / Organization to Appear on the License	Mandana Azmi
Requestor Location	Miss. Mandana Azmi Wiedner Hauptstraße 8-10/E134 Vienna, 1040 Austria
Publisher Tax ID	EU826007151
Total	**0.00 EUR**
Terms and Conditions	

TERMS AND CONDITIONS

This copyrighted material is owned by or exclusively licensed to John Wiley & Sons, Inc. or one of its group companies (each a"Wiley Company") or handled on behalf of a society with which a Wiley Company has exclusive publishing rights in relation to a particular work (collectively "WILEY"). By clicking "accept" in connection with completing this licensing transaction, you agree that the following terms and conditions apply to this transaction (along with the billing and payment terms and conditions established by the Copyright Clearance Center Inc., ("CCC's Billing and Payment terms and conditions"), at the time that you opened your RightsLink account (these are available at any time at http://myaccount.copyright.com).

Terms and Conditions

- The materials you have requested permission to reproduce or reuse (the "Wiley Materials") are protected by copyright.

ELSEVIER LICENSE TERMS AND CONDITIONS

Mar 20, 2025

This Agreement between Mandana Azmi ("You") and Elsevier ("Elsevier") consists of your license details and the terms and conditions provided by Elsevier and Copyright Clearance Center.

License Number	5953740637654
License date	Jan 21, 2025
Licensed Content Publisher	Elsevier
Licensed Content Publication	Hydrometallurgy
Licensed Content Title	Electrochemical behavior of gold in iodide solutions
Licensed Content Author	P.H. Qi,J.B. Hiskey
Licensed Content Date	Mar 1, 1993
Licensed Content Volume	32
Licensed Content Issue	2
Licensed Content Pages	19
Start Page	161
End Page	179
Type of Use	reuse in a thesis/dissertation
Portion	figures/tables/illustrations
Number of figures/tables/illustrations	3
Format	both print and electronic
Are you the author of this Elsevier article?	No
Will you be translating?	No
Title of new work	Additive and subtractive processes at solid-liquid interfaces
Institution name	applied Physics (TU Wien)
Expected presentation date	Feb 2025
Portions	Figure 2 on page 163 Table 1 on page 168 Table 2 on page 168
The Requesting Person / Organization to Appear on the License	Mandana Azmi
Requestor Location	Miss. Mandana Azmi Wiedner Hauptstraße 8-10/E134 Vienna, 1040 Austria
Order reference number	1
Publisher Tax ID	GB 494 6272 12
Total	**0.00 USD**
Terms and Conditions	

INTRODUCTION

1. The publisher for this copyrighted material is Elsevier. By clicking "accept" in connection with completing this licensing transaction, you agree that the following terms and conditions apply to this transaction (along with the Billing and Payment terms and conditions established by Copyright Clearance Center, Inc. ("CCC"), at the time that you opened your RightsLink account and that are available at any time at https://myaccount.copyright.com).

GENERAL TERMS

Bibliography

[1] A. J. Bard. Chemical modification of electrodes. *Journal of Chemical Education*, 60(4):302, 1983.

[2] Manfred Buck. Structure, electrochemistry and applications of self-assembled monolayers of thiols. In R. C. Alkire, D. M. Kolb, J. Lipkowski, and P. N. Ross, editors, *Chemically Modified Electrodes*, pages 197–255. John Wiley & Sons, 2009.

[3] J. C. Love, L.A. Estroff, J. K. Kriebel, R. G. Nuzzo, and G. M. Whitesides. Self-assembled monolayers of thiolates on metals as a form of nanotechnology. *Chemical Reviews*, 105(4):1103–1170, 2005.

[4] A. Ulman. Formation and structure of self-assembled monolayers. *Chemical Reviews*, 96(4):1533–1554, 1996.

[5] C. Vericat, M. E. Vela, G. Corthey, E. Pensa, E. Cortés, M. H. Fonticelli, F. Ibañez, G. E. Benitez, P. Carro, and R. C. Salvarezza. Self-assembled monolayers of thiolates on metals: a review article on sulfur-metal chemistry and surface structures. *RSC Advances*, 4(53):27730–27754, 2014.

[6] C. Vericat, M. E. Vela, G. Benitez, P. Carro, and R. C. Salvarezza. Self-assembled monolayers of thiols and dithiols on gold: new challenges for a well-known system. *Chemical Society Reviews*, 39(5):1805–1834, 2010.

[7] P. Allongue, M. Delamar, B. Desbat, O. Fagebaume, R. Hitmi, J. Pinson, and J. M. Savéant. Covalent modification of carbon surfaces by aryl radicals generated from the electrochemical reduction of diazonium salts. *Journal of the American Chemical Society*, 119(1):201–207, 1997.

[8] M. D'Amours and D. Bélanger. Stability of substituted phenyl groups electrochemically grafted at carbon electrode surface. *The Journal of Physical Chemistry B*, 107(20):4811–4817, 2003.

[9] P. Hapiot, C. Lagrost, and Y. R. Leroux. Molecular nano-structuration of carbon surfaces through reductive diazonium salts grafting. *Current Opinion in Electrochemistry*, 7:103–108, 2018.

[10] S. Baranton and D. Bélanger. Electrochemical derivatization of carbon surface by reduction of in situ generated diazonium cations. *The Journal of Physical Chemistry B*, 109(51):24401–24410, 2005.

[11] J. Greenwood, T. H. Phan, Y. Fujita, Z. Li, O. Ivasenko, W. Vanderlinden, H. Van Gorp, W. Frederickx, G. Lu, K. Tahara, Y. Tobe, H. Uji-i, S. F. L. Mertens, and S. De Feyter. Covalent modification of graphene and graphite using diazonium chemistry: Tunable grafting and nanomanipulation. *ACS Nano*, 9(5):5520–5535, 2015.

[12] T. H. Phan, H. Van Gorp, Zhi Li, T. M. T. Huynh, Y. Fujita, L. Verstraete, S. Eyley, W. Thielemans, H. Uji-i, B. E. Hirsch, et al. Graphite and graphene fairy circles: a bottom-up approach for the formation of nanocorrals. *ACS Nano*, 13(5):5559–5571, 2019.

[13] K. Tahara, Y. Kubo, B. Lindner, S. Hashimoto, S. Hirose, A. Brown, B. Hirsch, L. Daukiya, S. De Feyter, and Y. Tobe. Steric and electronic effects of electrochemically generated aryl radicals on grafting of the graphite surface. *Langmuir*, 35(6):2089–2098, 2019.

[14] B. P. Corgier, C. A. Marquette, and L. Blum. Diazonium-protein adducts for graphite electrode microarrays modification: direct and addressed electrochemical immobilization. *Journal of the American Chemical Society*, 127(51):18328–18332, 2005.

[15] J. J. Gooding. Advances in interfacial design for electrochemical biosensors and sensors: aryl diazonium salts for modifying carbon and metal electrodes. *Electroanalysis: An International Journal Devoted to Fundamental and Practical Aspects of Electroanalysis*, 20(6):573–582, 2008.

[16] J. L. Bahr, J. Yang, D. V. Kosynkin, M. J. Bronikowski, R. E. Smalley, and J. M. Tour. Functionalization of carbon nanotubes by electrochemical reduction of aryl diazonium salts: a bucky paper electrode. *Journal of the American Chemical Society*, 123(27):6536–6542, 2001.

[17] L. Laurentius, S. R. Stoyanov, S. Gusarov, A. Kovalenko, R. Du, G. P. Lopinski, and M. T. McDermott. Diazonium-derived aryl films on gold nanoparticles: Evidence for a carbon–gold covalent bond. *ACS Nano*, 5(5):4219–4227, 2011.

[18] A. A. Mohamed, Z. Salmi, S. A. Dahoumane, A. Mekki, B. Carbonnier, and M. M. Chehimi. Functionalization of nanomaterials with aryldiazonium salts. *Advances in Colloid and Interface Science*, 225:16–36, 2015.

[19] R. McCreery, J. Dieringer, A. O. Solak, B. Snyder, A. M. Nowak, W. R. McGovern, and S. DuVall. Molecular rectification and conductance switching in carbon-based molecular junctions by structural rearrangement accompanying electron injection. *Journal of the American Chemical Society*, 125(35):10748–10758, 2003.

[20] E. M. Dief and N. Darwish. Electrochemically fabricated molecule–electrode contacts for molecular electronics. *Current Opinion in Electrochemistry*, 34:101019, 2022.

[21] B. D. Assresahegn, T. Brousse, and D. Bélanger. Advances on the use of diazonium chemistry for functionalization of materials used in energy storage systems. *Carbon*, 92:362–381, 2015.

[22] P. Mirzaei, S. Bastide, A. Aghajani, J. Bourgon, E. Leroy, J. Zhang, Y. Snoussi, A. Bensghaier, O. Hamouma, M. M. Chehimi, et al. Bimetallic Cu–Rh nanoparticles on diazonium-modified carbon powders for the electrocatalytic reduction of nitrates. *Langmuir*, 35(45):14428–14436, 2019.

[23] S. Han, Y. Yuan, L. Hu, and G. Xu. Electrochemical derivatization of carbon surface by reduction of diazonium salts in situ generated from nitro precursors in aqueous solutions and electrocatalytic ability of the modified electrode toward hydrogen peroxide. *Electrochemistry Communications*, 12(12):1746–1748, 2010.

[24] X. T. Le, G. Zeb, P. Jégou, and T. Berthelot. Electrografting of stainless steel by the diazonium salt of 4-aminobenzylphosphonic acid. *Electrochimica Acta*, 71:66–72, 2012.

[25] A. Chaussé, M. M. Chehimi, N. Karsi, J. Pinson, F. Podvorica, and C. Vautrin-Ul. The electrochemical reduction of diazonium salts on iron electrodes. the formation of covalently bonded organic layers and their effect on corrosion. *Chemistry of Materials*, 14(1):392–400, 2002.

[26] M. Delamar, R. Hitmi, J. Pinson, and J. M. Saveant. Covalent modification of carbon surfaces by grafting of functionalized aryl radicals produced from electrochemical reduction of diazonium salts. *Journal of the American Chemical Society*, 114(14):5883–5884, 1992.

[27] C. Galli. Radical reactions of arenediazonium ions: An easy entry into the chemistry of the aryl radical. *Chemical Reviews*, 88(5):765–792, 1988.

[28] K. Ray and R. L. McCreery. Spatially resolved Raman spectroscopy of carbon electrode surfaces: Observations of structural and chemical heterogeneity. *Analytical Chemistry*, 69(22):4680–4687, 1997.

[29] C. Saby, B. Ortiz, G. Y. Champagne, and D. Bélanger. Electrochemical modification of glassy carbon electrode using aromatic diazonium salts. 1. blocking effect of 4-nitrophenyl and 4-carboxyphenyl groups. *Langmuir*, 13(25):6805–6813, 1997.

[30] V. Bui-Thi-Tuyet, C. Cannizzo, C. Legros, M. Andrieux, and A. Chaussé. Modification of fluorine-doped tin oxide surface: Optimization of the electrochemical grafting of diazonium salt. *Surfaces and Interfaces*, 15:110–116, 2019.

[31] B. L. Hurley and R. L. McCreery. Covalent bonding of organic molecules to Cu and Al alloy 2024 T3 surfaces via diazonium ion reduction. *Journal of The Electrochemical Society*, 151(5):B252, 2004.

[32] J. Pinson and F. Podvorica. Attachment of organic layers to conductive or semiconductive surfaces by reduction of diazonium salts. *Chemical Society Reviews*, 34(5):429–439, 2005.

[33] M. C. Bernard, A. Chaussé, E. Cabet-Deliry, M. M. Chehimi, J. Pinson, F. Podvorica, and C. Vautrin-Ul. Organic layers bonded to industrial, coinage, and noble metals through electrochemical reduction of aryldiazonium salts. *Chemistry of Materials*, 15(18):3450–3462, 2003.

[34] A. Adenier, E. Cabet-Deliry, A. Chaussé, S. Griveau, F. Mercier, J. Pinson, and C. Vautrin-Ul. Grafting of nitrophenyl groups on carbon and metallic surfaces without electrochemical induction. *Chemistry of Materials*, 17(3):491–501, 2005.

[35] L. Daukiya, J. Teyssandier, S. Eyley, S. El Kazzi, M. C. R. Gonzalez, B. Pradhan, W. Thielemans, J. Hofkens, and S. De Feyter. Covalent functionalization of molybdenum disulfide by chemically activated diazonium salts. *Nanoscale*, 13(5):2972–2981, 2021.

[36] M. Delamar, G. Desarmot, O. Fagebaume, R. Hitmi, J. Pinsonc, and J. M. Savéant. Modification of carbon fiber surfaces by electrochemical reduction of aryl diazonium salts: Application to carbon epoxy composites. *Carbon*, 35(6):801–807, 1997.

[37] M. Toupin and D. Bélanger. Thermal stability study of aryl modified carbon black by in situ generated diazonium salt. *The Journal of Physical Chemistry C*, 111(14):5394–5401, 2007.

[38] H. Van Gorp, P. Walke, J. Teyssandier, B. E. Hirsch, H. Uji-i, K. Tahara, Y. Tobe, M. Van der Auweraer, and S. De Feyter. On the thermal stability of aryl groups chemisorbed on graphite. *The Journal of Physical Chemistry C*, 124(3):1980–1990, 2019.

[39] C. Combellas, F. Kanoufi, J. Pinson, and F. I. Podvorica. Sterically hindered diazonium salts for the grafting of a monolayer on metals. *Journal of the American Chemical Society*, 130(27):8576–8577, 2008.

[40] C. Combellas, D. Jiang, F. Kanoufi, J. Pinson, and F. I. Podvorica. Steric effects in the reaction of aryl radicals on surfaces. *Langmuir*, 25(1):286–293, 2009.

[41] A. Adenier, N. Barré, E. Cabet-Deliry, A. Chaussé, S. Griveau, F. Mercier, J. Pinson, and C. Vautrin-Ul. Study of the spontaneous formation of organic layers on carbon and metal surfaces from diazonium salts. *Surface Science*, 600(21):4801–4812, 2006.

[42] J. Lehr, B. E. Williamson, B. S. Flavel, and A. J. Downard. Reaction of gold substrates with diazonium salts in acidic solution at open-circuit potential. *Langmuir*, 25(23):13503–13509, 2009.

[43] F. Barrière and A. J. Downard. Covalent modification of graphitic carbon substrates by non-electrochemical methods. *Journal of Solid State Electrochemistry*, 12:1231–1244, 2008.

[44] M. Toupin and D. Bélanger. Spontaneous functionalization of carbon black by reaction with 4-nitrophenyldiazonium cations. *Langmuir*, 24(5):1910–1917, 2008.

[45] F. Mirkhalaf, J. Paprotny, and D. J. Schiffrin. Synthesis of metal nanoparticles stabilized by metal-carbon bonds. *Journal of the American Chemical Society*, 128(23):7400–7401, 2006.

[46] C. A. Dyke and J. M. Tour. Unbundled and highly functionalized carbon nanotubes from aqueous reactions. *Nano Letters*, 3(9):1215–1218, 2003.

[47] A. Berisha, C. Combellas, F. Kanoufi, J. Pinson, S. Ustaze, and F. I Podvorica. Indirect grafting of acetonitrile-derived films on metallic substrates. *Chemistry of Materials*, 22(9):2962–2969, 2010.

[48] G. Chamoulaud and D. Belanger. Spontaneous derivatization of a copper electrode with in situ generated diazonium cations in aprotic and aqueous media. *The Journal of Physical Chemistry C*, 111(20):7501–7507, 2007.

[49] A. Adenier, M. C. Bernard, M. M. Chehimi, E. Cabet-Deliry, B. Desbat, O. Fagebaume, J. Pinson, and F. Podvorica. Covalent modification of iron surfaces by electrochemical reduction of aryldiazonium salts. *Journal of the American Chemical Society*, 123(19):4541–4549, 2001.

[50] V. Mévellec, S. Roussel, L. Tessier, J. Chancolon, M. Mayne-L'Hermite, G. Deniau, P. Viel, and S. Palacin. Grafting polymers on surfaces: A new powerful and versatile diazonium salt-based one-step process in aqueous media. *Chemistry of Materials*, 19(25):6323–6330, 2007.

[51] D. O. Li, M. S. Gilliam, X. S. Chu, A. Yousaf, Y. Q. Guo, A. A. Green, and Q. H. Wang. Covalent chemical functionalization of semiconducting layered chalcogenide nanosheets. *Molecular Systems Design & Engineering*, 4(4):962–973, 2019.

[52] M. Busson, A. Berisha, C. Combellas, F. Kanoufi, and J. Pinson. Photochemical grafting of diazonium salts on metals. *Chemical Communications*, 47(47):12631–12633, 2011.

[53] M. Bouriga, M. M. Chehimi, C. Combellas, P. Decorse, F. Kanoufi, A. Deronzier, and J. Pinson. Sensitized photografting of diazonium salts by visible light. *Chemistry of Materials*, 25(1):90–97, 2013.

[54] V. Q. Nguyen, Y. Ai, P. Martin, and J. C. Lacroix. Plasmon-induced nanolocalized reduction of diazonium salts. *ACS omega*, 2(5):1947–1955, 2017.

[55] J. Pinson. Attachment of organic layers to materials surfaces by reduction of diazonium salts. In M. M. Chehimi, editor, *Aryl diazonium salts: new coupling agents in polymer and surface science*, pages 1–35, Weinheim, Germany, 2012. John Wiley & Sons.

[56] J. M. Kolotyrkin. Effects of anions on the dissolution kinetics of metals. *Journal of the Electrochemical Society*, 108(3):209, 1961.

[57] G. Y. Wu and W. Schwarzacher. The effect of halide additives on the electrodeposition of Pb on polycrystalline Au. *Journal of Electroanalytical Chemistry*, 629(1-2):164–168, 2009.

[58] G. Y. Wu, S. E. Bae, A. A. Gewirth, J. Gray, X. D. Zhu, T. P. Moffat, and W. Schwarzacher. Pb electrodeposition on polycrystalline Cu in the presence and absence of Cl^-: A combined oblique incidence reflectivity difference and in situ AFM study. *Surface Science*, 601(8):1886–1891, 2007.

[59] T. Yuan, T. Wang, G. Zhang, W. Deng, D. Cheng, H. Gao, J. Zhao, J. Yu, P. Zhang, and J. Gong. The effect of specific adsorption of halide ions on electrochemical CO_2 reduction. *Chemical Science*, 13(27):8117–8123, 2022.

[60] M. Moura de Salles Pupo and R. Kortlever. Electrolyte effects on the electrochemical reduction of CO_2. *ChemPhysChem*, 20(22):2926–2935, 2019.

[61] J. X. Wang, N. S. Marinković, and R. R. Adžić. Structure of Br adlayers in the course of electrocatalytic reactions O_2 reduction of Pt (111) and Au (100). *Colloids and Surfaces A: Physicochemical and Engineering Aspects*, 134(1-2):165–171, 1998.

[62] N. M. Marković, H. A. Gasteiger, B. N. Grgur, and P. N. Ross. Oxygen reduction reaction on Pt (111): effects of bromide. *Journal of Electroanalytical Chemistry*, 467(1-2):157–163, 1999.

[63] V. Stamenkovic, N. M. Markovic, and P. N. Ross. Structure-relationships in electrocatalysis: oxygen reduction and hydrogen oxidation reactions on Pt (111) and Pt (100) in solutions containing chloride ions. *Journal of Electroanalytical Chemistry*, 500(1-2):44–51, 2001.

[64] N. Batina, M. Kunitake, and K. Itaya. Highly ordered molecular arrays formed on iodine-modified Au (111) in solution: in situ STM imaging. *Journal of Electroanalytical Chemistry*, 405(1-2):245–250, 1996.

[65] D. T. Pham, S. L. Tsay, K. Gentz, C. Zoerlein, S. Kossmann, J. S. Tsay, B. Kirchner, K. Wandelt, and P. Broekmann. Quasi-reversible chloride adsorption/desorption through a polycationic organic film on Cu (100). *The Journal of Physical Chemistry C*, 111(44):16428–16436, 2007.

[66] T. H. Phan and K. Wandelt. Molecular self-assembly at metal-electrolyte interfaces. *International Journal of Molecular Sciences*, 14(3):4498–4524, 2013.

[67] K. Itaya, N. Batina, M. Kunitake, K. Ogaki, Y. G. Kim, L. J. Wan, and T. Yamada. In situ scanning tunneling microscopy of organic molecules adsorbed on iodine-modified Au (111), Ag (111), and Pt (111) electrodes. In Gregory Jerkiewicz, Manuel P. Soriaga, Kohei Uosaki, and Andrzej Wieckowski, editors, *Solid-Liquid Electrochemical Interfaces*, pages 171–188, Washington, DC, 1997. American Chemical Society.

[68] S. N. Thorgaard and P. Bühlmann. Bromine-passivated Au (111) as a platform for the formation of organic self-assembled monolayers under electrochemical conditions. *Langmuir*, 26(10):7133–7137, 2010.

[69] Y. C. Yang, C. Y. Chen, and Y. L. Lee. Highly ordered C_{60} monolayer self-assembled by using an iodine template on an Au (111) surface in solution. *Langmuir*, 24(20):11611–11615, 2008.

[70] T. Kosmala, M. Blanco, G. Granozzi, and K. Wandelt. Porphyrin bi-layer formation induced by a surface confined reduction on an iodine-modified Au (100) electrode surface. *Electrochimica Acta*, 360:137026, 2020.

[71] T. M. T. Huynh, T. H. Phan, P. H. Nguyen, and K. Wandelt. Self-assembly of porphyrin molecules on a Cu (111) electrode: Influence of different anions and electrode potential. *Surface Science*, 694:121554, 2020.

[72] M. Nakamura, Y. Tanaka, M. Takahasi, H. Tajiri, O. Sakata, and N. Hoshi. Structural dynamics of adsorption equilibrium for iodine adsorbed on Au (111). *The Journal of Physical Chemistry C*, 124(32):17711–17716, 2020.

[73] X. Wang, Z. Y. Yi, Y. Q. Wang, and D. Wang. Molecular evidence for the axial coordination effect of atomic iodine on Fe$-$N$_4$ sites in oxygen reduction reaction. *Angewandte Chemie International Edition*, (e202413673), 2024.

[74] O. M. Magnussen. Ordered anion adlayers on metal electrode surfaces. *Chemical Reviews*, 102(3):679–726, 2002.

[75] A. Chen, Z. Shi, D. Bizzotto, J. Lipkowski, B. Pettinger, and C. Bilger. Iodide adsorption at the Au (111) electrode surface. *Journal of Electroanalytical Chemistry*, 467(1-2):342–353, 1999.

[76] B. G. Bravo, S. L. Michelhaugh, M. P. Soriaga, I. Villegas, D. W. Suggs, and J. L. Stickney. Anodic underpotential deposition and cathodic stripping of iodine at polycrystalline and single-crystal gold: studies by LEED, AES, XPS, and electrochemistry. *The Journal of Physical Chemistry*, 95(13):5245–5249, 1991.

[77] R. L. McCarley and A. J. Bard. Scanning tunneling microscopy studies of iodide adsorption on gold (111): direct observation of adlattice orientation. *The Journal of Physical Chemistry*, 95(24):9618–9620, 1991.

[78] X. Gao and M. J. Weaver. Probing redox-induced molecular transformations by atomic-resolution scanning tunneling microscopy: iodide adsorption and electrooxidation on gold (111) in aqueous solution. *Journal of the American Chemical Society*, 114(22):8544–8551, 1992.

[79] N. Tao and S. M. Lindsay. In situ scanning tunneling microscopy study of iodine and bromine adsorption on Au (111) under potential control. *The Journal of Physical Chemistry*, 96(13):5213–5217, 1992.

[80] T. Yamada, N. Batina, and K. Itaya. Interfacial structure of iodine electrodeposited on Au (111): studies by LEED and in situ STM. *Surface Science*, 335:204–209, 1995.

[81] R. McHardy, W. H. Haiss, and R. J. Nichols. An STM investigation of surface diffusion on iodine modified Au (111). *Physical Chemistry Chemical Physics*, 2(7):1439–1444, 2000.

[82] T. Utsunomiya, S. Tatsumi, Y. Yokota, and K. Fukui. Potential-dependent structures investigated at the perchloric acid solution/iodine modified Au (111) interface by electrochemical frequency-modulation atomic force microscopy. *Physical Chemistry Chemical Physics*, 17(19):12616–12622, 2015.

[83] S. A. Cochran and H. H. Farrell. The chemisorption of iodine on gold. *Surface Science*, 95(2-3):359–366, 1980.

[84] N. Batina, T. Yamada, and K. Itaya. Atomic level characterization of the iodine-modified Au (111) electrode surface in perchloric acid solution by in-situ STM and ex-situ LEED. *Langmuir*, 11(11):4568–4576, 1995.

[85] Z. V. Zheleva, V. R. Dhanak, and G. Held. Experimental structure determination of the chemisorbed overlayers of chlorine and iodine on Au {111}. *Physical Chemistry Chemical Physics*, 12(36):10754–10758, 2010.

[86] X. Gao and M. J. Weaver. New type of periodic long-range restructuring of ordered metal surfaces induced by lateral adsorbate interactions: Iodide on Au (110) electrodes. *Physical Review Letters*, 73(6):846, 1994.

[87] M. A. Tadayyoni, P. Gao, and M. J. Weaver. Application of surface-enhanced Raman spectroscopy to mechanistic electrochemistry: Oxidation of iodide at gold electrodes. *Journal of Electroanalytical Chemistry and Interfacial Electrochemistry*, 198(1):125–136, 1986.

[88] P. H. Svensson and L. Kloo. Synthesis, structure, and bonding in polyiodide and metal iodide - iodine systems. *Chemical Reviews*, 103(5):1649–1684, 2003.

[89] T. Yamada, N. Batina, and K. Itaya. Structure of electrochemically deposited iodine adlayer on Au (111) studied by ultrahigh-vacuum instrumentation and in situ STM. *The Journal of Physical Chemistry*, 99(21):8817–8823, 1995.

[90] M. J. Weaver and X. Gao. In-situ electrochemical surface science. *Annual Review of Physical Chemistry*, 44(1):459–494, 1993.

[91] B. M. Ocko, G. M. T. Watson, and J. Wang. Structure and electrocompression of electrodeposited iodine monolayers on gold (111). *The Journal of Physical Chemistry*, 98(3):897–906, 1994.

[92] O. A. Oviedo, L. Reinaudi, S. G. García, and E. P. M. Leiva. *Underpotential deposition*. Springer Cham, 2016.

[93] H. H. Girault. *Analytical and physical electrochemistry*. EPFL Press, 2004.

[94] C. H. Hamann. *Electrochemistry 2nd Edition*. Wiley-VCH, 2007.

[95] A. J. Bard and L. R. Faulkner. *Electrochemical Methods: Fundamentals and Applications, 2nd Edition*. Wiley, 2001.

[96] R. G. Compton and C. E. Banks. *Understanding voltammetry*. World Scientific, 2018.

[97] H. Matsuda and Y. Ayabe. On the theory of the Randles-Sevcik cathode-ray polarography. *Zeitschrift für Elektrochemie, Berichte der Bunsengesellschaft für physikalische Chemie*, 59:494–503, 1955.

[98] R. S. Nicholson. Theory and application of cyclic voltammetry for measurement of electrode reaction kinetics. *Analytical chemistry*, 37(11):1351–1355, 1965.

[99] D. A. C. Brownson, D. K. Kampouris, and C. E. Banks. Graphene electrochemistry: fundamental concepts through to prominent applications. *Chemical Society Reviews*, 41(21):6944–6976, 2012.

[100] I. Lavagnini, R. Antiochia, and F. Magno. An extended method for the practical evaluation of the standard rate constant from cyclic voltammetric data. *Electroanalysis: An International Journal Devoted to Fundamental and Practical Aspects of Electroanalysis*, 16(6):505–506, 2004.

[101] R. J. Klingler and J. K. Kochi. Electron-transfer kinetics from cyclic voltammetry. quantitative description of electrochemical reversibility. *The Journal of Physical Chemistry*, 85(12):1731–1741, 1981.

[102] G. P. Morris, A. N. Simonov, E. A. Mashkina, R. Bordas, K. Gillow, R. E. Baker, D. J. Gavaghan, and A. M. Bond. A comparison of fully automated methods of data analysis and computer assisted heuristic methods in an electrode kinetic study of the pathologically variable $[\mathrm{Fe(CN)}_6]^{\frac{3-}{4-}}$ process by AC voltammetry. *Analytical Chemistry*, 85(24):11780–11787, 2013.

[103] T. J. Davies and R. G. Compton. The cyclic and linear sweep voltammetry of regular and random arrays of microdisc electrodes: Theory. *Journal of Electroanalytical Chemistry*, 585(1):63–82, 2005.

[104] A. S. Peinetti, R. S. Gilardoni, M. Mizrahi, F. G. Requejo, G. A. González, and F. Battaglini. Numerical simulation of the diffusion processes in nanoelectrode arrays using an axial neighbor symmetry approximation. *Analytical Chemistry*, 88(11):5752–5759, 2016.

[105] M. E. Orazem and B. Tribollet. *Electrochemical Impedance Spectroscopy, 2nd Edition*. Wiley, 2017.

[106] S. M. Park and J. S. Yoo. Peer reviewed: electrochemical impedance spectroscopy for better electrochemical measurements. *Analytical Chemistry*, 75(21):455–461A, 2003.

[107] B. Hirschorn, M. E. Orazem, B. Tribollet, V. Vivier, I. Frateur, and M. Musiani. Determination of effective capacitance and film thickness from constant-phase-element parameters. *Electrochimica Acta*, 55(21):6218–6227, 2010.

[108] C. H. Hsu and F. Mansfeld. Concerning the conversion of the constant phase element parameter Y^0 into a capacitance. *Corrosion*, 57(09):747–748, 2001.

[109] A. C. Lazanas and M. I. Prodromidis. Electrochemical impedance spectroscopy-A tutorial. *ACS Measurement Science Au*, 3(3):162–193, 2023.

[110] V. Ganesh, S. K. Pal, S. Kumar, and V. Lakshminarayanan. Self-assembled monolayers (SAMs) of alkoxycyanobiphenyl thiols on gold - A study of electron transfer reaction using cyclic voltammetry and electrochemical impedance spectroscopy. *Journal of Colloid and Interface Science*, 296(1):195–203, 2006.

[111] G. Binnig, H. Rohrer, Ch. Gerber, and E. Weibel. Tunneling through a controllable vacuum gap. *Applied Physics Letters*, 40(2):178–180, 1982.

[112] J. C. Chen. *Introduction to scanning tunneling microscopy*. Oxford university Press, 1993.

[113] K. S. Mali, N. Pearce, S. De Feyter, and N. R. Champness. Frontiers of supramolecular chemistry at solid surfaces. *Chemical Society Reviews*, 46(9):2520–2542, 2017.

[114] W. Mamdouh, H. Uji-i, J. S. Ladislaw, A. E. Dulcey, V. Percec, F. C. De Schryver, and S. De Feyter. Solvent controlled self-assembly at the liquid-solid interface revealed by STM. *Journal of the American Chemical Society*, 128(1):317–325, 2006.

[115] Y. Yang and C. Wang. Solvent effects on two-dimensional molecular self-assemblies investigated by using scanning tunneling microscopy. *Current Opinion in Colloid and Interface Science*, 14(2):135–147, 2009.

[116] I. V. Pobelov, C. Li, and T. Wandlowski. Electrochemical scanning tunneling microscopy. In Bharat Bhushan, editor, *Encyclopedia of Nanotechnology*, pages 688–702. Springer Netherlands, Dordrecht, 2016.

[117] K. Gentz and K. Wandelt. Electrochemical scanning tunneling microscopy. *Chimia*, 66(1-2):44–51, 2012.

[118] S. Ernst, S. Wirth, M. Rams, V. O. Dolocan, and F. Steglich. Tip preparation for usage in an ultra-low temperature UHV scanning tunneling microscope. *Science and Technology of Advanced Materials*, 8(5):347–351, 2007.

[119] L. Bartels, G. Meyer, and K-H Rieder. Controlled vertical manipulation of single CO molecules with the scanning tunneling microscope: A route to chemical contrast. *Applied Physics Letters*, 71(2):213–215, 1997.

[120] L. Gross, N. Moll, F. Mohn, A. Curioni, G. Meyer, F. Hanke, and M. Persson. High-resolution molecular orbital imaging using ap-wave STM tip. *Physical Review Letters*, 107(8):086101, 2011.

[121] S. W. Hla, K. F. Braun, V. Iancu, and A. Deshpande. Single-atom extraction by scanning tunneling microscope tip crash and nanoscale surface engineering. *Nano Letters*, 4(10):1997–2001, 2004.

[122] G. Binnig, H. Rohrer, Ch. Gerber, and E. Weibel. Surface studies by scanning tunneling microscopy. *Physical Review Letters*, 49(1):57, 1982.

[123] M. Müllner. *Oxides in Aqueous Solution: Stability and Activity at the Atomic Scale*. PhD thesis, Faculty of Physics, Vienna University of Technology, 2021.

[124] T. M. T. Huynh, T. H. Phan, O. Ivasenko, S. F. L. Mertens, and S. De Feyter. Nanoconfined self-assembly on a grafted graphitic surface under electrochemical control. *Nanoscale*, 9(1):362–368, 2017.

[125] M. Azmi, E. De Bonis, S. K. Guin, L. Ashton, and S. F. L. Mertens. A new look at metal–carbon hybrids: Molecular-scale study of covalently grafted gold. *Electrochimica Acta*, 500:144743, 2024.

[126] M. Kullapere, J. Kozlova, L. Matisen, V. Sammelselg, H. A. Menezes, G. Maia, D. J. Schiffrin, and K. Tammeveski. Electrochemical properties of aryl-modified gold electrodes. *Journal of Electroanalytical Chemistry*, 641(1-2):90–98, 2010.

[127] A. Laforgue, T. Addou, and D. Bélanger. Characterization of the deposition of organic molecules at the surface of gold by the electrochemical reduction of aryldiazonium cations. *Langmuir*, 21(15):6855–6865, 2005.

[128] J. Lyskawa and D. Bélanger. Direct modification of a gold electrode with aminophenyl groups by electrochemical reduction of in situ generated aminophenyl monodiazonium cations. *Chemistry of Materials*, 18(20):4755–4763, 2006.

[129] G. Liu, T. Böcking, and J. J. Gooding. Diazonium salts: Stable monolayers on gold electrodes for sensing applications. *Journal of Electroanalytical Chemistry*, 600(2):335–344, 2007.

[130] C. L. Chevalier and E. C. Landis. Electrochemical attachment of diazonium-generated films on nanoporous gold. *Langmuir*, 31(31):8633–8641, 2015.

[131] M. G. Paulik, P. A. Brooksby, A. D. Abell, and A. J. Downard. Grafting aryl diazonium cations to polycrystalline gold: Insights into film structure using gold oxide reduction, redox probe electrochemistry, and contact angle behavior. *The Journal of Physical Chemistry C*, 111(21):7808–7815, 2007.

[132] A. J. Downard and M. J. Prince. Barrier properties of organic monolayers on glassy carbon electrodes. *Langmuir*, 17(18):5581–5586, 2001.

[133] X. Cui, D. Jiang, P. Diao, J. Li, R. Tong, and X. Wang. Assessing the apparent effective thickness of alkanethiol self-assembled monolayers in different concentrations of $[\mathrm{Fe(CN)_6}]^{3-}/[\mathrm{Fe(CN)_6}]^{4-}$ by ac impedance spectroscopy. *Journal of Electroanalytical Chemistry*, 470(1):9–13, 1999.

[134] P. Diao, M. Guo, D. Jiang, Z. Jia, X. Cui, D. Gu, R. Tong, and B. Zhong. Fractional coverage of defects in self-assembled thiol monolayers on gold. *Journal of Electroanalytical Chemistry*, 480(1-2):59–63, 2000.

[135] D. M. Kolb. Reconstruction phenomena at metal-electrolyte interfaces. *Progress in Surface Science*, 51(2):109–173, 1996.

[136] A. Cuesta, M. Kleinert, and D. M. Kolb. The adsorption of sulfate and phosphate on Au (111) and Au (100) electrodes: an in situ STM study. *Physical Chemistry Chemical Physics*, 2(24):5684–5690, 2000.

[137] S. F. L. Mertens. Adsorption and self-organization of organic molecules under electrochemical control. In *Encyclopedia of Interfacial Chemistry: Surface Science and Electrochemistry; Ed. Klaus Wandelt*, pages 13–23. Elsevier, 2018.

[138] O. M. Magnussen, J. Hageböck, J. Hotlos, and R. J. Behm. In situ scanning tunnelling microscopy observations of a disorder–order phase transition in hydrogensulfate adlayers on Au (111). *Faraday Discussions*, 94:329–338, 1992.

[139] G. J. Edens, X. Gao, and M. J. Weaver. The adsorption of sulfate on gold (111) in acidic aqueous media: adlayer structural inferences from infrared spectroscopy and scanning tunneling microscope. *Journal of Electroanalytical Chemistry*, 375(1-2):357–366, 1994.

[140] D. Jiang, B. G. Sumpter, and S. Dai. Structure and bonding between an aryl group and metal surfaces. *Journal of the American Chemical Society*, 128(18):6030–6031, 2006.

[141] K. Cui, K. S. Mali, O. Ivasenko, D. Wu, X. Feng, M. Walter, K. Müllen, S. De Feyter, and S. F. L. Mertens. Squeezing, then stacking: From breathing pores to three-dimensional ionic self-assembly under electrochemical control. *Angewandte Chemie International Edition*, 53(47):12951–12954, 2014.

[142] K. Cui, K. S. Mali, D. Wu, X. Feng, K. Müllen, M. Walter, S. De Feyter, and S. F. L. Mertens. Reversible anion-driven switching of an organic 2d crystal at a solid–liquid interface. *Small*, 13(46):1702379, 2017.

[143] K. Cui, I. Dorner, and S. F. L. Mertens. Interfacial supramolecular electrochemistry. *Current Opinion in Electrochemistry*, 8:156–163, 2018.

[144] K. Cui, K. S. Mali, D. Wu, X. Feng, K. Müllen, M. Walter, S. De Feyter, and S. F. L. Mertens. Ambient bistable single dipole switching in a molecular monolayer. *Angewandte Chemie International Edition*, 59(33):14049–14053, 2020.

[145] Z. Li, K. Mali, P. Hapiot, S. De Feyter, A. J. Attias, and S. F. L. Mertens. Reversible redox-driven crystallization in a paracyclophane monolayer at a solid–liquid interface. *Advanced Functional Materials*, page 2315861, 2024.

[146] B. Han, Z. Li, T. Wandlowski, A. Błaszczyk, and M. Mayor. Potential-induced redox switching in viologen self-assembled monolayers: an ATR-SEIRAS approach. *The Journal of Physical Chemistry C*, 111(37):13855–13863, 2007.

[147] U. Zhumaev, A. V. Rudnev, J. F. Li, A. Kuzume, T. H. Vu, and T. Wandlowski. Electro-oxidation of Au (111) in contact with aqueous electrolytes: New insight from in situ vibration spectroscopy. *Electrochimica Acta*, 112:853–863, 2013.

[148] S. Cherevko, A. A. Topalov, A. R. Zeradjanin, I. Katsounaros, and K. J. J. Mayrhofer. Gold dissolution: towards understanding of noble metal corrosion. *RSC Advances*, 3(37):16516–16527, 2013.

[149] S. F. L. Mertens, A. Bütikofer, L. Siffert, and T. Wandlowski. Covalent versus electrostatic strategies for nanoparticle immobilisation. *Electroanalysis*, 22(24):2940–2946, 2010.

[150] S. F. L. Mertens. Copper underpotential deposition on boron nitride nanomesh. *Electrochimica Acta*, 246:730–736, 2017.

[151] L. M. Malard, M. A. Pimenta, G. Dresselhaus, and M. S. Dresselhaus. Raman spectroscopy in graphene. *Physics Reports*, 473(5-6):51–87, 2009.

[152] X. Wang, D. MacKenzie, and Z. Cui. Complement or competitior? comparing car2go and transit travel times, prices, and usage patterns in seattle. Technical report, Transportation Research Board, National Academies, 2017.

[153] M. Inagaki, T. Isogai, K. Motobayashi, K. Q. Lin, B. Ren, and K. Ikeda. Electronic and vibrational surface-enhanced Raman scattering: from atomically defined Au (111) and (100) to roughened Au. *Chemical Science*, 11(36):9807–9817, 2020.

[154] G. Socrates. *Infrared and Raman characteristic group frequencies: tables and charts*. John Wiley & Sons, 2004.

[155] H. Li, G. Kopiec, F. Müller, F. Nyßen, K. Shimizu, M. Ceccato, K. Daasbjerg, and N. Plumeré. Spectroscopic evidence for a covalent sigma Au–C bond on Au surfaces using ^{13}C isotope labeling. *JACS Au*, 1(3):362–368, 2021.

[156] D. M. Shewchuk and M. T. McDermott. Comparison of diazonium salt derived and thiol derived nitrobenzene layers on gold. *Langmuir*, 25(8):4556–4563, 2009.

[157] S. J. Konopka and B. McDuffie. Diffusion coefficients of ferri-and ferrocyanide ions in aqueous media, using twin-electrode thin-layer electrochemistry. *Analytical Chemistry*, 42(14):1741–1746, 1970.

[158] J. Moldenhauer, M. Meier, and D. W. Paul. Rapid and direct determination of diffusion coefficients using microelectrode arrays. *Journal of The Electrochemical Society*, 163(8):H672, 2016.

[159] O. Seri. Kinetic parameter determination of ferri/ferrocyanide redox reaction using differentiating polarization curve technique. *Electrochimica Acta*, 323:134776, 2019.

[160] J. Oslonovitch, Y. J. Li, C. Donner, and K. Krischer. The $\mathrm{Fe(CN)_6}^{3-}/\mathrm{Fe(CN)_6}^{4-}$ charge transfer reaction on Au (111) revisited in the presence and absence of a two-dimensional, condensed organic film. *Journal of Electroanalytical Chemistry*, 541:163–174, 2003.

[161] C. A. Amatore, J. M. Savéant, and D. Tessier. Charge transfer at partially blocked surfaces: A model for the case of microscopic active and inactive sites. *Journal of Electroanalytical Chemistry and Interfacial Electrochemistry*, 147(1-2):39–51, 1983.

[162] T. J. Davies, C. E. Banks, and R. G. Compton. Voltammetry at spatially heterogeneous electrodes. *Journal of Solid State Electrochemistry*, 9:797–808, 2005.

[163] R. C. Alkire, D. M. Kolb, J. Lipkowski, and P. N. Ross. *Chemically modified electrodes*. John Wiley & Sons, 2009.

[164] K. Jackowska and P. Krysiński. *Applied Electrochemistry: Aspects in Material and Environmental Science*. Walter de Gruyter GmbH & Co KG, 2020.

[165] M.A. Schneeweiss, H. Hagenström, M. J. Esplandiu, and D. M. Kolb. Electrolytic metal deposition onto chemically modified electrodes. *Applied Physics A*, 69:537–551, 1999.

[166] A. Kuzume, E. Herrero, J. M. Feliu, R. J. Nichols, and D. J. Schiffrin. Copper underpotential deposition at high index single crystal surfaces of Au. *Journal of Electroanalytical Chemistry*, 570(2):157–161, 2004.

[167] M. A. Schneeweiss and D. M. Kolb. The initial stages of copper deposition on bare and chemically modified gold electrodes. *physica status solidi (a)*, 173(1):51–71, 1999.

[168] Z. Shi, S. Wu, and J. Lipkowski. Coadsorption of metal atoms and anions: Cu upd in the presence of $\mathrm{SO_4}^{2-}$, $\mathrm{Cl^-}$ and $\mathrm{Br^-}$. *Electrochimica Acta*, 40(1):9–15, 1995.

[169] J. Hotlos, O. M. Magnussen, and R. J. Behm. Effect of trace amounts of Cl^- in Cu underpotential deposition on Au (111) in perchlorate solutions: an in-situ scanning tunneling microscopy study. *Surface Science*, 335:129–144, 1995.

[170] E. Herrero, L. J. Buller, and H. D. Abruña. Underpotential deposition at single crystal surfaces of Au, Pt, Ag and other materials. *Chemical Reviews*, 101(7):1897–1930, 2001.

[171] I. V. Pobelov, G. Nagy, and T. Wandlowski. Structure transitions between copper-sulphate and copper-chloride UPD phases on Au (111). *Journal of Chemical Sciences*, 121:745–756, 2009.

[172] S. Wu, Z. Shi, J. Lipkowski, A. P. Hitchcock, and T. Tyliszczak. Early stages of copper electrocrystallization: electrochemical and in situ X-ray absorption fine structure studies of coadsorption of copper and chloride at the Au (111) electrode surface. *The Journal of Physical Chemistry B*, 101(49):10310–10322, 1997.

[173] H. Aitchison, N. Meyerbröker, T. L. Lee, J. Zegenhagen, T. Potter, H. Früchtl, I. Cebula, and M. Buck. Underpotential deposition of Cu on Au (111) from neutral chloride containing electrolyte. *Physical Chemistry Chemical Physics*, 19(35):24146–24153, 2017.

[174] D. Chen, Q. Tao, L. W. Liao, S. X. Liu, Y. X. Chen, and S. Ye. Determining the active surface area for various platinum electrodes. *Electrocatalysis*, 2:207–219, 2011.

[175] C. L. Green and A. Kucernak. Determination of the platinum and ruthenium surface areas in platinum-ruthenium alloy electrocatalysts by underpotential deposition of copper. I. unsupported catalysts. *The Journal of Physical Chemistry B*, 106(5):1036–1047, 2002.

[176] S. Trasatti and O. A. Petrii. Real surface area measurements in electrochemistry. *Journal of Electroanalytical Chemistry*, 327(1-2):353–376, 1992.

[177] Y. Liu, S. Bliznakov, and N. Dimitrov. Comprehensive study of the application of a Pb underpotential deposition-assisted method for surface area measurement of metallic nanoporous materials. *The Journal of Physical Chemistry C*, 113(28):12362–12372, 2009.

[178] E. Garnier, F. J. Vidal-Iglesias, J. M. Feliu, and J. Solla-Gullón. Surface structure characterization of shape and size controlled Pd nanoparticles by Cu UPD: a quantitative approach. *Frontiers in Chemistry*, 7:527, 2019.

[179] H. Tang, J. H. Chen, M. Y. Wang, L. H. Nie, Kuang Y. F., and S. Z. Yao. Controlled synthesis of platinum catalysts on Au nanoparticles and their electrocatalytic property for methanol oxidation. *Applied Catalysis A: General*, 275(1-2):43–48, 2004.

[180] S. W. T. Price, J. D. Speed, P. Kannan, and A. E. Russell. Exploring the first steps in core-shell electrocatalyst preparation: in situ characterization of the underpotential deposition of Cu on supported Au nanoparticles. *Journal of the American Chemical Society*, 133(48):19448–19458, 2011.

[181] J. X. Wang, H. Inada, L. Wu, Y. Zhu, Y. M. Choi, P. Liu, W. P. Zhou, and R. R. Adzic. Oxygen reduction on well-defined core-shell nanocatalysts: particle size, facet, and Pt shell thickness effects. *Journal of the American Chemical Society*, 131(47):17298–17302, 2009.

[182] J. Zhang, Y. Mo, M. B. Vukmirovic, R. Klie, K. Sasaki, and R. R. Adzic. Platinum monolayer electrocatalysts for O_2 reduction: Pt monolayer on Pd (111) and on carbon-supported Pd nanoparticles. *The Journal of Physical Chemistry B*, 108(30):10955–10964, 2004.

[183] Y. Yanson, J. W. M. Frenken, and M. J. Rost. A general model of metal underpotential deposition in the presence of thiolbased additives based on an in situ STM study. *Physical Chemistry Chemical Physics*, 13(35):16095–16103, 2011.

[184] A. Kumar, H. A. Biebuyck, N. L. Abbott, and G. M. Whitesides. The use of self-assembled monolayers and a selective etch to generate patterned gold features. *Journal of the American Chemical Society*, 114(23):9188–9189, 1992.

[185] A. Kumar and G. M. Whitesides. Features of gold having micrometer to centimeter dimensions can be formed through a combination of stamping with an elastomeric stamp and an alkanethiol “ink” followed by chemical etching. *Applied Physics Letters*, 63(14):2002–2004, 1993.

[186] T. Schmaltz, G. Sforazzini, T. Reichert, and H. Frauenrath. Self-assembled monolayers as patterning tool for organic electronic devices. *Advanced Materials*, 29(18):1605286, 2017.

[187] T. Baunach, V. Ivanova, D. M. Kolb, H-G Boyen, P. Ziemann, M. Büttner, and P. Oelhafen. A new approach to the electrochemical metallization of organic monolayers: Palladium deposition onto a 4, 4’-Dithiodipyridine self-assembled monolayer. *Advanced Materials*, 16(22):2024–2028, 2004.

[188] M. Nishizawa, T. Sunagawa, and H. Yoneyama. Underpotential deposition of copper on gold electrodes through self-assembled monolayers of propanethiol. *Langmuir*, 13(20):5215–5217, 1997.

[189] L. Sun and R. M. Crooks. Imaging of defects contained within n-alkylthiol monolayers by combination of underpotential deposition and scanning tunneling microscopy: Kinetics of self-assembly. *Journal of the Electrochemical Society*, 138(8):L23, 1991.

[190] D. M. Kolb. The initial stages of metal deposition as viewed by scanning tunneling microscopy. *Advances in Electrochemical Science and Engineering*, 7:107–150, 2002.

[191] C. Silien and M. Buck. On the role of extrinsic and intrinsic defects in the underpotential deposition of Cu on thiol-modified Au (111) electrodes. *The Journal of Physical Chemistry C*, 112(10):3881–3890, 2008.

[192] J. A. M. Sondag-Huethorst and L. G. J. Fokkink. Galvanic copper deposition on thiol-modified gold electrodes. *Langmuir*, 11(12):4823–4831, 1995.

[193] T. Hachiya, H. Honbo, and K. Itaya. Detailed underpotential deposition of copper on gold (III) in aqueous solutions. *Journal of Electroanalytical Chemistry and Interfacial Electrochemistry*, 315(1-2):275–291, 1991.

[194] M. H. Hölzle, T. Wandlowski, and D. M. Kolb. Phase transition in uracil adlayers on electrochemically prepared island-free Au (100)-(1×1). *Journal of Electroanalytical Chemistry*, 394(1-2):271–275, 1995.

[195] S. Ye, C. Ishibashi, and K. Uosaki. Anisotropic dissolution of an Au (111) electrode in perchloric acid solution containing chloride anion investigated by in situ STM the important role of adsorbed chloride anion. *Langmuir*, 15(3):807–812, 1999.

[196] S. Ye, C. Ishibashi, K. Shimazu, and K. Uosaki. An in situ electrochemical quartz crystal microbalance study of the dissolution process of a gold electrode in perchloric acid solution containing chloride ion. *Journal of The Electrochemical Society*, 145(5):1614, 1998.

[197] S. F. L. Mertens, C. Vollmer, A. Held, M. H. Aguirre, M. Walter, C. Janiak, and T. Wandlowski. Ligand-free cluster quantized charging in an ionic liquid. *Angewandte Chemie International Edition*, 50(41):9735–9738, 2011.

[198] U. Bilibio, L. H. de Oliveira, V. S. Ferreira, and M. A. G. Trindade. Enhanced simultaneous electroanalytical determination of two fluoroquinolones by using surfactant media and a peak deconvolution procedure. *Microchemical Journal*, 116:47–54, 2014.

[199] J. V. Kamat, S. K. Guin, J. S. Pillai, and S. K. Aggarwal. Scope of detection and determination of gallium (III) in industrial ground water by square wave anodic stripping voltammetry on bismuth film electrode. *Talanta*, 86:256–265, 2011.

[200] M. A. M. Rodrigo, J. Molina-López, A. M. J. Jimenez, E. P. Del Pozo, P. Adam, T. Eckschlager, O. Zitka, L. Richtera, and V. Adam. The application of curve fitting on the voltammograms of various isoforms of metallothioneins–metal complexes. *International Journal of Molecular Sciences*, 18(3):610, 2017.

[201] M. H. Hölzle, V. Zwing, and D. M. Kolb. The influence of steps on the deposition of Cu onto Au (111). *Electrochimica Acta*, 40(10):1237–1247, 1995.

[202] M. H. Hölzle, C. W. Apsel, T. Will, and D. M. Kolb. Copper deposition onto Au (111) in the presence of thiourea. *Journal of the Electrochemical Society*, 142(11):3741, 1995.

[203] C. M. Whelan, M. R. Smyth, and C. J. Barnes. The influence of heterocyclic thiols on the electrodeposition of Cu on Au (111). *Journal of Electroanalytical Chemistry*, 441(1):109–129, 1998.

[204] D. Oyamatsu, S. Kuwabata, and H. Yoneyama. Underpotential deposition behavior of metals onto gold electrodes coated with self-assembled monolayers of alkanethiols. *Journal of Electroanalytical Chemistry*, 473(1):59–67, 1999.

[205] D. Oyamatsu, M. Nishizawa, S. Kuwabata, and H. Yoneyama. Underpotential deposition of silver onto gold substrates covered with self-assembled monolayers of alkanethiols to induce intervention of the silver between the monolayer and the gold substrate. *Langmuir*, 14(12):3298–3302, 1998.

[206] J. R. I. Lee, R. L. O'Malley, T. J. O'Connell, A. Vollmer, and T. Rayment. X-ray absorption spectroscopy characterization of Cu underpotential deposition on Au (111) and organothiol-self-assembled-monolayer-modified Au (111) electrodes from sulfate supporting electrolyte. *The Journal of Physical Chemistry C*, 113(28):12260–12271, 2009.

[207] R. J. Nichols, W. Beckmann, H. Meyer, N. Batina, and D. M. Kolb. An in situ scanning tunnelling microscopy study of bulk copper deposition and the influence of an organic additive. *Journal of Electroanalytical Chemistry*, 330(1-2):381–394, 1992.

[208] D. M. Kolb. Electrochemical surface science. *Angewandte Chemie International Edition*, 40(7):1162–1181, 2001.

[209] S. Niyogi, E. Bekyarova, M. E. Itkis, H. Zhang, K. Shepperd, J. Hicks, M. Sprinkle, C. Berger, C. N. Lau, W. A. DeHeer, et al. Spectroscopy of covalently functionalized graphene. *Nano Letters*, 10(10):4061–4066, 2010.

[210] Q. H. Wang, Z. Jin, K. K. Kim, A. J. Hilmer, G. L. C. Paulus, C. J. Shih, M. H. Ham, J. D. Sanchez-Yamagishi, K. Watanabe, T. Taniguchi, et al. Understanding and controlling the substrate effect on graphene electron-transfer chemistry via reactivity imprint lithography. *Nature Chemistry*, 4(9):724–732, 2012.

[211] A. C. Ferrari and J. Robertson. Interpretation of Raman spectra of disordered and amorphous carbon. *Physical Review B*, 61(20):14095, 2000.

[212] B. Cui, J. Y. Gu, T. Chen, H. J. Yan, D. Wang, and L. J. Wan. Solution effect on diazonium-modified Au (111): Reactions and structures. *Langmuir*, 29(9):2955–2960, 2013.

[213] Y. T. Kim and A. J. Bard. Imaging and etching of self-assembled n-octadecanethiol layers on gold with the scanning tunneling microscope. *Langmuir*, 8(4):1096–1102, 1992.

[214] J. V. Barth, H. Brune, G. Ertl, and R. J. Behm. Scanning tunneling microscopy observations on the reconstructed Au (111) surface: Atomic structure, long-range superstructure, rotational domains, and surface defects. *Physical Review B*, 42(15):9307, 1990.

[215] T. Smith. The hydrophilic nature of a clean gold surface. *Journal of Colloid and Interface Science*, 75(1):51–55, 1980.

[216] C. D. Wagner. Studies of the charging of insulators in ESCA. *Journal of Electron Spectroscopy and Related Phenomena*, 18(3):345–349, 1980.

[217] T. L. Barr and S. Seal. Nature of the use of adventitious carbon as a binding energy standard. *Journal of Vacuum Science & Technology A: Vacuum, Surfaces, and Films*, 13(3):1239–1246, 1995.

[218] K. Siegbahn. ESCA: atomic, molecular and solid state structure studies by means of electron spectroscopy. *Nova Acta Regiae Societatis Scientiarum Upsaliensis*, 1967.

[219] G. Greczynski and L. Hultman. Xray photoelectron spectroscopy: towards reliable binding energy referencing. *Progress in Materials Science*, 107:100591, 2020.

[220] C. E. Taylor, S. D. Garvey, and J. E. Pemberton. Carbon contamination at silver surfaces: surface preparation procedures evaluated by Raman spectroscopy and X-ray photoelectron spectroscopy. *Analytical Chemistry*, 68(14):2401–2408, 1996.

[221] S. Hüfner, G. K. Wertheim, and R. Laham Cohen. Argon ion sputtering of metallic surfaces for ESCA studies. *Physica Scripta*, 5(1-2):91, 1972.

[222] E. Taglauer. Surface cleaning using sputtering. *Applied Physics A*, 51:238–251, 1990.

[223] M. D. Li, Y. Cui, M. X. Gao, J. Luo, B. Ren, and Z. Q. Tian. Clean substrates prepared by chemical adsorption of iodide followed by electrochemical oxidation for surface-enhanced Raman spectroscopic study of cell membrane. *Analytical Chemistry*, 80(13):5118–5125, 2008.

[224] P. Qi and J. B. Hiskey. Electrochemical behavior of gold in iodide solutions. *Hydrometallurgy*, 32(2):161–179, 1993.

[225] L. M. Yang and S. L. Yau. The structures of iodine and carbon monoxide overlayers on Ir (111) electrodes: An in situ scanning tunneling microscopy study. *The Journal of Physical Chemistry B*, 104(8):1769–1776, 2000.

[226] L. Huang, P. Zeppenfeld, S. Horch, and G. Comsa. Determination of iodine adlayer structures on Au (111) by scanning tunneling microscopy. *The Journal of Chemical Physics*, 107(2):585–591, 1997.

[227] A. Migani and F. Illas. A systematic study of the structure and bonding of halogens on low-index transition metal surfaces. *The Journal of Physical Chemistry B*, 110(24):11894–11906, 2006.

[228] E. de la Llave, A. Ricci, E. J. Calvo, and D. A. Scherlis. Binding between carbon and the Au (111) surface and what makes it different from the S-Au (111) bond. *The Journal of Physical Chemistry C*, 112(45):17611–17617, 2008.

[229] M. Gomberg and W. E. Bachmann. The synthesis of biaryl compounds by means of the diazo reaction. *Journal of the American Chemical Society*, 46(10):2339–2343, 1924.

[230] S. F. L. Mertens and E. Temmerman. Study of interfacial film growth with ac measurements. *Journal of Colloid and Interface Science*, 227(2):517–524, 2000.

[231] R. P. Janek, W. R. Fawcett, and A. Ulman. Impedance spectroscopy of self-assembled monolayers on Au (111): sodium ferrocyanide charge transfer at modified electrodes. *Langmuir*, 14(11):3011–3018, 1998.

[232] K. Ariyoshi, Z. Siroma, A. Mineshige, M. Takeno, T. Fukutsuka, T. Abe, and S. Uchida. Electrochemical impedance spectroscopy part 1: fundamentals. *Electrochemistry*, 90(10):102007–102007, 2022.

[233] D. Qu, G. Wang, J. Kafle, J. Harris, L. Crain, Z. Jin, and D. Zheng. Electrochemical impedance and its applications in energy-storage systems. *Small Methods*, 2(8):1700342, 2018.

[234] C. Ho, I. D. Raistrick, and R. A. Huggins. Application of a-c techniques to the study of lithium diffusion in tungsten trioxide thin films. *Journal of The Electrochemical Society*, 127(2):343, 1980.

[235] T. Pajkossy, M. U. Ceblin, and G. Meszaros. Dynamic electrochemical impedance spectroscopy for the charge transfer rate measurement of the ferro/ferricyanide redox couple on gold. *Journal of Electroanalytical Chemistry*, 899:115655, 2021.

[236] C. Ribaut, K. Reybier, B. Torbiero, J. Launay, A. Valentin, O. Reynes, P. L. Fabre, and F. Nepveu. Strategy of red blood cells immobilisation onto a gold electrode: Characterization by electrochemical impedance spectroscopy and quartz crystal microbalance. *IRBM*, 29(2-3):141–148, 2008.

[237] S. F. L. Mertens and E. Temmerman. Study of zinc passivation in chromium (VI)-containing electrolytes with short-term impedance measurements. *Corrosion Science*, 43(2):301–316, 2001.

[238] P. Allongue, C. H. de Villeneuve, G. Cherouvrier, R. Cortes, and M. C. Bernard. Phenyl layers on H-Si (111) by electrochemical reduction of diazonium salts: monolayer versus multilayer formation. *Journal of Electroanalytical Chemistry*, 550-551:161–174, 2003.

[239] J. Wu. Understanding the electric double-layer structure, capacitance, and charging dynamics. *Chemical Reviews*, 122(12):10821–10859, 2022.

[240] S. F. L. Mertens and E. Temmerman. Electrical models for shielded electrodes. *ACH-Models in Chemistry*, 137:95–102, 2000.

[241] D. R. Jayasundara, R. J. Cullen, L. Soldi, and P. E. Colavita. In situ studies of the adsorption kinetics of 4-nitrobenzenediazonium salt on gold. *Langmuir*, 27(21):13029–13036, 2011.

[242] D. R. Jayasundara, R. J. Cullen, and P. E. Colavita. In situ and real time characterization of spontaneous grafting of aryldiazonium salts at carbon surfaces. *Chemistry of Materials*, 25(7):1144–1152, 2013.

[243] M. S. Strano, C. A. Dyke, M. L. Usrey, P. W. Barone, M. J. Allen, H. Shan, C. Kittrell, R. H. Hauge, J. M. Tour, and R. E. Smalley. Electronic structure control of single-walled carbon nanotube functionalization. *Science*, 301(5639):1519–1522, 2003.

[244] M. L. Usrey, E. S. Lippmann, and M. S. Strano. Evidence for a two-step mechanism in electronically selective single-walled carbon nanotube reactions. *Journal of the American Chemical Society*, 127(46):16129–16135, 2005.

[245] N. Nair, W. J. Kim, M. L. Usrey, and M. S. Strano. A structure-reactivity relationship for single walled carbon nanotubes reacting with 4-hydroxybenzene diazonium salt. *Journal of the American Chemical Society*, 129(13):3946–3954, 2007.

[246] F. M. Koehler, A. Jacobsen, K. Ensslin, C. Stampfer, and W. J. Stark. Selective chemical modification of graphene surfaces: distinction between single-and bilayer graphene. *Small*, 6(10):1125–1130, 2010.

[247] A. Berisha, C. Combellas, F. Kanoufi, P. Decorse, N. Oturan, J. Médard, M. Seydou, F. Maurel, and J. Pinson. Some theoretical and experimental insights on the mechanistic routes leading to the spontaneous grafting of gold surfaces by diazonium salts. *Langmuir*, 33(35):8730–8738, 2017.

[248] C. Gabrielli, F. Huet, and R. P. Nogueira. Electrochemical impedance of H_2-evolving Pt electrode under bubble-induced and forced convections in alkaline solutions. *Electrochimica Acta*, 47(13-14):2043–2048, 2002.

[249] R. Ozbay, A. Kibar, and C. H. Choi. Bubble adhesion to superhydrophilic surfaces. *Advances in Contact Angle, Wettability and Adhesion*, 2:149–164, 2015.

[250] A. Kibar, R. Ozbay, M. A. Sarshar, Y. T. Kang, and C. H. Choi. Bubble movement on inclined hydrophobic surfaces. *Langmuir*, 33(43):12016–12027, 2017.

[251] V. T. Calabrese and A. Khan. Polyiodine and polyiodide species in an aqueous solution of iodine + KI: Theoretical and experimental studies. *The Journal of Physical Chemistry A*, 104(6):1287–1292, 2000.

[252] O. M. Magnussen. Atomic-scale insights into electrode surface dynamics by high-speed scanning probe microscopy. *Chemistry–A European Journal*, 25(56):12865–12883, 2019.

[253] M. Müllner, J. Balajka, M. Schmid, U. Diebold, and S. F. L. Mertens. Self-limiting adsorption of WO_3 oligomers on oxide substrates in solution. *The Journal of Physical Chemistry C*, 121(36):19743–19750, 2017.

[254] J. Gottschalck and B. Hammer. A density functional theory study of the adsorption of sulfur, mercapto, and methylthiolate on Au (111). *The Journal of Chemical Physics*, 116(2):784–790, 2002.

[255] I. A. Pašti and S. V. Mentus. Halogen adsorption on crystallographic (111) planes of Pt, Pd, Cu and Au, and on Pd-monolayer catalyst surfaces: First-principles study. *Electrochimica Acta*, 55(6):1995–2003, 2010.

[256] X. Gao, Y. Zhang, and M. J. Weaver. Observing surface chemical transformations by atomic-resolution scanning tunneling microscopy: sulfide electrooxidation on gold (111). *The Journal of Physical Chemistry*, 96(11):4156–4159, 1992.

[257] C. Schlaup, D. Friebel, P. Broekmann, and K. Wandelt. Potential dependent adlayer structures of a sulfur-covered Au (111) electrode in alkaline solution: An in situ STM study. *Surface Science*, 602(4):864–870, 2008.

[258] L. Pang and H. Wang. Inorganic aqueous anionic redox liquid electrolyte for supercapacitors. *Advanced Materials Technologies*, 7(4):2100501, 2022.

[259] C. Vericat, G. Andreasen, M. E. Vela, and R. C. Salvarezza. Dynamics of potential-dependent transformations in sulfur adlayers on Au (111) electrodes. *The Journal of Physical Chemistry B*, 104(2):302–307, 2000.

[260] M. D. Lay, K. Varazo, and J. L. Stickney. Formation of sulfur atomic layers on gold from aqueous solutions of sulfide and thiosulfate: studies using EC-STM, UHV-EC, and TLEC. *Langmuir*, 19(20):8416–8427, 2003.

[261] A. Houel, D. Tonneau, N. Bonnail, H. Dallaporta, and V. I. Safarov. Direct patterning of nanostructures by field-induced deposition from a scanning tunneling microscope tip. *Journal of Vacuum Science & Technology B: Microelectronics and Nanometer Structures Processing, Measurement, and Phenomena*, 20(6):2337–2345, 2002.

[262] H. J. Mamin, P. H. Guethner, and D. Rugar. Atomic emission from a gold scanning-tunneling-microscope tip. *Physical Review Letters*, 65(19):2418, 1990.

[263] H. J. Mamin, S. Chiang, H. Birk, P. H. Guethner, and D. Rugar. Gold deposition from a scanning tunneling microscope tip. *Journal of Vacuum Science & Technology B: Microelectronics and Nanometer Structures Processing, Measurement, and Phenomena*, 9(2):1398–1402, 1991.

[264] K. Bessho and S. Hashimoto. Fabricating nanoscale structures on Au surface with scanning tunneling microscope. *Applied Physics Letters*, 65(17):2142–2144, 1994.

[265] M. Olsen, M. Hummelgård, and H. Olin. Surface modifications by field induced diffusion. *PLOS One*, 7(1):1–8, 2012.

[266] D. Erts, A. Lohmus, R. Lohmus, H. Olin, A. V. Pokropivny, L. Ryen, and K. Svensson. Force interactions and adhesion of gold contacts using a combined atomic force microscope and transmission electron microscope. *Applied Surface Science*, 188(3-4):460–466, 2002.